Role of interstitial atoms in microstructures and mechanical properties of TiNbZr and TiNbZrHfTa complex concentrated alloys

Von der Fakultät für Georessourcen und Materialtechnik der

Rheinisch-Westfälischen Technischen Hochschule Aachen

zur Erlangung des akademischen Grades eines

Doktors der Ingenieurwissenschaften

genehmigte Dissertation

vorgelegt von

Chengguang Wu, M.Sc.

Berichter: apl. Prof. Dr.-Ing. Dierk Raabe

Asst. Prof. Yan Ma

Tag der mündlichen Prüfung: 30.06.2025

Diese Dissertation ist auf den Internetseiten der Universitätsbibliothek online verfügbar

路漫漫其修远兮，吾将上下而求索

Long, long is my road, and far, far is the journey; high and low, up and down, I'll search with will

-Yuan Qu (屈原), 《*Li Sao (The Lament)*》

Declaration on Publications

This thesis is a cumulative one, encompassing the following articles that have been published, submitted, or are ready for submission to peer-reviewed journals. These manuscripts are:

Hydrogen accommodation and its role in lattice symmetry in a TiNbZr medium-entropy alloy

Chengguang Wu, Yilun Gong, Chang Liu, Xuehan Li, Gökhan Gizer, Claudio Pistidda, Fritz Körmann, Yan Ma, Jörg Neugebauer, Dierk Raabe

Acta Materialia, DOI: 10.1016/j.actamat.2025.120852

In this study, I characterized the alloys by using *in-situ* HEXRD and SEM. I analyzed the data and discussed it with all the authors. I wrote the draft of the manuscript and conceptualized it with Y. Ma and D. Raabe.

Hydrogen-assisted spinodal decomposition in a TiNbZrHfTa complex concentrated alloy

Chengguang Wu, Leonardo Shoji Aota, Jing Rao, Xukai Zhang, Loïc Perrière, Maria Jazmin Duarte Correa, Dierk Raabe, Yan Ma

Acta Materialia, DOI: 10.1016/j.actamat.2024.120707

In this study, I characterized the alloys by using HEXRD, SEM, and APT. I did the calculation. I analyzed the data and discussed it with all the authors. I wrote the draft of the manuscript and conceptualized it with Y. Ma and D. Raabe.

Role of boron in yield strength softening and plastic deformation mechanisms in a refractory high-entropy alloy

Chengguang Wu, Shaolou Wei, Unai Aizpurua, Loïc Perriere, Jean-Philippe Couzinié, Yan Ma, Dierk Raabe

Ready for submission

In this study, I characterized the alloys by using SEM and APT. I did the tensile tests. I analyzed the data and discussed it with all the authors. I wrote the draft of the manuscript and conceptualized it with S.L. Wei, Y. Ma, and D. Raabe

Enhanced ductility in a TiNbZr alloy via nanoscale elemental heterogeneity induced by a short-term induction treatment

Chengguang Wu, Shaolou Wei, Guillaume Hachet, Yan Ma, Dierk Raabe

In preparation

In this study, I characterized the alloys by using SEM, SAXS and APT. I did the tensile tests. I analyzed the data and discussed it with all the authors. I wrote the draft of the manuscript and conceptualized it with S.L. Wei, Y. Ma, and D. Raabe

Acknowledgment

Since beginning my PhD journey on November 1st, 2021, more than three years have flown by in what feels like the blink of an eye. Undoubtedly, this marks another significant turning point in my life. At every such juncture, it's natural to feel a sense of uncertainty or being momentarily adrift.

After nearly four years at the Max Planck Institute for Sustainable Materials (MPI-Susmat, formerly Max-Planck-Institut für Eisenforschung), I have found it to be an enjoyable and fulfilling place to study. This journey has undoubtedly been a meaningful and treasured experience—pleasant and rewarding, albeit sometimes challenging. At this moment, I would like to take some time to express my gratitude:

A big thank you to Prof. Raabe, for accepting me into your team and providing me with the opportunity to learn and embark on my research journey within such a prestigious, world-renowned platform. I am deeply grateful for your unwavering support and supervision throughout my entire PhD. Although you are always busy with your work, you always make time to listen to my "naïve and silly" thoughts and patiently offer your valuable suggestions. Your unwavering passion for truth, resilience in overcoming challenges, and boundless enthusiasm for science are truly unmatched. These qualities have profoundly influenced me and laid the foundation for my scientific understanding and approach.

I am also sincerely thankful to Prof. Jochen M. Schneider for your interest and co-advising of the present work.

To Prof. Dr. Yan Ma (my second supervisor), for your unwavering support, continuous encouragement, and insightful guidance throughout my PhD journey. Your constructive discussions, invaluable suggestions, and thoughtful feedback have been instrumental in my growth as a researcher. With your help, I have overcome numerous obstacles, and for that, I sincerely thank you.

To Dr. Shaolou Wei (both a senior and a friend): I have deeply benefited from your extensive expertise in materials science and physical metallurgy, which has guided my decisions through ongoing discussions and insightful feedback. Your positive approach and unwavering enthusiasm for research have been truly inspiring, constantly motivating me to move forward and grow as an independent and critical-thinking researcher.

I would also like to express my sincere gratitude to Dr. Liuliu Han and his family (Dr. Jin Wang and their lovely daughter, Ximu Han) for their unwavering support throughout my entire PhD journey. Their kindness has made me feel at home, even while being overseas. The time we spent together—playing basketball, having discussions, chatting, and even venting our complaints—will undoubtedly become cherished memories, ones I will recall fondly, even after many years.

Many thanks to Prof. Dr. Stefan Zaefferer for his nurturing nature to all PhD students/Postdoc researchers and the unconditional support in his fields of expertise (SEM-related techniques).

I would like to extend my heartfelt gratitude to my supportive colleagues at/outside MPI-Susmat: Dr. Xizhen Dong, for the invaluable guidance and support during the final stages of my PhD studies; Dr. Xinren Chen, my friendly roommate throughout most of my PhD journey; Prof. Dr. Alfons Fischer, for the enlightenment and encouragement, particularly at the beginning of my challenging times; Mr. Daniel Otto de Mentock, my dear friend at MPIE, who was always willing to lend an ear and listen to my thoughts; Dr. Guillaume Hachet, for the technical exchanges and fruitful discussions; Prof. Jean-Philippe Couzinié, for his kind support and technical exchanges on my topics; Mr. Lennart Hitzemann, for his kind support on my PhD thesis. I would also like to thank Prof. Baptise Gault, Dr. Dirk Ponge, Dr. Mohamed Naguib Elkot, Dr. Leonardo Shoji Aota, Dr. Jing Rao, Dr. Xin Geng, Dr. Xuyang Zhou, Dr. Ziyuan Rao, Dr. Yue Li, Dr. Chuanlai Liu, Dr. Yuxiang Wu, Dr. Chang Liu, Dr. Yilun Gong, Dr. Anurag Bajpai, Dr. Faisal Waqar Syed, Dr. Yujun Zhao, Dr. Barak Ratzker, Dr. Eric Woods, Mr. Guangyi Guo, Mr. Longqi Bai, Ms. Hongyu Chen, Mr. Waleed Mohammed, Mr. Manuel Gathmann, Ms. Özge Özgün, Mr. Ubaid Manzoor, Mr. Kartik Sunil Umate, and Mr. Shiv Shankar for their invaluable supports and encouragements.

To the most reliable, supportive, and friendly technicians, Ms. Monika Nellessen (for the training of SEM), Ms. Katja Angenendet, Mr. Christian Broß, Ms. Heidi Bögershausen (Hardness and nanoindentation tests), Mr. Jürgen Wichert (for the heat treatment), Mr. Simon Reckort, Mr. Frank Rüters, Mr. Tristan Wickfeld, Mr. Sascha Flaum, Mr. Andreas Sturm (FIB training), Mr. Herbert Faul, Mr. Uwe Tezins, and Mr. Zakarya Meshou. Special thanks to Mr. Michael Adamek, who has been an invaluable professional technician, assisting with mechanical testing such as tensile tests, dilatometry, and white-light confocal microscopy. Beyond his technical expertise, he is also an exceptional ping-pong player and a thoughtful friend, making my time at the institute both fruitful and enjoyable.

Special thanks to the China Scholarship Council for the financial support during my PhD study (Number: 202106780003).

To my best friends outside MPI-Susmat—Xiang Wang, Xin Liu, Wenbo Wang, Haowen Gu, Guanfeng Wu, and Chongfu Hu—thank you for staying in touch and for sharing in both the challenges and aspirations of each other's journeys.

Last but certainly not least, I would like to express my deepest gratitude to my beloved family—my partner, my parents, and my brothers—for their endless love and unwavering support throughout my life. Your encouragement has been my anchor in the past, my strength in the present, and my inspiration for the future. You are the reason I continue to persevere on this long and challenging journey.

Abstract

To address the growing global demand for transportation and energy, the development of more efficient turbine engines and power generators capable of operating at higher temperatures and tolerating extreme conditions (*e.g.*, H_2 exposure) is essential. Over the past decade, refractory complex concentrated alloys (RCCAs), consisting of three or more transition elements from groups IV, V, and VI, have emerged as promising materials due to the vast compositional versatility and superior mechanical properties at elevated temperatures compared to the conventional refractory alloys. However, the brittleness of RCCAs at room temperature significantly limits their practical applications. Recent findings indicate that interstitial elements contribute to the brittle behavior of RCCAs at ambient conditions. Moreover, the strong affinities between interstitials and refractory elements underscore the influence of these small atoms on microstructure and phase stability, which, in turn, alter macroscopic mechanical performances. This thesis seeks to offer an in-depth understanding of the interplay between interstitial atoms (especially H) and RCCAs, focusing on their effects on microstructure, phase stability, and consequent mechanical properties, to advance the design of RCCAs with optimized performance under extreme conditions:

(1) **Hydrogen Accommodation in TiNbZr RCCA**: *In-situ* synchrotron high-energy X-ray diffraction combined with density functional theory reveal hydrogen-induced lattice expansion (holding at 500 °C) and transformation (body-centered cubic to body-centered tetragonal cubic structure upon cooling) in a TiNbZr RCCA. Hydrogen prefers to accommodate at tetrahedral sites, while the ordered distribution of hydrogen solutes results in the occurrence of tetragonality.

(2) **Hydrogen-Assisted Spinodal Decomposition**: In a TiNbZrHfTa RCCA, hydrogen modulates nanoscale spinodal decomposition, creating chemical fluctuations and enhancing hardness. A thermodynamic model demonstrates the role of hydrogen in destabilizing single-phase structures, enabling novel microstructure tailoring strategies.

(3) **Boron Effects on Grain Boundary Chemistry**: Boron segregation alters grain boundary chemistry in a TiNbZrHfTa RCCA, reducing yield strength and enabling grain boundary shear localization. Enhanced slip transfers upon boron doping highlight the role of segregation engineering in optimizing mechanical performance.

(4) **Ductilization via Oxygen-Induced Nanoscale Chemical Heterogeneity**: The incorporation of oxygen interstitials in a TiNbZr RCCA induces the formation of nanoscale chemical heterogeneity, characterized by Ti concentration fluctuations. The presence of Ti-

enriched regions strongly pins dislocation, resulting in an increase in strain-hardening rate and strain rate sensitivity, accompanied by the refinement of deformation bands. These microstructural characteristics collectively contribute to improved ductility while preserving yield strength, offering a promising strategy for overcoming the strength-ductility trade-off in RCCAs.

These findings highlight the critical role of interstitial atoms in influencing microstructure and phase stability, ultimately shaping macroscopic mechanical performance, and providing a foundation for designing RCCAs with tailored properties for demanding applications.

Kurzfassung

Um der wachsenden globalen Nachfrage nach Transport und Energie gerecht zu werden, ist die Entwicklung effizienterer Turbinen und Kernreaktoren erforderlich, die bei höheren Temperaturen betrieben werden können und extremen Bedingungen (z. B. H_2-Exposition) standhalten. In den letzten zehn Jahren haben sich refraktäre komplex konzentrierte Legierungen (engl.: refractory complex concentrated alloys, kurz: RCCAs), bestehend aus drei oder mehr Übergangselementen der Gruppen IV, V und VI, als vielversprechende Materialien erwiesen. Sie bieten eine breite Zusammensetzungsvielfalt und verbesserte mechanische Eigenschaften bei erhöhten Temperaturen im Vergleich zu herkömmlichen refraktären Legierungen. Die Sprödigkeit von RCCAs bei Raumtemperatur schränkt jedoch ihre praktische Anwendbarkeit erheblich ein. Aktuelle Studien zeigen, dass interstitielle Elemente maßgeblich zum spröden Verhalten von RCCAs bei Umgebungsbedingungen beitragen. Darüber hinaus verdeutlichen die starken Affinitäten zwischen interstitiellen Atomen und refraktären Elementen deren Einfluss auf die Mikrostruktur und Phasenstabilität, was wiederum die makroskopischen mechanischen Eigenschaften verändert. Diese Arbeit zielt darauf ab, ein tiefgreifendes Verständnis der Wechselwirkungen zwischen interstitiellen Atomen (insbesondere H) und RCCAs zu erlangen, wobei der Fokus auf deren Auswirkungen auf die Mikrostruktur, Phasenstabilität und mechanischen Eigenschaften liegt, um die Entwicklung von RCCAs mit optimierten Eigenschaften unter extremen Bedingungen voranzutreiben.

(1) **Wasserstoffaufnahme in TiNbZr-RCCA**: *In-situ* Synchrotron Hochenergie-Röntgenbeugung kombiniert mit Dichtefunktionaltheorie zeigt eine durch Wasserstoff induzierte Gitterexpansion (stabil bei 500 °C) und eine Umwandlung (kubisch-raumzentriert zu raumzentrierte tetragonale beim Abkühlen) in TiNbZr RCCA. Wasserstoff besetzt bevorzugt die Tetraederlücken. Bei geordneter Verteilung von H im Kristallgitter, wird dieses tetragonal.

(2) **Wasserstoffunterstützte Spinodale Entmischung**: In der untersuchten TiNbZrHfTa RCCA Legierung beeinflusst die Anwesenheit von H die spinodale Entmischung. Dadurch verändert sich die Phasenzusammensetzung und die Werkstoffhärte wird gesteigert. Ein thermodynamisches Modell zeigt, wie Wasserstoff zur Destabilisierung von Einphasenstrukturen beiträgt und so neue Möglichkeiten der Mikrostrukturmodifikation eröffnet.

(3) **Einfluss von Bor auf die Korngrenzenchemie**: Die Segregation von Bor an der Korngrenze verändert die lokale chemische Zusammensetzung in TiNbZrHfTa-RCCA,

reduziert die Streckgrenze und ermöglicht gleiten an der Korngrenze. Der verbesserte Gleittransfer durch Bor-Dotierung verdeutlichen den großen Einfluss, den gezielte Ausscheidungen auf die mechanischen Eigenschaften haben.

(4) **Erhöhung der Duktilität durch Sauerstoff induzierte nanoskalige chemische Heterogenität:**

Die interstitielle Einlagerung von Sauerstoff in TiNbZr-RCCA führt zur Bildung einer nanoskaligen chemischen Heterogenität, die sich in Ti-Konzentrationsfluktuationen manifestiert. Die Ti-angereicherten Bereiche wirken als starke Versetzungsbarrieren, was zu einer erhöhten Verfestigungsrate und gesteigerten Dehnratenempfindlichkeit führt, diese Effekte werden begleitet von einer Verfeinerung der Deformationsbänder begleitet. Die mikrostrukturellen Merkmale tragen gemeinsam zur verbesserten Duktilität bei, während die Streckgrenze erhalten bleibt, und stellen somit eine vielversprechende Strategie zur Überwindung Festigkeits-Duktilitäts-Kompromisses in RCCAs dar.

Diese Ergebnisse unterstreichen die entscheidende Rolle interstitieller Atome bei der Beeinflussung der Mikrostruktur und Phasenstabilität, welche letztlich die makroskopischen mechanischen Eigenschaften prägen, und bieten eine Grundlage für die Entwicklung von RCCAs mit maßgeschneiderten Eigenschaften für anspruchsvolle Anwendungen.

List of symbols

Symbols	**Full name**	**Unit**
ϕ	Azimuth angle	°
τ	Shear stress	MPa
ρ	Dislocation density	m^{-2}
λ	Wavelength of the beamline	Å
θ	Diffraction angle	°
ε	Microstrain	-
Ω	Interaction parameter	$kJ\cdot mol^{-1}$
Λ	Spinodal wavelength	nm
t	Time	s
r	Radius	Å
q	Scattering vector	$Å^{-1}$
κ	Thermal conductivity	$W\cdot m^{-1}\cdot K^{-1}$
k	Slope	-
d	Grain size	µm
a, c	Lattice parameter	Å
V	Lattice volume	$Å^3$
U	Internal energy	$kJ\cdot mol^{-1}$
T	Temperature	°C
p	Pressure	bar
S	Entropy	$J\cdot K^{-1}$
Q	Activation energy	$kJ\cdot mol^{-1}$
H	Enthalpy	J
D	Diffusion coefficient	$m2\cdot s^{-1}$
C	Concentration	mol^{-1}
$V_{app.}$	Apparent activation volume	b^3
R / k_B	Boltzmann constant	$J\cdot K^{-1}$
m	Strain rate sensitivity	-
M	Taylor factor	-

l	Distance between two clusters	nm
I	Diffraction intensity	-
G	Shear modulus	GPa
E	Elastic modulus	GPa
D	Crystallite size	μm
b	Burgers vector	-
ΔG	Gibbs free energy	kJ·mol^{-1}
$\boldsymbol{\epsilon}_{\mathbf{ij}}$	Strain tensor	Pa
χ^2	Chi-squared coefficient	-
$\boldsymbol{\sigma}_{\mathbf{ij}}$	Stress tensor	Pa
$\dot{\varepsilon}$	Strain rate	s^{-1}
$\boldsymbol{s}_{\mathbf{ij}}$	Elastic compliance tensor	GPa
d_{hkl}	Interspacing of lattice planes	Å
K_y	Hall-Petch coefficient	MPa·μm$^{1/2}$
$\dot{\gamma}_{\mathrm{gbs}}$	Shear stress rate	s^{-1}

List of abbreviations

Abbreviations	**Full name**	**Unit**
ACC	Autocorrelation coefficient	-
APT	Atom probe tomography	-
BCC	Body-centered cubic	-
BCT	Body-centered tetragonal	-
BSE	Backscattered electron	-
DFT	Density function theory	-
DI	Dictionary indexing	-
DIC	Digital image correlation	-
EBSD	Electron backscatter diffraction	-
EDS	Electron-dispersive X-ray spectroscopy	-
FCC	Face-centered cubic	-
FDA	Frequency distribution analysis	-
FFT	Fast Fourier transform	-
FIB	Focused ion beam	-
FWHM (β)	Full width of half maximum	-
GB	Grain boundary	-
GND	Geometrically necessary dislocation	-
GPA	Geometrical phase analysis	-
H/M	Hydrogen-to-metal ratio	-
HAGB	High-angle grain boundary	-
HCP	Hexagonal close-packed	-
HEXRD	High-energy X-ray diffraction	-
HR	High-resolution	-
IPF	Inverse pole figure	-
IQ	Image quality	-
KAM	Kernel average misorientation	-
LAGB	Low-angle grain boundary	-
MCPs	Microchannel plates	-

NND	Nearest neighboring distribution	-
OM	Optical microscopy	-
OPS	Silica oxide polishing suspension	-
RCCA	Refractory complex concentrated alloy	-
RD	Rolling direction	-
ROI	Region of interest	-
SAED	Selected area electron diffraction	-
SAXS	Small-angle X-ray scattering	-
SEM	Scanning electron microscopy	-
SHT	Spherical Harmonic Transform	-
STEM	Scanning transmission electron microscopy	-
TCD	Thermal conductivity detector	-
TD	Transverse direction	-
TDS	Thermal desorption spectroscopy	-
TEM	Transmission electron microscopy	-
TOF	Time-of-flight	-
TRIP	Transformation-induced plasticity	-
UHV	Ultra-high vacuum	-
WAXS	Wide-angle X-ray scattering	-
XRD	X-ray diffraction	-
ZA	Zone axis	-

Table of contents

Acknowledgment I

Abstract IV

Kurzfassung VI

List of symbols VIII

List of abbreviations X

Table of contents XII

1. Introduction 1
  1.1. Background and motivation 1
    1.1.1. The burgeoning of complex concentrated alloy 1
    1.1.2. Interaction between interstitials and refractory complex concentrated alloy 7
    1.1.3. Motivations and the thesis structure 18
2. Principles of research methodologies 20
  2.1. Material processing and mechanical property assessment 20
    2.1.1. Materials 20
    2.1.2. Dilatometer 20
    2.1.3. Uniaxial tensile test 21
    2.1.4. *In-situ* tensile test 22
  2.2. Micro/nano-structural characterization 22
    2.2.1. Thermal conductivity detector 22
    2.2.2. High-energy X-ray diffraction 23
    2.2.3. Small-angle X-ray scattering 25
    2.2.4. Scanning electron microscopy 27
    2.2.5. Transmission electron microscopy 32
    2.2.6. Atom probe tomography 33
    2.2.7. Density functional theory-based simulations 36
3. Hydrogen accommodation and its role in lattice symmetry in a TiNbZr medium-entropy alloy 38
  3.1. Introduction 38
  3.2. Materials and methods 40
    3.2.1. Materials 40
    3.2.2. Microstructure characterization 40
    3.2.3. In-situ synchrotron high-energy X-ray diffraction 41
    3.2.4. Density functional theory (DFT) calculations 42
  3.3. Results 43
    3.3.1. Microstructure of the pristine TiNbZr sample 43
    3.3.2. Evolution of lattice structure upon heating 46
    3.3.3. Hydrogen uptake during isothermal treatment at 500 °C 46
    3.3.4. Change in lattice structure upon cooling 48
    3.3.5. Change in lattice volume during hydrogenation 50
    3.3.6. Microstructure after the treatment in H_2 52
  3.4. Discussion 54

3.4.1. Site occupancy of hydrogen atoms in the TiNbZr crystal lattice 54
3.4.2. Occurrence of lattice tetragonality upon cooling 58
3.4.3. Preference of hydrogen accommodation towards Ti/Zr 62
3.5. Conclusions 63
3.6. Supplementary materials 65
4. Hydrogen-assisted spinodal decomposition in a TiNbZrHfTa complex concentrated alloy 80
4.1. Introduction 80
4.2. Materials and methods 81
4.2.1. Material fabrications 81
4.2.2. Material characterizations 82
4.2.3. Microhardness and scratch tests 83
4.3. Results 83
4.3.1. Hydrogen-assisted spinodal decomposition 83
4.3.2. Enhance in hardness and wear resistance via hydrogen-assisted spinodal decomposition 89
4.4. Discussion 93
4.5. Conclusions 96
4.6. Supplementary materials 97
5. Role of boron in yield strength softening and plastic deformation mechanisms in a refractory high-entropy alloy 108
5.1. Introduction 108
5.2. Experimental section 109
5.2.1. Materials 109
5.2.2. Microstructure characterization 110
5.2.3. Uniaxial tensile testing 112
5.3. Results 112
5.3.1. Microstructure and GB segregation 112
5.3.2. Tensile properties 115
5.3.3. Slip trace assessments 116
5.4. Discussion 118
5.4.1. Competitive effect between Hall-Petch coefficient ($\boldsymbol{Ky}$) and grain size ($\boldsymbol{d}$) on the change of yield strength 118
5.4.2. Activation of GB shear localization upon B doping 121
5.4.3. Competition between GB shear localization and slip transfer 125
5.5. Conclusions 128
5.6. Supplementary materials 131
6. Ductilization of a TiNbZr refractory complex concentrated alloy via the strain delocalization by nanoscale chemical heterogeneity 146
6.1. Introduction 146
6.2. Experimental sections 148
6.2.1. Materials 148
6.2.2. Microstructure characterization and uniaxial tensile test 149
6.3. Results 150

6.3.1. Microstructure 150
6.3.2. Mechanical properties 152
6.3.3. Deformation behaviors 153
6.4. Discussion 159
6.4.1. Increased strain-hardening rate during stage II 159
6.4.2. Increase in total elongation during the stage III 161
6.5. Conclusions 163
6.6. Supplementary materials 165
7. Summary and outlooks 172

7.1. Summary 172
7.2. Outlooks 174
7.2.1. On advancing techniques for detecting small interstitial atoms 174
7.2.2. On understanding time-resolved microstructural changes induced by interstitials 174
7.2.3. Perspectives on understanding the effects of the incorporated interstitial atoms on mechanical/functional properties 175
Reference 179

List of figures 199

List of tables 218

Curriculum Vitae 221

List of publications 222

1. Introduction

1.1. Background and motivation

1.1.1. The burgeoning of complex concentrated alloy

Since the Bronze Age, seeking mechanically strong but intrinsically ductile materials has always been a goal for humans. One well-established approach is to add alloying materials, a practice that remains essential today. For example, steels containing a small amount of carbon are the most important metallic materials worldwide, with a production quantity of 1.95 billion tons in 2021, serving industries such as construction, infrastructure, transportation, *etc.* [1]. The small addition of carbon can help improve the strength of steel, and this alloying strategy has endured for millennia. Similar alloying practices involve adding minor amounts of secondary elements to principal-element alloys, such as Ti alloys (*e.g.*, by adding Al, V), Al alloys (*e.g.*, by adding Cu, Mg), Cu alloys (*e.g.*, by adding Zn, Sn), *etc.* [2]. However, limited possible combinations can be anticipated on the basis of this primary-element strategy, resulting in the fact that most such alloys were identified and extensively studied during the last century.

To expand the compositional space, researchers have begun to explore new strategies for mixing multiple principle elements with relatively high concentrations (usually >5 at.%). It is worth noting that intermetallic phases are prone to form when increasing the amounts of secondary alloying elements, even for the binary systems. Not to mention the quinary and other higher-order systems, where numerous combinations of secondary phases are available, making the prediction of phase composition tough. Generally, the tendency of an alloy to form a solid solution or the intermetallic phases (one or more) can be judged by the change in Gibbs free energy (**Fig. 1.1**),

$$\Delta G = \Delta H - T\Delta S \tag{1.1}$$

where ΔG, ΔH, and ΔS represent the Gibbs free energy, enthalpy, and entropy, respectively, while T denotes the absolute temperature. From this equation, the phases present within the system at the thermodynamic equilibrium state can be identified by comparing the Gibbs free energy of all possible phases consisting of the principle elements. Inspired by the "high entropy" concept, Jien-Wei Yeh et al. and Brain Cantor et al. pioneered the fabrication of the so-called high-entropy alloy with five or more equiatomic elements (often ranging from 5 at.% to 35 at.%), forming a single solid phase [3]. The underpinning hypothesis of this concept is that the presence of multiple elements in equiatomic concentrations would significantly increase the configurational entropy of mixing ($\Delta S_{con.}$), counteracting the enthalpies of secondary phase formation and thus preventing the occurrence of intermetallics potentially harmful to mechanical properties. This concept has sparked a significant global effort in alloy design, resulting in the development of a broader family of alloys.

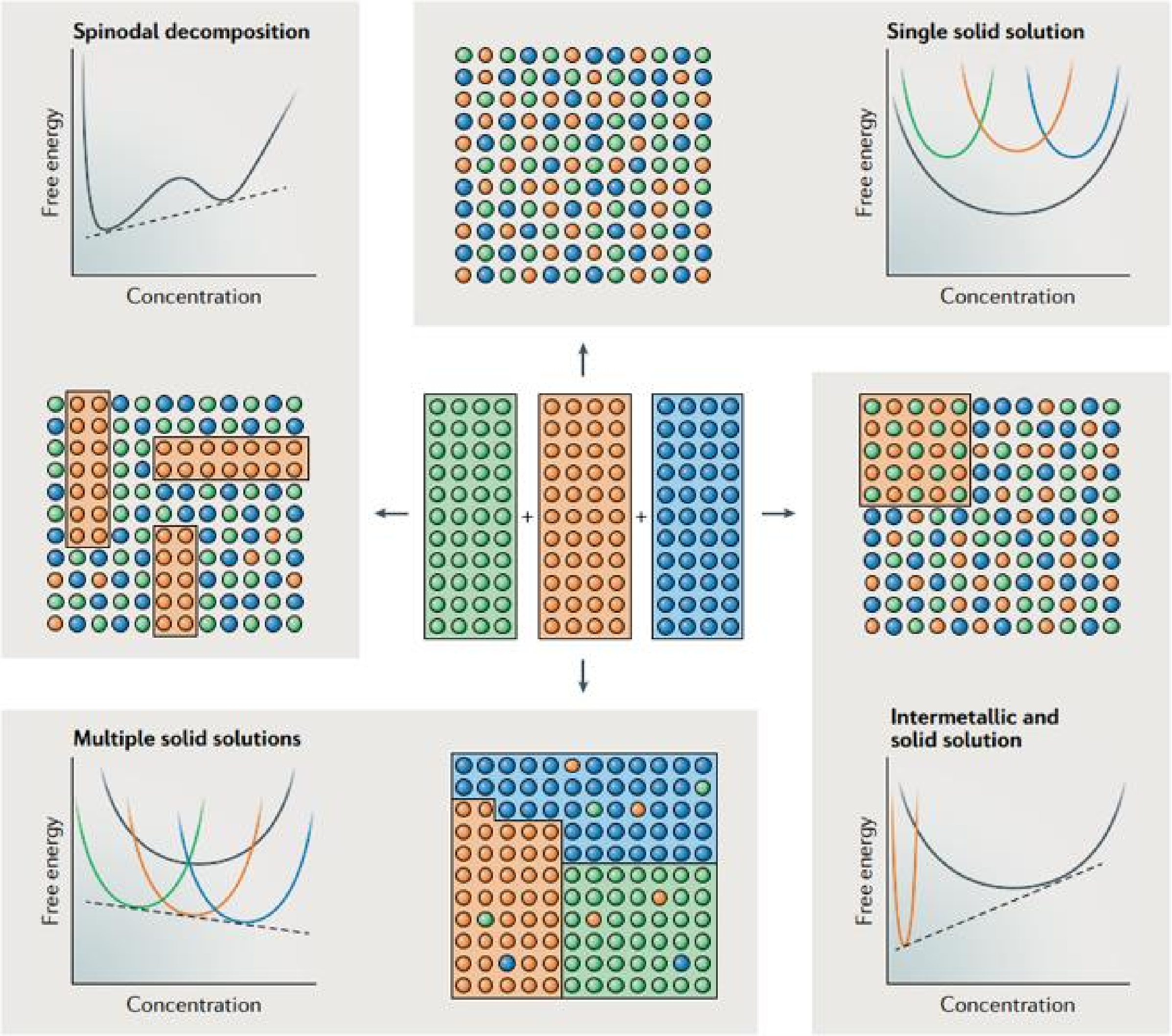
Spinodal decomposition
Free energy
Concentration
Single solid solution
Free energy
Concentration
Multiple solid solutions
Free energy
Concentration
Intermetallic and solid solution
Free energy
Concentration

Fig. 1.1 Possible mixing reactions for the case of an alloy containing three principle elements [2].

The popularity of the term, high-entropy alloys, currently specifically points to a class of metallic alloys with five or more principle elements in relatively high concentrations (5-35 at.%) [2, 3]. By assuming an ideal solid solution (where mixing enthalpy (($\Delta H_{mix}^{S.S.}$) is zero, and the configuration entropy ($\Delta S_{con.}^{I.P.}$) of the competing intermetallic phases is also zero), Yeh and co-workers simplified the problem that the final phase composition of this complex system mainly depended on the difference between $-T\Delta S_{con.}^{S.S.}$ and $\Delta H_{mix}^{I.P.}$ [3, 4]. The entropy of this ideal solid solution ($\Delta S_{con.}^{S.S.}$) can be defined as,

$$\Delta S_{con.}^{S.S.} = -R\sum x_i \ln x_i \tag{1.2}$$

where R, and x_i represent the gas constant and the mole fraction of the *i* element, respectively. Assuming an equiatomic ternary or higher-order alloy, we would have $x_1 = x_2 = x_3 = \ldots = x_n$,

$$\Delta S_{con.}^{S.S.} = -R \ln n \tag{1.3}$$

Here, *n* denotes the number of elements in this alloy systme. Based on this simplification, alloys are categorized by their magnitude of entropy: low-entropy alloys ($\Delta S_{con.}^{S.S.} < 0.69\ R$), medium-entropy alloys ($0.69 < R\Delta S_{con.}^{S.S.} < 1.61\ R$), and high-entropy alloys ($\Delta S_{con.}^{S.S.} > 1.61\ R$) [3]. However, such a definition still prevents these multi-principle alloys from embracing a broad space of composition combinations, such as non-equiatomic, multi-phase, metastable high-entropy alloys, or alloys with interstitial alloying elements. Additionally, researchers found out that the so-called "high-entropy" is not the primary factor responsible for their structure and properties of them. Others have proposed alternative terms for this nascent class of alloys, including multi-component alloys, compositionally complex alloys, complex concentrated alloys, *etc.*, reflecting an expanded definition. This broader scope includes: (1) removing the limitations of equiatomic concentrations; (2) accommodating small additions of secondary elements; and (3) eliminating boundaries on entropy magnitude and phase composition [5]. Herein, we adopt the term ***complex concentrated alloys (CCAs)*** for this study, focusing primarily on the ternary TiNbZr alloy, and the quinary TiNbZrHfTa alloy.

The expanded degrees of freedom resulting from the multi-component and evolving definition of CCAs have driven the alloy design community to explore diverse strategies in pursuit of exceptional mechanical properties. Therefore, the next focus of CCAs lies in understanding the correlations between composition, microstructure, or processing parameters, and their resulting mechanical properties. The mechanical behavior of CCAs under stress and the underlying deformation mechanisms have been extensively investigated [5, 6]. Similar to conventional metals, CCAs contain various kinds of defects that disrupt the regular three-dimensional atomic arrangement of a perfect crystal (**Fig. 1.2**a). These fundamental properties of CCAs are closely correlated to specific deformation mechanisms, which subsequently lead to the corresponding various macroscopic mechanical behaviors (**Fig. 1.2**b). Gaining a fundamental understanding of the factors driving these mechanical responses is crucial for advancing the mechanistic design of materials with enhanced mechanical properties. Four core effects of CCAs are summarized as compared with the conventional metals: (1) the high-entropy effect (helps to stabilize the single solid solution phase), (2) sluggish diffusion effect (change in the kinetic of phase transformations), (3) severe lattice distortion effect (influence the mechanical and functional behaviors), and (4) cocktail effect (composite effect from both the basic features and interactions among all the principle elements) [7]. Even within single-phase solid solutions, a broad range of CCAs has been identified, including face-centered cubic (FCC), body-centered cubic (BCC), hexagonal close-packed (HCP), and orthorhombic crystal structures [2, 5-7]. Here, to maintain focus and avoid redundancy, this discussion is limited to two extensively studied alloys: the FCC CrMnFeCoNi (Cantor) and the BCC TiNbZrHfTa CCAs.

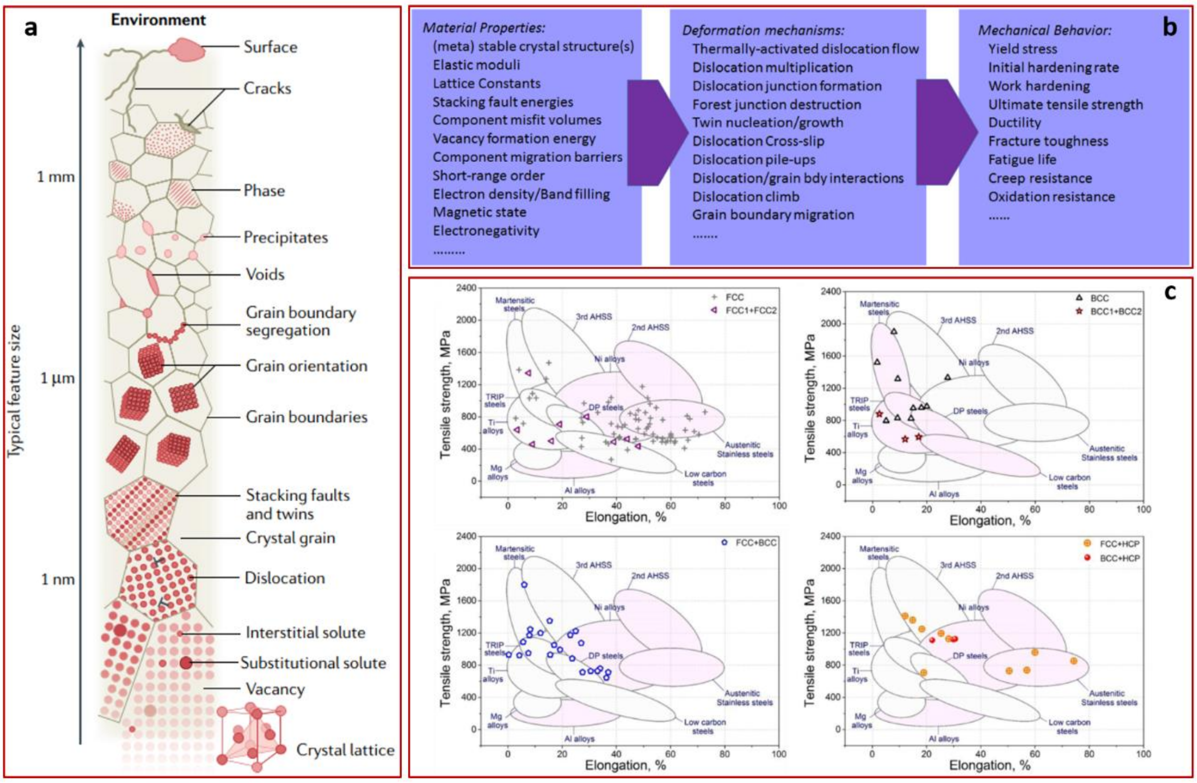
a
Environment
Typical feature size
1 mm
1 µm
1 nm
Surface
Cracks
Phase
Precipitates
Voids
Grain boundary segregation
Grain orientation
Grain boundaries
Stacking faults and twins
Crystal grain
Dislocation
Interstitial solute
Substitutional solute
Vacancy
Crystal lattice
b
Material Properties:
(meta) stable crystal structure(s)
Elastic moduli
Lattice Constants
Stacking fault energies
Component misfit volumes
Vacancy formation energy
Component migration barriers
Short-range order
Electron density/Band filling
Magnetic state
Electronegativity
....
Deformation mechanisms:
Thermally-activated dislocation flow
Dislocation multiplication
Dislocation junction formation
Forest junction destruction
Twin nucleation/growth
Dislocation Cross-slip
Dislocation pile-ups
Dislocation/grain bdy interactions
Dislocation climb
Grain boundary migration
......
Mechanical Behavior:
Yield stress
Initial hardening rate
Work hardening
Ultimate tensile strength
Ductility
Fracture toughness
Fatigue life
Creep resistance
Oxidation resistance
......
c
Tensile strength, MPa
Elongation, %
FCC
FCC1+FCC2
BCC
BCC1+BCC2
FCC+BCC
FCC+HCP
BCC+HCP
Martensitic steels
3rd AHSS
2nd AHSS
Ni alloys
TRIP steels
Ti alloys
DP steels
Mg alloys
Al alloys
Low carbon steels
Austenitic Stainless steels
0
400
800
1200
1600
2000
2400
0
20
40
60
80
100

Fig. 1.2 (a) Schematic diagram depicting the typical microstructural features with the corresponding size [8]. (b) Scheme illustrating the connection of fundamental properties of materials to the associated deformation mechanisms, which in turn, result in the observable macroscopic mechanical behaviors [6]. (c) Room-temperature uniaxial tensile strength *vs.* elongation of complex concentrated alloys (CCAs), categorized according to the presence of constituent phases [6].

FCC CrMnFeCoNi CCA. Deformation mechanisms involve the motion and interaction of defects within the crystalline lattice. The primary defects driving plasticity are dislocations, which serve as the carriers of plastic deformation, leading to plastic strain. Grain boundaries are also crucial, as they interact with or generate dislocations, contributing to the strengthening of metals (Hall-Petch effects). The deformation mechanism of CrMnFeCoNi, the so-called Cantor alloys, is governed by its unique multi-elemental nature and slip system activation under varying conditions. At room temperature, deformation primarily occurs through dislocation glide on the $\{111\}\langle 110\rangle$ slip system, typical of FCC structures with high ductility. The high strain-hardening rate is attributed to dislocation interactions and forest hardening (**Fig. 1.3**a), where dislocations are pinned by atomic-scale lattice distortions caused by the multi-elemental nature of the CCA [6, 9]. Additionally, the *in-situ* TEM studies reveal the wavy dislocation line and its jagged glide motion inside this CCA under external loading (**Fig. 1.3**b) [10]. This dislocation behavior is mainly attributed to local fluctuations in the Peierls friction, as suggested by atomistic simulations. At cryogenic temperatures, deformation twinning (**Fig. 1.3**c) is activated due to the increased stacking fault energy (SFE), transitioning the mechanism from dislocation glide to twinning-induced plasticity (TWIP) [9]. The activation of $\{111\}\langle112\rangle$ twinning systems contributes to additional strain hardening, as twin boundaries act as obstacles to dislocation motion. In some cases, the Cantor-analogous alloy may also exhibit transformation-induced plasticity (TRIP) effects, especially when external factors like stress or compositional adjustments (*i.e.*, with reduced Mn concentration) induce a phase transformation (*e.g.*, FCC to HCP) [11]. These combined effects—solid-solution strengthening, TWIP, and potential TRIP—result in exceptional ductility, high strength, and superior strain hardening capabilities, making the Cantor alloy a benchmark material for understanding the deformation behavior of high-entropy alloys.

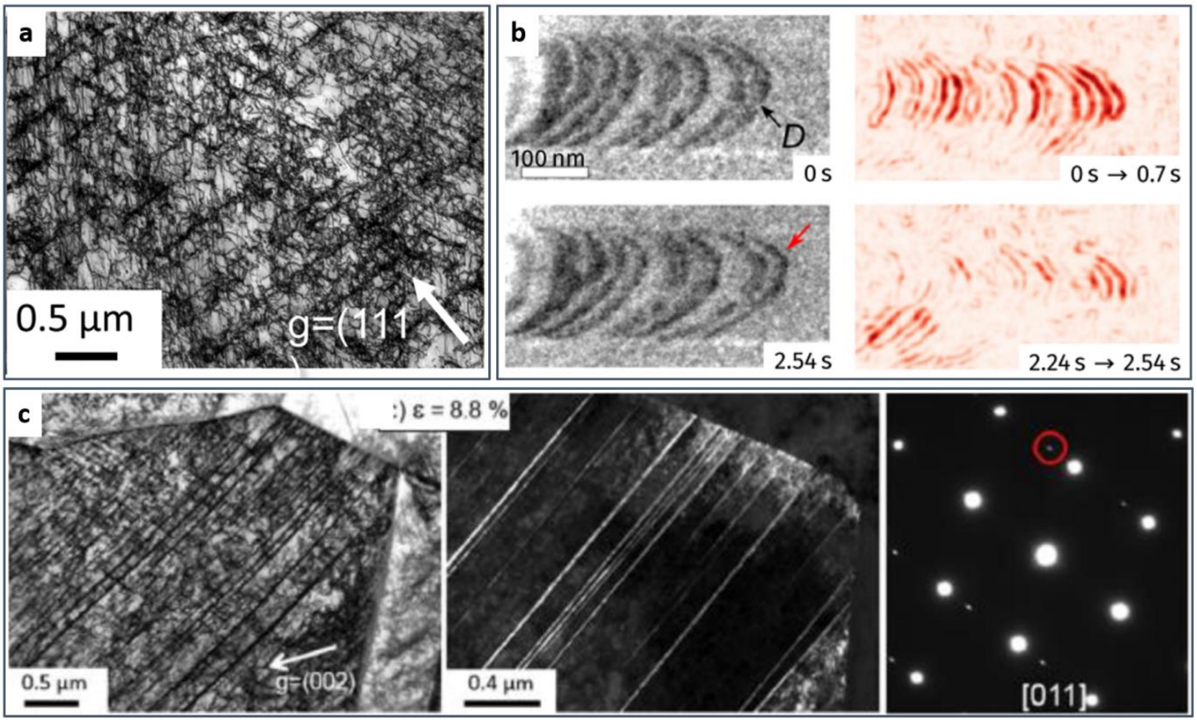

Fig. 1.3 (a) The formation of tangled dislocations, forming dislocation cell structures at a true strain of ~22% at room temperature, leading to forest hardening [9]. (b) *In-situ* TEM snapshots showing a sequence of gliding dislocations ($\{111\}\langle110\rangle$) activated under external loading [10]. (c) Representative TEM images showing the formation of deformation twinning in a CrMnFeCoNi CCA when strained to ~9% under cryogenic condition (77 K) [9].

BCC TiNbZrHfTa CCA. The TiNbZrHfTa alloy, a refractory CCA (RCCA) with a BCC crystal structure, is characterized by its high strength and limited ductility due to the inherent properties of BCC metals [12, 13]. The high Peierls barrier in BCC RCCAs indeed results in high strength. However, this barrier also leads to the subtle differences between the ideal strengths for shear instability and atomic-level cleavage inception (*i.e.*, the ideal ultimate tensile strength), thus giving rise to the limited ductility in this class of alloys [12, 14] The deformation mechanism of this RCCA is complex as compared with the aforementioned FCC CCA. The glide of a/2<111> screw dislocations with a non-planar degenerated core structure has been recognized as the predominant slip mode for plastic strain accommodating in this RCCA (**Fig. 1.4**a) [15]. Cross slip of screw dislocations can also occur, moving from the primary slip plane to another intersecting slip plane among various crystal planes that share the common Burgers vector, for example, the {110}, {112}, and {123} planes, which is also known as pencil glide (**Fig. 1.4**b) [16]. Additionally, the significant plasticity often is accompanied by the activation of additional slip systems such as {112}⟨111⟩ and {123}⟨111⟩ slip systems [16-18]. As compared with the conventional BCC alloys, the RCCA exhibits strong solid-solution strengthening due to the severe lattice distortion caused by the significant atomic size mismatch among its constituent elements, thus resulting in high strength [19-21]. At elevated temperatures, thermally activated dislocation motion, along with mechanisms such as grain boundary sliding and potential phase transformations, enhances plasticity. This behavior endows TiNbZrHfTa RCCA with promise for strength and ductility across the entire temperature spectrum (**Fig. 1.4**c), which makes it suitable for high-temperature applications, including extreme environments such as aerospace engineering and hydrogen-powered engines [19]. Additionally, localized stress concentrations at grain boundaries or phase interfaces can lead to deformation-induced phase transformations, which may further influence mechanical behavior [22]. These characteristics make TiNbZrHfTa a promising material for high-temperature applications, but its deformation mechanisms highlight the trade-off between strength and ductility in RCCAs.

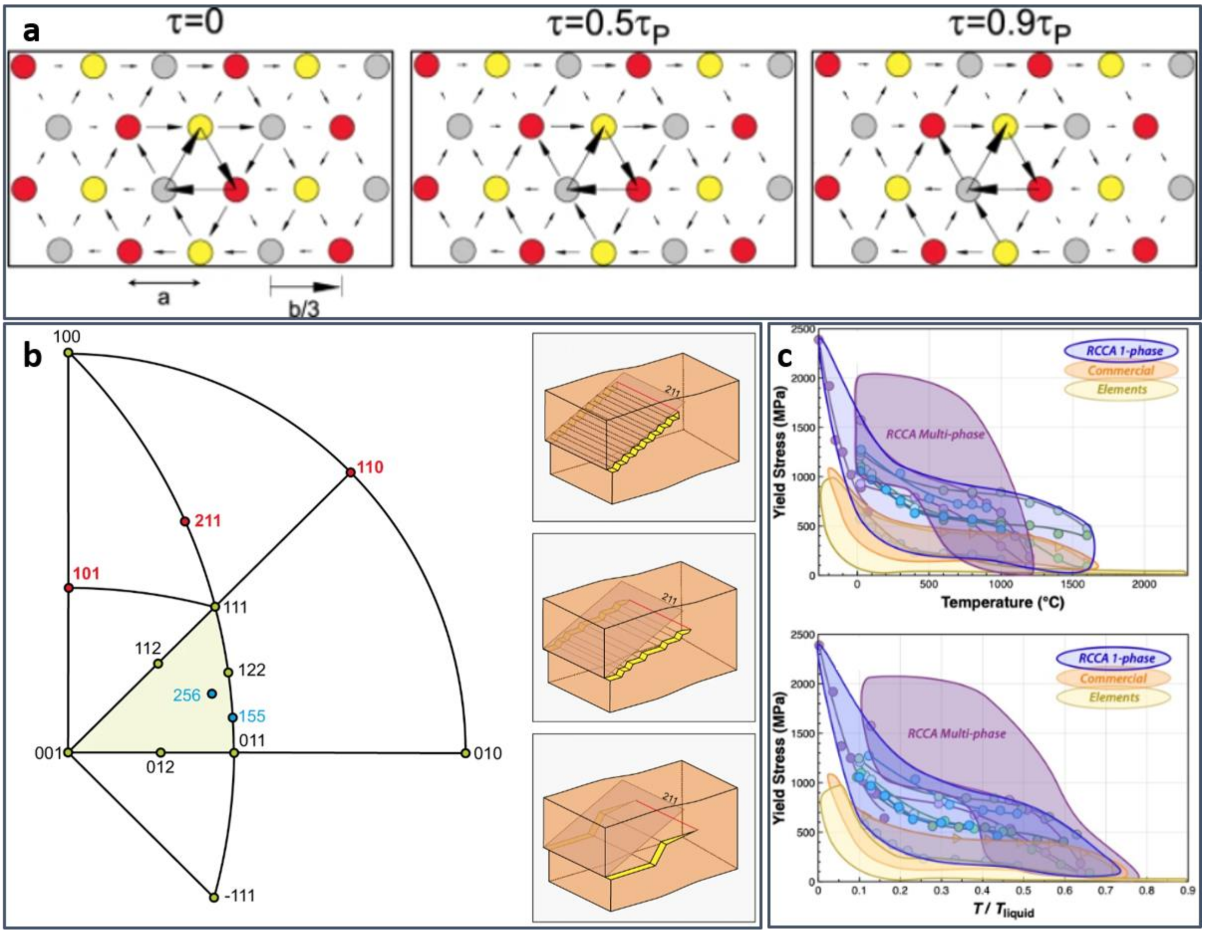

Fig. 1.4 (a) Differential displacement maps for the non-degenerate core structure as a function of shear stress (τ) [15]. (b) Schematic diagram demonstrating the composite slip in RCCA, where slip producing macroscopic strain on one particular {110} plane is accompanied by the second system to fulfill the boundary conditions [16]. (c) The yield strength of refractory alloys as a function of temperature and T/T_{liquid}, where T_{liquid} denotes the melting temperature, showing the high strength of this class of RCCA across the entire temperature spectrum [19].

1.1.2. Interaction between interstitials and refractory complex concentrated alloy

The emergence of the "complex concentrated alloy" concept has also significantly accelerated the development of RCCAs. Unlike conventional refractory alloys with one or two principal elements, RCCAs are composed of multiple (often three or more) refractory elements in near-equimolar ratios [2, 21]. RCCAs represent a significant advancement in the field of metallurgy and materials science. These RCCAs were developed to address the need for materials that can maintain good mechanical performance under high-temperature and extreme environments, such as aerospace, nuclear reactors, and energy applications [23, 24]. Refractory elements can be classified into two categories: (1) those with melting temperatures above 2000 °C, such as Nb, Ta, Mo, W, and Re [25, 26]; and (2) transition elements from subgroups IV, V, and VI of the periodic table (the broader definition) [21]. The high melting points, exceptional oxidation resistance, and superior mechanical properties of these refractory elements make them ideal candidates for RCCAs. Additionally, the concept of high configurational entropy stabilizing single-phase microstructures has further propelled the exploration of these alloys, enabling significant advancements in the optimization of mechanical properties for high-temperature applications.

RCCAs typically crystallize in BCC structures and form a random solid solution, characterized by some degree of lattice distortion, though some may exhibit dual-phase microstructures depending on compositions [20, 21]. The BCC structure is particularly notable for its low atomic packing efficiency (68%) and its abundance of interstitial sites (6 octahedral sites and 12 tetrahedral sites within one BCC lattice), in contrast to FCC and HCP crystal structures (**Fig. 1.5**a) [12, 27]. The size of tetrahedral and octahedral sites are 0.155 R and 0.291 R for BCC crystal structures, respectively (where R is the atomic radius) [12, 28]. These interstitial sites provide ample room for the accommodation of small atoms such as carbon (C), nitrogen (N), oxygen (O), boron (B), and hydrogen (H), which can significantly influence the mechanical properties of RCCAs [23, 29]. For example, C and N readily occupy these interstitial sites, causing severe lattice distortions and thus resulting in enhanced solid-solution strengthening [30, 31]. Beyond occupying the interstitial sites, these interstitial atoms also interact with other microstructural features within the materials (**Fig. 1.5**b), such as dislocations and grain boundaries (GBs), or bind with principle elements to form ordered structures like precipitates [32, 33]. These interactions profoundly impact the mechanical behavior of RCCAs. For instance, the segregation of O impurities to the GBs of NbMoTaW RCCA has been shown to cause GB decohesion, leading to catastrophic failure (*i.e.*, significant loss in ductility) [32]. On the other hand, controlled incorporation of interstitials, such as O, can enhance strength and thermal stability, making these elements both a challenge and an opportunity for optimizing RCCAs [33, 34]. The detailed interactions between interstitial atoms and RCCAs, along with their influence on macroscopic mechanical responses, will be elaborated in the following sections.

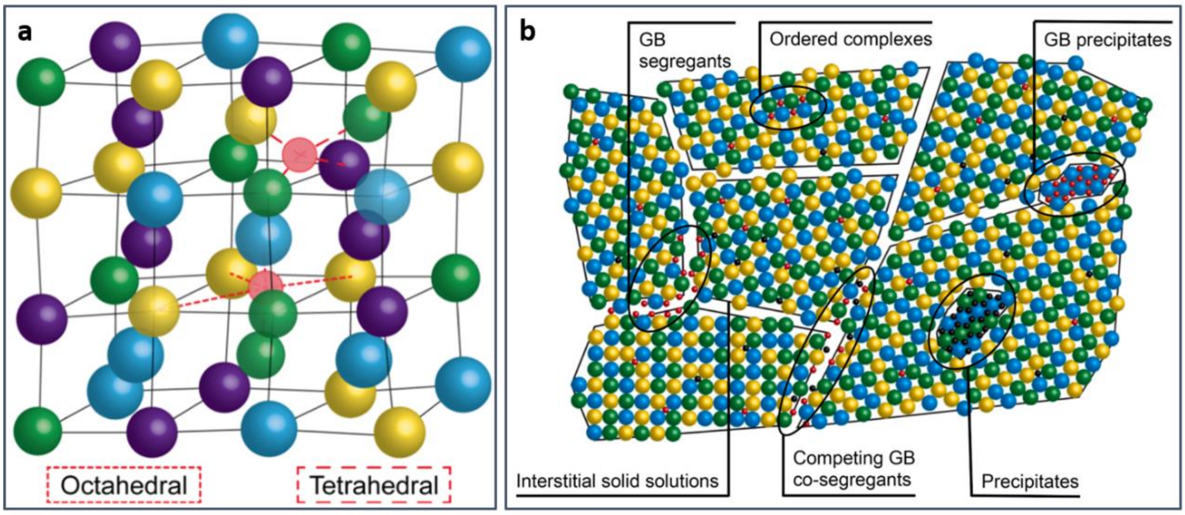

Fig. 1.5 (a) Illustrations of the prototypical body-centered cubic (BCC) lattice structure of a refractory complex concentrated alloy (RCCA) consisting of four principle elements [23]. Two kinds of interstitial sites (tetrahedral and octahedral) are pointed out with red spheres. (b) Scheme showing the various microstructural features in RCCA and the possible accommodation sites for interstitial atoms [23].

Apart from the availability of accommodation sites within BCC RCCAs, the strong chemical affinities of these refractory elements to interstitial atoms (with corresponding mixing enthalpies listed in **Table 1.1**, and Ellingham diagrams for compounds shown in **Fig. 1.6**) underscore the critical role of these small atoms in microstructure and phase stability [35-38]. Interstitial constituents that end up in RCCAs, and influence their mechanical behaviors, often exist in these relatively high abundances as diatomic gaseous molecules in the atmosphere, such as O_2, N_2, H_2O, and H_2 (*e.g.*, in hydrogen engines). These interstitials can be introduced into RCCAs during the synthesis and processing through exposure to the external atmosphere. Furthermore, RCCAs are specifically designed to operate in extreme service environments, including the high-temperature and corrosive conditions encountered in aerospace, nuclear reactors, and energy systems. Such harsh environments expose RCCAs to interstitial elements from the external atmosphere, facilitating the dissolution and subsequent diffusion of these atoms into the RCCA lattice [39-41]. The BCC structure of RCCAs, characterized by its low packing density (68%), offers larger and more accessible interstitial sites compared to FCC and HCP structures. This structural characteristic further promotes the diffusion of interstitial atoms particularly under high-temperature conditions where diffusion rates are significantly elevated [28, 41]. Therefore, interactions between interstitial atoms and RCCAs during services are both unavoidable and influential, necessitating careful consideration. The diffusion of interstitials into RCCAs can lead to substantial changes in their properties.

Table 1.1 The values of mixing enthalpy (ΔH_{AB}^{mix}, kJ/mol) between refractory elements and interstitial elements (H, B, C, and N) [35].

Elements	$\Delta H_{\mathrm{AB}}^{mix}$ with H (kJ/mol)	$\Delta H_{\mathrm{AB}}^{mix}$ with B (kJ/mol)	$\Delta H_{\mathrm{AB}}^{mix}$ with C (kJ/mol)	$\Delta H_{\mathrm{AB}}^{mix}$ with N (kJ/mol)
Ti	-54	-58	-109	-190
Zr	-69	-71	-131	-233
Hf	-63	-66	-123	-218
V	-39	-42	-82	-143
Nb	-46	-54	-102	-174
Ta	-46	-54	-101	-173
Cr	-28	-31	-61	-107
Mo	-28	-34	-67	-115
W	-24	-31	-60	-103

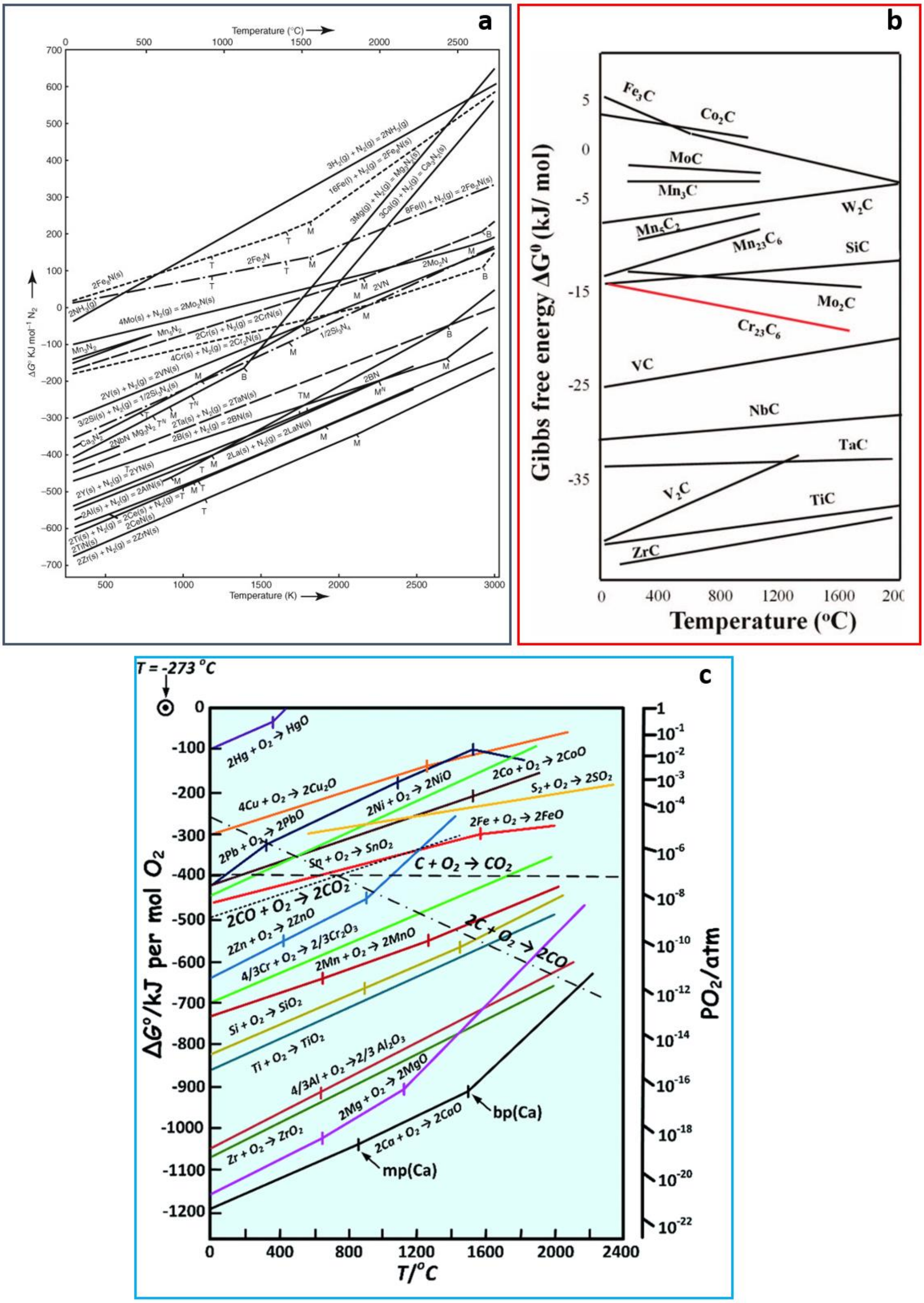

Fig. 1.6 Ellingham diagrams for (a) nitrides [36], (b) carbides [37], and (c) oxides [38].

The interaction between interstitials and RCCAs is a complex but critical aspect of their behavior, influencing mechanical properties, and phase stability. Some interstitial impurities intentionally added to RCCAs activate mechanisms that enhance both strength and ductility [30-32]. Conversely, trace amounts of interstitials have been observed to segregate to grain boundaries, causing severe embrittlement of the alloys [32]. By understanding the mechanisms through which interstitial impurities affect RCCAs and their influence on mechanical properties, additional criteria can be established for the holistic design of RCCAs with optimization of mechanical properties.

On Grain boundary segregation. Interstitial elements including H, B, C, N, and O have a tendency to segregate at GBs due to their lower energy state at these sites. This segregation behavior can be straightforwardly derived from classical thermodynamics, a certain element *i* may preferentially reside in grain boundaries due to the reduction in free energy [42-44],

$$dG = \left(\gamma_{\mathrm{GB}}^{\mathrm{o}} - \frac{N_{\mathrm{i}}^{\mathrm{ex}}}{A_{\mathrm{GB}}} \Delta E_{\mathrm{seg.}}\right) dA_{\mathrm{GB}} \tag{1.4}$$

where the excess amount of solute $N_{\mathrm{i}}^{\mathrm{ex}}$ lowers the reference-state grain boundary energy $\gamma_{\mathrm{GB}}^{\mathrm{o}}$ by means of a segregation energy term, $\Delta E_{\mathrm{seg.}}$. A_{GB} represents the surface area of the GBs. Furthermore, the excess quantity can be ideally approximated using the Langmuir-McLean adsorb isotherm, assuming a dynamic equilibrium between the adsorption and the desorption rates at a monolayer level [42, 45, 46],

$$\frac{x_i^{GB}}{x_i^{GB,0} - x_i^{GB}} = \frac{x_i^{B}}{(1 - x_i^{B})} \exp\left(-\frac{\Delta E_i^{GB}}{RT}\right) \tag{1.5}$$

where x_i^{GB} and x_i^{B} denote the molar concentration of element *i* in the GB and the bulk, respectively. $x_i^{GB,0}$ represents the molar GB occupantion fraction of the same element in saturation. *R*, *T*, and ΔE_i^{GB} are the gas constant, temperature, and the free molar energy of segregation, respectively. The segregation coefficient (β_i), also referred to as GB enrichment factor, as can then be obtained via [42],

$$\beta_i = \frac{x_i^{GB}}{x_i^{B}} = \exp\left(-\frac{\Delta E_i^{GB}}{RT}\right) \tag{1.6}$$

to advance tailored-design segregation characteristics. As compared with the Gibbs concept, the Langmuir-McLean equation is usually more practical for quantifying segregation at solid-state interfaces since we do not need detailed information on the GB energy, as well as its variations with temperatures and compositions.

For RCCAs, the segregation of interstitial constituent atoms at GBs and the consequent reduction in GB cohesion are key contributors to the brittle, intergranular fracture of these alloys. For instance, as revealed in **Fig. 1.7**a, the segregation of O impurities at GBs has been observed in the as-cast NbMoTaW RCCA [32]. The iso-concentration surfaces (2.1 at.%) of O clearly indicated a higher concentration of O at GBs as compared with that in the matrix. This segregation behavior leads to embrittlement due to the decohesion of GBs caused by O impurities. However, such a brittle behavior can be mitigated by the intentional addition of B and C, which compete with O for GB accommodation sites (**Fig. 1.7**b). As suggested by density functional theory (DFT) calculations, B and C both exhibit lower segregation energies than O, leading to a higher tendency for them to segregate to GBs. This competitive segregation not only prevents O from occupying GBs but also strengthens GBs through the stronger bonding between the dopants and neighboring constituent elements, thus improving the cohesion of GBs. B is a commonly used dopant for strengthening GBs due to the increase in GB cohesion, a strategy that has also been applied to strengthen $Hf_xMo_{0.5}NbTa_xTiV_{1.5-x}Zr_x$ (x=0.5 or 1), and VNbMoTaW [47, 48]. A similar strengthening effect was reported for C and N interstitials in the equiatomic TiNbZr RCCA (**Fig. 1.7**c), where their segregation reduces GB energy and stabilizes the GB [49]. The critical role of GBs in governing plastic strain inhomogeneity in RCCAs has attracted significant attention due to the influence of interstitial solutes. This sort of experimental observation has motivated the proposition of grain boundary engineering, and more recently, inspired the coming of segregation engineering, a class of microstructural design paradigm that centers on atomic-scale fine-tuning of the GB excess quantity. The integration of thermodynamic theory with experimental observation provides a robust framework for leveraging solute segregation to enhance the mechanical performance of RCCAs. By modulating site-specific GB chemistry or structure, it becomes possible to extend the mechanical property limits of these advanced RCCAs.

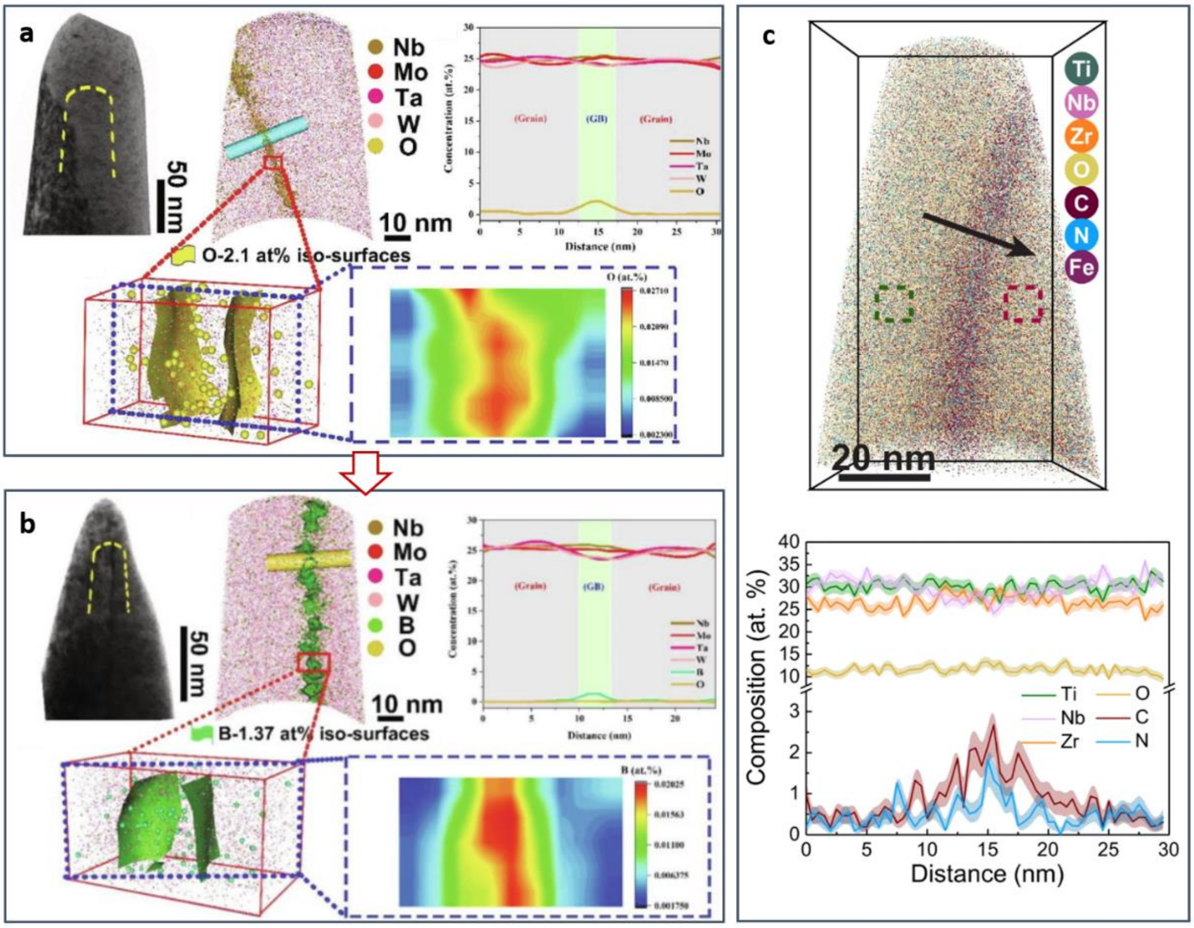

Fig. 1.7 (a) Three-dimensional elemental distribution in the as-cast NbMoTaW RCCA, illustrating the segregation of O impurities at the grain boundaries (GBs) [32]. (b) Three-dimensional elemental distribution for the B-doped NbMoTaW RCCA, showing the B segregation at the GBs [32]. (c) Three-dimensional reconstruction of a TiNbZr RCCA tip including the GB, and the corresponding 1D compositional profile following the arrow across the GB [49].

On Phase Stability. Generally, refractory elements exhibit high solubilities for interstitial elements due to their low enthalpies of solution and formation of metal-nonmetal compounds [35-38]. On the other hand, these refractory elements exhibit low electron affinity, attracting those elements with high electronegativities—such as H, B, C, N, and O—to form stable compounds [36-38]. These compounds, including carbides, nitrides, and oxides, significantly influence the phase stability of RCCAs. Therefore, the presence of interstitials can stabilize or destabilize specific phases by modifying the thermodynamic free energy landscape of RCCAs, thereby affecting phase equilibria or promoting the formation of multi-phase microstructures. For example, the exposure of TiZrNbTa RCCA to an H-enriched environment at 800 °C for 30 min induces phase separation (Fig. 1.8a) [50]. Single BCC phase decomposes into a composite of nanoscale Nb/Ta-rich BCC1 phase and Ti/Zr-rich BCC2 phase, following an orientation relationship of $(110)_{BCC2}//(110)_{BCC1}$, $[001]_{BCC2}//[001]_{BCC1}$. A similar phase decomposition process is also observed in TiNbZrHfTa RCCA after the heat treatment under H_2 (500 °C) [51]. The decomposition involves a time-dependent increase in the wavelength of modulated patterns, consistent with a spinodal decomposition pathway. Thermodynamic modeling suggests that hydrogen thermodynamically modifies the Gibbs free energy landscape by expanding the spinodal region, thereby destabilizing the single-phase BCC structure. Such a spinodal decomposition can also be triggered by a small number of other interstitials, such as O. For instance, 2 at.% of O can control the formation of the spinodal structures by altering the spinodal gap in the Ti-V-Hf-Nb system [52]. The incorporation of interstitial solutes and the associated formation of nanoscale spinodal features induce lattice distortion and mismatch within the matrix, thus enhancing mechanical properties (*i.e.*, solid solution strengthening, and spinodal hardening).

In addition to spinodal decomposition induced by a small addition of interstitials, the transition of crystal structure can also be observed due to the interactions of RCCAs with interstitials. A crystal structure transition from BCC to BCT in equiatomic TiNbZr RCCA has been revealed via *in-situ* X-ray diffraction and post-mortem structural analysis (TEM) []. The ordered distribution of H solutes causes an asymmetric expansion along the *c*-axis, thus resulting in the occurrence of tetragonality. Similarly, in the BCC TiNbZrHfTa RCCA, the addition of O triggers the structure transition from BCC to HCP as O is a strong HCP stabilizer (**Fig. 1.8**b) [34].

The formation of related compounds (*e.g.*, hydride, oxide, nitride, carbide, and boride) in RCCAs can also be anticipated due to their strong chemical affinities to these interstitials. For example, the intentional addition of N in as-cast NbMoTaWHf RCCAs leads to the formation of nitrides (**Fig. 1.8**c) [53]. Two kinds of nitrides are observed, one is the HfN with an FCC crystal structure, while the other one is the multicomponent nitride phase with an HCP structure. The introduction of nitride phases strengthens the material, particularly at elevated temperatures, due to their high structural stability and resistance to grain coarsening. Notably, a reversible phase transformation from the BCC phase to the FCC (or BCT) hydride phase is also observed in RCCAs under high H_2 pressure (>10 bar), highlighting their potential for hydrogen storage applications [54-58]. The vast compositional space (*i.e.*, optimization of desirable properties) and severe lattice distortion (*i.e.*, offering more available sites for hydrogen accommodation) of RCCAs make them potential candidates for hydrogen storage materials [56-58]. As for O, O uptake from the external environment at elevated temperatures can lead to oxidation in RCCAs, influencing both the phase stability and mechanical properties of RCCAs [59, 60]. These intricate interactions between interstitial atoms and refractory elements underscore the critical role of interstitials in tuning the phase stability and the associated mechanical performance of RCCAs.

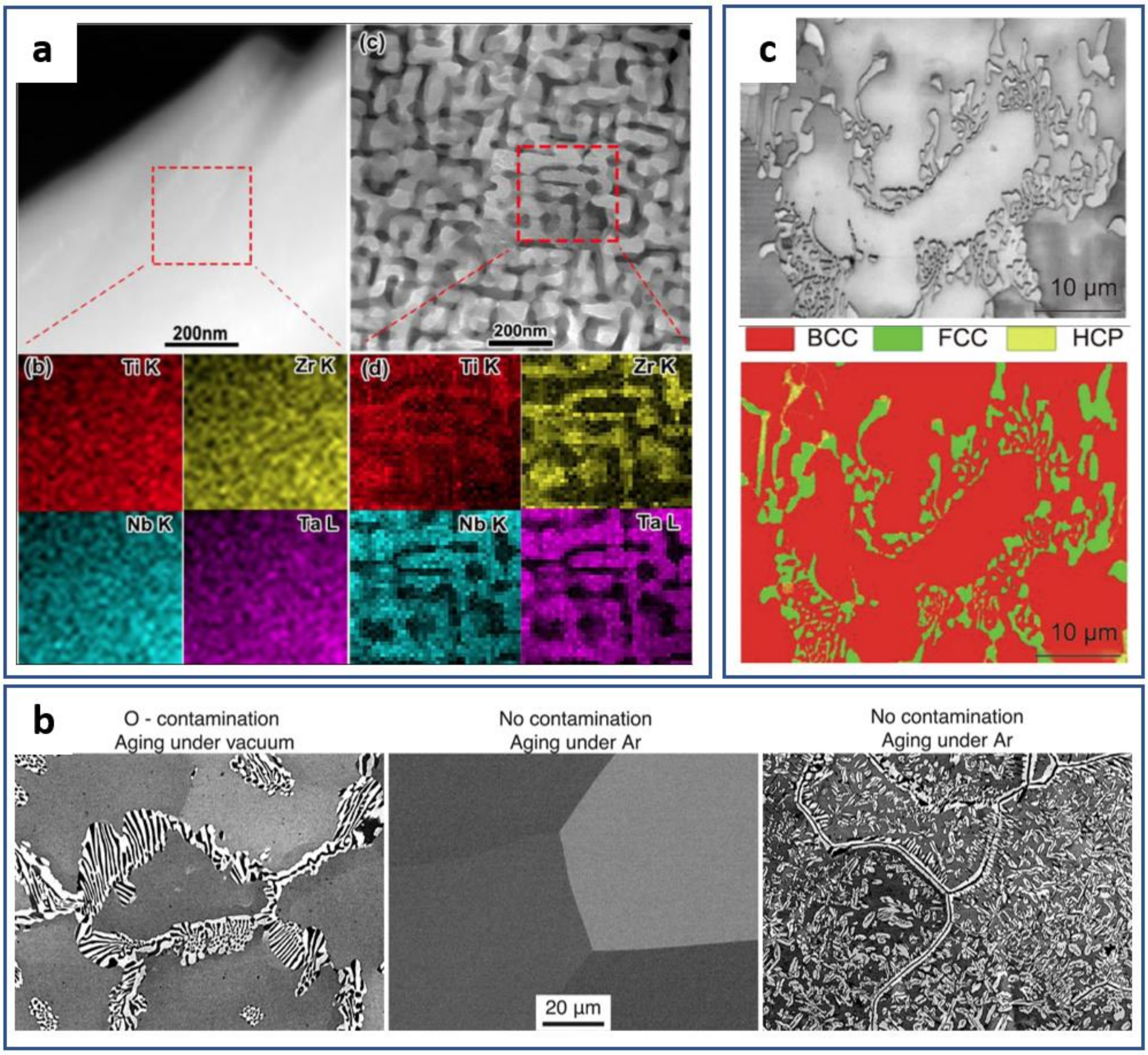
a
(c)
200nm
200nm
(b)
Ti K
Zr K
Nb K
Ta L
(d)
Ti K
Zr K
Nb K
Ta L
c
10 μm
BCC
FCC
HCP
10 μm
b
O - contamination
Aging under vacuum
No contamination
Aging under Ar
No contamination
Aging under Ar
20 μm

Fig. 1.8 (a) Scanning transmission electron microscopy (STEM) images and the corresponding elemental distribution maps of the as-received and H-absorbed TiZrNbTa RCCA [50]. (b) Comparison of the microstructures of the TiNbZrHfTa RCCAs (left: contaminated with O, middle: no contamination, right: with the addition of 3 at.% O) aged at 900 °C for 1000 h [34]. (c) Image quality map and the corresponding electron backscattered diffraction (EBSD) phase map of the as-cast NbMoTaWHfN RCCA [53].

On the Interaction with Dislocations. The interaction between interstitial atoms and dislocations plays a pivotal role in determining the mechanical properties of RCCAs. Interstitial atoms, such as H, B, C, N, and O, tend to accumulate around dislocations due to the strain fields they produce and the associated reduction in system free energy [12, 13]. This interaction leads to the formation of Cottrell atmospheres, which effectively pin dislocations and increase the critical stress required for their movement [12, 13]. Such a pinning effect contributes to an increase in the yield strength of RCCAs through interstitial solid-solution strengthening [30, 31]. Since the high solubility of interstitial atoms in BCC RCCAs, a compressive yield strength of 4.2 GPa, approaching the theoretical limit, has been achieved by incorporating ~12 at.% of O solutes without the formation of secondary phases [49]. At this solubility limit, the strong local force fields created by O atoms significantly impede dislocation nucleation and motion. On the contrary, H atoms can reduce the Peierls barrier—the energy required for dislocation motion—facilitating dislocation glide. This reduction in the Peierls barrier can also lead to hydrogen-enhanced localized plasticity, which may promote ductility but can also exacerbate embrittlement [61]. Additionally, interstitial-dislocation interactions lead to the formation of ordered oxygen complexes in RCCAs (*e.g.*, TiZrHfNb and TiNbZr), particularly with the intentional incorporation of interstitials (**Fig. 1.9**a and b). These complexes not only hinder dislocation motion (enhanced yield strength) but can also alter the slip mode from planar to wavy slip (homogenization of plastic flow), surmounting the strength-ductility trade-off [33, 62]. This shift from planar to wavy glide mode of dislocations has also been observed in the O-doped TiVHfNb system [52]. The incorporation of O induces the formation of nanoscale spinodal features, impeding the movement of dislocations and promoting the accumulation of dislocation density during plastic deformation (**Fig. 1.9**c). This accumulation contributes to strain hardening, thereby improving both the strength and ductility of RCCAs during mechanical loading.

In some cases, interstitials can influence dislocation dynamics by altering the core structures of dislocations for pure BCC metals [29, 63, 64]. However, the atomistic simulations show the interstitial solute atoms (such as O, C, and N) do not lead to any core reconstruction of the screw dislocation cores in TiNbZrHfTa RCCA [29]. A similar non-compact, spread-out configuration of screw dislocation core is observed in both the presence and absence of solute atoms. The interaction energy between dislocation cores and interstitial atoms spans a wide range (from -0.25 to -0.18 eV), indicative of dynamic strain aging. This dispersion in interaction energy can be rationalized by the variations in solute types and local chemical environments. Stronger attractions are observed when solutes are surrounded by HCP-forming elements such as Ti, Zr, and Hf. Therefore, the interactions between interstitial atoms and dislocations play a dual role: they can enhance the macroscopic mechanical performances of RCCAs under controlled conditions but may also pose challenges related to embrittlement and ductility loss in extreme environments. Understanding and tailoring these intricate interactions are essential for the development of RCCAs with optimized mechanical properties.

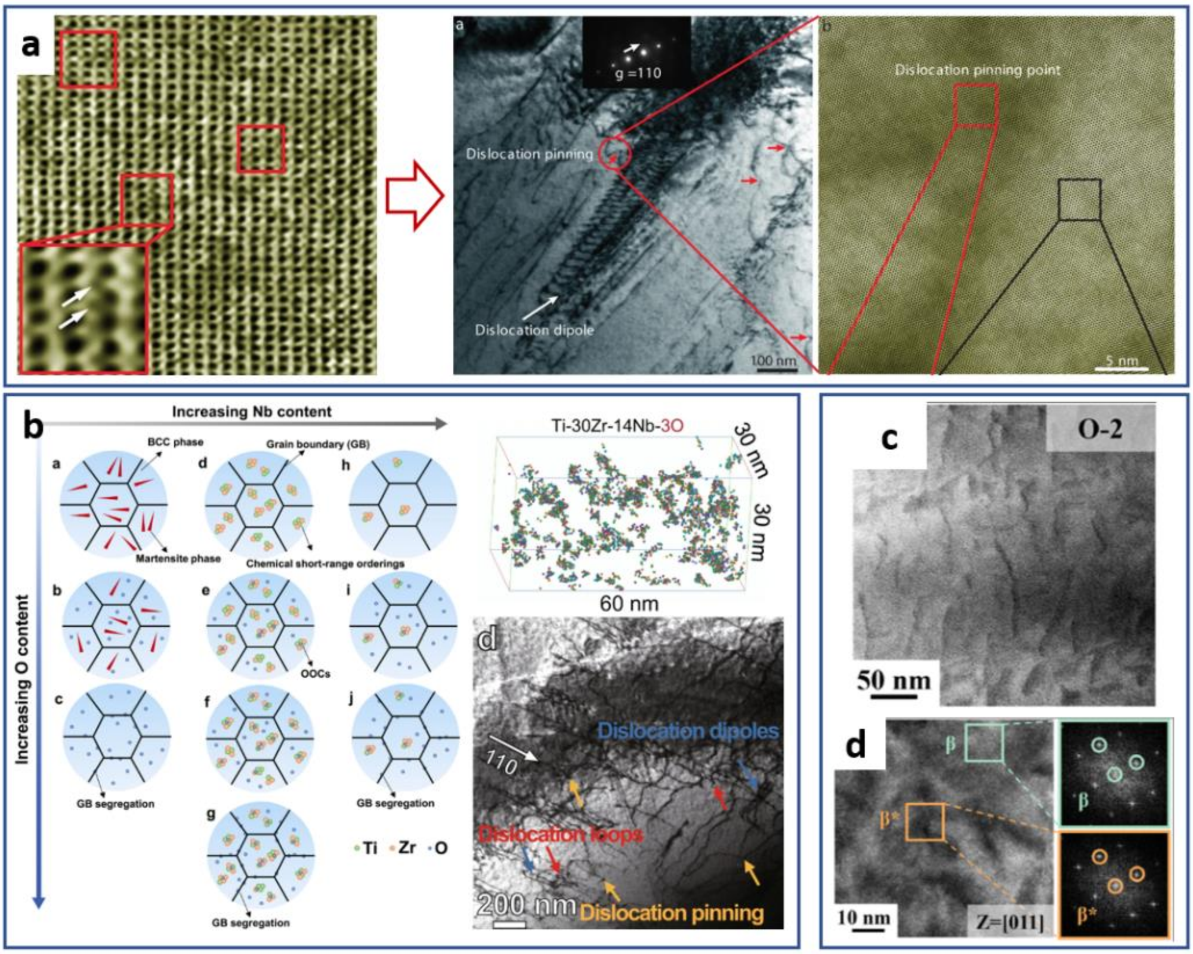
a
a
g =110
Dislocation pinning
Dislocation dipole
100 nm
b
Dislocation pinning point
5 nm
b
Increasing Nb content
Increasing O content
BCC phase
Grain boundary (GB)
Martensite phase
Chemical short-range orderings
OOCs
GB segregation
GB segregation
GB segregation
a
b
c
d
e
f
g
h
i
j
•Ti •Zr •O
Ti-30Zr-14Nb-3O
30 nm
30 nm
60 nm
d
110
Dislocation dipoles
Dislocation loops
Dislocation pinning
200 nm
c
O-2
50 nm
d
β
β*
β
β*
10 nm
Z=[011]

Fig. 1.9 (a) STEM-HAADF image revealing the existence of the ordered oxygen complexes in $(TiZrHfNb)_{98}O_2$ alloy, and the associated dislocation pinning occurring at these ordered oxygen complexes [33]. (b) Schematic diagram for the design of ordered oxygen complexes, and the 3D reconstruction of ordered oxygen complexes obtained in $TiZr_{30}Nb_{26}O_3$, along with their pinning effects on dislocations [62]. (c) Representative STEM-BF image and (d) TEM image, along with the marked selected-area electron diffraction (SAED) patterns of the O-incorporated TiVHfNb RCCA [52].

1.1.3. Motivations and the thesis structure

As introduced in the above sections, interstitial elements, such as oxygen, nitrogen, and hydrogen, play a crucial role in shaping the microstructure and phase stability of RCCAs due to their strong chemical affinity with the constituent refractory elements. Consequently, these microstructural modifications can significantly influence mechanical properties via the alternation of dislocation behaviors. Despite the potential benefits, the interactions between interstitials and RCCAs remain largely unexplored. A deep understanding of these interactions is essential for optimizing RCCA performance and expanding their applicability in demanding environments. Therefore, this study aims to systematically investigate the interplay between interstitial atoms (especially H) and RCCAs, with a focus on their effects on microstructure, phase stability, and consequent mechanical properties. The gained insights will contribute to the development of RCCAs with enhanced performance under extreme conditions. This study specifically targets the following aspects:

(1)The influence of the incorporation of hydrogen interstitials (also for boron and oxygen in this study) in microstructures and phase stabilities of RCCAs, along with the underlying mechanisms of their effects;

(2)The consequent change in mechanical properties of RCCAs due to the incorporation of environmental interstitials and the alternations of microstructures, and the associated deformation mechanisms.

To address the questions listed above, the thesis is organized as follows: **Chapter 2** presents the processing of the investigated materials and the principles of the applied characterization techniques. **Chapter 3** to **Chapter 6** focus on the microstructure evolution, phase stability, and mechanical properties of TiNbZr and TiNbZrHfTa RCCAs after the incorporation of different interstitial atoms. In **Chapter 3**, the evolution of lattice structure during the heat treatment under H_2 is studied, and the impact of H on the microstructure evolution is discussed. The phase stability of TiNbZrHfTa RCCAs with and without H incorporation is clarified in **Chapter 4**. In **Chapter 5**, the effect of B on the mechanical property and the alternation in deformation mechanisms of TiNbZrHfTa RCCAs is revealed. In **Chapter 6**, nanoscale chemical heterogeneity caused by O interstitials is observed and its impact on mechanical properties is investigated. In the end, **Chapter 7** summarizes the key findings in this thesis and outlines the future work.

2. Principles of research methodologies

2.1. Material processing and mechanical property assessment

2.1.1. Materials

The pure metals with a purity of higher than 99.9 wt.% were utilized as the base alloy. The equiatomic TiNbZr and TiNbZrHfTa RCCAs were cast using arc-melting under the Ar atmosphere. During the arc-melting process, the RCCA ingots were flipped upside down and remelted at least five times to ensure a homogeneous distribution of all the principle elements. A piece of Ti getter was employed to prevent potential oxygen contamination. The as-casted samples were cold-rolled with a thickness reduction of 80% and then homogenized at 1000 °C for 5 h, followed by air quenching to ambient temperature (**Fig. 2.1**a). The aforementioned processing describes the procedure for the as-received (or as-homogenized) RCCAs. Details of subsequent heat treatments (*e.g.*, annealing treatment under H_2, the addition of B, or induction treatment, *etc.*) will be provided in the respective chapters.

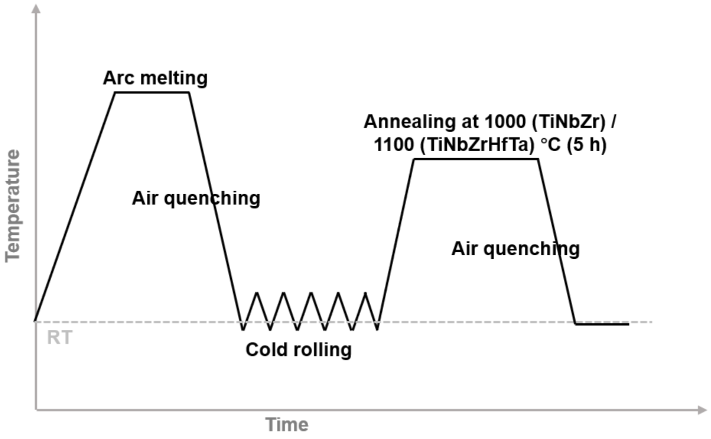

Fig. 2.1 Scheme depicting the processing of as-received (or as-homogenized) equiatomic TiNbZr and TiNbZrHfTa refractory complex concentrated alloys (RCCAs).

2.1.2. Dilatometer

Fig. 2.2a represents the overview of the dilatometer used in this study. Dilatometer has been utilized in the fabrication of metallic alloys, the study of martensitic transformations, and the compression and sintering of refractory alloys and other materials including ceramic products, composite materials, plastics, *etc.* [65-67]. The progress of chemical reactions (usually with a substantial volume change) can also be monitored by a dilatometer [68]. One common application for the dilatometer is measuring the thermal expansion, which is an important engineering parameter for the materials. The thermal expansion coefficient (α) can be defined as, $\alpha = \frac{1}{V}\left(\frac{\partial V}{\partial T}\right)_{p,N}$, where V, T, p, and N denote the volume of the material, temperature, pressure, and the load applied on the material, respectively [69]. A dilatometer (DIL 805, TA Instruments) is employed in this study for heat treatment under specific atmospheric environments (*e.g.*, Ar and H_2).

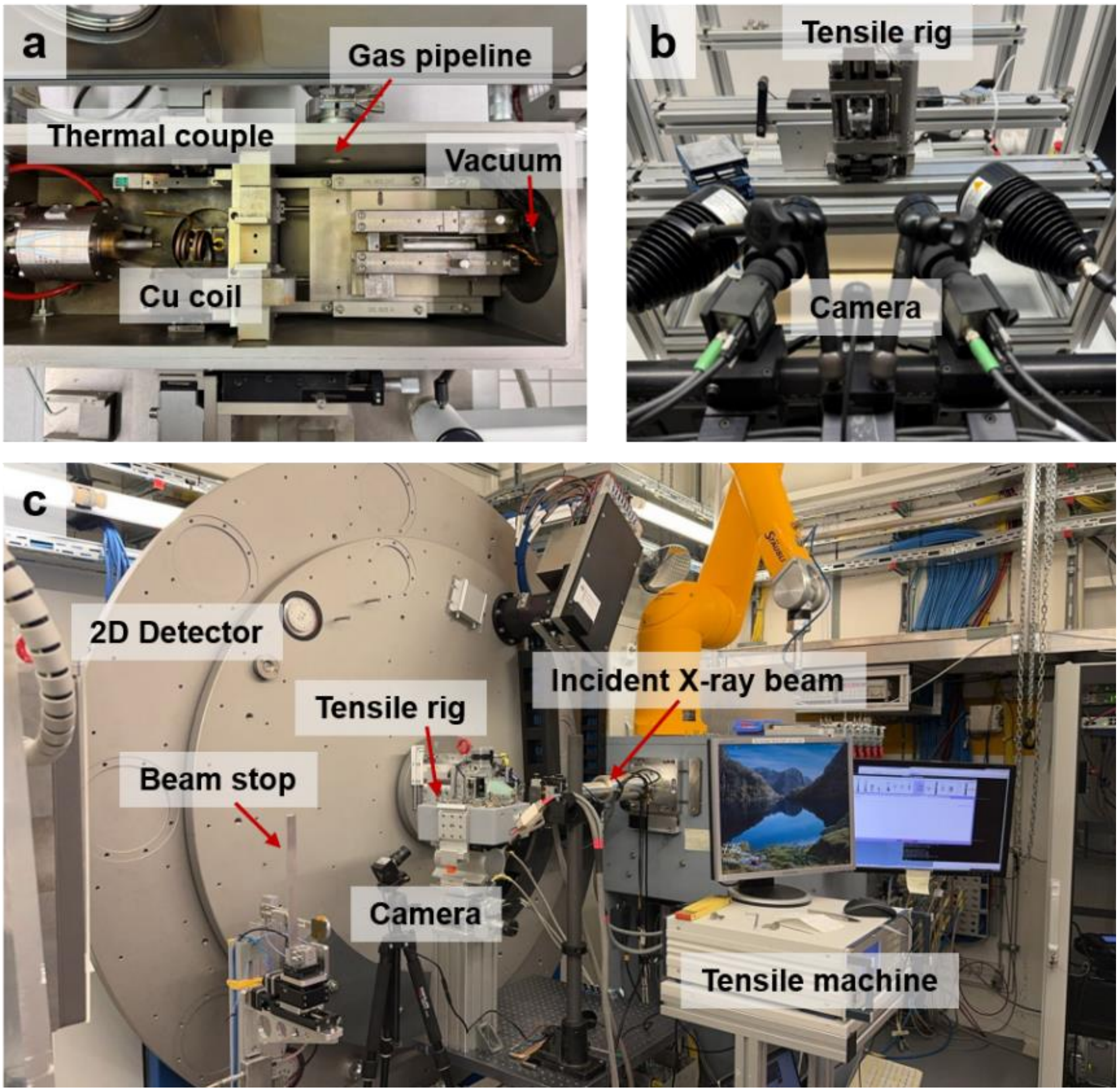
a
Gas pipeline
Thermal couple
Vacuum
Cu coil
b
Tensile rig
Camera
c
2D Detector
Incident X-ray beam
Tensile rig
Beam stop
Camera
Tensile machine

Fig. 2.2 Overviews of the (a) dilatometer (DIL 805, TA Instruments), (b) tensile rig (Kammrath & Weiss stage) equipped with an optical camera for digital image correction (DIC), and (c) set-up for *in-situ* tensile test at Powder Diffraction and Total Scattering Beamline P02.1 of PETRA III, at Deutsches Elektronen Synchrotron (DESY, Hamburg, Germany) employed in this study [70].

2.1.3. Uniaxial tensile test

Tensile testing is a fundamental mechanical test that applies force to a material specimen to evaluate its response to tensile stress. This test provides critical insights into the mechanical properties of materials, aiding in the development of next-generation materials with improved mechanical performance. By plotting the engineering stress-strain curves, valuable information about mechanical properties such as yield strength, ultimate tensile strength, elastic modulus, and ductility, can be obtained. For the tensile testing, a dog-bone-shaped specimen was prepared by the electrical discharge machining (EDM) method, followed by sample grinding to remove the oxide layer formed during the cutting process. The gauge geometry is 4 × 2 × 1 (length × width × thickness) mm. A Kammrath and Weiss stage equipped with an optical camera (every 1 s) for digital image correlation (DIC) analysis was employed for the tensile tests (**Fig. 2.2**b). A virtual extensometer (speckle patterns) was adopted to measure the local strains, and the data was processed using the Aramis GOM Correlate 2020 software (V6.3.0, GOM GmbH). At least three individual tensile tests were repeated for each microstructural condition to achieve reasonable statistics.

2.1.4. *In-situ* tensile test

In addition to uniaxial tensile tests, this study employed *in-situ* tensile testing combined with X-ray diffraction (XRD), a powerful technique for investigating the mechanical behavior and structural evolution of materials under applied stress. This approach enables real-time observation of changes in crystal structure, phase composition, and texture during tensile deformation, allowing researchers to correlate structural changes with mechanical behaviors as the specimen is stretched [71-73]. This technique is widely used in materials science, metallurgy, and mechanical engineering to study the mechanical properties and deformation mechanisms of advanced materials under realistic conditions [71-73]. The experimental setup for the *in-situ* tensile test is shown in **Fig. 2.2**c and was conducted at the Powder Diffraction and Total Scattering Beamline P02.1 of PETRA III, Deutsches Elektronen Synchrotron (DESY, Hamburg, Germany).

2.2. Micro/nano-structural characterization

2.2.1. Thermal conductivity detector

The dissolved hydrogen, nitrogen, and oxygen contents trapped within the samples are determined by the thermal conductivity detector (TCD) method. The TCD method utilizes the inherent characteristics of gases for the thermal transfer (thermal conductivity, κ) to quantify the gas concentrations (6.97, 1.00, and 1.02 ($\kappa_{gas}/\kappa_{air}$) for hydrogen, nitrogen, and oxygen, respectively at 0 °C, 1 atm) [74]. The change in temperature due to the heat transfer between a thermal wire sensor (*i.e.*, platinum) and the sample gas is detected as a variation in electrical resistance (**Fig. 2.3**a). This change in electrical signal allows us to obtain the corresponding concentration of the hydrogen, nitrogen, and oxygen dissolved in the samples. The measurement is facilitated by a standard linear calibration curve, developed by using standard samples with known concentrations of these elements.

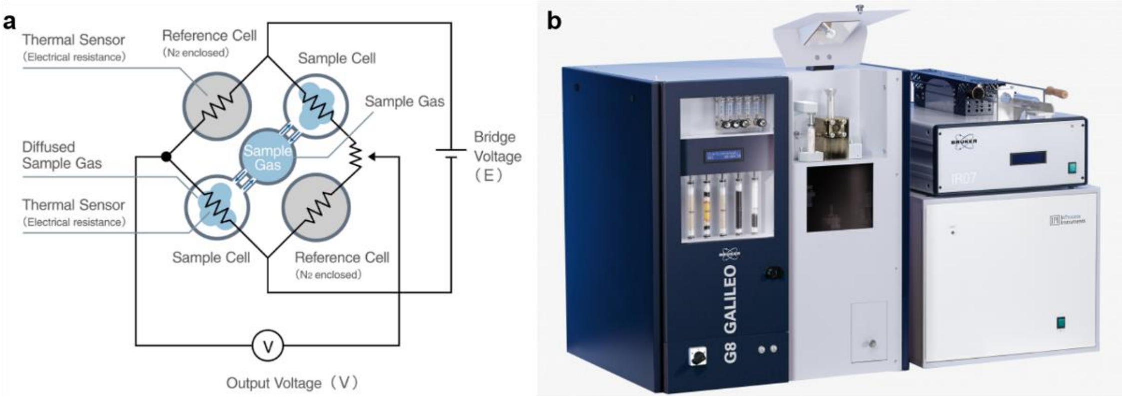

Fig. 2.3 (a) Schematics illustrating the basic circuit and principle of the equipment using the thermal conductivity detector (TCD) method [https://www.horiba.com/int/process-and-environmental/measuring-principles/thermal-conductivity-detector/#TCD-0]. (b) Overview of the thermal desorption spectroscopy (TDS) for determining the dissolved hydrogen, nitrogen, and oxygen contents.

Thermal desorption spectroscopy (TDS, G8 GALILEO ONH) equipped with an infrared furnace and mass spectrometer is employed for determining the dissolved hydrogen and oxygen contents of the specimens (**Fig. 2.3**b). A melt extraction method is used at a power of 35% to fully melt the tested alloys and release the trapped interstitial elements. Tin baskets are used as the carrier to lower the melting temperature of the refractory alloys, while helium is selected as the carrying gas for the measurements. The measurements were performed immediately after heat treatment with a transferring time shorter than 12 h, particularly for the detection of hydrogen. The specimen surfaces were ground with 1000-grit SiC paper to eliminate the surficial oxide layer formed after heat treatment and during sample transfer.

2.2.2. High-energy X-ray diffraction

Powder X-ray diffraction is a non-destructive analytical technique widely used for characterizing materials, ranging from polymers to metals. Based on one single measurement, a huge amount of crystallographic information can be obtained, including crystal structure, phase composition, crystallite size, microstrain, texture, etc [75]. As compared with laboratory X-ray diffraction (low spatial resolution and limited flux), high-energy X-ray diffraction (HEXRD) enables data acquisition in transmission mode with sub-second resolution. This capability facilitates time-resolved studies and allows the probing of a larger sample volume, making HEXRD particularly suitable for dynamic experiments and *in-situ* investigations.

HEXRD measurements are experimentally simple in principle, with the underpinning physics behind diffraction being well-established and thoroughly understood. When a monochromatic incident beam of high-energy X-rays hits the sample, either discrete diffracted spots (for single crystals) or continuous diffracted Debye-Scherrer rings (for polycrystals) are obtained (**Fig.**

2.4a). The crystal structure can be determined from the positions of the Bragg peaks, while the width and shape of the peaks in the Debye-Scherrer rings yield information related to the size and strain of the crystallites. Bragg peaks appear at discrete θ angles, once θ satisfies the following equation (**Fig. 2.4**b),

$$n\lambda = 2d\sin\theta \tag{2.1}$$

where n and λ are the order of diffraction and the wavelength of the incident beamline, respectively. d is the interspacing between the specific crystal planes. In the case of HEXRD, the scattering vector (q) is usually adopted instead of θ, namely, $q = 4\pi\sin\frac{\theta}{\lambda}$. There is a reciprocal relationship between the q and the length scales probed inside the sample, $d = \frac{2\pi}{q}$. At each set of well-defined crystallographic planes in the crystal lattice, there will be a corresponding diffraction peak due to the constructive interference of X-rays scattered by these planes.

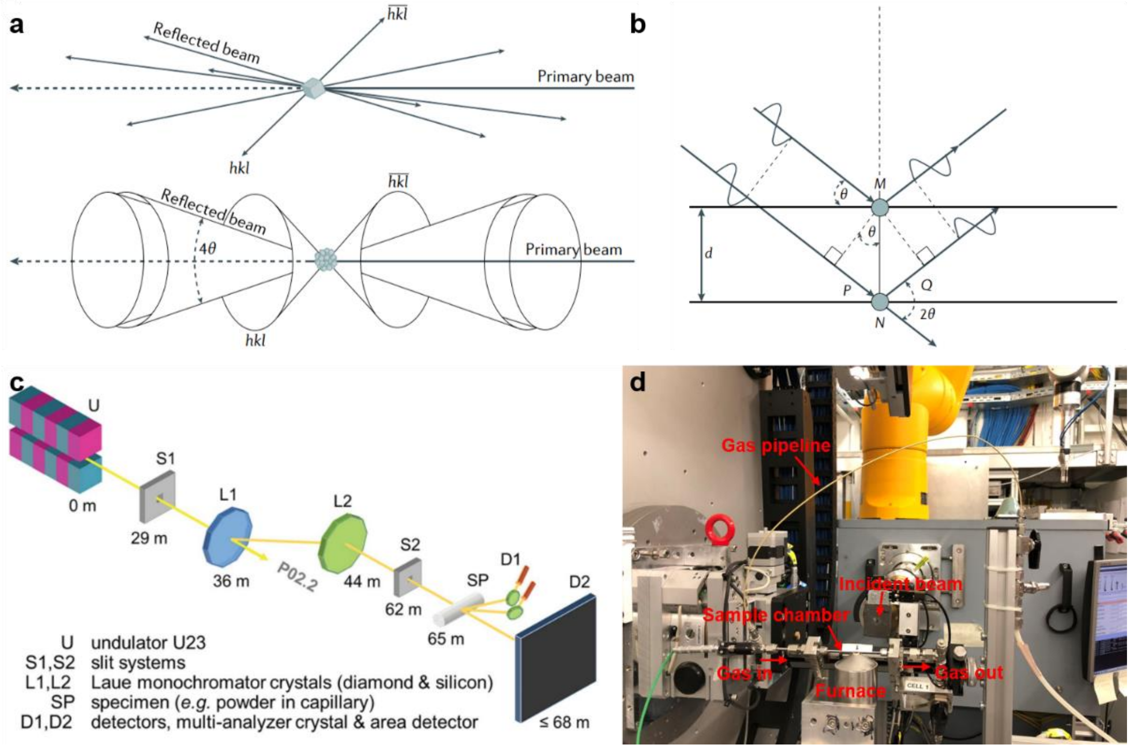
a
Reflected beam
$\overline{hkl}$
Primary beam
hkl
Reflected beam
4θ
$\overline{hkl}$
Primary beam
hkl
b
θ
M
θ
d
P
Q
N
2θ
c
U
0 m
S1
29 m
L1
36 m
P02.2
L2
44 m
S2
62 m
SP
65 m
D1
D2
≤ 68 m
U undulator U23
S1,S2 slit systems
L1,L2 Laue monochromator crystals (diamond & silicon)
SP specimen (e.g. powder in capillary)
D1,D2 detectors, multi-analyzer crystal & area detector
d
Gas pipeline
Incident beam
Sample chamber
Gas in
Gas out
Furnace

Fig. 2.4 Schematics depicting (a) the comparison between scattered beams stemming from one single crystal (top) and a powder (bottom) and (b) the simplified derivation of Bragg's law. (c) Optical train with the major optical elements and the associated distances to the undulator at Powder Diffraction and Total Scattering Beamline P02.1 of PETRA III, at DESY (Hamburg, Germany) [70]. (d) Snapshot of the beamline P02.1 and the corresponding *in-situ* setup for heat treatment under H_2 and Ar.

Fig. 2.4c and d illustrate the beamline optics and the corresponding *in-situ* setup used for this study at Powder Diffraction and Total Scattering Beamline P02.1 of PETRA III, at DESY in Hamburg (Germany). This beamline is dedicated to the investigation of the atomic scale structure of polycrystalline materials. The beam energy of the X-ray was fixed at 60 keV to obtain a monochromatic X-ray with a wavelength of ~0.207 Å. The beam size of the incident beam was 1 mm × 1 mm, allowing for a sufficient sample volume to ensure reliable statistical analysis. The Debby-Scherrer patterns were recorded every second by the fast area detector Varex XRpad 4343CT (2880 pixels × 2880 pixels, with a pixel size of 150 µm × 150 µm). A sample-to-detector distance of around 1.4 m was selected, enabling the collection of five diffraction rings for further detailed analysis (*e.g.*, Rietveld refinement). The post-processing of the acquired HEXRD data was conducted using GSAS-II software [76].

2.2.3. Small-angle X-ray scattering

Similar to XRD, small-angle X-ray scattering (SAXS) is a technique on the basis of the principles of diffraction, measuring the intensity (*I*) of scattered X-rays as a function of the scattering angle (q). However, SAXS predominantly focuses on the scattering behavior of X-ray beams at low q values (typically below 1 Å^{-1}), probing the structural organization in materials and quantifying its response to changes under external conditions (**Fig. 2.5**a-d) [77]. The intensity pattern resulting from coherent scattering events provides information regarding the morphological information of the subcomponents within the materials, including size, morphology, and volume density. SASX can be applied to almost any material, ranging from biomolecules, and polymers to nanoprecipitates in metal alloys. Furthermore, SAXS can be coupled with WAXS (wide-angle X-ray scattering) to provide complementary information, capturing both the nanoscale structural organization and the atomic-scale crystalline details of materials (an *in-situ* deformation setup coupled with WAXS/SAXS is shown in **Fig. 2.5**e).

Although SAXS measurements are experimentally straightforward, similar to XRD, the subsequent data post-processing demands greater attention to accurately interpret the scattering patterns and extract precise structural information. Complementary techniques such as TEM or APT are sometimes required to validate the selected model used for data fitting. The resulting intensity pattern, *I*(*q*), is expressed as a function of q,

$$I(q) = n|F(q)|^2 S(q) \tag{2.2}$$

where n, $F(q)$, and $S(q)$ represent the number density of the subcomponents, the form factor (related to shape morphology), and the structure factor (related to the interaction between subcomponents). Chi-squared (χ^2) optimization is typically adopted for fitting model to data, which reflects the discrepancy between the experimental and theoretical models,

$$\chi^2 = \sum \left[\left(I_q - \mathrm{theory}_q \right) / \mathrm{weight}_q^2 \right] \tag{2.3}$$

A good fit is indicated when χ^2 closes to 0. The aim of SAXS studies is the interpretation of $F(q)$ as well as $S(q)$ to extract information about excess length density, and the interactions between the subcomponents within the material.

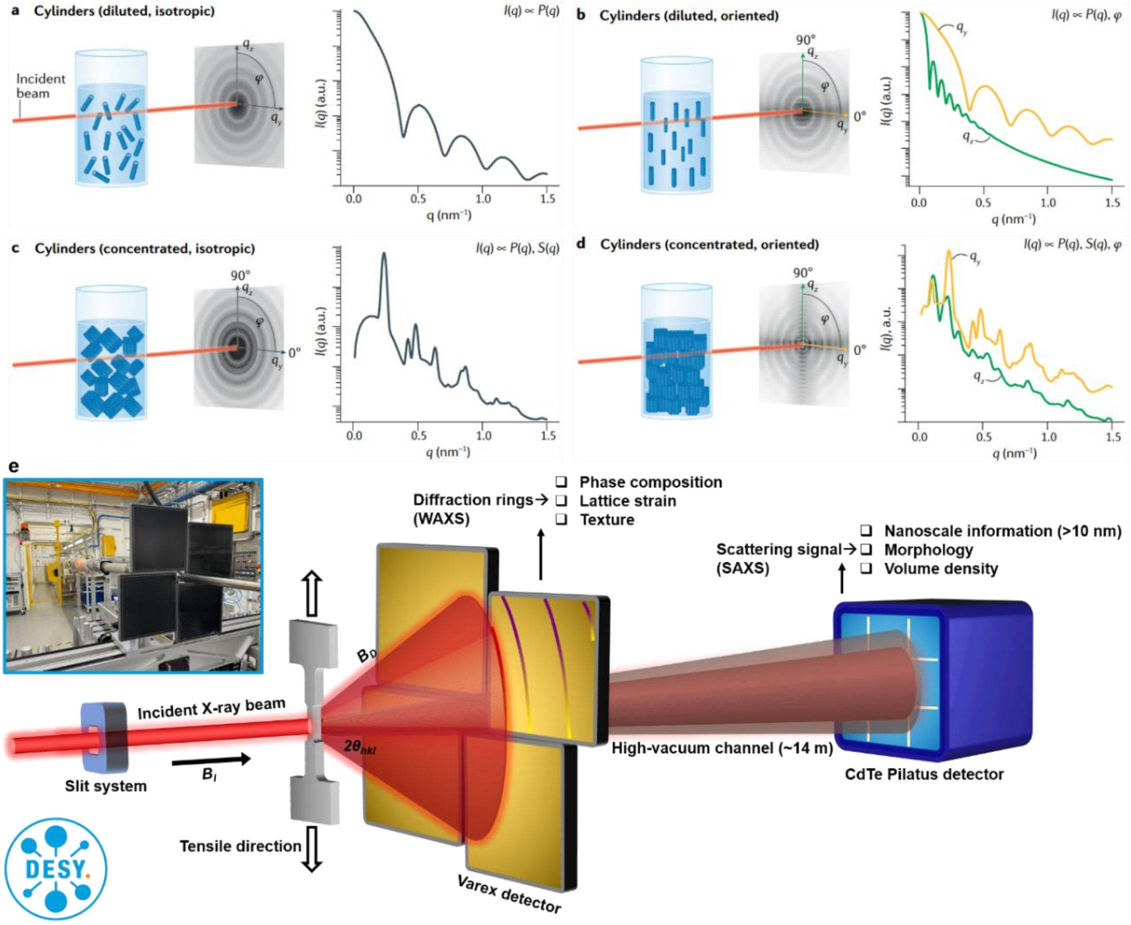
a Cylinders (diluted, isotropic)
Incident beam
q_z
q_y
φ
$I(q) \propto P(q)$
I(q) (a.u.)
0.0
0.5
1.0
1.5
q (nm⁻¹)
b Cylinders (diluted, oriented)
90°
0°
$I(q) \propto P(q), \varphi$
c Cylinders (concentrated, isotropic)
$I(q) \propto P(q), S(q)$
d Cylinders (concentrated, oriented)
$I(q) \propto P(q), S(q), \varphi$
I(q), a.u.
e
Diffraction rings→ (WAXS)
☐ Phase composition
☐ Lattice strain
☐ Texture
Scattering signal→ (SAXS)
☐ Nanoscale information (>10 nm)
☐ Morphology
☐ Volume density
Incident X-ray beam
Slit system
B_l
B_0
$2\theta_{hkl}$
Tensile direction
High-vacuum channel (~14 m)
CdTe Pilatus detector
Varex detector
DESY.

Fig. 2.5 Schematic representation of scattering patterns for: (a) diluted, randomly oriented rod-like cylindrical particles, (b) non-interacting but oriented rod-like cylindrical particles, (c) concentrated hexagonal cylindrical clusters that are randomly oriented, and (d) concentrated hexagonal cylindrical clusters that are oriented, respectively. (e) Illustration of the Diffraction & Imaging at the Swedish Beamline P21.2 of PETRA III, at DESY (Hamburg, Germany) for *in-situ* deformation test coupled with WAXS/SAXS study. Insert is the snapshot of the Beamline P21.2 [78].

Fig. 2.5e briefly shows an overview of the *in-situ* deformation setup at the Diffraction & Imaging at the Swedish Beamline P21.2 of PETRA III, at DESY (Hamburg, Germany) [78]. The diffraction station EH3 in Beamline P21.2 provides flexible positioning of various detector types including 4 WAXS detectors (Varex detectors) and a SAXS detector (high-resolution CdTe Pilatus detector) approximately 14 m behind the sample position, enabling the couple WAXS/SAXS study. The SAXS experiments were conducted with a fixed photon energy of 70 keV (λ = 0.175864 Å). The SAXS data was post-analyzed using the SasView software.

2.2.4. Scanning electron microscopy

After optical microscopy (OM), the burgeoning of electron microscopy has revolutionized our understanding of materials by completing the processing-structure-properties links down to the micrometer scale (scanning electron microscopy, SEM), even to atomistic levels (transmission electron microscopy, TEM). Electron microscopy was developed since the wavelength of visible light (~500 nm) imposed the limited image resolution. In this chapter, we will mainly focus on the brief introduction of SEM and the associated techniques used in this study. SEM is currently one of the most frequently used tools for most solid materials (from metal alloys to polymers). The lateral resolution of SEM can vary from 1 nm to 1 mm, enabling the surface-morphology observations and elemental-composition measurements respectively. As illustrated in **Fig. 2.6**a, when the primary electron beam finely focused by the electron gun scans over a surface, a variety of signals emanate from the interaction volume [79, 80]. In addition to obtaining the morphological information from the material's surface (by collecting secondary electrons), the chemical identity (by electron dispersive X-ray spectroscopy, EDXS) and crystallographic features (by electron backscattered diffraction, EBSD) can also be determined. Furthermore, SEM enables the measurements of the chemical bonding (by Auger electrons) and the electronic state (by cathodoluminescence) of microscopically small-volume elements. The *in-situ* observations and interrupted tests of the evolution of microstructures during the measurements (*e.g.*, heating, mechanical loading, or both) can also be achieved, and this approach has gained increasing attention over the past decades [79]. **Fig. 2.6**b represents the SEM (Zeiss Sigma 500, Germany) machine used in this study.

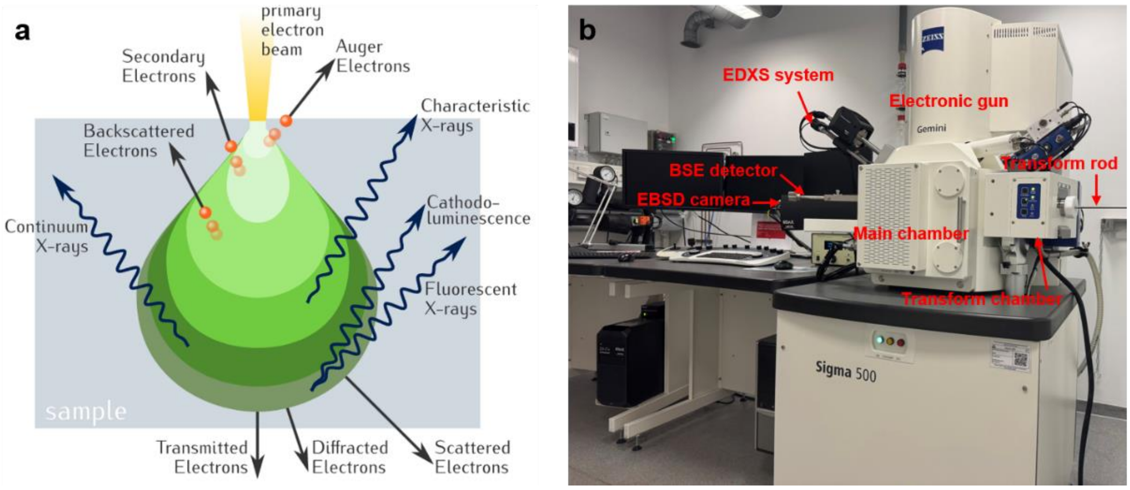
a
primary electron beam
Secondary Electrons
Auger Electrons
Characteristic X-rays
Backscattered Electrons
Cathodo-luminescence
Continuum X-rays
Fluorescent X-rays
sample
Transmitted Electrons
Diffracted Electrons
Scattered Electrons
b
EDXS system
Electronic gun
Gemini
Transform rod
BSE detector
EBSD camera
Main chamber
Transform chamber
Sigma 500

Fig. 2.6 (a) Illustration showing the interaction between the primary beam and the specimen in scanning electron microscopy (SEM), generating multiple species for imaging and chemical composition determination [From Wikipedia]. (b) Overview of the used SEM in this study.

Here, the EBSD technique will be elaborated since it is powerful for the characterization of crystalline materials (*e.g.*, crystallographic orientation, defect arrangement, etc.), especially metal alloys (the investigated materials in this study). In the case of crystalline materials, local discrepancies in density and surface inclination give rise to the corresponding compositional and topographical contrasts. These contrasts are highly dependent on the backscattered electron density, which is influenced by the orientation of the crystal lattice with respect to the incident direction of the electron beam as well as the lattice parameters. In principle, the primary electrons are scattered coherently by the lattice atoms (following Bragg's equation), and form a lattice-coherent electron wave field (Bloch waves) (**Fig. 2.7**). The orientation of the crystal lattice relative to the direction of the primary electron beam leads to different density in the electron wave field, thus resulting in the formation of channeling contrast (diffraction contrast) and Kikuchi patterns. A typical schematic diagram of the formation of Kikuchi diffraction bands is shown in **Fig. 2.7**b, and the backscattering profile for a two-beam case is illustrated in **Fig. 2.7**c. EBSD patterns, consisting of a series of Kikuchi bands superimposed on a continuous background of backscattered electrons, are usually indexed to offer crystallographic information and defect arrangement of the studied material. The formation of EBSD patterns can be understood using dynamical theory based on electron-matter interaction. Bloch waves can be expressed as a time-independent Schrödinger equation, demonstrating the interaction between the wave function (Ψ) of a high-energy electron and the periodic potential of atomic nuclei of the lattice [81],

$$\nabla^2\Psi + \frac{2m}{\hbar^2}\left[E - \sum V_h \exp(2\pi i \boldsymbol{h}\cdot\boldsymbol{r})\right]\Psi = 0 \qquad (2.4)$$

Here m, and E indicate the electron mass and kinetic energy of the primary electron, respectively, while the sum over h (a Fourier series) describes the periodic potential of the lattice. V_h represents the complex Fourier coefficients for the reciprocal lattice vectors $\boldsymbol{h}$. $\boldsymbol{r}$ is the real space vector of the spatial position at which the electron intensity is to be evaluated. One solution for the above equation is considered as a linear combination of Bloch waves $\psi^{(j)}$ [81],

$$\Psi(\boldsymbol{r}) = \sum_j \varepsilon^{(j)}\,\psi^{(j)}(\boldsymbol{r}) = \sum_j \varepsilon^{(j)} \sum_{\mathrm{g}} C_{\mathrm{g}}^{(j)} \exp\left[2\pi i\left(\boldsymbol{k}_0^{(j)} + \mathbf{g}\right)\cdot\boldsymbol{r}\right]\exp\left(-2\pi q^{(j)} z\right) \qquad (2.5)$$

In this equation, $\varepsilon^{(j)}$ denotes the excitation amplictude of the Bloch wave $\psi^{(j)}$, while $C_{\mathrm{g}}^{(j)}$ is the cofficients of the partial Bloch waves with wave vectors $\boldsymbol{k}_0^{(j)} + \mathbf{g}$. $q^{(j)}$ and z are the damping coefficient and the corresponding depth below the crystal surface. The last exponential term mainly describes the incoherent(inelastic) interaction between the Bloch wave (j) and the crystal lattice, resulting in the backscattering of electrons out of the Bloch wave field. In principle, backscattering occurs from the total electron wave field, which is calculated as a sum over all the individual Bloch waves. Therefore, the total electron wave density at position ***r*** in the crystal can be calculated (Dependent Bloch wave model) [81],

$$P(\boldsymbol{r}) = \Psi\Psi^* \left| \sum_{j} \sum_{\mathrm{g}} C_0^{(j)} C_{\mathrm{g}}^{(j)} \exp\left[2\pi i \left(\boldsymbol{k}_0^{(j)} + \mathbf{g}\right) \cdot \boldsymbol{r}\right] \exp\left(-2\pi q^{(j)} z\right) \right|^2 \tag{2.6}$$

This equation demonstrates that the probability of a backscattering event at the given position ***r*** is proportional to the total electron wave density. For an idealized two-beam case, the Bloch wave coefficients can be simplified as follows [81],

$$C_0^{(j)} C_0^{(j)} = \frac{1}{2}\left[1 + (-1)^j \frac{w}{\sqrt{1+w^2}}\right] \tag{2.7}$$

$$C_0^{(j)} C_{\mathrm{g}}^{(j)} = -\frac{1}{2}\frac{(-1)^j}{\sqrt{1+w^2}}, j = 1,\ 2 \tag{2.8}$$

where $w = s\xi_{\mathrm{g}}$, is the dimensionless orientation parameter, where ξ_{g} and s represent the extinction distance and excitation error, respectively. When the orientation parameter satisfies $w = 0$, it indicates the incident beam is right at the Bragg angle. $w > 0$ suggests a weak backscattering signal (the primary beam tends to be vertical to the lattice planes), while a strong backscattering signal is indicated by $w > 0$ (the primary beam tends to be parallel with the lattice planes).

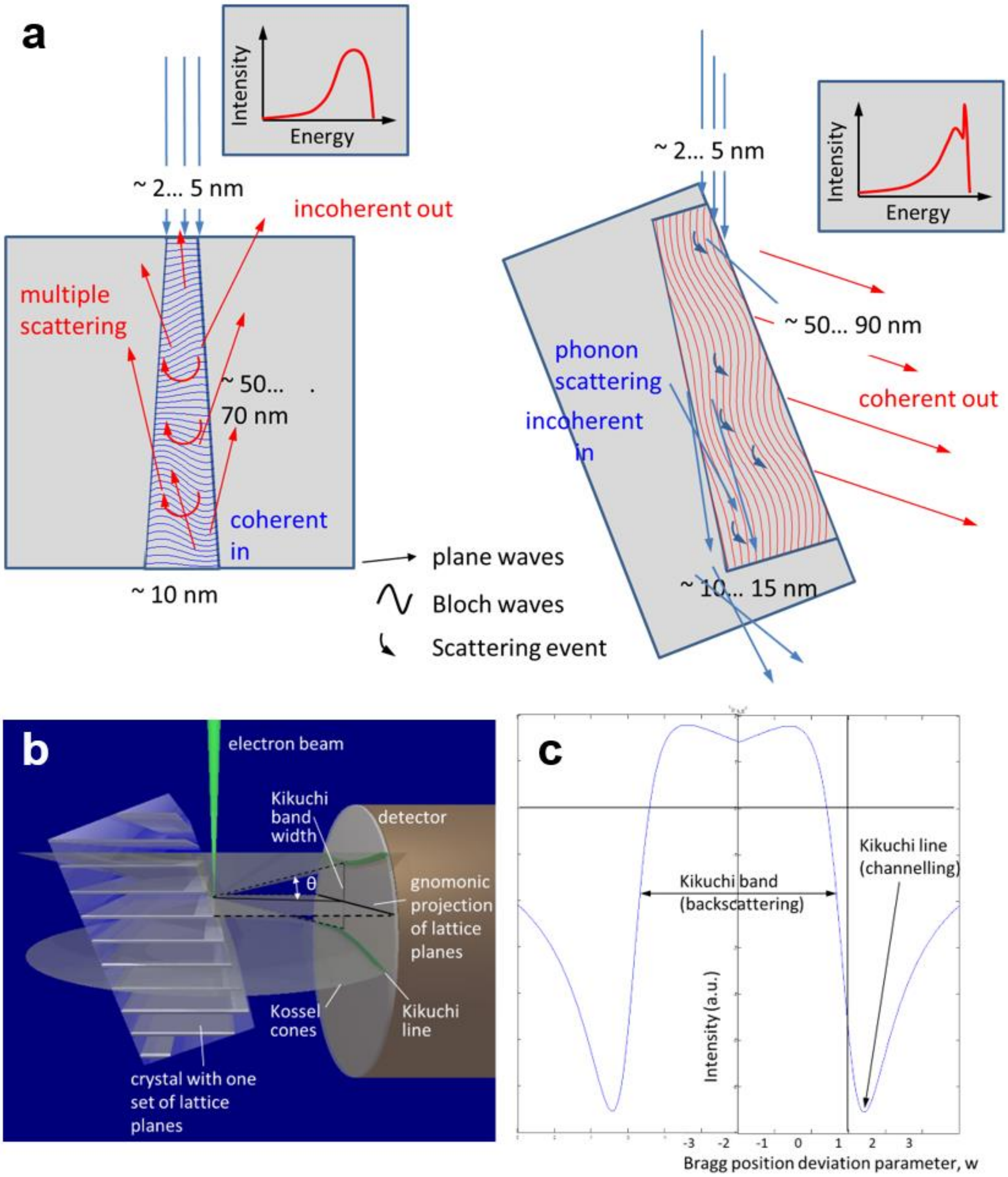
a
Intensity
Energy
~ 2... 5 nm
incoherent out
multiple scattering
~ 50... 70 nm
coherent in
~ 10 nm
plane waves
Bloch waves
Scattering event
~ 2... 5 nm
Intensity
Energy
~ 50... 90 nm
phonon scattering
incoherent in
coherent out
~ 10... 15 nm
b
electron beam
Kikuchi band width
detector
θ
gnomonic projection of lattice planes
Kossel cones
Kikuchi line
crystal with one set of lattice planes
c
Kikuchi line (channelling)
Kikuchi band (backscattering)
Intensity (a.u.)
-3
-2
-1
0
1
2
3
Bragg position deviation parameter, w

Fig. 2.7 (a) The basic pinciples of backscttering and forward scattering for SEM [81]. Illustration showing the (b) formation of (backscatter) Kikuchi patterns due to the interaction of the electron beam with specimen, and (c) the corresponding backscattering profile for the two-beam case.

Hough transform has been typically employed to index the EBSD patterns by extracting positions and orientations of the bands [82]. Briefly, with the calibrated detector geometry, the normals of lattice planes that lead to the formation of bands can be identified. The orientation of the lattice plane is then determined by means of a comparison of the angles between pairs of zone axes with pre-computed angles derived from the known crystal structure. The inefficiency in analyzing the patterns with poor quality of the Hough transform leads to the development of the dictionary indexing (DI) method [83]. This method relies on a similarity metric (dot product between the normalized patterns), comparing the theoretical patterns (computed for a uniform sampling of the orientation space) with experimental ones to determine the best match. The DI method indeed offers high robustness for the analysis of low-quality patterns by using full pattern information, albeit with the increasing computational requirements with descending crystal symmetry. Nowadays, a new approach, namely spherical indexing, is proposed for the indexing of the patterns [84]. The underpinning algorithm lies in the cross-correlation between a spherical EBSD pattern (master pattern) with a back-projected experimental pattern employing the spherical harmonic transform (SHT). The continuous SHT of a function on a sphere $f(\theta, \phi)$ can be defined as,

$$f(\theta, \phi) = \sum_{l=0}^{\infty} \sum_{m=-l}^{+l} \hat{f}_m^l Y_m^l(\theta, \phi) \tag{2.9}$$

with

$$\hat{f}_m^l = \int_0^{\pi} \mathrm{d}\theta \sin\theta \int_0^{2\pi} \mathrm{d}\phi f(\theta, \phi) \overline{Y_m^l(\theta, \phi)} \tag{2.10}$$

$$Y_m^l(\theta, \phi) = \sqrt{\frac{(2l+1)!\,(l-1)!}{4(l+m)!}} P_m^l\,(\cos\theta)\mathrm{e}^{im\phi}\#(2.11)$$

where $\hat{f}_m^l$ and $Y_m^l(\theta, \phi)$ denote the weight functions and spherical harmonics functions, while P_m^l is the Legendre polynomial of degree *l* and order *m*. The over-bar represents the complex conjugate. Once we have two SHTs from both the master pattern and experimental pattern, we can proceed with cross correlation using the Wigner *D* function. If we consider a 3D rotation in three Euler angles $R(\alpha, \beta, \gamma)$, the rotated spherical harmonic function is,

$$Y_m^l(\omega) = \sum_n Y_n^l(R^{-1}\omega) D_{m,n}^l(R) \tag{2.12}$$

where ω denotes the spherical coordinates, while $D_{m,n}^l(R)$ demonstrates the Wigner *D* function,

$$D_{m,n}^l(\alpha, \beta, \gamma) = d_{k,m}^l(\beta)\mathrm{e}^{im\alpha}\mathrm{e}^{im\gamma} \tag{2.13}$$

with the Wigner *d* function defining as,

$$d_{k,m}^l(\beta) = \sqrt{\frac{(l+k)!\,(l-k)!}{(l+m)!\,(l-m)!}} \cos\left(\frac{\beta}{2}\right)^{k+m} \sin\left(\frac{\beta}{2}\right)^{k-m} P_{l-k}^{k-m,k+m}(\cos\beta) \tag{2.14}$$

where $P_l^{k,m}(x)$ is a Jacobi polynomial. By computing the spherical cross correlation between two spherical functions (*f* and g),

$$(f\bigstar \mathrm{g})(R) = \sum_{l,m,n} \hat{f}^l_m \, \overline{\hat{\mathrm{g}}^l_m} D^l_{m,n}(R) \tag{2.15}$$

The cross correlation can then be computed via a 3D Fast Fourier Transform (FFT) by decomposing *D* into tow rotations,

$$(f\bigstar \mathrm{g})(\alpha, \beta, \gamma) = \mathscr{F}^{-1} \left\{ \sum_{l} \hat{f}^l_m \, \overline{\hat{\mathrm{g}}^l_m} d^l_{m,k}\left(\frac{\pi}{2}\right) d^l_{k,n}\left(\frac{\pi}{2}\right) \right\} \left(\alpha + \frac{\pi}{2}, \beta + \frac{\pi}{2}, \gamma + \frac{\pi}{2}\right) \tag{2.16}$$

Therefore, a best fit position (α, β, γ) between the experimental pattern and the master pattern can then be found. This approach retains the robustness against the noise of the DI method while offering improved computational efficiency.

2.2.5. Transmission electron microscopy

Different from SEM, TEM has emerged as an advanced tool for atomic-scale compositional and structural analysis. It can offer us not only direct proofs of materials and associated defects with atomic resolution but also spectroscopic information as well as diffraction patterns from sub-nanometer views. This character is mainly due to the achieved high electron energy (*E*) in TEM (> 100 keV). Ignoring the relativistic effects, the wavelength of electrons (λ) can be approximately expressed as [85],

$$\lambda = \frac{1.22}{E^{\frac{1}{2}}} \tag{2.17}$$

Therefore, take 100 keV of electrons for an example, a λ of around 4 pm can be worked out, which is much smaller than the radius of an atom. The high electron energy in TEM is generated by a gun assembly, which consists of several sets of magnetic lenses that focus the electrons coming from the source (**Fig. 2.8**). The electron beams transmit through the specimen with a thickness typically below 100 nm, projecting either onto a phosphor screen (for diffraction) or a camera (for micrograph). The underlying mechanism of the diffraction in TEM is consistent with the X-ray techniques because of the wave nature of electrons. In the case of a micrograph, the image contrast appears due to the scattering of the incident electron beam by the inserted sample. The interaction between electron beams and samples will result in a change in both the amplitude (amplitude contrast) and the phase (phase contrast) of the electron beam, giving rise to image contrast. The amplitude contrast, consisting of mass-thickness contrast and diffraction contrast, is commonly observed in conventional TEM in both bright-field and dark-field images, while the latter is primarily used to acquire atomic-level images, especially in scanning transmission electron microscopy (STEM).

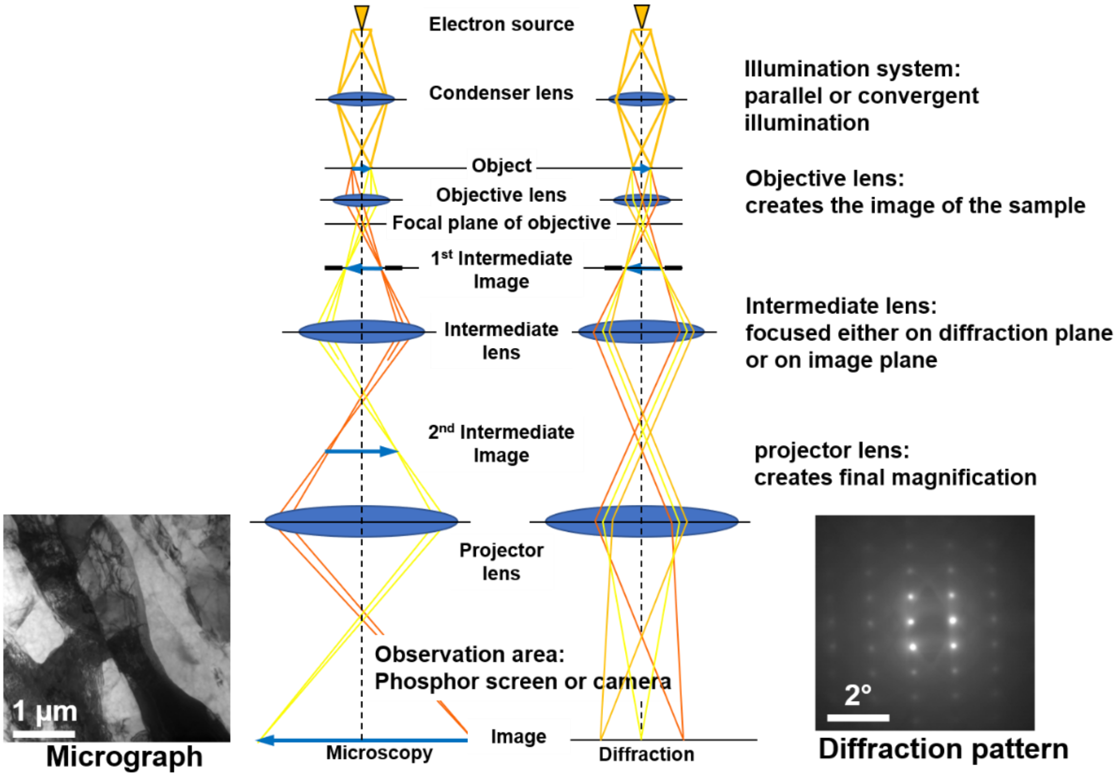
Electron source
Condenser lens
Illumination system:
parallel or convergent
illumination
Object
Objective lens
Focal plane of objective
Objective lens:
creates the image of the sample
1st Intermediate
Image
Intermediate
lens
Intermediate lens:
focused either on diffraction plane
or on image plane
2nd Intermediate
Image
projector lens:
creates final magnification
Projector
lens
Observation area:
Phosphor screen or camera
1 µm
Micrograph
Microscopy
Image
Diffraction
2°
Diffraction pattern

Fig. 2.8 Schematic drawing of the principles of micrograph and diffraction modes in a transmission electron microscopy (TEM) [81].

2.2.6. Atom probe tomography

Atom probe tomography (APT) acts as a powerful characterization technique that provides three-dimensional compositional mapping with near-atomic resolution by identifying the chemical identity and spatial position of individual atoms. The combination of time-of-flight (TOF) mass spectrometry and ion projection microscopy offers a high sensitivity of APT to distinguish each isotope for all elements, including light elements (*e.g.*, hydrogen, boron, and carbon) [8]. Insights from APT enhance the understanding of phase transformations, interfacial segregation, phase partitioning, and other phenomena, offering valuable knowledge on failure mechanisms and aiding the design of advanced materials.

APT stems from field ion microscopy, primarily based on the principle of field evaporation [86]. More specifically, when a high voltage is applied to a sharp tip-shaped specimen, an intense electrostatic field can be generated (**Fig. 2.9**). Once the electrostatic field approaches the threshold for breaking the bonds between the surface atoms, the atoms can be ionized and desorbed. The ionized atoms are further driven toward a position-sensitive detector due to the voltage bias set between the specimen and the detector. The ionized atoms eventually reach the position-sensitive detector, which consists of a combination of microchannel plates (MCPs) and an anode. The MCPs amplify the ion signal by creating a cascade of secondary electrons upon impact, while the anode detects the position of the amplified signal, allowing precise determination of the spatial origin of individual ions on the sample surface. The processing of these signals, *i.e.*, the chemical identity and the associated spatial position of each detected ion, are done digitally, during either the acquisition process or the post-analyzing process using the commercial AP Suite software (Version 6.1).

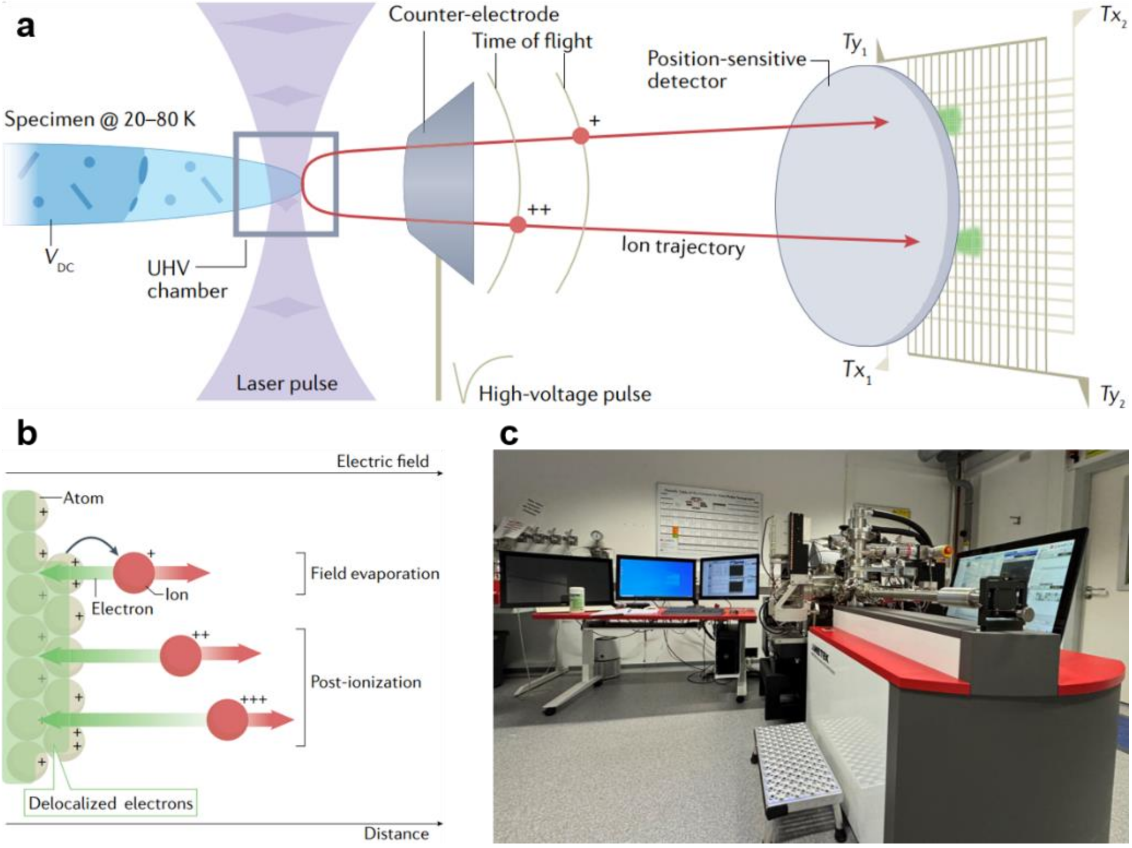
a
Counter-electrode
Time of flight
Position-sensitive detector
Tx_2
Ty_1
Specimen @ 20–80 K
+
++
V_{DC}
UHV chamber
Ion trajectory
Laser pulse
High-voltage pulse
Tx_1
Ty_2
b
Electric field
Atom
Ion
Electron
Field evaporation
Post-ionization
+++
Delocalized electrons
Distance
c

Fig. 2.9 Schematics of (a) working mechanism of an atom probe tomography (APT) with a straight flight-path instrument, and (b) field evaporation and post-ionization processes in the case of a metal [8]. (c) Overview of the local electrode atom probe (LEAP 5000 XR) used for the study. UHV denotes ultra-high vacuum.

To achieve the required evaporation fields, sharp tip-shaped specimens with an apex radius below 100 nm are typically prepared by a standard lift-out procedure and circular milling process using a focus ion beam (FIB) [8]. The electrostatic field (F) at the specimen apex can be given by an analytical model [8],

$$F = \frac{V}{kr} \tag{2.18}$$

where V, k, and r denote the applied voltage, constant derived from simple electrostatics (usually from 2 to 8), and the radius of the tip, respectively.

Apart from being applied for metals, APT can now be utilized for a wider range of materials, including ice, minerals, and biological materials with the advancement of cryogenic FIB and transformation systems [8]. **Fig. 2.9** illustrates the workflow for cryogenic APT measurement and a specific example for the investigation of frozen liquids in three dimensions [87]. This technique demonstrates the viability of using frozen water as a carrier for analyzing objects in solution by APT with a near-atomic resolution. Furthermore, this sub-nanometer resolution technique can be effectively correlated with other experimental methods, such as electron-based microscopies and X-ray-based spectroscopies, as well as computational approaches like DFT-based simulations [88, 89].

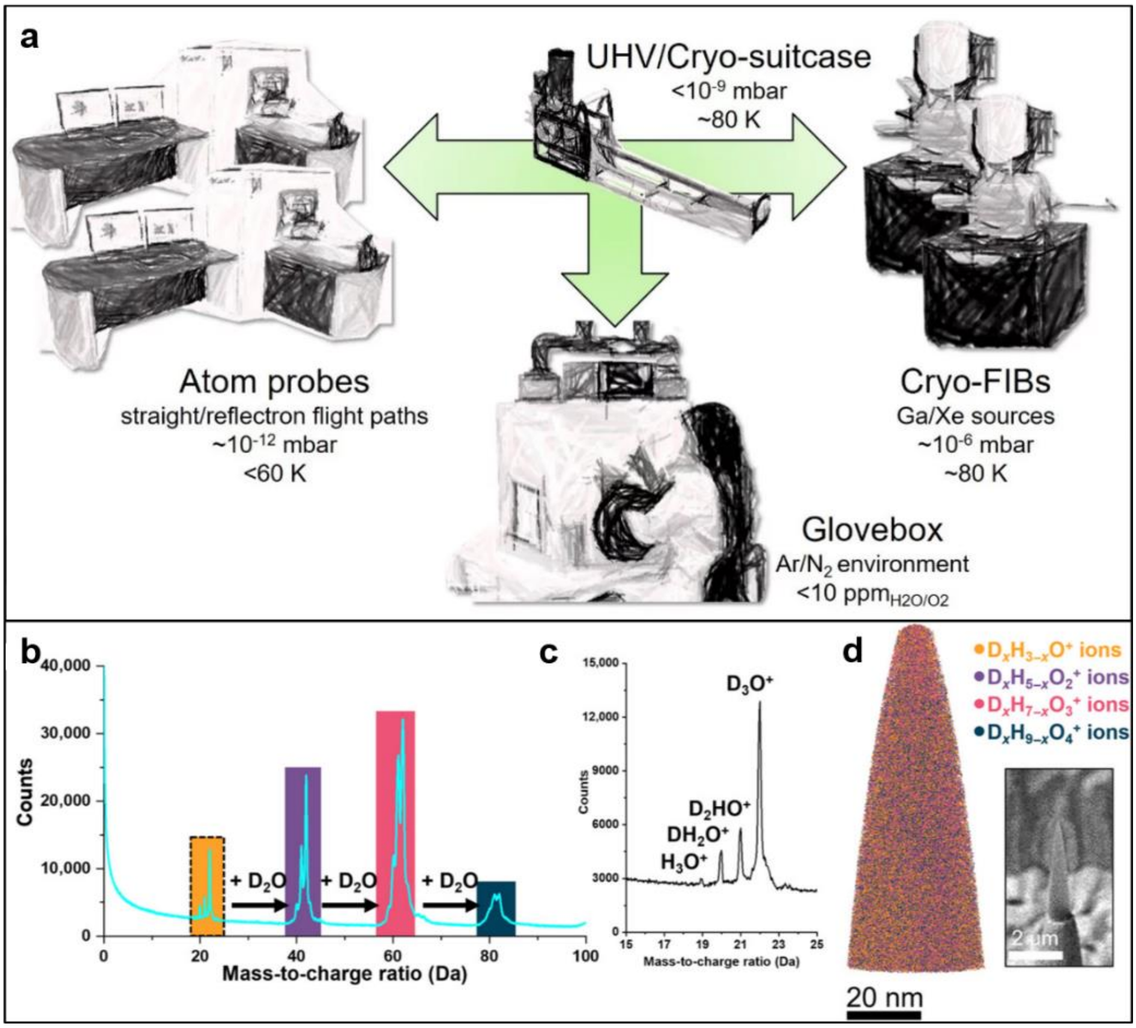
a
UHV/Cryo-suitcase
<10-9 mbar
~80 K
Atom probes
straight/reflectron flight paths
~10-12 mbar
<60 K
Cryo-FIBs
Ga/Xe sources
~10-6 mbar
~80 K
Glovebox
Ar/N2 environment
<10 ppmH2O/O2
b
Counts
40,000
30,000
20,000
10,000
0
+ D2O
+ D2O
+ D2O
0
20
40
60
80
100
Mass-to-charge ratio (Da)
c
Counts
15,000
12,000
9000
6000
3000
0
D3O+
D2HO+
DH2O+
H3O+
15
17
19
21
23
25
Mass-to-charge ratio (Da)
d
DxH3-xO+ ions
DxH5-xO2+ ions
DxH7-xO3+ ions
DxH9-xO4+ ions
2 µm
20 nm

Fig. 2.10 (a) The developed cryogenic APT infrastructure in Max Planck Institute for Sustainable Materials. (b) Overall mass spectrum and (c) the corresponding sectioned mass spectrum of an acquired dataset of D_2O ice [87]. (d) Three-dimensional reconstruction map of D_2O. Insert shows the SEM image of the prepared tip for APT measurement [87].

2.2.7. Density functional theory-based simulations

Density functional theory (DFT) is a quantum mechanical computational method widely used to study the electronic structure of atoms, molecules, and condensed matter systems. The underpinning physics is based on the principles of quantum mechanics, providing an efficient framework for solving the complex many-body Schrödinger equation by focusing on the electron density ($\rho(\boldsymbol{r})$) [90].

In principle, a stationary electronic state can be described by a wavefunction $\Psi(\boldsymbol{r_1},\ldots,\boldsymbol{r}_N)$ satisfying the Schrödinger equation of the *N*-electron system,

$$\hat{H}\Psi = [\hat{T} + \hat{V} + \hat{U}]\Psi = \left[\sum_{i=1}^{N}\left(-\frac{\hbar^2}{2m}\nabla^2\right) + \sum_{i=1}^{N} V(\boldsymbol{r}_i) + \sum_{i<j}^{N} U(\boldsymbol{r}_i, \boldsymbol{r}_j)\right] = E\Psi \qquad (2.19)$$

where $\hat{H}$, *E,* and *N* are the Hamiltonian, the total energy, and the number of electrons, respectively, while $\hat{T}$, $\hat{V}$, and $\hat{U}$ represent the kinetic energy, potential energy from the external field, and eletron-electron interaction energy. The basics of DFT is the Hohenberg-Kohn theorems, stating that (1) the ground-state properties of a system are determined by $\rho(\boldsymbol{r})$; (2) the total energy of the system is a function of the electron density, $E[\rho(\boldsymbol{r})]$, which can be minimized to obtain the $\rho(\boldsymbol{r})$. Therefore, the total energy of the system is expressed as a function of $\rho(\boldsymbol{r})$,

$$E[\rho(\boldsymbol{r})] = T[\rho(\boldsymbol{r})] + \int \rho(\boldsymbol{r})v(\boldsymbol{r})\mathrm{d}\boldsymbol{r} + U(\rho(\boldsymbol{r})) \qquad (2.20)$$

In this equation, $v(\boldsymbol{r})$ is the external potential determined by $\rho(\boldsymbol{r})$. Since $\rho(\boldsymbol{r})$ determines $v(\boldsymbol{r})$, *N*, and then $\hat{H}$, it actually determines all properties of the investigated system, even under excited state, assuming one has reliable expressions for $T[\rho(\boldsymbol{r})]$ and $U(\rho(\boldsymbol{r}))$. In order to find the ground-state density, DFT offers an attractive approach to solving this *N*-electron Schrödinger equation by reducing it to a single-body problem, eliminating the interaction term, $U(\rho(\boldsymbol{r}))$. This is also known as Kohn-Sham equation,

$$\left[-\frac{\hbar^2}{2m}\nabla^2 + V_{eff}(\boldsymbol{r})\right]\psi_i(\boldsymbol{r}) = \epsilon_i\psi_i(\boldsymbol{r}) \qquad (2.21)$$

which gives rise to Kohn-Sham orbitals $\psi_i(\boldsymbol{r})$ that give the $\rho(\boldsymbol{r})$ of the original *N*-electron system,

$$\rho(\boldsymbol{r}) = \sum_{i=1}^{N} |\psi_i(\boldsymbol{r})|^2 \qquad (2.22)$$

Additionally, $V_{eff}(\boldsymbol{r})$ is the effective single-particle potential,

$$V_{eff}(\boldsymbol{r}) = V_{ext}(\boldsymbol{r}) + \int \frac{\rho(\boldsymbol{r}')}{|\boldsymbol{r}-\boldsymbol{r}'|} d^3\boldsymbol{r}' + V_{xc}(\boldsymbol{r}) \tag{2.23}$$

where $V_{ext}(\boldsymbol{r})$ and $V_{xc}(\boldsymbol{r})$ represent the external potential and exchange–correlation potential, respectively. The second term is the Hartree term describing the electron–electron Coulomb repulsion. This framework (**Fig. 2.11**) allows efficient computation of the ground-state properties (*e.g.*, energy, charge density, *etc.*) of complex systems,making DFT a versatile tool in materials science, chemistry, and condensed matter physics.

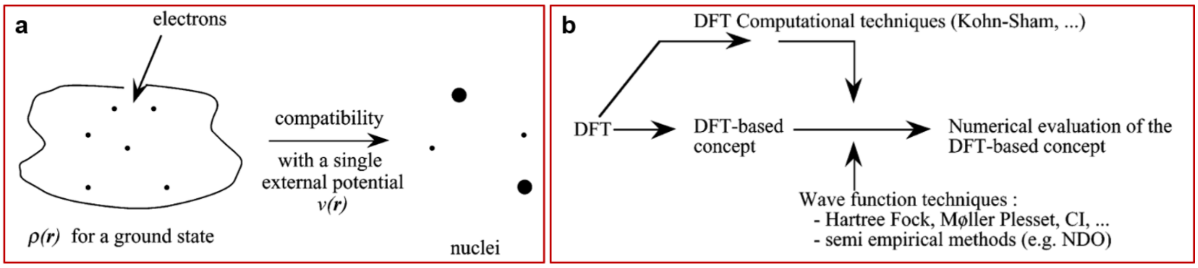
a
electrons
compatibility
with a single
external potential
v(r)
ρ(r) for a ground state
nuclei
b
DFT Computational techniques (Kohn-Sham, ...)
DFT
DFT-based
concept
Numerical evaluation of the
DFT-based concept
Wave function techniques :
- Hartree Fock, Møller Plesset, CI, ...
- semi empirical methods (e.g. NDO)

Fig. 2.11 Schematic diagrams illustrating (a) the visualization of the Hohenberg-Kohn theorem, and (b) the framework of DFT computational methods [90].

3. Hydrogen accommodation and its role in lattice symmetry in a TiNbZr medium-entropy alloy

This chapter is a modified version based on the paper entitled "*Hydrogen accommodation and its role in lattice symmetry in a TiNbZr medium-entropy alloy*" submitted to the journal *Acta Materialia* (DOI: 10.1016/j.actamat.2025.120852) [91]

3.1. Introduction

The hydrogen economy can provide sustainable solutions to reducing the use of fossil fuels, thus mitigating CO_2 emissions and combating global warming [92-94]. Such a paradigm shift necessitates the rapid development of advanced metallic alloys, particularly for hydrogen storage and transportation as well as for applications in which safety-critical components where hydrogen is used as an energy carrier (for example, in hydrogen combustion engines or electrochemical energy-related devices) are exposed to hydrogen-rich reactive atmospheres [24, 93, 95]. Body-centered cubic (BCC) refractory complex concentrated alloys (CCAs), as an emerging alloy class, have been considered to be potential candidates for hydrogen storage and high-temperature applications [54, 57, 58, 96-99]. The compositional complexity of CCAs systems provides a broad spectrum of mechanical and functional properties for various applications [2, 57]. For example, Ti-based refractory CCAs stand out, exhibiting decent room-temperature tensile ductility [98]. Moreover, a carefully adjusted composition of Ti-based refractory CCAs shows promising performance for hydrogen storage, with a hydrogen-to-metal ratio of ~2.5 and favorable thermodynamics and kinetics required for rapid and low-barrier hydrogen absorption and desorption [95, 100, 101]. Both thermodynamic and kinetic aspects are fundamental in the field of hydrogen storage. Increasing the concentrations of trapping sites and stored hydrogen atoms is an essential thermodynamic requirement, yet they are insufficient as standalone design targets for hydrogen storage. Additionally, applications require adequately tailored reaction and diffusion kinetics enabling tunable hydrogen absorption and release, pertaining to the targeted used case scenario.

The interactions between hydrogen and the host alloying atoms that constitute refractory CCAs play a salient role in that respect [100, 102, 103]. Hydrogen was reported to accommodate to the tetrahedral sites of the face-centered cubic (FCC) hydride phase during hydrogenation [95, 103]. In contrast to such hydrogen storage considerations (where both hydrogen storage capacity and remobilization upon dehydrogenation are essential criteria), it is also well known that hydrogen-induced embrittlement can drastically and abruptly reduce the lifespan of metallic components under mixed mechanical, thermal and chemical boundary conditions, already with as little as a few wppm diffusible hydrogen present [104-108]. Hydrogen has a high tendency to segregate to grain boundaries driven by the reduction of the free energy of the system, thereby reducing the cohesion between grains and leading to crack formation and propagation along grain boundaries and catastrophic failure of metallic structures [109, 110]. Hence, an in-depth understanding of the hydrogen-metal interaction associated with hydrogen ingression becomes critical to the design of novel metallic alloys that might be potentially applicable to the hydrogen economy [61, 111-113]. However, one major problem to making profound progress in this field lies in directly observing the dynamic interaction of hydrogen atoms with metals, due to the challenging intrinsic features of hydrogen, *e.g.* it is the lightest element (1.008 u), has the smallest atomic radius (53 pm), and highest diffusion coefficient in metals ($\sim 10^{-10}$ m^2/s at ~500 °C) [41, 114].

In this study, the time-resolved microstructural transitions and associated hydrogen accommodation in an equiatomic TiNbZr alloy were quantitatively probed using *in-situ* synchrotron high-energy X-ray diffraction (HEXRD) during heat treatment in H_2 and Ar atmosphere at 500 °C under atmospheric pressure. The reasons for selecting the equiatomic TiNbZr alloy as a model material for this study are as follows: (1) Most of the alloys that have been considered so far for hydrogen-related applications belong to the TiNbZr alloy family and variants of it, *e.g.*, TiNbZr-Ta, TiNbZr-V, and TiNbZr-HfTa (see **Table S3.1**) [56-58, 98, 115, 116]. (2) Ti, Zr, and Nb are the three most critical elements in this CCA class, where Ti and Zr are the major elements in more than 80% of the reported CCAs systems for hydrogen storage due to their high affinity to hydrogen, and Nb is the main element to stabilize a BCC crystal structure (a low packing density of 68%, facilitating hydrogen diffusion). (3) Compared with the quaternary and quinary alloys mentioned above, the TiNbZr alloy is a system that is on the one hand common to most of these more complex alloys. On the other hand, it is thermodynamically their simplest possible phenotype. Both features qualify this ternary system as a core alloy for studying hydrogen effects on the microstructural transition using both experiments and simulations, to provide an in-depth understanding of the underlying mechanisms along the spirit ‘as simple as possible but not simpler’. (4) This alloy reveals a hydrogen-to-metal ratio of up to ~1.9, which is attractive for hydrogen storage. The advantage of the HEXRD method lies in the capability of providing the real-time evolution of lattice structures in a statistically representative volume with an excellent time resolution (down to the sub-second regime) [117, 118]. Additionally, density functional theory (DFT) calculations were employed to reveal the thermodynamically favorable sites for hydrogen in the crystal lattice. For a fundamental understanding of various properties of the metal-hydrogen systems, such as phase stability, fracture toughness, and hence structural integrity, it is essential to know the relationship between hydrogen concentration and site occupancy. Such a combination of experimental and computational results offers new insights into the hydrogen-metal interactions in refractory MEA and the corresponding impact on lattice structure.

3.2. Materials and methods

3.2.1. Materials

The equiatomic TiNbZr alloy was prepared using high-purity elements (99.9%) in an arc-melting furnace with a water-cooled copper crucible. To prevent the alloy from oxidation during melting, the furnace was filled with high-purity Ar (99.999%), and an oxygen-getter material (*i.e.*, a piece of pure Ti) was placed in the furnace. Fine TiNbZr powders (dendrite microstructure) with a median particle size of 30 μm were then prepared from the ingot by gas atomization (Angstrom Sciences, Germany). The oxygen content of the pristine TiNbZr powder is 0.81 at.% as determined by thermal desorption spectroscopy (TDS). The potential influence of oxygen contamination on hydrogen storage and release kinetics might consist of several aspects (1) A reduction in hydrogen storage capacity because oxygen occupies the same sites in the host crystal otherwise used by hydrogen; (2) The surface oxidation with a dense structure might act as an additional entry and release barrier for hydrogen [119-121]. However, the latter point is of moderate concern as the high solubility of oxygen in this alloy (*i.e.*, ~8 at.% oxygen for β-Ti) implies that oxide formation is unlikely in the present alloy [122].

3.2.2. Microstructure characterization

The microstructure of the pristine and hydrogen-charged powders was characterized by a combination of backscattered electron (BSE) imaging and electron backscatter diffraction (EBSD) techniques in a Zeiss Sigma 500 scanning electron microscope (SEM). To observe the cross-sectional area of the TiNbZr powders, they were embedded in a conductive phenolic resin contacting carbon fillers (Polyfast Struers) and then ground with sand-paper of 400-4000 grit size. Subsequently, the samples were polished with 50 nm colloidal silica (OPS) suspension mixed with hydrogen peroxide (H_2O_2, 30 vol.%). The EBSD measurements were performed with a step size of 50 nm under an accelerating voltage and probe current of 15 kV and 2 nA and the collected data were analyzed using the software OIM Analysis^{TM} V8.0. In addition, the local chemistry of powders was probed by electron dispersive spectroscopy (EDS) in the SEM. Moreover, the surface morphology of the TiNbZr powders was characterized by secondary electron (SE) imaging. In this case, the TiNbZr powders were directly dispersed on a copper tape holder and coated with 4-nm thick carbon. To analyze the local crystallographic information of the hydrogen-charged specimen, the selected area electron diffraction (SAED) pattern was collected using transmission electron microscopy (TEM). The TEM lamella was prepared using focused ion beam (FIB, FEI Helios NanoLab 600i dual-beam FIB/SEM instrument). The TEM analysis was conducted using a Titan Themis instrument G2 300 operated at 300 kV.

3.2.3. In-situ synchrotron high-energy X-ray diffraction

In-situ synchrotron high-energy X-ray diffraction (HEXRD) was employed to study the hydrogenation behavior of the TiNbZr alloy. The HEXRD experiments were conducted at the Powder Diffraction and Total Scattering Beamline P02.1 of PETRA III at Deutsches Elektronen-Synchrotron (DESY) in Hamburg, Germany [70]. **Fig. 3.1** schematically shows the HEXRD experimental setup. A chemical reaction cell for gaseous charging was placed between the incident X-ray beam and a two-dimensional detector. TiNbZr powders (3-5 mg) were loaded into a single-crystal sapphire capillary with an inner diameter of 0.6 mm, which was assembled in the reaction cell [123, 124]. A hot air blower (Oxford Instrument) was employed to heat the sample. The temperature of the sample was measured using a type K thermocouple. Both pure H_2 gas (for hydrogenation) and Ar (as reference) gases with a purity of 99.999% were used in the experiments at a pressure of 1 bar. The flow rate was kept at 50 mL/min, which was controlled by a mass flow controller. Prior to heating, the capillary was purged with the H_2 or Ar gas for 30 mins to remove residual air in the cell for the hydrogenation or reference experiment, respectively. Then, the sample was heated to 500 °C with a heating rate of 0.3 °C/s and subsequently held at 500 °C for ~1800 s, followed by cooling the cell in air. During the heat treatment, the HEXRD patterns were recorded to investigate the real-time microstructure evolution. The beam energy of the X-ray was fixed at 60 keV to obtain a monochromatic X-ray with a wavelength of ~0.207 Å. The beam size of the incident beam was 1 mm × 1 mm. The Debby-Scherrer patterns were recorded every second by the fast area detector Varex XRpad 4343CT (2880 pixels × 2880 pixels, with a pixel size of 150 µm × 150 µm). Thanks to the ‘powder’ feature of the sample, it revealed isotropic scattering behavior along the azimuth angle. Thus, half-ring configuration was employed, *i.e.*, half of the Debby-Scherrer rings were captured. In this case, the crystal information at a high scattering vector (with a Q_{max} up to ~15 Å^{-1}) could be accessed simultaneously.

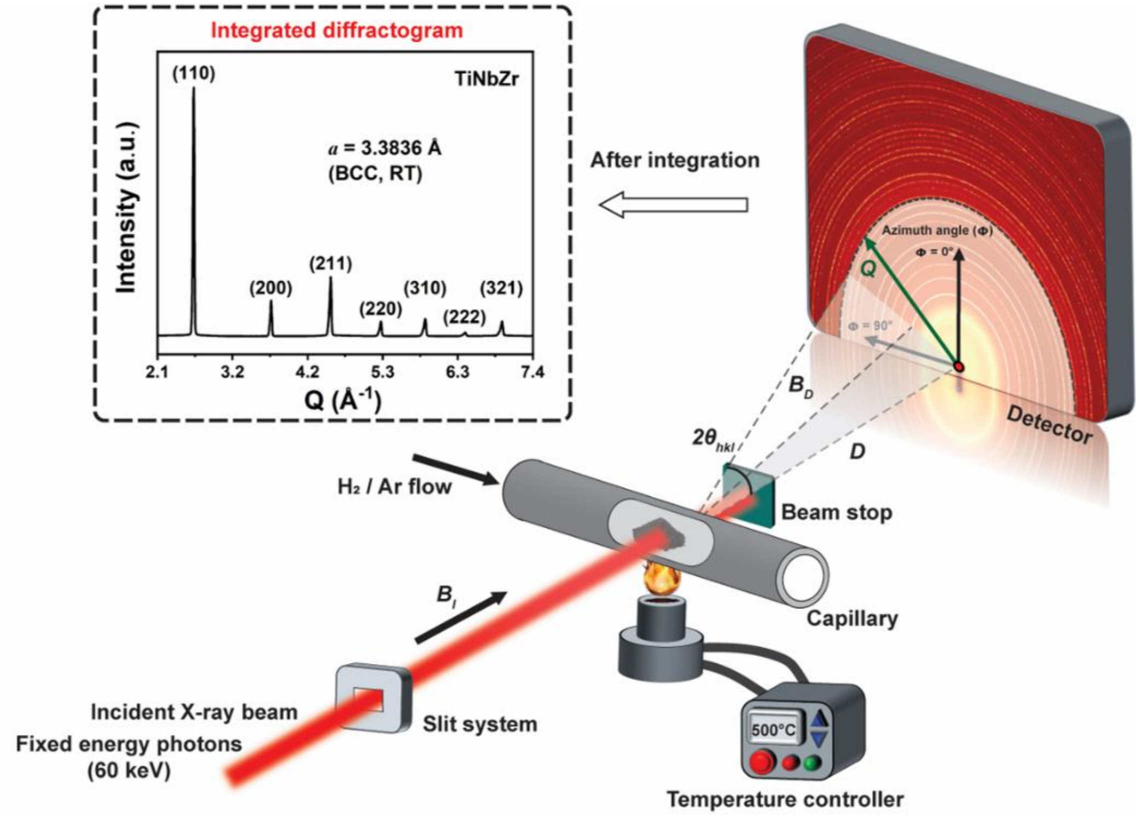
Integrated diffractogram
(110)
TiNbZr
a = 3.3836 Å
(BCC, RT)
Intensity (a.u.)
(211)
(200)
(310)
(321)
(220)
(222)
2.1
3.2
4.2
5.3
6.3
7.4
Q (Å^{-1})
After integration
Azimuth angle (Φ)
Φ = 0°
Q
Φ = 90°
B_D
Detector
$2\theta_{hkl}$
D
H₂ / Ar flow
Beam stop
B_I
Capillary
Incident X-ray beam
Fixed energy photons
(60 keV)
Slit system
500°C
Temperature controller

Fig. 3.1 Schematic illustration of the experimental setup of the in-situ synchrotron high-energy X-ray diffraction (B_I and B_D indicate the vectors of the incident and diffracted beams, respectively; D is the distance between the sample and the two-dimensional detector; $2\theta_{\mathrm{hkl}}$ indicates scattering angle; Q stands for the scattering vector). Insert figure (marked by the black dash box) shows the integrated diffractogram of pristine TiNbZr powders at 30 °C, demonstrating a single body-centered cubic (BCC) structure with a lattice parameter of 3.3836 Å.

The HEXRD patterns were integrated over an azimuth angle of 180° into intensity-scatter vector Q plots using the GSAS-II software [76]. The sequential Rietveld refinement was conducted for selected data points to deconvolute the HEXRD patterns and quantitatively analyze the fraction of individual phases as well as their corresponding lattice parameters. The values of the weighted profile R-factor (R_{wp}) for all the refinements were below 8.0%, demonstrating the high reliability of the results obtained. Furthermore, the pair distribution function (PDF) profiles ($G(r)$) were obtained from the total scattering data with a $Q_{\max}$ of around 15 Å^{-1} via the Fourier transform of the structural function ($S(Q)$). The peak widths (σ) and interatomic distances of the first three coordination shells were also determined from the PDF analysis.

3.2.4. Density functional theory (DFT) calculations

DFT calculations were performed to identify and verify the experimentally observed lattice structures of the TiNbZr alloy charged with hydrogen. The DFT calculations used the projector augmented wave (PAW) method [125] as implemented in the Vienna Ab initio Simulation

Package (VASP) [126, 127]. The provided PAW potentials [128] were employed, treating the $4p^6 4d^4 5s^1$, $3p^6 3d^3 4s^1$, $4s^2 5s^1 4d^6 4p^3$, and $1s^1$ orbitals as valence electrons for Nb, Ti, Zr, and H, respectively. The generalized gradient approximation (GGA) with Perdew-Burke-Ernzerhof (PBE) [129] parameterization was used for the exchange-correlation function. All calculations were performed using a 500 eV kinetic-energy cutoff and a 6 × 6 × 6 k-point mesh according to the Monkhorst-Pack scheme [130, 131]. Fermi-Dirac smearing with an electronic temperature of 0.07 eV (corresponding to about 800 K) was used. Electronic minimization and stress relaxation with total energy convergence parameters of 2×10^{-4} meV/atom and 2×10^{-3} meV/atom were employed respectively. A 3 × 3 × 3 MEA bcc conventional supercell with 54 metallic atoms was used in the simulation, which allows to conduct calculations for an equiatomic composition. The supercell was constructed using the special quasirandom structure (SQS) method [132]. An averaged, effective solution enthalpy, ΔH_{sol} (per hydrogen atom) was calculated by,

$$\Delta H_{\mathrm{sol}} = \frac{E_{\mathrm{M}+n\mathrm{H}} - E_{\mathrm{M}}}{n} - \mu_{\mathrm{H}} \tag{3.1}$$

where n indicates the number of hydrogen atoms in the supercell. The total energy E for each supercell was calculated allowing for stress relaxation (*i.e.*, supercell volume/shape and atomic positions). The chemical potential of hydrogen, μ_{H}, was calculated as half of the total energy of the H_2 molecule.

3.3. Results

3.3.1. Microstructure of the pristine TiNbZr sample

The pristine TiNbZr sample exhibits a spherical morphology (**Fig. 3.2**a-b) and the average diameter of the particles is 23.56±0.82 µm, as quantified by analyzing more than 200 particles (**Fig. 3.2**c). As shown in the cross-sectional SEM image (**Fig. 3.2**d), the pristine powders reveals a typical dendritic microstructure formed during solidification after the atomization process. Nb accumulates in the dendritic regions (with an area fraction of 52%) while the interdendritic regions (with an area fraction of 48%) are enriched in Ti and Zr (**Fig. 3.2**d-e). Such a dendritic microstructure was also observed in as-cast refractory CCAs [50, 115, 133]. The segregation behavior is attributed to the large solidification temperature region (~300 °C) among these elements [27, 134]. The tendency of Ti and Zr to undergo co-segregation is mainly due to the lower mixing enthalpy between these two elements (0 kJ/mol as compared to 2 kJ/mol for Ti-Nb and 4 kJ/mol for Zr-Nb) [35, 50]. The composition of the dendritic region was quantified by EDX as $Ti_{33.38}Nb_{31.70}Zr_{34.92}$ (in at.%), while the composition of the interdendritic region is $Ti_{31.29}Nb_{37.46}Zr_{31.25}$ (in at.%, **Table S3.2**). Such a small chemical fluctuation has negligible effects on phase stability, as confirmed by the HEXED measurements (in **Section 3.3.2**). Despite the local chemical fluctuation, the average concentration is consistent with the nominal composition (**Table S3.2**). The sample possesses randomly oriented grains with an average grain size of 8.83±2.74 µm (**Fig. 3.2**f). Additionally, the high-angle grain boundaries constitute a major part of the grain boundaries, accounting for 83.8%, whereas low-angle grain boundaries occupy 16.2%.

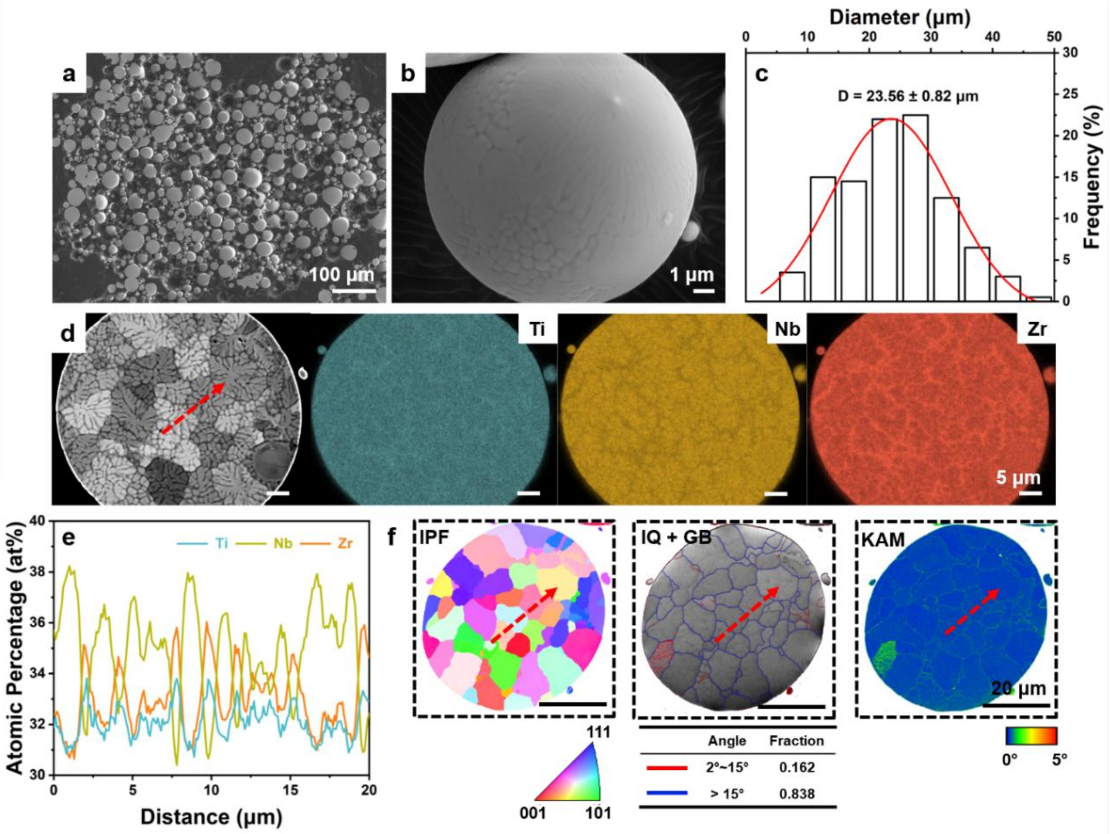

Fig. 3.2 Secondary electron images of (a) TiNbZr powder and (b) a particle at high magnification in the pristine state. (c) The corresponding size distribution measured from (a) using the software ImageJ over 200 particles. (d) Backscattered electron imaging of a particle and the corresponding individual elemental maps of Ti, Nb, and Zr probed by electron dispersive spectroscopy. (e) Elemental distribution across dendrites along the red arrow in (d). (f) Inverse pole figure (IPF), image quality overlaid with grain boundaries (IQ + GB), and kernel average misorientation (KAM) maps of the particle probed by the electron backscatter diffraction. The red arrow in (f) represents the the same line scan in (d).

The hydrogenation behavior of the TiNbZr powder was investigated by employing *in-situ* HEXRD during hydrogen charging. **Fig. 3.3**a and c show the overall evolution of the integrated HEXRD peaks of TiNbZr samples upon heat treatment in pure H_2 (**Fig. 3.3**b) and Ar (as a reference, **Fig. 3.3**d). The HEXRD confirms that the pristine sample possesses a single body-centered cubic (BCC, $Im\bar{3}m$ space group). In both cases, an evident peak shift to a lower scattering vector (Q) is observed during heating from room temperature to 500 °C, suggesting an increase in interplanar spacing of the crystal lattice. During the isothermal treatment at 500 °C, a further systemic peak shift to a lower *Q* and peak broadening is observed for the sample treated in pure H_2 (**Fig. 3.3**a). In comparison, no change in the diffraction peaks is found in the reference sample that treated in Ar under the same heat treatment (**Fig. 3.3**c). This fact confirms that the peak shift and broadening in the sample treated in H_2 is related to hydrogen ingression in the crystal lattice, resulting in lattice expansion. Upon cooling, the sample treated in H_2 reveals further peak broadening with gradual loss of symmetry of the diffraction peaks (**Fig. 3.3**f), suggesting the formation of a crystal structure with low symmetry. In contrast, the reference sample treated in Ar reveals only thermal contraction [135, 136], implying that the TiNbZr alloy remains a BCC structure in Ar.

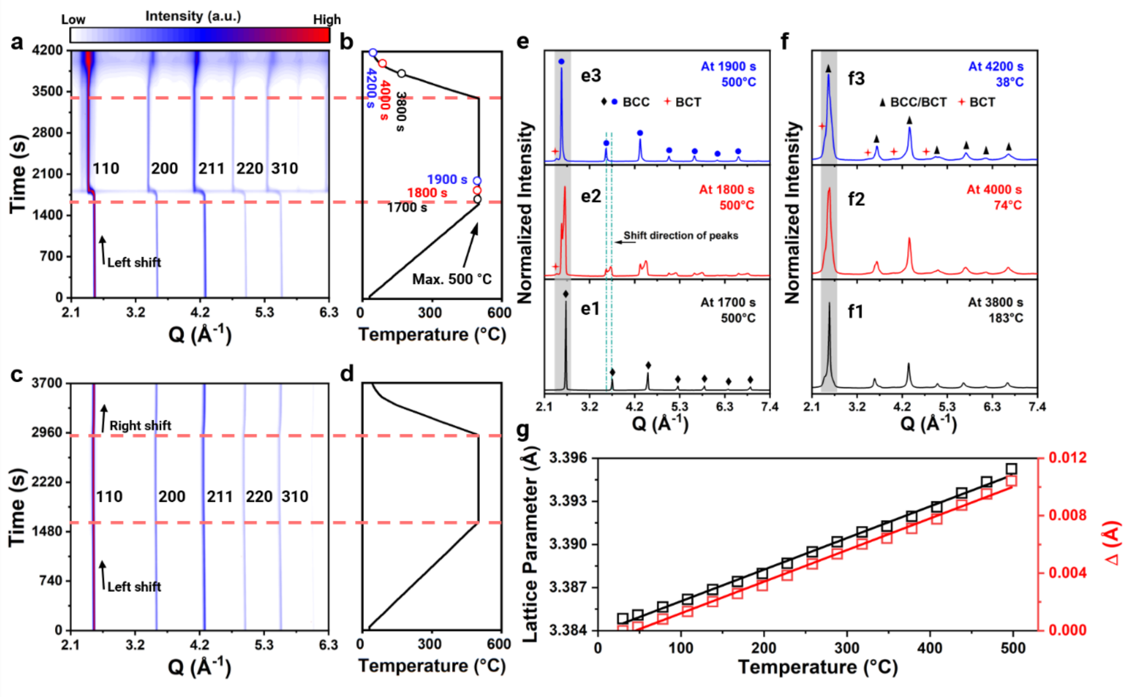

Fig. 3.3 Contour maps of the diffraction intensity integrated over the azimuth angle of 180° probed by in-situ high-energy X-ray diffraction (HEXRD) during heat treatment of the TiNbZr alloy in (a) H_2 and (c) Ar. (b) and (d)The corresponding temperature profiles. HEXRD profiles of the sample treated in H_2 for (e1) 1700 s, (e2) 1800 s, (e3) 1900 s (at the beginning of the isothermal process at 500 °C), (f1) 3800 s, (f2) 4000 s, and (f3) 4200 s (upon cooling). (g) Lattice parameter and the relative change (Δ) in the lattice parameters of the sample during heating from room temperature to 500 °C in H_2.

The response of crystal structure to heat treatment in the two samples was further studied by analyzing the pair distribution function (PDF) profiles (**Fig. S3.3** and **Fig. S3.4**). This method reveals the probability of finding two atoms within the alloy by a distance *r*, based on the Fourier transformed from the reciprocal space to the real space [75]. For the reference sample, no obvious change is detected in the PDF profiles along the whole heat treatment. In contrast, the loss of long-range correlations is observed in the sample treated in H_2, particularly during the onset of isothermal treatment and subsequent cooling processes, indicating the disordering of the metal matrix [75]. Such disorder implies possible transitions of the crystal structure, which will be analyzed in detail in the following chapters.

3.3.2. Evolution of lattice structure upon heating

During heating the sample in H_2 up to 500 °C, the lattice parameter increases linearly as a function of temperature (**Fig. 3.3**g). Such linear behavior is mainly due to an increase in lattice vibration stimulated by increasing temperature [135, 136]. The linear thermal expansion of the TiNbZr alloy is subtle (Δ = 0.010 Å) with a thermal expansion coefficient α of 6.578×10^{-6}/K in the temperature range from 30 °C to 500 °C. These results are consistent with those for the sample treated in Ar (Δ = 0.012 Å, α = 6.578×10^{-6}/K, **Fig. S3.6**a). This comparison suggests that no significant H_2 uptake in the sample heated in H_2 to 500 °C, which otherwise is supposed to result in an additional change in the lattice parameter.

3.3.3. Hydrogen uptake during isothermal treatment at 500 °C

The temperature of 500 °C has been selected for the isothermal treatment as it falls within the temperature range (300-600 °C), typical for studying phase transformations during hydrogenation (**Table S3.3**). It is worth noting that temperatures can impact phase stability via the change in free energy (*i.e.* hydrogen solubility) and thus can influence also the kinetics of structural transitions (*i.e.* hydrogen absorption rate) by affecting vacancy concentration and atomic diffusion [12, 28, 41]. During isothermal treatment in H_2 at 500 °C, the diffraction peaks shift significantly to a lower *Q*-vector (**Fig. 3.3**a) within the initial 200 s (the elapsed time from 1700 s to 1900 s), suggesting a rapid increase in the lattice parameter. Such lattice expansion is attributed to the fast hydrogen uptake in the TiNbZr powder. There is no further shift of the diffraction peaks after the elapsed time of 2000 s (**Fig. S3.7**). Such stagnation indicates the saturation of the TiNbZr lattice with hydrogen atoms. To better understand the hydrogen absorption process, we next focus on the microstructure evolution within the first 200 s of the isothermal treatment. The integrated HEXRD profiles, as shown in **Fig. 3.3**e, reveal that the original BCC peaks (a = 3.391 Å at 500 °C, 1700 s) split into multiple sets of BCC peaks, and then transit back to one set of BCC peaks, yet, with a larger lattice parameter (a = 3.540 Å at 500 °C, 1900 s). A small peak at the left shoulder of the {110} reflection of the BCC phase is observed (**Fig. 3.3**e), which is most likely a sign of the occurrence of a body-centered tetragonal (BCT, *I4/mmm* space group) structure. Due to its very small fraction (< 5.0 wt.%), this BCT peak is not taken into consideration in the Rietveld refinements for the isothermal treatment.

As exemplarily revealed in **Fig. 3.4**a, two BCC_{110} peaks are further distinguished at slightly different *Q* values (2.600 $Å^{-1}$ and 2.615$Å^{-1}$) at 1700 s, suggesting two BCC structures, namely

BCC-1 (85.7 wt.%, a = 3.391 Å) and BCC-2 (14.3 wt.%, a = 3.411 Å). During isothermal treatment, three more sets of BCC peaks can be deconvoluted and noted as BCC-3, BCC-4, and BCC-5 with an increase in the lattice parameters (**Fig. 3.4**b and **Fig. S3.8**a-c). The fraction of initial BCC-1 peaks gradually decreases and disappears at 1900 s, while the fraction of BCC-2, BCC-3, and BCC-4 peaks first increases followed by a decrease (**Fig. 3.4**f), suggesting that they are the transient structures. The appearance of these transient structures with the intermediate lattice parameters is attributed to the evolution of the hydrogen concentration gradient along the radius of the particles depending on the penetration depth of hydrogen as a function of time [137, 138]. As shown in **Fig. 3.4**g, when hydrogen diffuses into the particle at the beginning of the isothermal process, it generates a corresponding local gradient in the hydrogen concentration (the concentration gradually decreases from the shell to the core) [139, 140]. The solute hydrogen atoms expand the BCC lattice (below the solubility limit), resulting in an increase in its local lattice parameter, which is proportional to the hydrogen concentration and indicated by the shift of the diffraction peaks to smaller Q values in the HEXRD profiles. Due to the hydrogen concentration gradient along the diffusion path, the BCC lattice reveals a continuous variation of the lattice parameter, as shown by the asymmetric broadening of the diffraction peaks. For the sake of simplicity, in total five transition BCC structures with distinct lattice parameters were considered in the HEXRD analysis, yielding reliable Rietveld refinement results. Finally, BCC-5 becomes the predominant structure in the microstructure (88.4 wt.%, a = 3.534 Å, **Fig. 3.4**d and f). Additionally, only BCC-5 can be detected after 2000 s (isothermal holding for 400 s) (**Fig. S3.7**). This fact can be ascribed to the saturated hydrogen concentration across the whole particle. For the sample treated in Ar, the lattice parameter increases only slightly by 0.006 Å to 3.406 Å after isothermal heat treatment for about 400 s (**Fig. S3.6**b). Then, there is no change observed in the HEXRD profiles (**Fig. S3.13**).

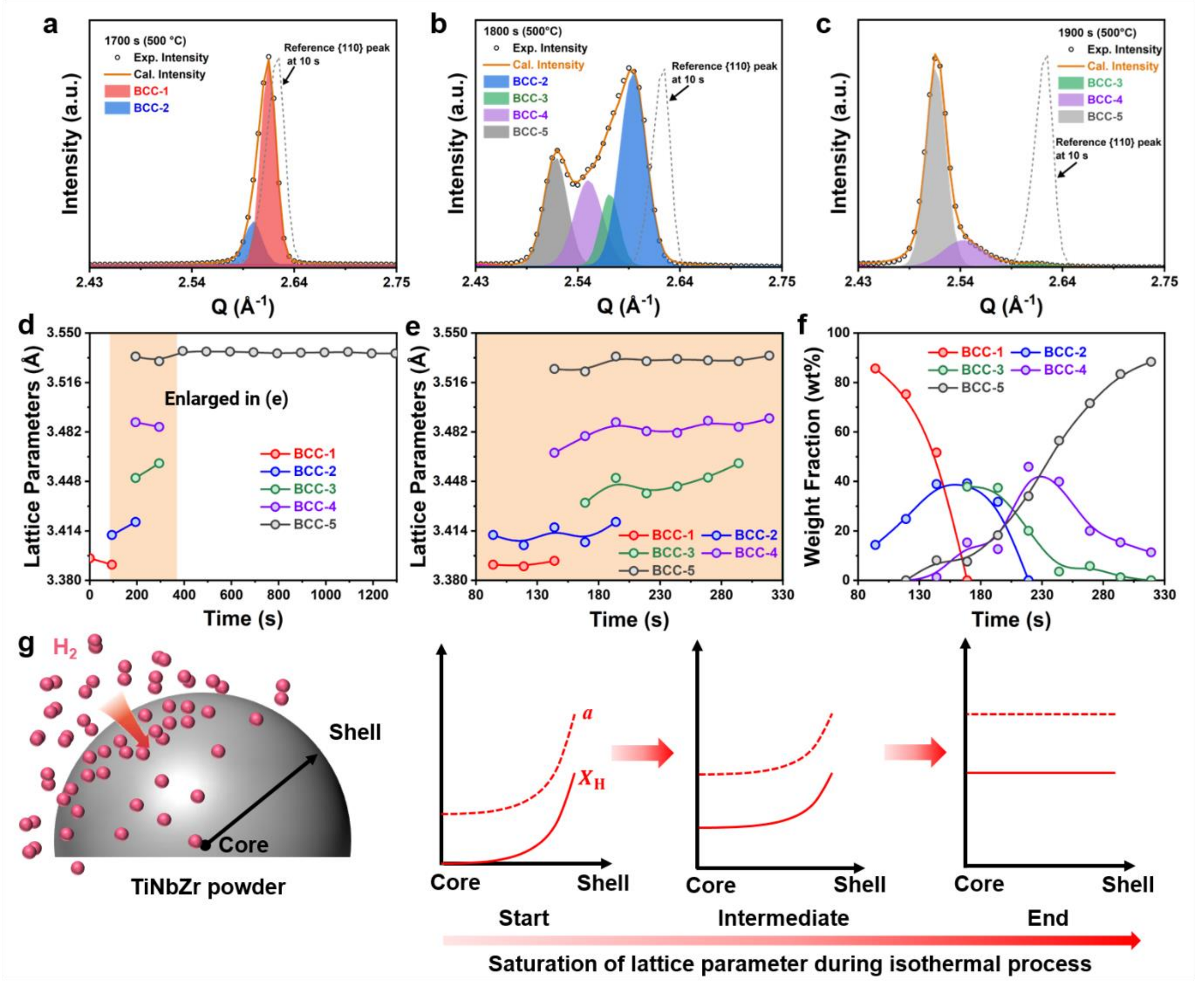

Fig. 3.4 Deconvoluted BCC$_{110}$ peaks of the sample treated in H$_2$ at 500 °C for (a) 1700 s (starting time for isothermal heat treatment), (b) 1800 s (isothermal holding for 100 s), and (c) 1900 s (isothermal holding for 200 s). (d) Evolution of the lattice parameters (Here the initial time point (0 s) represents 1700 s during the elapsed time for the HEXRD experiment, which is the starting point for isothermal heat treatment). (e) Detailed view of lattice parameters and (f) corresponding fractions of multiple BCC structures in the early stage of the hydrogen uptake. (g) Schematic diagram showing the gradual expansion of the BCC lattices during the isothermal heat treatment process at 500 °C. a and X_H represent lattice parameter and hydrogen concentration, respectively.

3.3.4. Change in lattice structure upon cooling

Compared with the isotropic expansion of the BCC lattice during isothermal heat treatment, the evolution of lattice structure upon cooling back to room temperature is more complex. An asymmetric broadening of the diffraction peaks is observed upon cooling, which is attributed to the presence of BCT crystal structure. The deconvoluted {110} peaks are shown in Fig. 3.5a-c. One BCC peak and two series of BCT peaks (BCT-1 and BCT-2) are determined upon cooling. Lattice parameters and phase fractions were extracted from the sequential Rietveld refinements (Fig. 3.5d-e). The fraction of the BCT-1 structure with a *c/a* ratio of 1.18 slowly increases to ~15.5 wt.% during the cooling process, while the fraction of the BCT-2 phase with a *c/a* ratio of around 1.06 finally reaches up to 59.3 wt.% at the final stage of cooling. In other words, in total ~80 wt.% of BCC transforms into tetragonal crystal structures upon cooling triggered by the saturated hydrogen in the BCC lattice. This transformation in crystal structure from BCC to BCT under hydrogen exposure upon cooling will be further discussed in **Section 3.4**. In the reference sample (treated with Ar), the BCC structure remains and there is no asymmetric broadening of the peaks observed (**Fig. S3.13**). In this case, its lattice parameter decreases linearly from 3.406 Å to 3.390 Å due to the lattice contraction induced by cooling (**Fig. S3.6**c). It should be noted that no FCC hydride (space group: $Fm\bar{3}m$) is found during the entire hydrogenation process under the treatment conditions in this study.

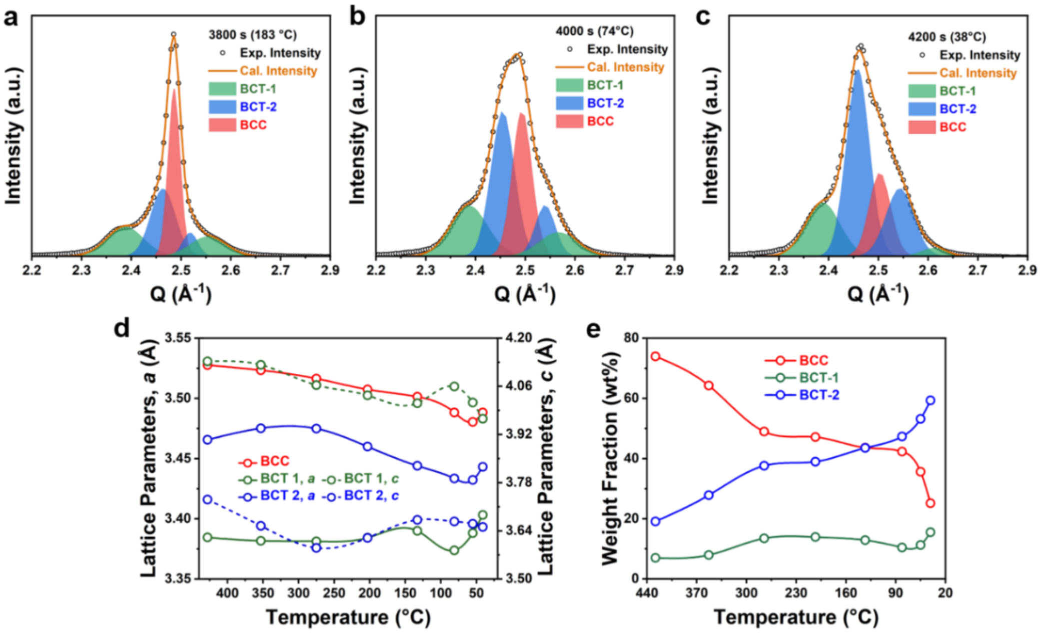

Fig. 3.5 Deconvoluted {110} peak of the sample treated in H_2 during cooling at (a) 3800 s, (b) 4000 s, and (c) 4200 s (elapsed time). The evolution of (d) lattice parameters and (e) phase fractions of the deconvoluted BCC, BCT-1 and BCT-2 crystal structures.

TEM was also employed to determine the tetragonality of the crystal structure after heat treatment in H_2 (**Fig. 3.6** and **Fig. S3.14**). Two overlapping diffraction patterns corresponding to the BCC and BCT crystal structures were distinguished in **Fig. 3.6**b. One set was found to stem from a BCC crystal structure with a lattice parameter of 3.395 Å, while the other indicates the occurrence of a BCT crystal structure (a = 3.249 Å and c = 3.475 Å). The corresponding BCT crystal structure is shown in the inverse fast Fourier transform (IFFT) image (**Fig. 3.6**c). The c/a ratio is approximately 1.07. Such results are consistent with the simulated patterns along the same <001> zone axis (**Fig. 3.6**d). This structural evolution from BCC to BCT results in the spontaneous symmetry breaking of the lattice structure and the discontinuous change in the lattice constant. These features meet the characteristics of a dilatation-dominated displacive phase transformation [141, 142]. In this case, the ordered distribution of the hydrogen interstitials, is supposed to be the main factor causing this transformation [114, 143]. The above findings provide strong evidence of tetragonality within the TiNbZr matrix after heat treatment in H_2. The underlying mechanisms for the presence of tetragonality will be discussed in the ***Discussion*** section (3.4.2).

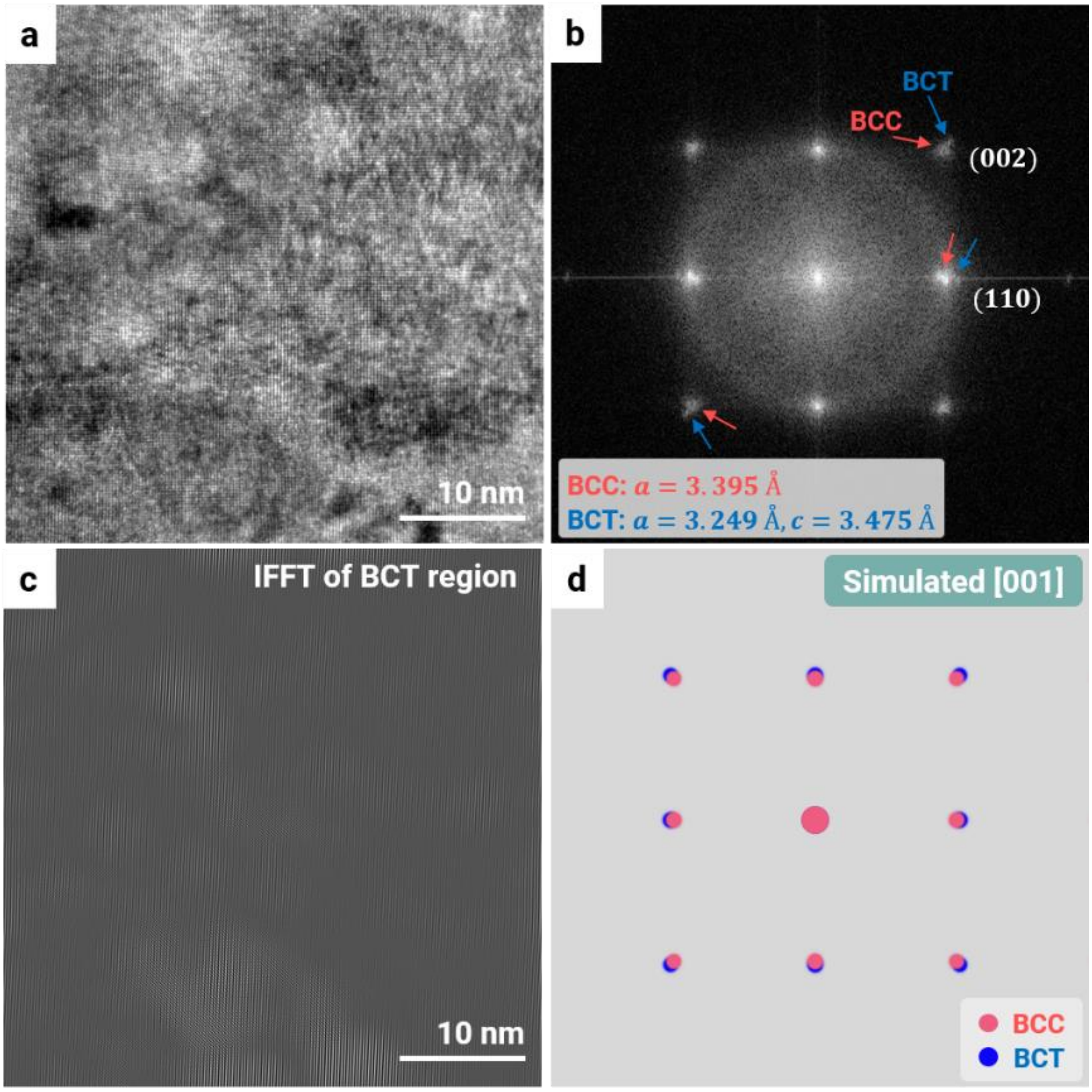

Fig. 3.6 (a) A representative high-resolution TEM (HRTEM) image of TiNbZr powder after heat treatment in H_2 with the zone direction of [001], along with (b) its corresponding Fast Fourier transform (FFT) pattern and (c) inverse FFT (IFFT) image of the body-centered tetragonal (BCT) crystal structure. (d) Simulated selected area electron diffraction (SAED) pattern of the coexistence of body-centered cubic (BCC) and BCT crystal structures along the [001] zone axis.

3.3.5. Change in lattice volume during hydrogenation

The relative changes in the lattice volume during the heat treatment in H_2 and Ar are shown in Fig. 3.7. The lattice volume is calculated with the equation, $V_t = \sum_1^n (f_i \times V_i)$, where V_t is the weighted average volume of a unit cell at time t, f_i and V_i represent the fraction and lattice volume of structure i, respectively. Here we use the change in relative volume, V_t/V_0 (V_0 is the initial lattice volume), to evaluate the evolution of lattice volume. The lattice parameters and corresponding volumes at different time points are listed in **Table S3.4** and **Table S3.5**. The volume changes of both samples treated in H_2 and Ar are consistent during heating to 500 °C, revealing a subtle increase by 0.627 Å^3, corresponding to the relative volume change (V_t/V_0, where V_0 indicates the initial lattice volume) of 1.010. Upon hydrogen uptake, the lattice volume is significantly increased by 4.845 Å^3 due to the hydrogen absorption and solution in the lattice, yielding a total relative volume change (V_t/V_0) of 1.142. This volume expansion corresponds to a hydrogen-to-metal atomic ratio of 0.865 (hydrogen concentration is determined to be 46.4 at.%), assuming that a volume expansion of 2.8 Å^3 is caused by introducing a single hydrogen atom in the unit cell [114, 144]. Such a high hydrogen concentration is mainly attributed to the high solubility of hydrogen in group IV elements [114]. It is worth noting that a slight drop in the relative volume change happens in the sample treated in H_2 before its steep increase. This reduction in lattice volume is supposed to be due to the endothermic effect caused by hydrogen dissolution, indicating the onset of hydrogen ingress [95]. A decrease in the lattice volume is observed in both samples treated in Ar (by 0.551 Å^3) and H_2 (by 0.726 Å^3) during cooling. In the former case, the lattice volume almost recovers to its original size with a relative volume change of 1.002 in the final stage. In the latter case, such a decrease is probably due to both the thermal effect and the decrease in hydrogen solubility upon cooling.

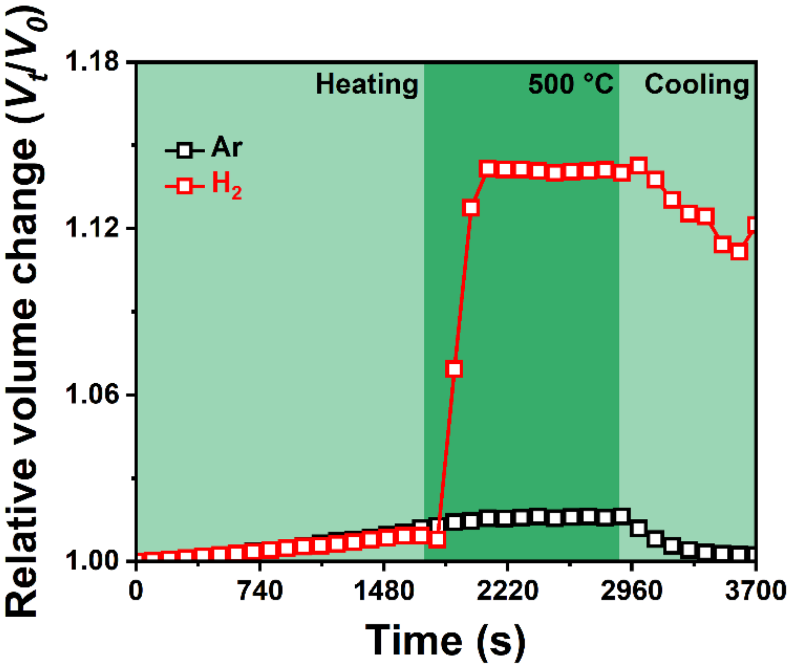

Fig. 3.7 Relative volume change of the crystal lattices in TiNbZr samples treated in H_2 and Ar.

3.3.6. Microstructure after the treatment in H_2

The microstructure of the TiNbZr sample after the treatment in H_2 is displayed in **Fig. 3.8**. The treatment causes no obvious change in the shape and surficial morphology of particles due to the low heat treatment temperature (500 °C) and short treatment time (0.5 h). The particle size is measured to be 22.90±0.44 μm, consistent with that of the pristine state (**Fig. 3.2**c). The dendritic microstructure remained, as revealed in the cross-sectional SEM images (**Fig. 3.8**d). In addition, the chemical fluctuation of individual elements between interdendritic and dendritic regions is the same as that in the pristine sample (**Fig. 3.8**e). Such unchanged microstructure features are mainly attributed to the slow diffusion of the refractory elements at 500 °C (T/T_m = ~0.29, where T_m is the liquidus temperature of TiNbZr. As shown in **Fig. S3.15**, T_m is determined to be ~1720 °C by Thermo-Calc in conjunction with the thermodynamics database TCTI2). Despite the random orientation of grains after the treatment in H_2 (**Fig. 3.8**f), an increasing number of low-angle grain boundaries (2-15° misorientation) is observed, accounting for 46.2% over all the boundaries (which is 16.2%, and 19.6% for the pristine sample and the sample after heat treatment under Ar (**Fig. S3.16**), respectively). Additionally, the local KAM value at these low-angle grain boundaries in the hydrogen-treated sample can reach values up to 2.04° as compared with 0.69° in the sample treated in Ar. The density of the geometric necessary dislocation (ρ) can be approximated following the equation,

$\rho = {}^{3 \times KAM}\!/_{b \times \Delta x}$, where b and Δx represent the magnitude of the Burgers vector and step size used for the EBSD scan, respectively [145, 146]. After the heat treatment in hydrogen, the dislocation density (7.07×10^{15} m^{-2}) is about three times higher than the reference sample (2.39×10^{15} m^{-2}), suggesting the significant internal distortion and associated strain localization caused by hydrogen ingress. The formation of low-angle grain boundaries can be attributed to the accommodation of internal stress induced by hydrogen interstitials [105, 147, 148]. Specifically, the incorporation of a substantial amount of hydrogen solutes (>40 at.%) into the lattice induces a crystal structure transition from BCC to BCT. The presence of hydrogen solutes and the associated structural transformation result in significant lattice distortion, leading to the build-up of misfit dislocations. As these dislocations accumulate and multiply, they relax the local stresses by reorganizing into low-angle grain boundaries. Interestingly, these low-angle grain boundaries are distributed along the interdendritic regions, where Ti and Zr are enriched, which is mainly ascribed to the higher affinity of hydrogen to Ti and Zr than to Nb [35].

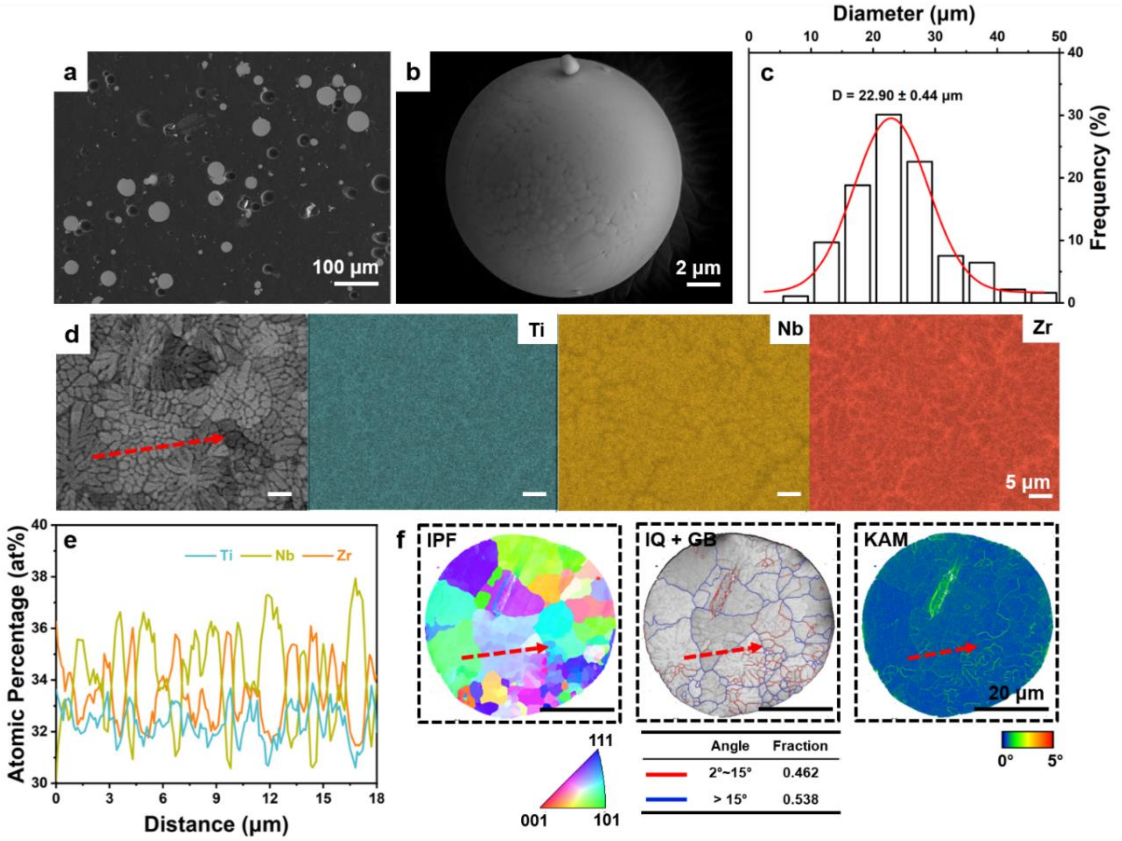

Fig. 3.8 Secondary electron images of (a) TiNbZr particles and (b) an individual TiNbZr particle after the treatment in H_2. (c) Size distribution of the TiNbZr particles. (d) Backscattered electron imaging of a particle and the corresponding elemental maps of Ti, Nb, and Zr probed by electron dispersive spectroscopy. (e) Elemental distribution across dendrites, as marked by the red arrow in (d). (f) Inverse pole figure (IPF), image quality overlaid with grain boundaries (IQ + GB), and kernel average misorientation (KAM) maps of the particle probed by the electron backscatter diffraction. The red arrow in (f) represents the same scan in (d).

3.4. Discussion

The results presented in **Section 3.3** show the evolution of the TiNbZr crystal lattice upon hydrogen uptake, *i.e.*, the isotropic lattice expansion during isothermal treatment in H_2 at 500 ° C and followed by anisotropic lattice expansion during the cooling schedule to room temperature. In this section, we discuss the preferred occupancy site of hydrogen atoms in the BCC lattice of TiNbZr alloy and the origin of the anisotropic tetragonal expansion of the lattice, to better understand the effect of hydrogen atoms on crystal structures.

3.4.1. Site occupancy of hydrogen atoms in the TiNbZr crystal lattice

The fundamental question is what the favorable accommodation site of one single hydrogen atom in the crystal lattice is, *i.e.*, devoid of any sublattice or Zener ordering correlations with other hydrogen atoms. The TiNbZr lattice with its BCC structure possesses two types of interstitial sites that can accommodate hydrogen atoms, namely, 12 tetrahedral sites and 6 octahedral sites per BCC unit cell [27]. For the following qualitative and geometry-based discussion, the reasoning is built on the simple BCC rigid lattice, with geometric considerations applied to tetrahedral and octahedral sites. Generally, the radius (r) of a tetrahedral site (0.291 R, R is the radius of the host metal atom) is approximately twice that of an octahedral site (0.155 R) [27]. Because of the larger accommodation space of a tetrahedral site in the TiNbZr alloy (calculated to be 0.426 Å, considering a lattice parameter of 3.3836 Å from **Fig. 3.1**), intuitively, a hydrogen atom (with a radius of 0.53 Å) should prefer to occupy a tetrahedral site rather than an octahedral site [114, 143, 149, 150]. The validity of this hypothesis is further rationalized by DFT calculations (**Fig. 3.9**). We therefore computed the H solution energies on the various symmetry inequivalent interstitial tetrahedral and octahedral sites in the constructed TiNbZr SQS supercell. After the relaxation of the atomic positions, about half of the considered octahedral sites turned out to be unstable: the hydrogen occupies a neighboring tetrahedral site (**Fig. 3.9**a). In contrast, the considered tetrahedral sites were almost all stable, and we observed that only for a few cases relaxation into an octahedral position after the full stress relaxation (**Fig. 3.9**b). Having the energy distribution over the different sites and knowing that a single site can only be occupied by a single hydrogen atom, we can use the Fermi-Dirac statistics to calculate the ratio of hydrogen in tetrahedral vs. octahedral sites as a function of temperature (T) and hydrogen concentration (X_H) [151]. Since a single interstitial site can accommodate no more than one single hydrogen atom, the statistics describing the hydrogen distribution is given by Fermi-Dirac distribution,

$$f(\Delta H_{\mathrm{sol}}; T, \mu) = \left[\exp\left(\frac{\Delta H_{\mathrm{sol}} - \mu}{k_{\mathrm{B}} T}\right) + 1\right]^{-1} \tag{3.2}$$

where ΔH_{sol} is the solution energy of a hydrogen interstitial on a specific site, and μ, k_{B}, and T stand for the chemical potential of hydrogen, Boltzmann constant, and temperature, respectively. The total hydrogen concentration x (relative to the total number of available interstitial sites (*i.e.*, tetrahedral and octahedral sites)) is given by,

$$\int_{-\infty}^{+\infty} n(\Delta H_{\mathrm{sol}}) f(\Delta H_{\mathrm{sol}}; T, \mu) \, \mathrm{d}\Delta H_{\mathrm{sol}} = x \tag{3.3}$$

where the density of states $n(\Delta H_{\mathrm{sol}})$ has been determined from the energies calculated by DFT for the various interstitial sites for a single hydrogen atom. Equations (2) and (3) are solved self-consistently to obtain the hydrogen chemical potential $\mu(T, x)$ for a given hydrogen concentration. As revealed in **Fig. 3.9**e, for a dilute hydrogen concentration (corresponding to a single hydrogen atom in the SQS supercell with 54 metallic atoms), $T = 0$ K gives almost 100% of tetrahedral occupancy. Higher temperature gives a lower tendency to occupy the tetrahedral sites, asymptotic to an approximately 2:1 ratio of the number of tetrahedral and octahedral interstitials when the temperature approaches infinitely large values. Over the temperature of interest, more than 80% of tetrahedral occupancy is the result. Thus, the above DFT calculations strongly indicate that tetrahedral sites are energetically preferable to accommodate a hydrogen atom no matter whether it is initially introduced to a tetrahedral or octahedral site. Such a preference for hydrogen accommodation at tetrahedral sites is in line with the previous studies in the literature with low hydrogen concentrations [55, 143, 152]. It is worth noting that the impact of the zero-point energy on the hydrogen binding energy is negligible. Explicit calculations showed that it gives rise to only very subtle contributions (-0.01 to 0.03 eV/H-atom) to the solution energies (~0.4 eV/H-atom) (**Fig. S3.17**). Additionally, unstable octahedral sites at T=0 K may be dynamically stabilized by temperature, including thermal vibrations and electronic excitations. However, given that this would require significantly computationally expensive molecular dynamics simulations, we consider this to be beyond the scope of the present work.

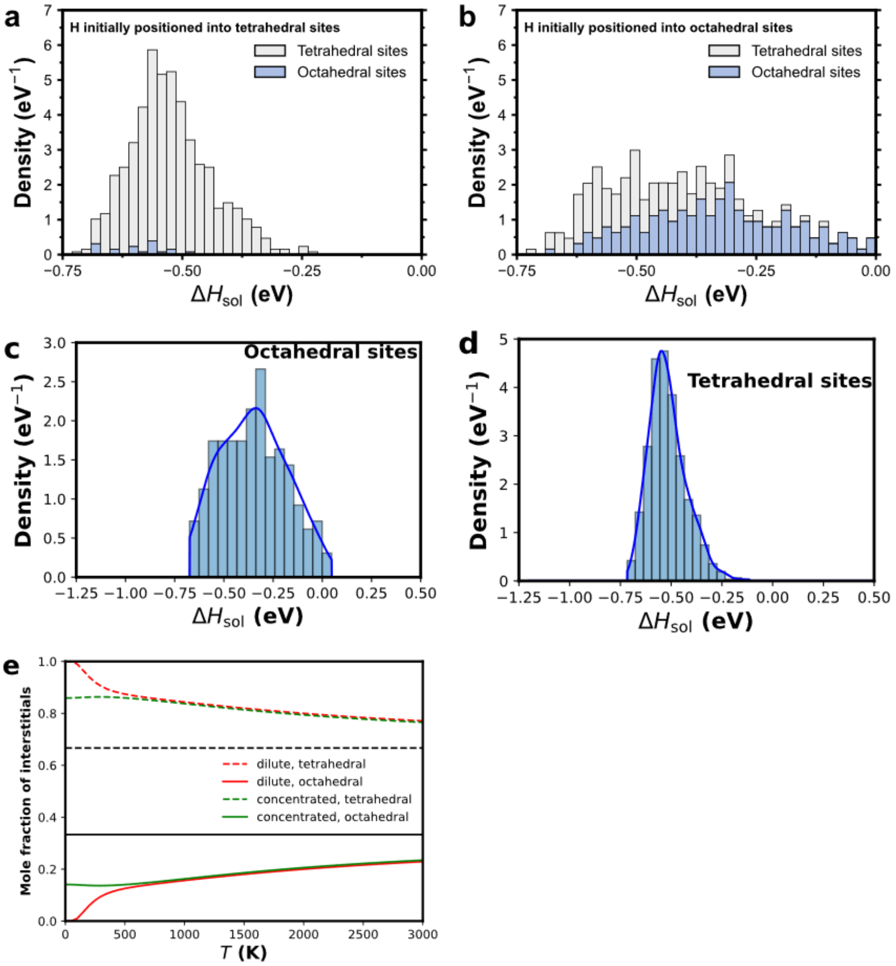

Fig. 3.9 Statistical distribution of solution enthalpy per hydrogen atom in a TiNbZr special quasirandom supercell after a full stress relaxation with one hydrogen atom initially positioned at all possible (a) octahedral interstitial sites and (b) tetrahedral interstitial sites. Corresponding distribution of relaxed hydrogen states in (c) octahedral and (d) tetrahedral sites. DFT calculations were conducted with a 3 × 3 × 3 supercell (54 metallic atoms) at T=0 K. (e) Calculated frequency for the tetrahedral and octahedral occupancy assuming a Fermi-Dirac distribution of energy states in the case of dilute and concentrated hydrogen solution corresponding to 1 and 45 hydrogen atoms in the supercell, respectively (hydrogen mole fraction: 2 at.% and 45.4 at.%, respectively).

Next, we discuss the scenario where a large number of hydrogen atoms are present. The Fermi-Dirac distribution of energy states gives a similar trend of the temperature-dependent tetrahedral occupancy when 45 hydrogen atoms are present in the supercell (corresponding to the saturated hydrogen concentration, following the experimental results shown in Fig. 3.7) except for the low-temperature region (<500 K) where the tetrahedral hydrogen stabilized at around 85% of occupancy. Nevertheless, the tetrahedral sites remain the preferred positions for the hydrogen atoms (Fig. 3.9e). It is worth noting that the above Fermi-Dirac analysis is suited mainly for qualitative interpretation. Three main assumptions have been made for the Fermi-Dirac analysis: (1) The volume change due to hydrogen is ignored, which might be important for cases where high hydrogen concentrations apply. (2) The predicted results for low hydrogen concentrations should be interpreted with caution, as they are highly sensitive to the sampling of the low-energy region. (3) The hydrogen-hydrogen interaction is neglected. To address those limitations, we explicitly introduced 45 randomly distributed hydrogen atoms in the supercell. For the sake of simplicity, a random distribution of hydrogen interstitials was assumed in the supercell using two different configurations with initial occupancy of all hydrogen atoms in only octahedral sites and only tetrahedral sites, respectively. In total, 200 different configurations with 45 hydrogen atoms have been considered for DFT calculations (**Table S3.7**). Specifically, two BCC SQS cells were utilized for DFT calculations, and we sampled 50 octahedral and 50 tetrahedral configurations for each SQS cell. The minimum distance of neighboring hydrogen-hydrogen bonds was constrained to values larger than 2.0 Å (see computed force and interactions between nearest-neighbor hydrogen atoms in **Fig. S3.18**) to avoid the large hydrogen-hydrogen repulsive interaction [114, 150, 153]. **Fig. 3.10**a shows the calculated solution enthalpy for the two cases before and after the full stress relaxation. For the former case, the presence of hydrogen interstitials on octahedral sites is unfavorable, as evidenced by the higher averaged solution enthalpy of 0.035 eV/H-atom than that (-0.469 eV/H-atom) of the tetrahedral configuration. Even after the full stress relaxation, the solution enthalpy of hydrogen atoms initially positioned at the octahedral sites remains higher (-0.336 eV/H-atom) compared with the latter case when hydrogen atoms are placed on the tetrahedral sites prior to relaxation. The solution enthalpy of the latter case with initial tetrahedral hydrogen configuration decreases further to -0.605 eV/H-atom upon full relaxation. Additionally, the volume expansion of the supercell is determined to be approximately 11.1±0.3% after the incorporation of 45 hydrogen atoms (randomly distributed, see **Fig. S3.19**), consistent with the value derived from the HEXRD experiment. These results confirm that even at such a high concentration of hydrogen (46.4 at.% hydrogen), tetrahedral sites are more favorable sites for hydrogen accommodation. As tetrahedral interstitial sites reveal isotropic geometry, hydrogen atoms exert a uniform force on the nearest neighboring host atoms, leading to an isotropic expansion of the lattice [143]. When hydrogen atoms are randomly distributed at tetrahedral sites, they result in almost isotropic expansion of TiNbZr lattices with a small *c/a* ratio of 1.007 (**Fig. 3.10**b). This *c/a* ratio is consistent with the constructed SQS supercell without hydrogen atoms (1.006, due to finite size of the supercell). Such a case reflects the situation at an elevated temperature during the isothermal heat treatment process, where hydrogen atoms can be expected to be randomly distributed within the TiNbZr crystal due to the configurational entropy effect at high temperatures [114]. Thus, the current BCC structure is predominantly stable with hydrogen interstitials randomly distributed at the tetrahedral sites at a high temperature, as also suggested in the *in-situ* HEXRD experiments (**Fig. 3.4**).

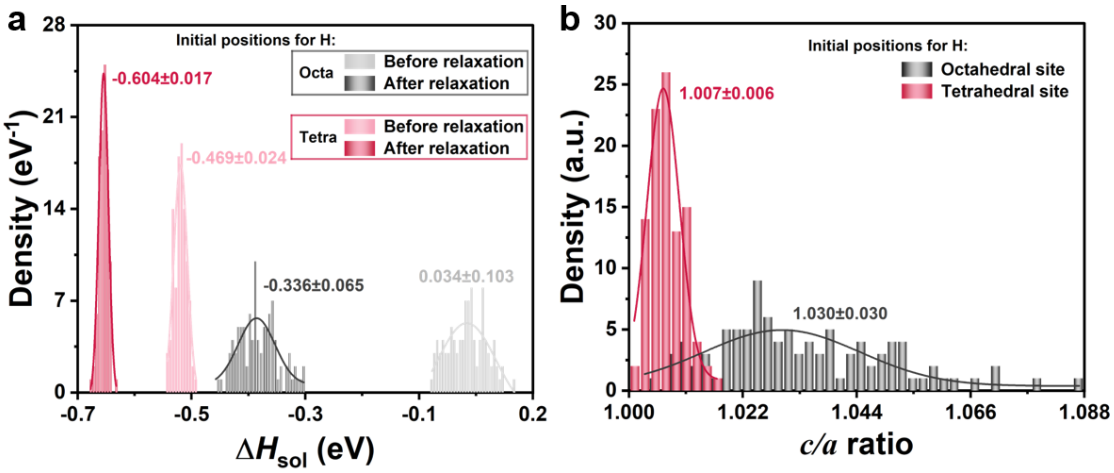

Fig. 3.10 (a) Statistical distribution of calculated solution enthalpy per hydrogen atom before and after atomic relaxation when 45 hydrogen atoms are positioned at octahedral or tetrahedral sites in a supercell with 54 metal atoms. The data has been obtained from DFT calculations. (b) Statistical distribution of calculated *c/a* ratio with all hydrogen initially settling at the tetrahedral and octahedral sites after relaxation based on DFT calculations. DFT calculations were conducted with a 3 × 3 × 3 supercell (54 metallic atoms) at T=0 K.

3.4.2. Occurrence of lattice tetragonality upon cooling

An intriguing observation is the tetragonal distortion of the hydrogen-saturated crystal lattice upon cooling as determined by HEXRD and TEM methods (**Fig. 3.5** and **Fig. 3.6**). The advantages and disadvantages of both methods shall be briefly summarized and discussed for the determination of tetragonality. HEXRD is commonly used in the detection of tetragonality, especially for the tetragonal distortion of Fe-C martensite [154, 155]. For HEXRD, the X-ray diffractograms reflect the crystal structures averaged over the probed volume (here, ~0.4 mm^3) with excellent statistical information [154, 155]. However, measuring tetragonality relies on indirect profile analysis of the peak splitting and broadening [156]. The uncertainty arising from the deconvolution of diffraction peaks (based on the least squares method) hinders its direct utility for interpreting tetragonality [156, 157]. In contrast, the TEM-based electron diffraction technique provides local but direct information, despite the challenging and time-intensive preparation of thin films for TEM observations. Concerning the micro-size powder sample in this study, the focused ion beam (FIB) cutting method was used for the site-specific TEM lamella preparation, although it can unavoidably introduce artifacts during the thinning process, limiting the explanation of the results [158, 159]. Therefore, in our study, a combination of HEXRD and TEM methods was employed to validate local lattice tetragonality, and to understand and minimize the inaccuracies resulting from relying solely on a single testing method. Both the occurrence of peak splitting and broadening in the HEXRD experiment, and the overlap of two diffraction spots in the TEM analysis strongly support the tetragonality of TiNbZr lattices upon cooling. Nevertheless, a slight variation of *c/a* ratios is observed for the samples measured using the two methods (ranging from 1.06 for HEXRD to 1.07 for TEM). Such a discrepancy in the *c/a* ratios might be due to the spatial/angular resolution limit associated with these two techniques, one being local (TEM) and the other integral (HEXRD).

The presence of tetragonality upon cooling indicates a change in the configuration of hydrogen atoms in the accommodation sites, which results in an asymmetric lattice expansion (expansion along the *c*-axis in this study). Based on the hydrogen concentration (~46.4 at.%) and the presence of tetragonality, two reasonable atomic configurations are considered (**Fig. 3.11**a). For the sake of simplicity, we only consider scenarios where hydrogen atoms occupy a single type of interstitial site, either a tetrahedral or octahedral site. Scenario I: all hydrogen interstitials are positioned at tetrahedral sites with a specific hydrogen occupancy of $(0, \frac{1}{2}, \frac{1}{4})$ and $(0, \frac{1}{2}, \frac{3}{4})$, as these sites are calculated to be the energetically favorable positions for hydrogen accommodation (see **Section 3.4.1**). Although a tetrahedral hydrogen atom applies uniform force on four neighboring metallic atoms, the specific arrangement of the hydrogen atoms in a lattice can result in a joint force along the *c*-axis, thus causing an asymmetric lattice expansion [143]. Scenario II: all hydrogen interstitials are positioned at octahedral sites with an ordering distribution (hydrogen occupancy: $(0, 0, \frac{1}{2})$ and $(\frac{1}{2}, \frac{1}{2}, 0)$). In comparison to the tetrahedral hydrogen atoms, octahedral hydrogen interstitials exert a non-uniform force, exhibiting higher forces on the two nearest neighboring atoms [143]. Owing to these ordered distributions of hydrogen interstitials, a reduction of the total energy of the system is expected [114]. This hypothesis will be further testified through *ab initio* DFT calculations.

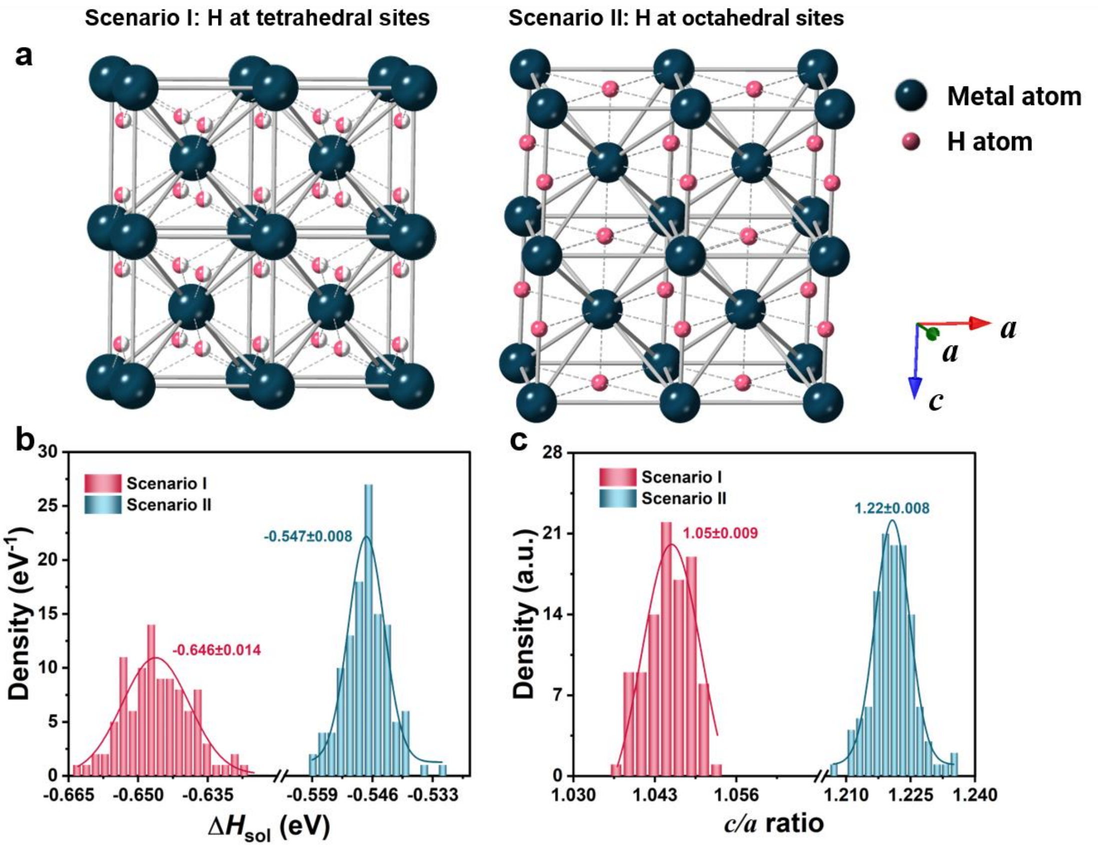

Fig. 3.11 (a) The proposed lattice configurations, which are possible to result in lattice tetragonality, namely, the asymmetric expansion along the *c*-axis. Scenario I with all hydrogen atoms positioned at the tetrahedral $(0, \frac{1}{2}, \frac{1}{4})$ and $(0, \frac{1}{2}, \frac{3}{4})$ sites (In this case, only half of the marked sites are occupied by hydrogen atoms), while about all hydrogen atoms are located at the octahedral sites (hydrogen occupancy: $(0, 0, \frac{1}{2})$ and $(\frac{1}{2}, \frac{1}{2}, 0)$) in Scenario II. Statistical distribution of (b) calculated solution enthalpy per hydrogen atom and (c) calculated *c/a* ratio of Scenario I and Scenario II after stress relaxation. DFT calculations were conducted with a 3 × 3 × 3 supercell (54 metallic atoms) at T=0 K.

To validate the tetragonal distortion caused by the ordering distribution of hydrogen atoms, all of them were located in tetrahedral or octahedral sites within the lattices. It is noted that the solution enthalpy of the Scenario I configuration reaches a lower value (-0.646±0.014 eV/H-atom) compared with the Scenario II (-0.547±0.008 eV/H-atom) (Fig. 3.11b), suggesting a more stable configuration for hydrogen accommodation. The difference in configurational entropy between random solid solution (in tetrahedral sites) and Scenario I configuration (under the ideal mixing assumption, see Supplementary **Note 3.1**) is determined to be $\Delta S_{\mathrm{conf}} \approx 1.24\ k_{\mathrm{B}}$ per hydrogen atom. With this value, the phase transformation temperature of Scenario I from a random solid solution is predicted to be 382K. Since other factors, such as composition variations, exchange-correlation functionals, and thermal vibrations, will also contribute to the transition temperature, this predicted temperature is in qualitative agreement with the BCT-2 transition temperature observed in HEXRD experiments (~723 K). Simultaneously, the *c/a* ratio of Scenario I is determined to be 1.05±0.009 (**Fig. 3.11**b), in agreement with that of the predominant BCT-2 crystal structure (~1.06) as evidenced by the HEXRD results (**Fig. 3.5**). Although the Scenario II configuration exhibits a higher solution enthalpy, the *c/a* ratio with 1.22±0.008 is in line with the BCT-1 crystal structure (~1.22). This result implies that the Scenario II configuration, in which all hydrogen atoms are periodically positioned at the octahedral sits, is likely to be an intermediate configuration. This configuration is considered to be a transformable state from BCC to FCC during the hydrogenation [100, 101]. Such octahedral occupancy of hydrogen atoms is thought to increase the disorder of hydrogen-hydrogen bonds, thus destabilizing the BCC crystal structure and inducing subsequent phase transformation. This metastable nature also explains why the Scenario II configuration with a *c/a* ratio of ~1.22 is challenging to be detected when using TEM characterization techniques, which are conducted several weeks after the *in-situ* HEXRD experiment. The underpinning physics leading to the presence of tetragonality upon cooling are mainly due to, (1) the occupation of a tetrahedral (or octahedral) site which produces an elongation of the *c*-axis, which, in turn, facilitates the occupancy of neighboring tetrahedral (or octahedral) sites by other hydrogen atoms, a phenomenon referred to as collective interstitial ordering [114]; (2) the local anharmonicity in the strain fields induced by interstitials, which substantially stabilizes the collective ordering [160].

In this study, a single-step BCC-to-BCT transformation is observed in the TiNbZr alloy upon cooling from 500 °C after hydrogenation (1 bar H_2). In the literature, a fully hydrogenated TiNbZr at 40 bar H_2 reveals a FCC crystal structure [161], which is a typical hydride phase in TiNbZr-based CCAs (**Table S3.1**). Notably, a different transformation pathway is also observed for some alloys with similar compositions, forming BCT hydride as the fully hydrogenated form, *e.g.* in TiVZrNbTa [162]. The discrepancy in transformation pathways can be attributed to: (1) Composition difference: Alloys appearing to form BCT metal hydrides often contain vanadium (V), where V tends to stabilize the BCT hydride phase at high hydrogen concentrations [114, 163]. Moreover, in the case of group IV elements (*i.e.*, Ti, and Zr in this study), tetragonal lattice distortions can be observed at hydrogen concentrations exceeding 60 at.% hydrogen [164, 165]. Refractory CCAs with a high proportion of these elements have a high tendency to form BCT hydrides; (2) Lattice distortion (δ): Variations in δ, calculated as $\delta = \sqrt{\sum_i c_i (1 - \frac{r_i}{\bar{r}})^2} \times 100$, where c_i, and r_i denote the atomic fractions, and radius of element i respectively, while $\bar{r}$ stands for the averaged atomic radius, can also influence the transformation pathway [100, 166]. This parameter is closely related to the availability of the interstitial sites within the lattices. Here, TiNbZr have a δ value of 4.3%, aligning with a classical BCC-to-FCC transformation that is typical for alloys with small δ values. In contrast, TiVNbZrTa, which forms BCT hydrides, has a δ value of 5.8%. Refractory CCAs with high δ values are accompanied with more available interstitial sites (especially for octahedral sites) within the lattice. The large lattice distortion can lead to the reduction in the energy barrier for hydrogen octahedral accommodation. The occupancy of octahedral sites can induce the elongation of the c-axis, thus favoring the formation of BCT hydrides. While these factors suggest a connection between phase transformations and composition/δ, establishing a quantitative relationship remains challenging. Additional physicochemical parameters, *i.e.* valence electron concentration (VEC), electronegativity (δ_x) might also influence phase transformation pathways [100, 161].

3.4.3. Preference of hydrogen accommodation towards Ti/Zr

It is also worth noting that an increase in the fraction of low-angle grain boundaries is found after the treatment in H_2 (**Fig. 3.2** and **Fig. 3.8**). Even though heat treatment typically results in recovery of low-angle grain boundaries [167, 168], the increase in their presence in this study is primarily attributed to the volume changes and lattice distortion associated with the uptake of hydrogen atoms within TiNbZr lattices. More specifically, the hydrogen atoms, especially in a high concentration, can severely distort the lattice structure, leading to the subsequent generation of low-angle grain boundaries [35, 105, 147, 148]. Moreover, these newly formed low-angle grain boundaries are mainly distributed along the Ti and Zr-rich interdendritic regions (**Fig. 3.8**), supporting the fact that hydrogen exhibits a higher tendency towards Ti and Zr rather than Nb due to the lower mixing enthalpy [35]. This tendency is known from these mixtures according to the elementary phase diagrams (*i.e.*, Ti-H), where only the phase diagrams of Nb+H, Zr+H, and Ti+H systems have been experimentally assessed or evaluated using the CALPHAD (CALculation of PHAse Diagram) method [164, 165, 169]. The partial molar enthalpy of hydrogen solution in β-Ti is nearly -59.4 kJ/mol as compared with 43.0 kJ/mol for that of Nb, indicating the higher affinity of hydrogen to Ti than that to Nb. A similar trend can be obtained for Zr (partial molar enthalpy of hydrogen solution in β-Zr is -74.5 kJ/mol), suggesting a higher affinity to hydrogen for Zr as compared with Nb. Our DFT calculations also revealed that the solution enthalpy of hydrogen is lower when more nearest neighboring Ti atoms are present (**Fig. 3.12**). The solution enthalpy drops from 0.23 eV/H-atom to approximately -0.32 eV/H-atom as the number of nearest neighboring Ti atoms increases from 0 to 2 for octahedral hydrogen interstitials. A similar trend is found for the tetrahedral hydrogen interstitials, with the lowest solution enthalpy of -0.63 eV/H-atom when surrounded by 4 nearest neighboring Ti atoms. The Nb atoms, however, exhibit an opposite effect on hydrogen interstitials compared to Ti. The solution enthalpy associated with hydrogen increases with the number of nearest neighboring Nb atoms, while Zr exhibits similar behavior as Ti. These findings are important, suggesting that the local chemical environment provided by the surrounding host alloying atoms can entail local hydrogen preference (*i.e.*, where the hydrogen is preferably stored or less preferably stored). The same fact applies to the kinetic barriers when extracting the hydrogen atoms from the metal again for generating hydrogen molecules [57, 170, 171]. Translated to the application of such MEAs as high-temperature materials exposed to hydrogen (*e.g.*, combustion engines), this fact also means that specific lattice regions enriched in Ti, Zr, or both might be particularly susceptible to an embrittling effect due to such hydrogen-induced local distortion.

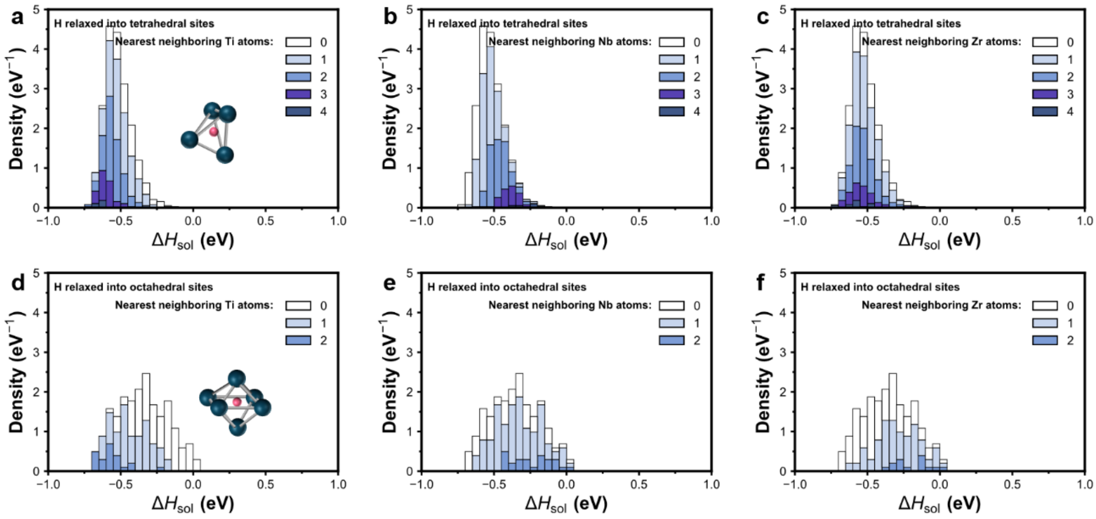

Fig. 3.12 Calculated statistical distribution of the hydrogen solution enthalpy per hydrogen atom of TiNbZr with one hydrogen solute relaxed to either tetrahedral interstitial sites or octahedral interstitial sites surrounded by different amounts of nearest neighbor (a, d) Ti atoms, (b, e) Nb atoms and (c, f) Zr atoms. DFT calculations were conducted with a 3×3×3 supercell (54 metallic atoms) at T=0 K.

3.5. Conclusions

This study investigated the real-time microstructural evolution of TiNbZr alloy during heat treatment in pure hydrogen using *in-situ* synchrotron high-energy X-ray diffraction combined with density functional theory calculations to understand the hydrogen accommodation down to the atomic scale. The main conclusions are:

(1) The body-centered cubic (BCC) lattice exhibited a significant isotropic expansion during hydrogen uptake at 500 °C, with a lattice volume increase of 4.845 Å^3 (corresponding to a hydrogen concentration of 46.4 at.%). It is worth noting that such a high hydrogen

concentration did not induce the formation of hydrides, due to the comparably high solubility of hydrogen within these metallic elements. The DFT calculations revealed that tetrahedral sites were the energetically more favorable positions for hydrogen accommodation for both dilute and high concentrations of hydrogen.

(2) The hydrogen-saturated BCC crystal structure transformed into a body-centered tetragonal (BCT) structure upon cooling to room temperature. The transformation followed the dilatation-dominant displacive transformation pathway with a spontaneous lattice symmetry breaking and discontinuous lattice constant change. The presence of tetragonality is due to the change in the distribution of hydrogen interstitials. The ordered distribution of hydrogen interstitials along tetrahedral sites (hydrogen positioned in tetrahedral $(0, \frac{1}{2}, \frac{1}{4})$ and $(0, \frac{1}{2}, \frac{3}{4})$ sites) led to the asymmetric lattice expansion along the c-axis. This ordered distribution of hydrogen atoms during the structural evolution is attributed to the minimization of the system solution enthalpy as also shown by DFT calculations. The underlying mechanisms resulting in tetragonality are mainly due to the collective interstitial ordering.

(3) Hydrogen atoms demonstrated a higher tendency to occupy Ti/Zr-rich interstitials compared with those surrounded by Nb atoms as analyzed from the elementary phase diagrams known from these mixtures (*e.g.*, Ti/Zr/Nb-H). As a consequence, a significant increase in the fraction of low-angle grain boundaries (by 30.0%) was found along Ti/Zr-enriched dendritic regions after the heat treatment in H_2. The DFT calculations also revealed a higher affinity of hydrogen to Ti/Zr atoms as compared to its affinity to Nb atoms.

Thus, this study provides fundamental new insights into hydrogen accommodation in the interstitial positions in the TiNbZr medium-entropy alloy, highlighting its impact on the lattice symmetry and distortion. These findings shed light on the potential applications of this alloy class in the emerging hydrogen economy.

3.6. Supplementary materials

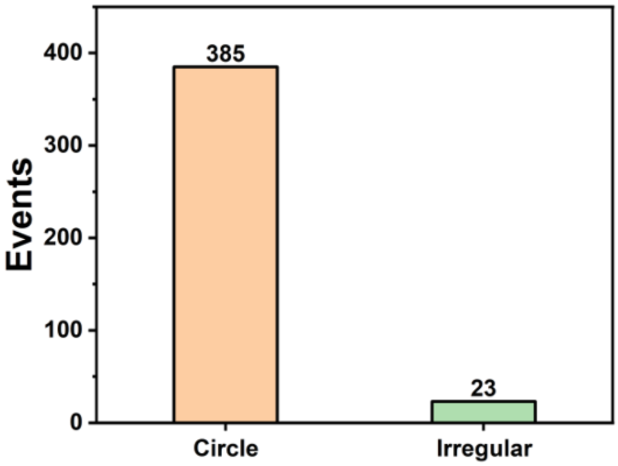

Fig. S3.1 Morphological statistic of TiNbZr powders determined from Fig. 3.2a, showing up to 94.4% of the prepared TiNbZr powders are spherical. Therefore, in this study, we can exclude the effects of size morphology on the microstructural evolution.

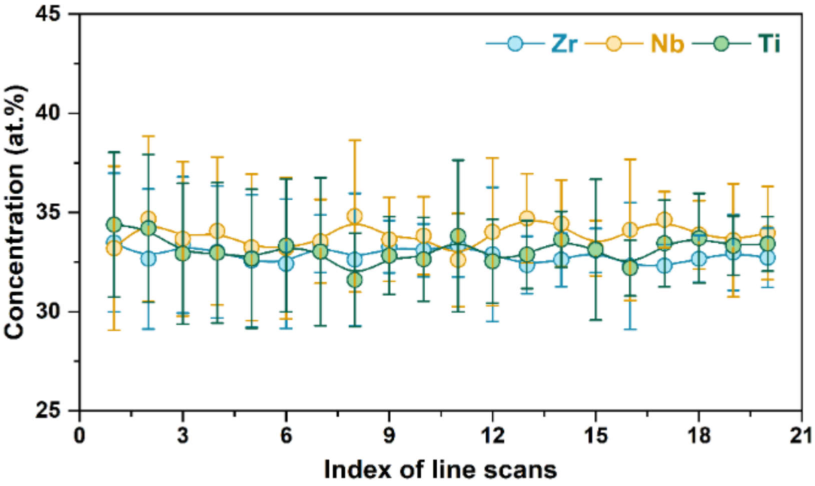

Fig. S3.2 Elemental distribution of all constituent elements (Ti, Nb, and Zr) across different particles. More specifically, in total 20 line scans are performed on 10 particles (2 line scans per particle). The mean and standard deviation values of each line scan are presented in the figure.

All the principal elements exhibit a composition of approximately 33.3 at.%, consistent with the nominated compositions. Additionally, they all show similar trends in elemental fluctuation, fluctuating from 30 at.% to 38 at.%. These results suggest good chemical homogeneity among particles.

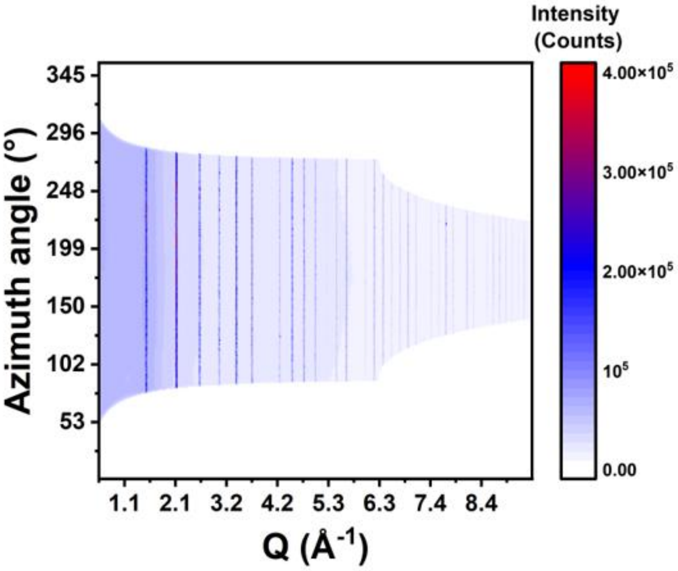

Fig. S3.3 Overall contour map of the intensity integrated over azimuth angle from 5° to 355° for the calibrant (LaB6). All the lines shown are relatively straightforward, indicating the good quality of the synchrotron experiment.

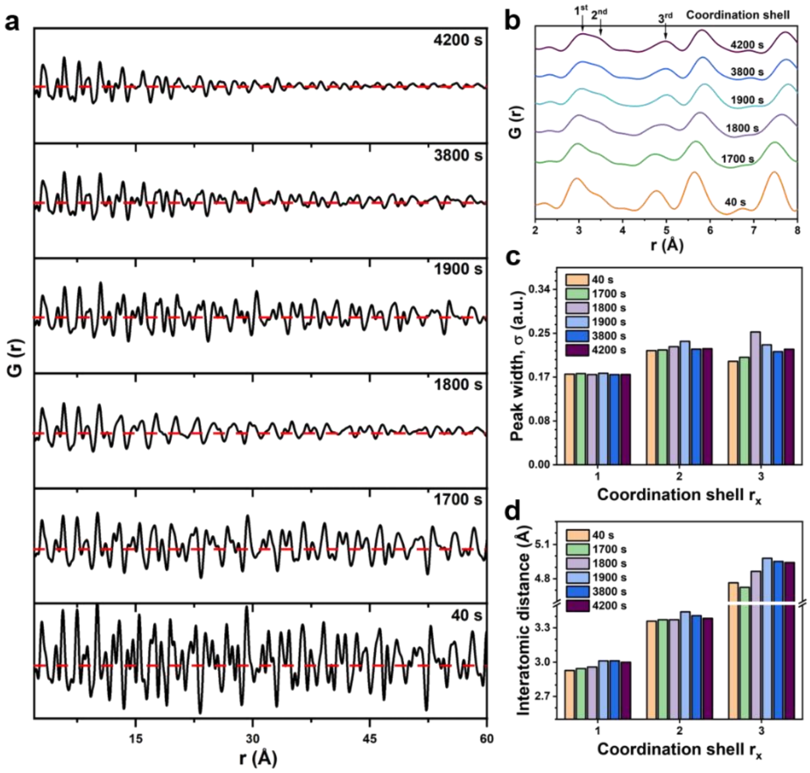

Fig. S3.4 (a) Overall and (b) local pair distribution function (PDF) profiles of the TiNbZr powders during H_2 charging. (c) Peak widths (σ) and (d) interatomic distance for the first three coordination shells.

The loss of long-range correlations is found in the H_2-charged TiNbZr during the initial isothermal process and final cooling, indicating the disordering within the metal matrix. The increase in peak width and interatomic distance also support the high distortion in the lattice.

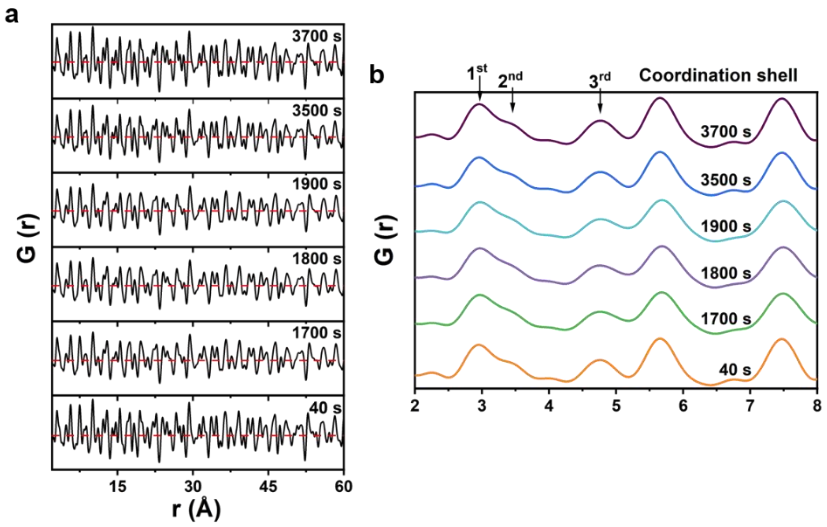

Fig. S3.5 (a) Overall and (b) local pair distribution function (PDF) profiles for the TiNbZr powders under Ar flow at different times.

During high-temperature Ar charging, no obvious change in the fluctuation is observed for the overall PDF profiles. And the peak positions and widths for the 1st, 2nd, and 3rd coordination shells are quite similar, indicating that Ar gas charged at 500°C could not cause such big distortion on TiNbZr lattice structures as H_2 did.

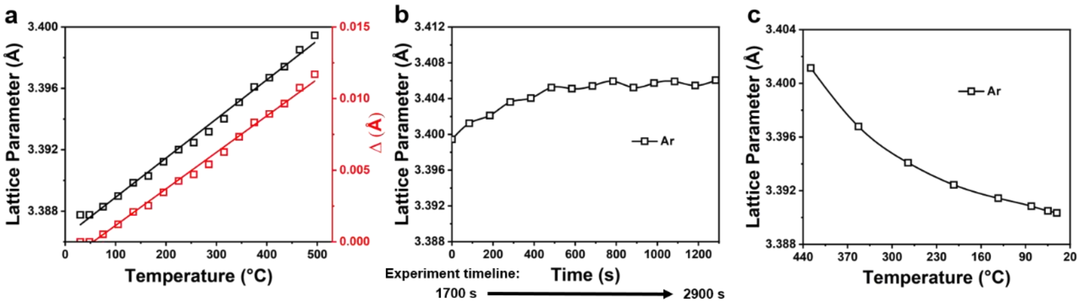

Fig. S3.6 Evolution of the lattice parameters of TiNbZr powders with pure Ar flow (a) during heating, (b) the isothermal heat treatment (500 °C), and (c) cooling.

Here, the TiNbZr lattice shows a linear expansion during heating under Ar, which is identical to the behavior of lattice under H_2. However, the TiNbZr lattice reaches a plateau with a subtle increase in lattice parameter ($\Delta =$ 0.006 Å) during the isothermal holding in Ar, while the increment for the TiNbZr lattice under H_2 is up to 0.143 Å. Another big difference occurs upon the cooling process, where the lattice under Ar goes through a shrinkage, with a lattice parameter close to its initial one (3.3903 Å), while there is a phase transition (BCC to BCT) upon cooling under H_2. More details can be found in the main text.

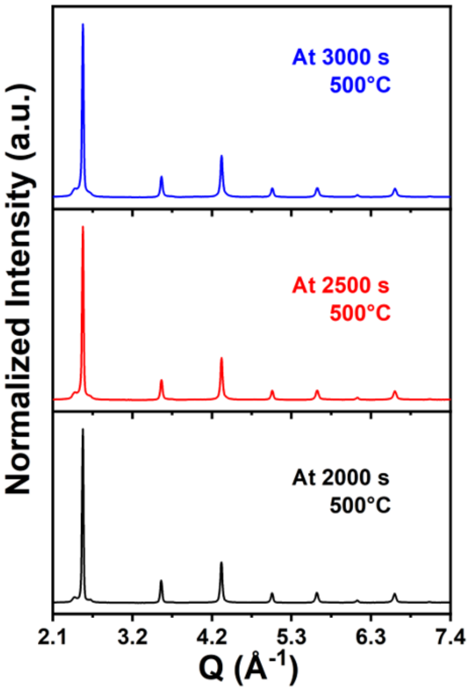

Fig. S3.7 Diffractograms of TiNbZr powders upon isothermal heat treatment (500 °C) with H_2 charging at 2000 s, 2500 s, and 3000 s. No obvious changes in shapes and positions are detected from 2000 s (isothermal holding for 400 s) on.

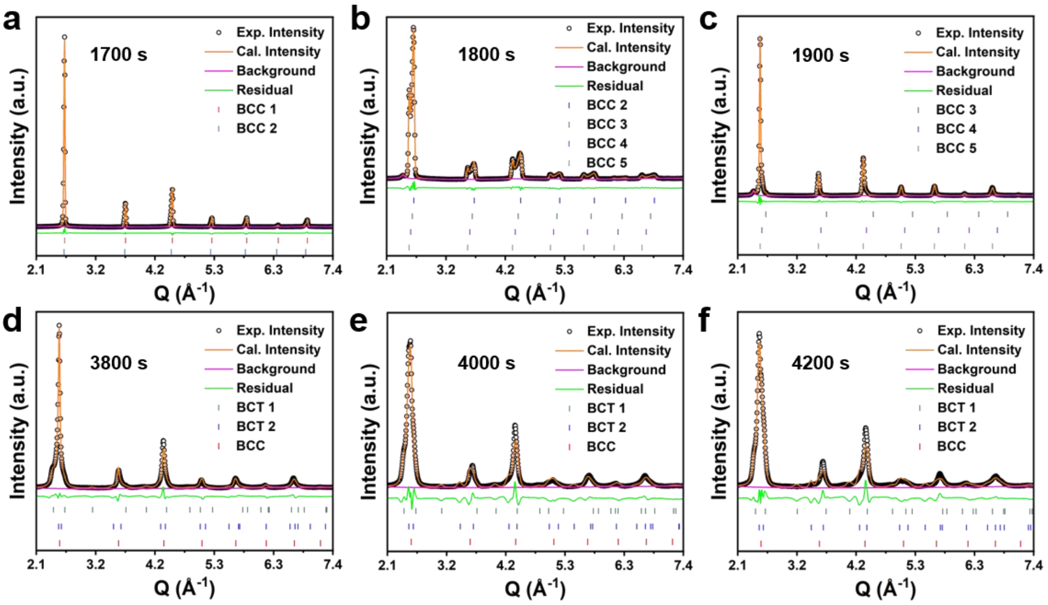

Fig. S3.8 Overall Rietveld refinement profiles of the X-ray diffractograms of the H_2-charged TiNbZr powders at (a) 1700 s, (b) 1800 s, (c) 1900 s, (d) 3800 s, (e) 4000 s, and (f) 4200 s. The weighted profile R-factor (R_{wp}) values for all the refinements are below 10.0%, indicating the high reliability of the refinement results.

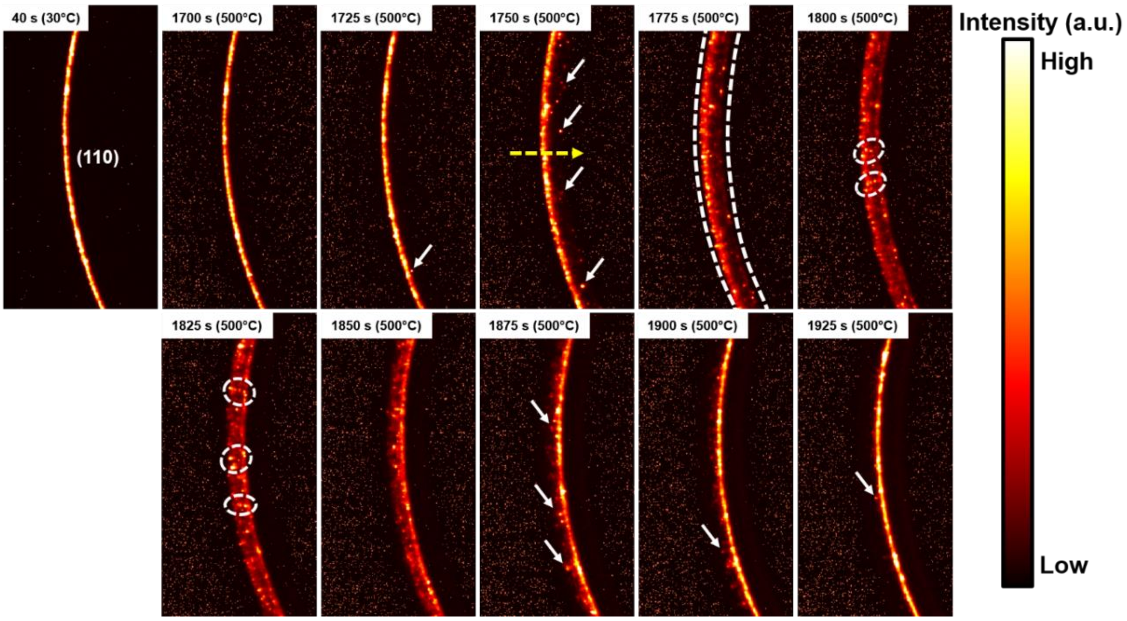

Fig. S3.9 Change of local Debye-Scherrer rings on (110) peaks of the H_2-charged TiNbZr powders during the isothermal process (500 °C), implying the gradual transition of the lattice structure and the co-existence of the BCC structures with different lattice parameters (indicated by white circles). The yellow arrow indicates the evolution direction from left to right of the Debye-Scherrer rings, indicating the gradual increase of the lattice parameters. One intense yellow spot indicates one series of specific crystal planes.

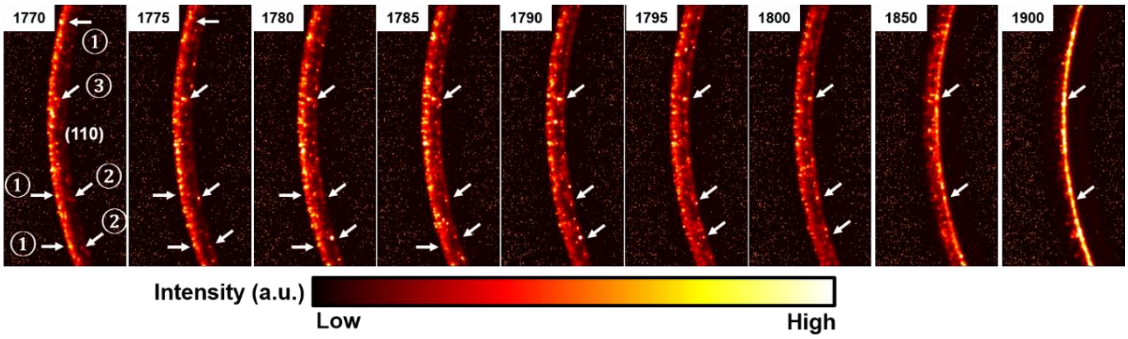

Fig. S3.10 Change of local Debye-Scherrer rings on (110) peaks of the H_2-charged TiNbZr powders during the isothermal process (500 °C). Data was collected every 5 s. Following the trajectory of ①, the intense spots on the left sides gradually disappear, indicating that the proportion of original (110) crystal planes with smaller lattice parameters decreases, whereas the gradual enhancement of the intensity of the spots on the right sides is detected following the trajectory of ②, showing the increase of the (110) crystal planes with larger lattice parameters. Meanwhile, although some intense spots have reached the rightmost region of the ring, they disappear during the isothermal process. This may be ascribed to the fact that not all H is trapped in stable sites during hydrogenation. Following the trajectory of ③, the gradual transition of the intense spot from the left side to the right is observed, demonstrating the sequential expansion of the lattice structure during the isothermal process.

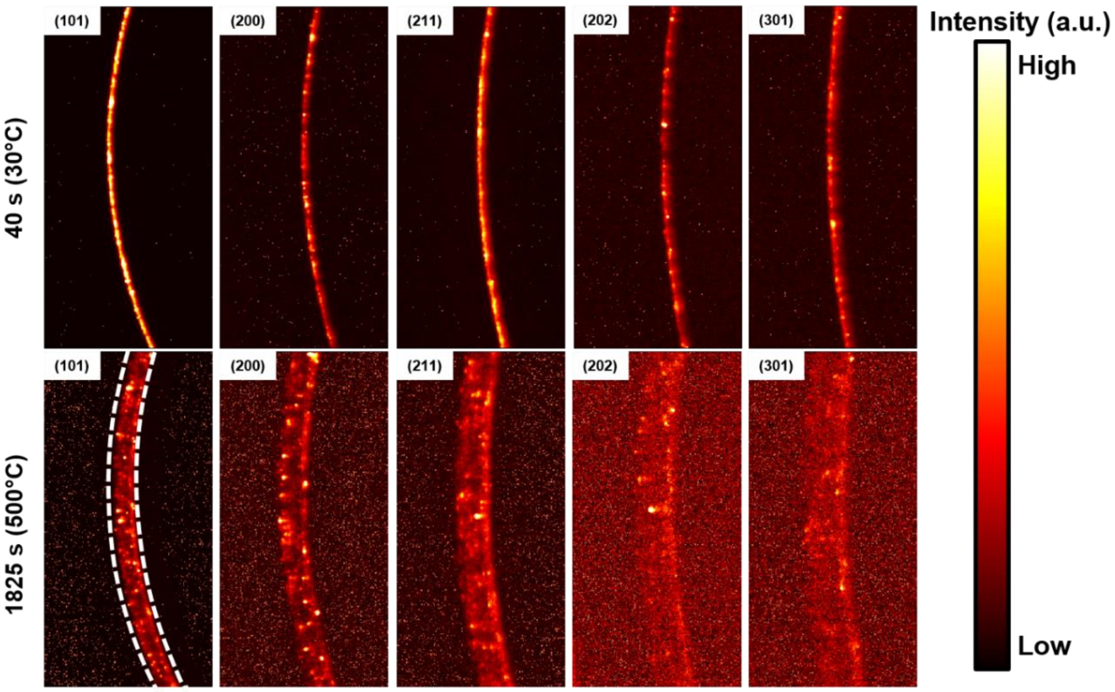

Fig. S3.11 Local Debye-Scherrer rings on different peaks of the TiNbZr powders after high-temperature H_2 charging for 40 s and 1825 s. All rings display similar phenomena with the broadening of rings and co-existence of a series of intense spots along the rings.

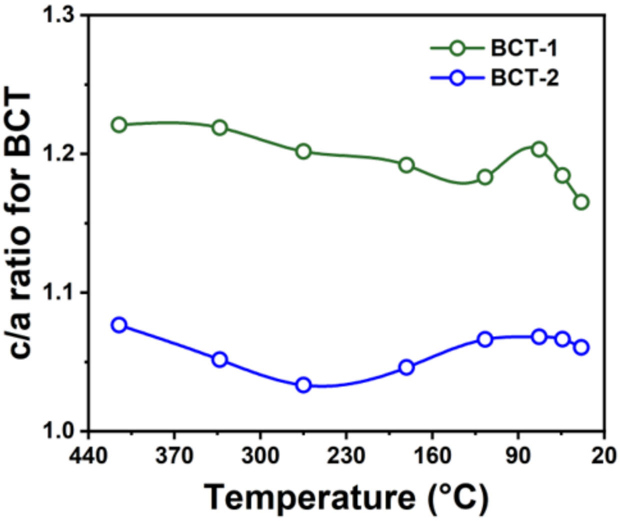

Fig. S3.12 The change of c/a ratio upon cooling for BCT-1 and BCT-2 crystal structures inside TiNbZr alloy while charging with pure H_2 flow.

The c/a ratio floats up and down around ~1.20 for BCT-1 crystal structure, while the c/a ratio for BCT-2 crystal structure is around 1.06.

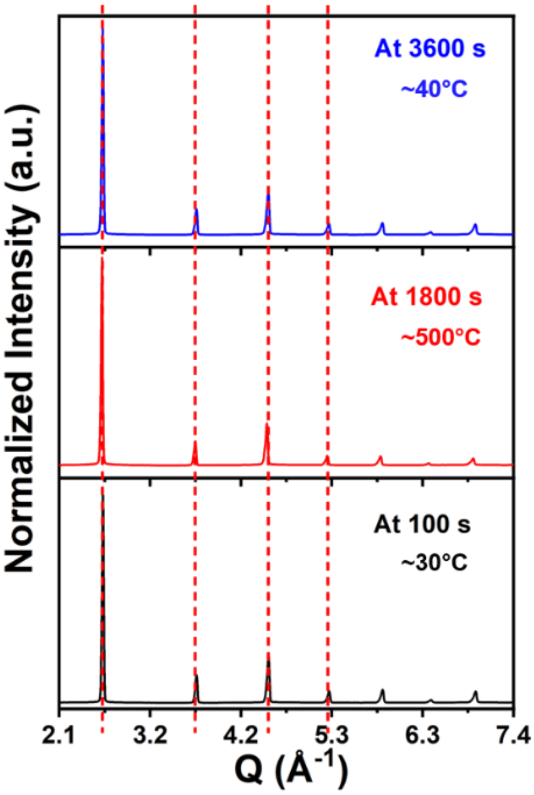

Fig. S3.13 Diffractograms of TiNbZr powders while charging with Ar for 100 s, 1800 s, and 3600 s, the related temperatures are also indicated. No obvious changes in shapes and positions are detected during the whole process of the Ar-charged TiNbZr powders.

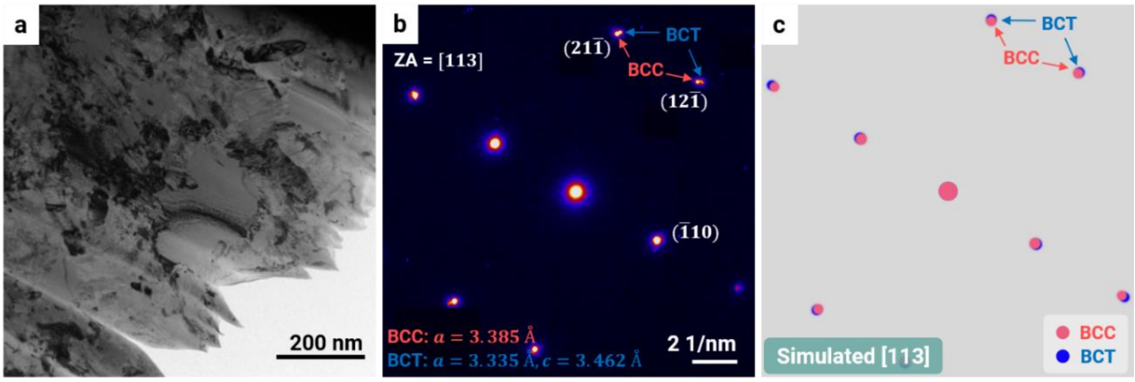
a
200 nm
b
ZA = [113]
$(21\bar{1})$
BCT
BCC
$(12\bar{1})$
$(\bar{1}10)$
BCC: $a = 3.385$ Å
BCT: $a = 3.335$ Å, $c = 3.462$ Å
2 1/nm
c
BCT
BCC
Simulated [113]
BCC
BCT

Fig. S3.14 (a) Representative TEM images of TiNbZr powder after heat treatment in H_2 along the [113] zone axis, and (b) its corresponding Fast Fourier transform (FFT) pattern. (c) Simulated SAED pattern of the coexistence of BCC and BCT crystal structures along the [113] zone axis. The split of diffraction spots can be observed from the experimental SAED pattern, indicating the coexistence of BCC (a = 3.385 Å) and BCT (a = 3.335 Å and c = 3.462 Å) crystal structures. The c/a ratio is calculated to be around 1.04. The simulated SAED pattern also confirms the coexistence of BCC and BCT crystal structures.

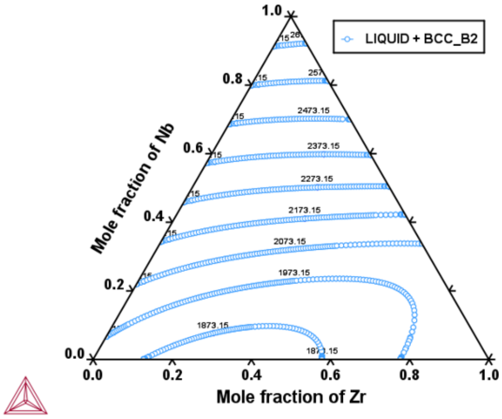

Fig. S3.15 Calculated liquidus temperature of the TiNbZr ternary alloy systems based on TCTI2 database by using Thermo-Calc 2024b. Iso-temperature lines indicating the onset of solidification (from the melt) are presented in the figure, with temperatures given in Kelvin (K).

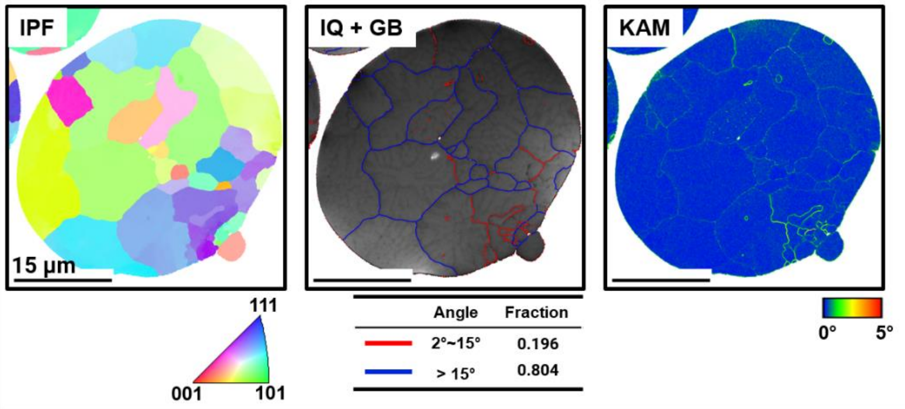

Fig. S3.16 Inverse pole figure (IPF, left), image quality overlaid with grain boundaries (IQ + GB, middle), and kernel average misorientation (KAM, right) maps of the particle after the heat treatment under Ar.

The amount of low-angle grain boundaries is determined to be 19.6%, identical to that of the pristine TiNbZr sample (16.2%), which is lower than that of the sample after heat treatment under H_2 (46.2%).

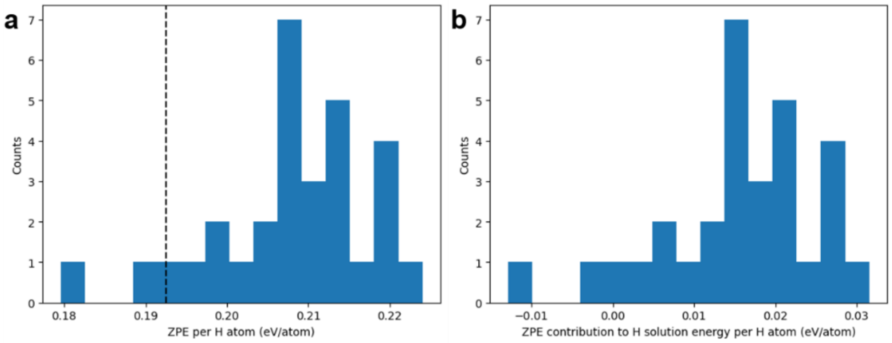

Fig. S3.17 (a) Calculated zero-point energies (ZPE) of H for selected tetrahedral interstitial H atoms. The dashed black line shows the ZPE calculated for H_2 molecular (per H atom) using the same harmonic approximation. (b) Calculated zero-point energies (ZPE) contribution to the H solution energy.

The results suggest that the impacts caused by zero-point-energy (ZPE) are negligible as estimated by the minor difference (-0.01 to 0.03 eV/H-atom) in solution energy with and without the incorporation of ZPEs.

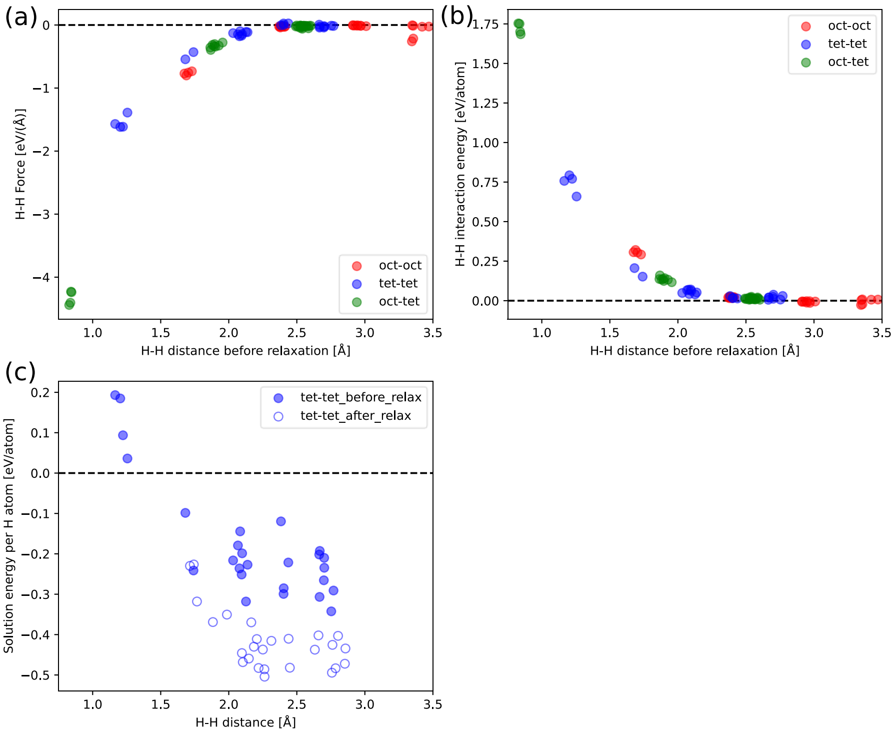

Fig. S3.18 (a) Calculated H-H force as a function of H-H distance before relaxation (positive means attractive, while negative means repulsive). (b) H-H interaction energy as a function of H-H distance before relaxation. (c) calculated solution energy per H atom (averaged over two H atoms) as a function of H-H distance before/after relaxation.

The results suggest that the H-H distance should be larger than ~1.75 Å.

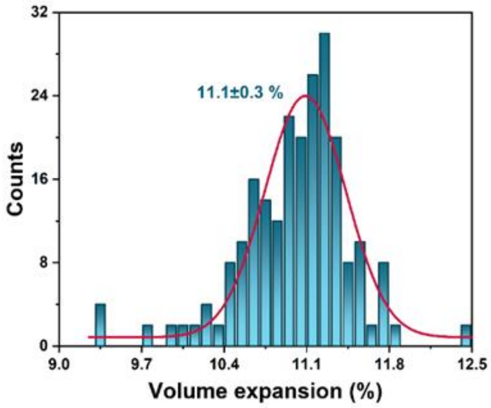

Fig. S3.19 Frequency of the calculated volume expansion ($V_H/V_{eq.} - 1$, where $V_{eq.}$ and V_H represent the volume before and after the incorporation of hydrogen solutes respectively) after each Murnaghan equation of state (EOS) fitting.

The volume expansion of the supercell is determined to be approximately 11.1±0.3% after the incorporation of 45 hydrogen atoms (randomly distributed), consistent with the value derived from the HEXRD experiment.

Table S3.1 Summary of reported characteristics and hydrogen-storage performances of the TiNbZr-based CCAs.

Alloys	H/M ratio	Alloy phase	Hydride phase	Steps upon hydrogenation	Reference
TiNbZrFeNi	1.17	C14 Laves	-	-	[172]
TiNbZrFeMnNi	~1.0	C14 Laves	-	-	[173]
TiNbZr	~1.9	BCC	FCC	-	[161]
$Ti_{0.22}V_{0.22}Zr_{0.22}Nb_{0.11}Hf_{0.22}$	1.82	BCC	BCT	-	[161]
$Ti_{0.22}V_{0.22}Zr_{0.11}Nb_{0.22}Hf_{0.22}$	1.99	BCC	FCC	-	[161]
$Ti_{0.22}V_{0.22}Zr_{0.22}Nb_{0.22}Hf_{0.11}$	2.00	BCC	FCC	-	[161]
$Ti_{0.22}V_{0.11}Zr_{0.22}Nb_{0.22}Hf_{0.22}$	1.96	BCC	FCC	1 step	[161]
$Ti_{0.11}V_{0.22}Zr_{0.22}Nb_{0.22}Hf_{0.22}$	1.97	BCC	FCC	-	[161]
TiVNbZr	1.98	BCC	FCC	1 step	[161]
$Ti_{0.30}V_{0.25}Zr_{0.10}Nb_{0.25}Ta_{0.10}$	1.73	BCC	FCC	1 step	[174]
TiZrNbTa	1.4	BCC	-	-	[133]
TiVZrNbHf	2.5	BCC	BCT	1 step	[101, 162]
TiZrNbHfTa	~2.0	BCC	FCC	2 steps	[100]
$Ti_{0.325}V_{0.275}Zr_{0.125}Nb_{0.275}$	1.75	BCC	BCT	1 step	[175]
$Ti_{0.24}V_{0.24}Zr_{0.28}Nb_{0.24}$	~1.9	BCC	FCC	1 step	[116]
$Ti_{0.22}V_{0.22}Zr_{0.33}Nb_{0.22}$	~1.9	BCC	FCC	1 step	[116]
$Ti_{0.21}V_{0.21}Zr_{0.37}Nb_{0.21}$	~1.9	BCC	FCC	1 step	[116]
$Ti_{0.2}V_{0.2}Zr_{0.4}Nb_{0.2}$	~1.9	BCC	FCC	1 step	[116]
$Ti_{0.25}V_{0.25}Zr_{0.04}Nb_{0.25}Ta_{0.21}$	~1.9	BCC	FCC/BCT	-	[116]
$Ti_{0.25}V_{0.25}Zr_{0.125}Nb_{0.25}Ta_{0.125}$	~1.9	BCC	FCC/BCC	1 step	[116]
$Ti_{0.25}V_{0.25}Zr_{0.19}Nb_{0.25}Ta_{0.06}$	~1.9	BCC	FCC/BCC	1 step	[116]
TiVZrNbMo	~1.9	BCC	FCC	1 step	[176]
TiVNbZr	~2	BCC	FCC	1 step	[171]
TiZrNbHf	~2	BCC	BCT	1 step	[171]
TiZrNbMoHf	~1.2	BCC	FCC	-	[177]
$Ti_{0.2}Zr_{0.2}Nb_{0.2}Mo_{0.1}Hf_{0.3}$	1.54	BCC	FCC	-	[178]
$Ti_{0.2}Zr_{0.2}Nb_{0.2}Mo_{0.2}Hf_{0.2}$	1.18	BCC	FCC	1 step	[178]
$Ti_{0.2}Zr_{0.2}Nb_{0.1}Mo_{0.3}Hf_{0.2}$	1.40	BCC	BCT	1 step	[178]
$Mg_{0.10}Ti_{0.30}V_{0.25}Zr_{0.10}Nb_{0.25}$	1.72	BCC	-	-	[179]

Table S3.2 Chemical compositions of TiNbZr powders. The values shown in the brackets indicate the nominated values.

Element		Ti	Nb	Zr
at.% （Overall）		33.39 (33.34)	34.24 (33.33)	32.37 (33.33)
at.% （pristine state）	Dendrite	33.38	31.70	34.92
	Inter-dendrite	31.29	37.46	31.25
at.% （after H_2 charging）	Dendrite	33.07	32.07	34.86
	Inter-dendrite	31.11	37.25	31.64

Table S3.3 The H/M ratios at 1 bar H_2 of TiNbZr MEA in our study as well as different refractory CCAs from the literature.

Alloys	H/M ratio at 1 bar H_2	Temperature / °C	Reference
TiNbZr	0.865	500	This study
TiNbZrFeNi	~0.8	32	[172]
TiNbZrFeMnNi	~0.82	32	[173]
TiVNbZr	~1.03	21	[161]
$\mathbf{Ti_{0.30}V_{0.25}Zr_{0.10}Nb_{0.25}Ta_{0.10}}$	~0.85	480	[133]
HfNbTiVZr	~1.10	300 to 600	[162]
TiZrNbHfTa	-0.80	300	[100]
$\mathbf{Ti_{0.325}V_{0.275}Zr_{0.125}Nb_{0.275}}$	~0.85	250	[175]
TiVZrNbHf	~0.27	305	[180]
AlTiVNbTa	~0.74	294	[180]
(TiVNb)85Cr15	~0.78	200	[181]

Table S3.4 Lattice parameters and volumes of the unit cell under Ar flow at different temperatures.

Time / s	**Lattice Parameter (a) / Å**	**Volume / Å^3**	**Temperature / °C**
	Fraction / wt.%		
1	3.3878	38.8824	30
	100		
2800	3.4059	39.5090	500
	100		
3200	3.3940	39.0963	275
	100		
3500	3.3908	38.9858	79
	100		
3700	3.3903	38.9582	41
	100		

Table S3.5 Lattice parameters and volumes of unit cells under H_2 flow at different temperatures. a_1, c_1 and a_2, c_2 indicate the lattice parameters of BCT-1 and BCT-2, respectively.

Time / s	Lattice Parameters, Å (Fraction, wt.%)									Volume / Å^3	Temperature / °C
	BCC-1	BCC-2	BCC-3	BCC-4	BCC-5	BCT-1		BCT-2			
40	3.3836 (100)	-	-	-	-	-		-		38.7379	30
1700	3.3908 (85.64)	3.4112 (14.36)	-	-	-	-		-		39.0882	500
1800	-	3.4202 (31.76)	3.4504 (37.40)	3.4887 (12.62)	3.5339 (18.22)	-		-		41.4685	500
1900	-	-	3.4604 (1.27)	3.4855 (15.34)	3.5306 (83.39)	-		-		43.7180	500
2800	-	-	-	-	3.5397 (100)	-		-		44.2091	500
3800	-	-	-	-	3.5074 (47.14)	3.4843 4.0335	13.91	3.4600 3.6193	38.98	43.6411	183
4000	-	-	-	-	3.4883 (42.29)	3.3738 4.0596	10.41	3.4335 3.6673	47.30	43.2096	74
4200	-	-	-	-	3.4882 (25.16)	3.4031 3.9654	15.52	3.4431 3.6512	59.32	43.4833	38

Table S3.6 The corresponding tetrahedral and octahedral interstitial sites of TiNbZr lattice with a lattice parameter of 3.3836 Å.

	r / Å
Tetrahedron	0.426
Octahedron	0.227

Table S3.7 Number of hydrogen atomic configurations used to calculate statistical distributions of solution enthalpy and *c/a* ratio, with the distribution 45 hydrogen atoms randomly.

Number of hydrogen configurations		Initial position of all hydrogen atoms	
		Tetrahedral	Octahedral
Permutation of metal supercell	SQS_1	50	50
	SQS_2	50	50

Note 3.1 The estimation of the critical temperature for phase transition

The mean effective solution energies per H-atom for Scenario I (hydride) and random solid solution are -0.646±0.014 eV/H-atom and -0.604±0.017 eV/H-atom, respectively, providing an energy difference (*i.e.*, the ordering energy) of about 0.042 eV/H-atom. The hydride scenario essentially restricts the H atoms on every second tetrahedral plane (we have chosen a [001] direction). Assuming an ideal configurational entropy, the available configurations for 45 H on all 27 (lattices) × 12 tetrahedral sites for the random solid solution can be expressed as a binomial coefficient ($\binom{324}{45}$). If we assume that only every second tetrahedral sites can be occupied (in the case of Scenario I), there are $\binom{108}{45} \times 3$ configurations. Therefore, the difference in configurational entropy is $\Delta S_{\mathrm{conf}} \approx 56 \cdot k_{\mathrm{B}}$ per supercell, *i.e.*, with an effective mean energy difference of 0.042 eV per H-atom, this would result in a transition temperature of about 382 K. Given that other factors likely contribute to the transition temperature (*e.g.*, thermal vibrations, compositional fluctuations, H-H distance constraint, and exchange-correlation functionals), the estimation is in reasonable qualitative agreement with the experimental findings of 723±10 K (the occurrence of tetragonality upon cooling).

4. Hydrogen-assisted spinodal decomposition in a TiNbZrHfTa complex concentrated alloy

This chapter is a modified version based on the paper entitled "*Hydrogen-assisted spinodal decomposition in a TiNbZrHfTa complex concentrated alloy*" published in the journal *Acta Materialia* (DOI: 10.1016/j.actamat.2024.120707) [182]

4.1. Introduction

Hydrogen has become attractive as a promising green energy source due to its potential to mitigate anthropogenic CO_2 emissions associated with the use of fossil fuels [92, 183, 184]. The deployment of hydrogen energy necessitates the development of advanced metallic alloys tolerating hydrogen-rich atmospheres, even at elevated temperatures [24, 185, 186]. Refractory complex concentrated alloys (CCAs), particularly those of the TiNbZrHfTa family, have been recognized as potential candidates under such application conditions due to their extensive compositional design space and excellent mechanical properties (with a yield strength of ~300 MPa at 1000 °C) [56, 57, 187, 188]. One of the key peculiarities in designing CCAs lies in the stabilization of a single-phase solid solution depending on the maximization of configuration entropy [2, 6, 189]. However, phase decomposition via secondary phase precipitation and ordered phase formation has been frequently observed in some refractory CCAs after heat treatment [190-192].

Hydrogen is bound in various chemicals, such as H_2, NH_3, and hydrocarbons, *etc*. It is worth noting that the size of a neutral H^0 atom, as measured by the Bohr radius, is only 0.529 Å [114]. This enables hydrogen to readily enter metal lattices, especially for loosely packed body-centered cubic (BCC) metals like refractory CCAs with a packing density of 68% [40, 193, 194]. This feature facilitates hydrogen diffusion and interaction with host metallic atoms in bulk materials. Additionally, the medium electronegativity of hydrogen (2.2) allows it to form various kinds of chemical bonds (ionic bond and covalent bond) with metallic elements [114, 195]. Hydrogen has long been treated as a detrimental element for structural materials, which can cause catastrophic failure of metallic components, known as hydrogen embrittlement [196-198]. On the other hand, hydrogen forms metal hydrides with several alkali (*e.g.*, Li, Na, K), alkaline earth (*e.g.*, Mg), and refractory (*e.g.*, Ti, Zr, Hf) metals via the reversible phase transformation, which is the basis of hydrogen storage materials [57, 199, 200]. Therefore, a better understanding of the interaction between hydrogen and constituent metallic elements in refractory CCAs is essential for optimizing their composition and microstructure suited for applications in hydrogen-rich environments as structural materials or hydrogen storage.

In this study, nanoscale spinodal decomposition is observed in an equiatomic TiNbZrHfTa CCA upon exposure to H_2 at 500 °C for 0.5 h, resulting in two phases enriched in Ti/Zr and Nb/Ta, respectively. A statistical thermodynamic model incorporating hydrogen has been developed to elucidate the mechanisms of such hydrogen-assisted spinodal decomposition. The hydrogen acquired from the environment expands the spinodal region of TiNbZrHfTa CCAs, thus promoting spinodal decomposition. Our findings highlight the significant role of hydrogen in altering the thermodynamic boundaries by expanding the spinodal decomposition region in the TiNbZrHfTa alloy. The spinodal features improve the hardness and wear resistance. This study provides a novel strategy for designing spinodal-strengthed refractory CCAs by deploying acquired hydrogen from the environment to modify the thermodynamic conditions of the alloy system and modulate local chemical and structural patterns at the nanoscale.

4.2. Materials and methods

4.2.1. Material fabrications

The five-component TiNbZrHfTa compositionally complex alloy (CCA) with an equiatomic ratio was fabricated using the corresponding pure metals with a purity of 99.95 wt.% by arc melting under an Ar atmosphere. To ensure the homogeneity of the constituent elements, the ingots were remelted at least five times during the arc-melting process. A piece of Ti getter was placed in the arc melter to avoid potential oxygen contamination. The as-cast material was cold-rolled down to ~1.2 mm with a thickness reduction of 80%. Subsequently, the material was annealed at 1100 °C for 5 h in a He-filled quartz tube, followed by forced cooling outside the furnace (air quenching), which was referred to as the as-received state in this study. The as-received specimens were exposed to pure H_2 gas with a purity of 99.999% in a thermal dilatometer (DIL 805A/D, TA Instruments, USA). Before the exposure to H_2 gas, the DIL chamber was evacuated by a vacuum pump to a pressure below 10^{-6} bar. Then H_2 gas was introduced into the DIL chamber up to 0.8 bar. The specimens were heated with the induction coil to 500 °C with a heating rate of 20 °C/min. The isothermal treatments were conducted for 0.5 h, 1 h, and 2 h, followed by furnace cooling. The corresponding samples were referred to as HT-H_2, HT-H_2-1h, and HT-H_2-2h, respectively. In addition, a reference specimen was exposed to pure Ar (99.999% purity) at 500 °C for 0.5 h, referred to as HT-Ar sample.

4.2.2. Material characterizations

The dissolved hydrogen and oxygen contents of the as-received, HT-Ar and HT-H_2 specimens were determined by a melt extraction method using the GALILEO G8 ONH (Bruker, Germany) equipment. The measurements were performed immediately after heat treatment with a transferring time shorter than 12 h. The specimen surfaces were ground with 1000-grit SiC paper to eliminate the surficial oxide layer during sample transfer. Measurements were conducted at a power of 35%, using tin baskets as the carrier. A thermal conductivity detector was employed to detect the hydrogen and oxygen contents, and helium was used as the carrying gas.

To identify crystal structures and quantify phase compositions, synchrotron high-energy X-ray diffraction (HEXRD) experiments were performed at the Powder Diffraction and Total Scattering Beamline, P02.1, of PETRA III at Deutsches Elektronen-Synchrotron (DESY, Hamburg). HEXRD profiles were acquired with a fixed beam energy of 60 keV ($\lambda = 0.207354$ Å) and processed with the aid of the GASA-II software [76].

The microstructures of the as-received and heat-treated samples were characterized by backscattered electron (BSE) imaging, energy dispersive X-ray spectroscopy (EDS), and electron backscatter diffraction (EBSD) techniques using a Zeiss Merlin scanning electron microscope (SEM). Specimens for SEM characterization were mechanically ground (from 400 to 4000 grits of SiC papers) and polished with 30 vol.% H_2O_2-contained colloidal silica suspension solution until a mirror-finish surface was obtained. EBSD data was acquired at an acceleration voltage of 15 kV with a step size of 0.1 μm. The datasets were analyzed using the software OIM Analysis^{TM} V8.0.

The nanoscale structures were further characterized using an image-corrected transmission electron microscopy (TEM, Titan Themis G2 300). The TEM specimens were prepared by the focused ion beam (FIB) lift-out method using the FEI Helios NanoLab 600i dual-beam FIB/SEM instrument. The TEM images were acquired at an acceleration voltage of 300 kV along the [001] zone axis. The local strain map was obtained from geometric phase analysis (GPA) using the open-source program Strain++ [201]. Atom probe tomography (APT, CAMECA LEAP 5000XR) was employed to investigate the elemental distribution at a near-atomic scale. The sharp-tip specimens were prepared by lift-out and annular milling procedures using the FIB. All the APT measurements were conducted under laser mode with a base temperature, laser energy, pulse rate, and detection rate of 70 K, 60 pJ, 100 kHz, and 0.5%, respectively. The reconstruction of the 3D atom maps and data analysis was conducted using the commercial software AP Suite 6.1.

4.2.3. Microhardness and scratch tests

The Vickers hardness measurements were performed using Zwick Roell ZHV 10 hardness testing machine with a load of 0.2 kg. A minimum of 6 indents were collected for each specimen, and the data was shown as the mean Vicker hardness values (HV0.2) plus the standard deviation. The wear behavior was evaluated in the Keysight G200 nanoindenter using a 5-µm-radius spherical diamond tip. The scratch tests were conducted with a constant load of 20 mN in ambient air and a wear velocity of 1 µm/s. The depth of the scratch was characterized using the same diamond tip with a force of 0.1 mN before and after scratch tests, while the surface topography was captured using white-light confocal microscopy.

4.3. Results

4.3.1. Hydrogen-assisted spinodal decomposition

The as-received TiNbZrHfTa sample reveals a single BCC phase with a lattice parameter of 3.406 Å, as suggested by the high-energy X-ray diffraction (HEXRD) profile (**Fig. 4.1**a). Upon the heat treatment in H_2 atmosphere at 500 °C for 0.5 h, a large amount of hydrogen is absorbed by the TiNbZrHfTa CCA (hereafter, referred to as HT-H_2 sample), which was quantified to be 8.60±0.41 at.% by TDS analysis. This content surpasses those in the as-received and Ar-treated samples (HT-Ar) by a factor of 19 and 8, respectively (**Table S4.1** and **Fig. S4.1**). The HEXRD measurements suggest that the HT-H_2 sample maintains a BCC crystal structure and no formation of hydride is observed in **Fig. 4.1**a. These facts are supposed to be due to the high solubility of hydrogen in these principal elements (54.55 at.% for β-Zr) [165]. Nevertheless, the diffraction peaks of the HT-H_2 sample shift to lower Bragg angles and become asymmetric (**Fig. 4.1**b). Such peak shift indicates an increase in the lattice parameter, and peak asymmetry suggests that two BCC phases possibly co-exist with different lattice parameters. For instance, the (211) peak can be deconvoluted into two peaks (**Fig. 4.1**c and d). From the Rietveld refinement on the full HEXRD profile, the BCC Phase 1 with a lattice parameter of 3.414 Å (a_1) accounts for 56.0 wt.%, and the fraction of BCC Phase 2 with a lattice parameter of 3.398 Å (a_2) is 44.0 wt.%.

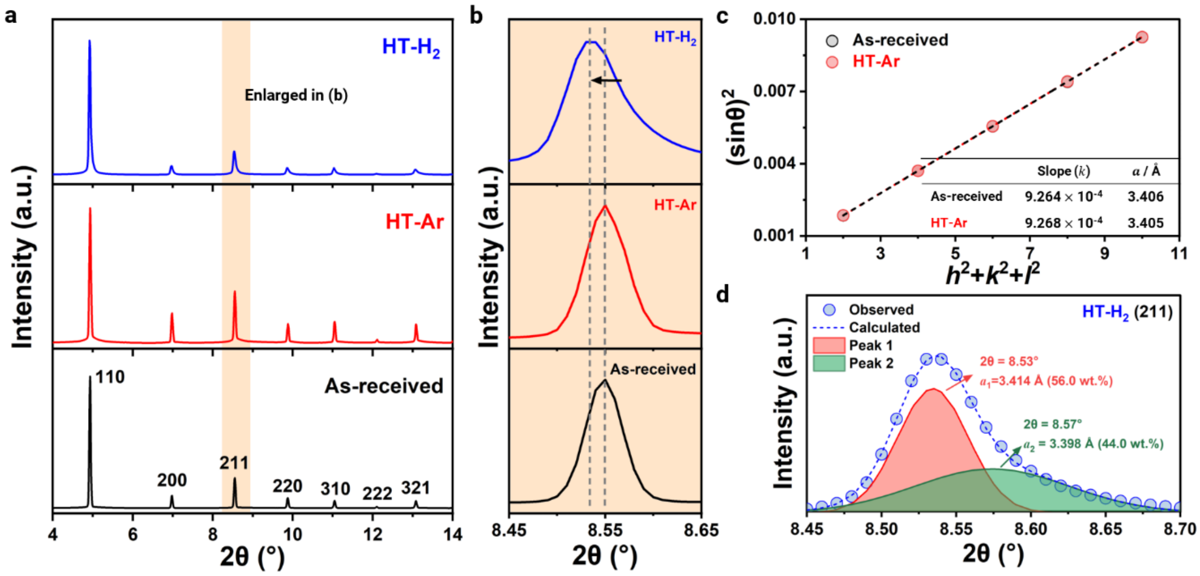

Fig. 4.1 (a) Overall high-energy X-ray diffraction (HEXRD) profiles and (b) enlarged view of BCC_{211} peaks of the as-received, HT-Ar, and HT-H_2 specimens. (c) The plot of $(\sin\theta)^2$ as a function of $(h^2+k^2+l^2)$ of individual HEXRD peaks to determine the lattice parameters of the As-received and HT-Ar samples. (d) Enlarged image showing the deconvolution of BCC_{211} peaks of the HT-H_2 specimen.

Microstructures were further evaluated by coupling BSE and EBSD analyses (**Fig. 4.2**a-c and **Fig. S4.2**). The as-received sample shows an equiaxed grain morphology (**Fig. 4.2**a) with a grain size of 78.79±27.40 μm (**Fig. S4.2**g). The inverse pole figure reveals that grains are randomly oriented and high-angle grain boundaries (>15°) constitute the major type of interfaces (>80%, **Fig. S4.2**a and b), suggesting complete recrystallization of the as-received sample. After heat treatment in H_2 and Ar gases, the HT-H_2 and HT-Ar samples maintain identical microstructural features compared to the as-received sample, in terms of grain morphology, size, and crystallographic orientation (**Fig. 4.2**a-c and **Fig. S4.2**). EDS elemental mapping across multiple grains confirms a spatially uniform distribution of all five constituent elements at the microscopic scale in all three samples (**Fig. S4.3**), and the bulk composition is determined to be $Ti_{22.95}Nb_{18.93}Zr_{20.89}Hf_{18.22}Ta_{19.01}$ (in at.%). These findings imply that heat treatment under both H_2 and Ar atmospheres has a negligible impact on structure and composition at the microscopic scale.

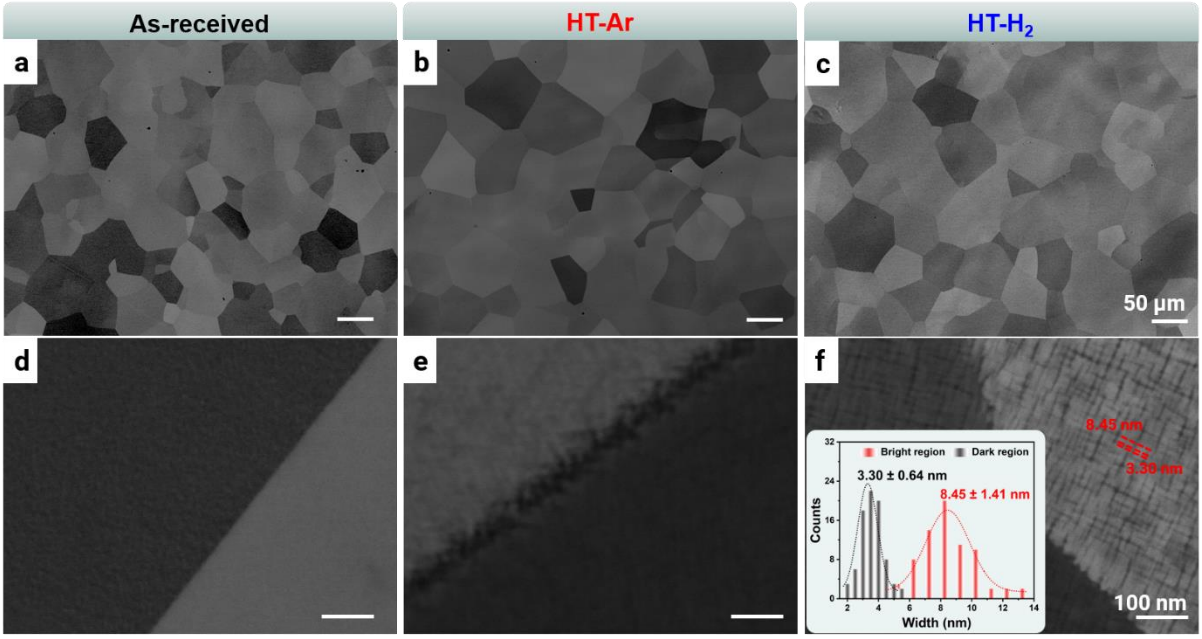

Fig. 4.2 Backscattered electron (BSE) and representative enlarged images of (a, d) As-received, (b, e) HT-Ar, and (c, f) HT-H_2 samples, respectively. Insert in (f) shows the width distribution of the region with dark (black) and bright (red) contrast.

At a higher magnification down to the nanometer scale, two distinct regions are identified in a modulated pattern in the sample treated in the H_2 atmosphere, as observed in terms of dark and bright contrast, respectively, in **Fig. 4.2**f. The dark regions with a width of 3.30±0.64 nm are homogeneously distributed and intersect at an angle of approximately 90°. The bright features with a width of 8.45±1.41 nm interwoven with the dark regions. Such an interwoven pattern was also observed using TEM, as shown in the bright-field image (**Fig. 4.3**a). The width of the bright and dark regions are quantified to be 3.56 nm and 7.97 nm, respectively, which concur well with the SEM observations (**Fig. 4.2**f). These interwoven structures are crystallographically aligned along the <100> directions, as determined by TEM analysis. Such an orientation dependence minimizes elastic strain energy in the TiNbZrHfTa alloy (see Supplementary Note 4.1) [202, 203]. The selected area electron diffraction in 12b also reveals a BCC crystal structure of the HT-H_2 sample and no secondary crystal structure is observed, being consistent with the HEXRD results. Thus, the contrast in **Fig. 4.2**f and **Fig. 4.3**a is primarily attributed to the inhomogeneous elemental distribution, as particularly the backscattered electron signal is sensitive to chemistry.

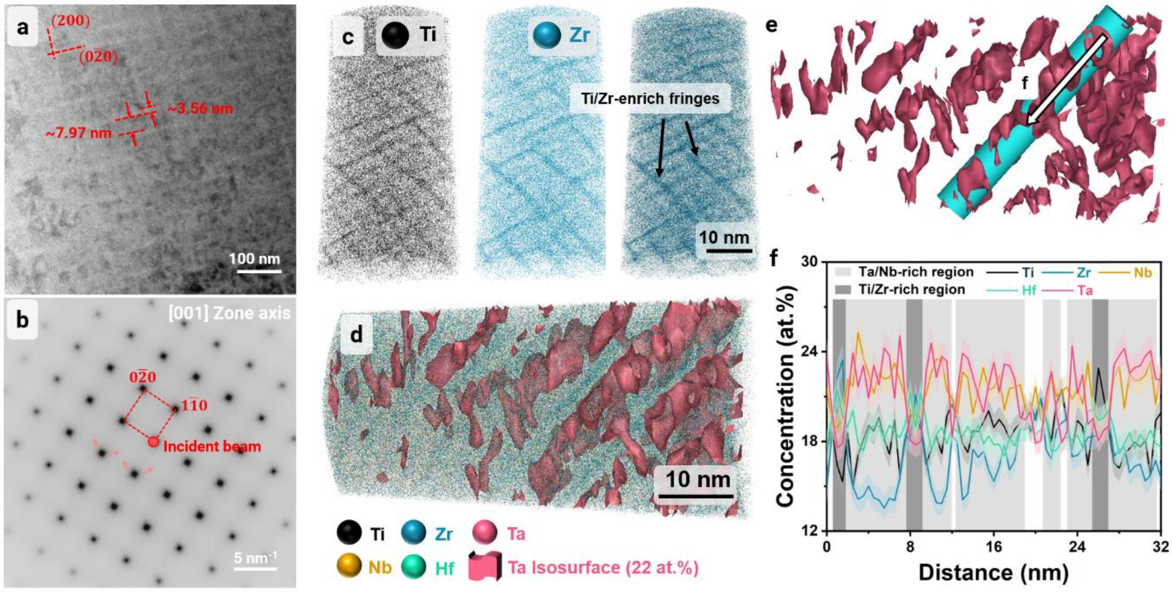

Fig. 4.3 (a) Typical bright-field transmission electron microscopy (TEM) image, and corresponding (b) selected area electron diffraction pattern exhibiting a single BCC phase. The electron beam is along the [001] zone axis. Three-dimensional reconstruction map of (c) Ti distribution, Zr distribution, and superimposed Ti and Zr distribution probed by atom probe tomography (APT). (d, e) APT maps showing the Ta-rich nanofeatures in the matrix. The Ta-rich nanofeatures are highlighted using iso-concentration surfaces containing 22 at.% Ta. (f) 1D concentration profiles computed along the cyan cylinder marked in (e) with a binning size of 0.5 nm. The error bar represents the standard deviation of the counting statistics in each bin.

To further assess the elemental distribution in the HT-H_2 sample, we employed APT, which allows for local chemical analysis down to near-atomic resolution. The overall composition of the HT-H_2 specimens is determined to be $Ti_{19.66\pm0.91}Nb_{21.02\pm0.91}Zr_{19.05\pm0.90}Hf_{19.05\pm0.06}Ta_{19.45\pm0.33}$ (in at.%) by averaging the composition of three APT tips, agreeing with the nominal bulk composition. The three-dimensional elemental distribution maps, *e.g.*, Ti and Zr maps (**Fig. 4.3**c), reveal a nano-structured interwoven pattern, similar to that observed in the BSE and TEM images. Two regions are distinguished by the periodic chemical modulation. A needle-shaped region with an average width of ~3.0 nm is enriched in Ti (21.34±0.73 at.%) and Zr (22.88±0.82 at.%), yet depleted in Ta (17.72±1.56 at.%) and Nb (19.20±0.33 at.%) as shown in **Fig. 4.3**c and f. The other region, marked by the iso-concentration surface of 22 at.% Ta (**Fig. 4.3**d), is depleted in Ti (16.86±0.78 at.%) and Zr (14.41±0.59 at.%), while it is enriched in Ta (23.85±1.46 at.%) and Nb (23.10±1.15 at.%). The average width of this Ta/Nb-rich region is about 8.0 nm. Such a nano-scale elemental separation is primarily attributed to the relatively low quantity of mixing enthalpy between Ti and Zr as well as Nb and Ta [35]. In comparison, the periodically modulated chemical pattern is not observed in the APT tips of the as-received and HT-Ar specimens (**Fig. 4.4**), where all five principal elements are homogeneously distributed in the whole tips. Moreover, the clustering behavior in the HT-H_2

sample is confirmed by the nearest neighboring distribution, describing the probability of another Ti atom existing within some distance of a Ti atom [204-206]. As shown in **Fig. 4.4**e-g, the experimental line of the HT-H_2 sample does not match well with the calculated line that indicates the random distribution of Ti atoms, suggesting the clustering of Ti atoms. Similar trends can be obtained from the μ values extracted from the APT datasets (**Fig. S4.4**). μ value reflects the local clustering of the principle element, where it is indicative of element clustering when μ closes to 1, while it means random distortion of elements when μ closes to 0 [207, 208]. The μ values for each principle element of the HT-H_2 specimen are larger than those of the other two specimens, suggesting the clustering and redistribution of elements in the HT-H_2 sample.

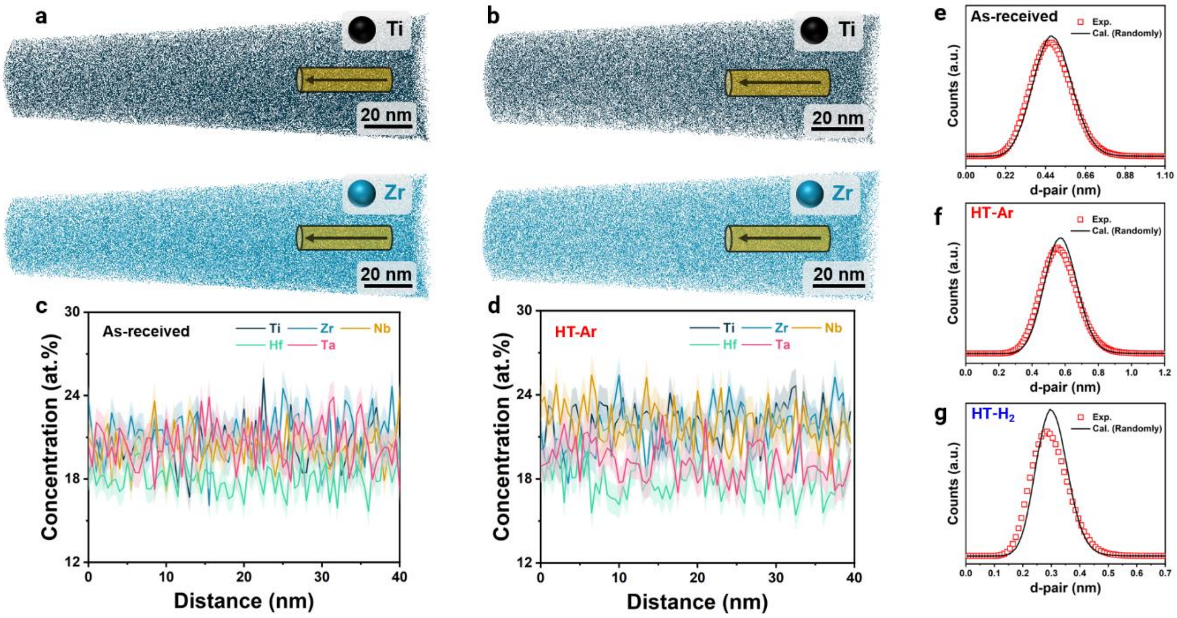

Fig. 4.4 Three-dimensional APT maps of the distribution of Ti and Zr in (a) as-received specimen and (b) HT-Ar specimen. Concentration profiles of principal elements along the yellow cylinders in (c) as-received specimen and (d) HT-Ar specimen, respectively. The fifth nearest neighboring distribution (NND) of Ti atoms of (e) as-received, (f) HT-Ar, and (g) HT-H_2 specimens, respectively.

Based on the above results, the original BCC matrix decomposed into two BCC phases with distinctive lattice parameters (a_1 and a_2) and constituent elements (enriched in Ti/Zr and Nb/Ta) is revealed after heat treatment under H_2. The process of this decomposition can proceed either via a nucleation and subsequent growth pathway or by a spontaneous spinodal decomposition without nucleation [28]. The nuclei for the nucleation pathway are formed with an equilibrium concentration (or deviate from the tie-line concentration for the case of a multicomponent system) in the initial state, maintaining this concentration (or evolving towards the equilibrium concentration) throughout the coarsening process [12, 28, 209, 210]. In such cases, a sharp change in local concentration can be anticipated. In contrast, the spinodal decomposition amplifies with time, and the local concentration gradually deviates from the initial concentration until the equilibrium concentration is attained [4]. Thus, the amplifications of local composition over time (0.5, 1, 2 h) for heat treatment in H_2 are investigated to elucidate the decomposition process in the present TiNbZrHfTa CCA. The characteristic uphill diffusion behavior of elements over time rationalizes a spinodal decomposition process, rendering the periodically modulated chemical pattern of the TiNbZrHfTa alloy treated in the H_2 atmosphere (**Fig. 4.5**). While the alloy maintains a BCC crystal structure (**Fig. S4.5**), an interwoven chemical pattern gradually develops with prolonged treatment durations. As exemplified by the Zr concentration profile, Zr concentration increases over time (0.5, 1, 2 h) in the needle-shaped region from 21.70 at.% at 0.5 h, to 27.07 at.% at 1 h, and reaching 34.39 at.% at 2 h (**Fig. 4.5**d). Such an uphill diffusion behavior and the iso-structure of the Ti/Zr-rich and Ta/Nb-rich regions (*i.e.*, both in BCC crystal structure with coherent interface) characterize a spinodal decomposition pathway [12, 28, 211]. An increase in the wavelength of the spinodal decomposition over annealing time under H_2 is observed, evolving from the initial range of 4.21±0.19 nm (0.5 h) to 9.17±0.90 nm and 11.21±0.45 nm for the HT-H_2-1h and HT-H_2-2h specimens, respectively (**Fig. 4.5**e and **Fig. S4.6**) [212, 213]. Such a hydrogen-assisted phase decomposition phenomenon has not been reported in the literature. Its underlying mechanism will be discussed in the **Discussion Section**.

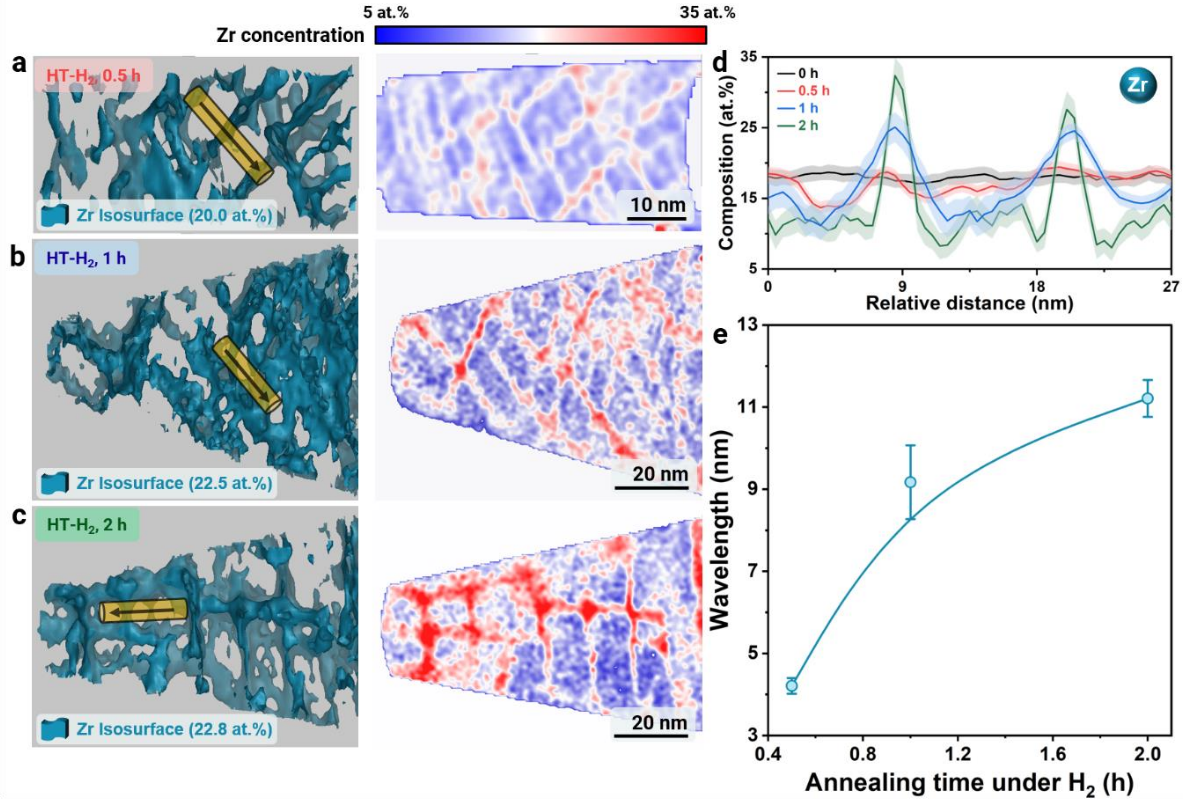

Fig. 4.5 APT reconstruction of Zr iso-concentration surfaces of the specimens treated in H_2 for (a) 0.5 h, (b) 1 h, and (c) 2 h and the corresponding 2D contour plots. (d) 1D concentration profiles of Zr along the yellow cylinders marked in (a-c), the error bar represents the standard deviation of the counting statistics in each bin of the cylinder. (e) Evolution of spinodal wavelength with annealing time under H_2.

4.3.2. Enhance in hardness and wear resistance via hydrogen-assisted spinodal decomposition

The hydrogen-assisted spinodal composition results in confined nanostructuring, associated with the generation of a periodic strain field (**Fig. 4.6**a and b). The crystal lattices of two isostructural phases possess slightly different lattice parameters ($\Delta = 0.007$ nm), due to the different atomic radii of Zr (0.155 nm) than that of Nb (0.145 nm) and Ta (0.145 nm) [214]. Thus, the coherent interface of the periodic isostructural phases is characterized by a subtle strain misfit of ~0.2% (**Fig. 4.6**b). Such a feature is attractive in enhancing mechanical properties [52, 215].

The micro Vickers hardness of the TiNbZrHfTa alloy is shown in **Fig. 4.6**c. The hardness values are similar for the as-received (312.10±5.03 HV0.2) and the HT-Ar (301.00±28.43 HV0.2) specimens. In contrast, the heat treatment in the H_2 atmosphere (HT-H_2) increases the hardness by ~91 HV0.2 to 401.83±27.92 HV0.2. Hydrogen is considered as a strengthening element in Ti alloys mainly due to its solid solution strengthening effect, and the occurrence of hydrogen-induced secondary phase formation [216-218]. For solid solution strengthening, the increment in yield strength (σ) is proportional to the hydrogen concentration ($\Delta\sigma \propto \sqrt{c_H}$, c_H is the H concentration). In addition, hydrogen will increase the lattice strain (ϵ), thus leading to larger lattice distortions which enhance the friction stress in the material [219]. In our case, the hydrogen concentration inside the alloy drops down to 108 ppm before the hardness measurement (one week after hydrogen charging) due to the high hydrogen diffusivity (~10^{-10} m^2/s for β-Ti) [220]. The HEXRD results shown in **Fig. 4.1** exhibit no significant change in lattice parameters between the HT-H_2 and the as-received specimen states. These results suggest that the solid solution strengthening effect from hydrogen is negligible in this specific case. Additionally, from our experimental results (**Fig. 4.1** and **Fig. 4.2**a), besides spinodal phases, no other secondary phases can be detected. Therefore, the enhanced hardness is supposed to be predominantly ascributed to the hydrogen-assisted spinodal decomposition effect. The strengthening effect of the spinodal features can be derived from both lattice misfit strengthening and modulus strengthening based on Kato's model [221]:

$$\Delta\sigma = \frac{A\kappa Y}{2} + \frac{0.65\Delta G b}{\lambda} \tag{4.1}$$

where A stands for the amplitude of composition modulation (A = 0.08, **Fig. 4.3**f), κ for the variation in lattice constant (κ = 0.063, **Fig. 4.1**d) with respect to the composition fluctuation, $Y = {(C_{11} + 2C_{12})(C_{11} - C_{12})}/{C_{11}}$ is related to the elastic constant C_{ij} [215], (Y = 55.7 GPa based on literature data [222]), and ΔG stands for the amplitude of the shear modulus fluctuation (ΔG = 3.1 GPa), b for Burgers vector ($b = 2.942 \times 10^{-10}$ m determined from **Fig. 4.1**a) and λ is referred to the wavelength of modulation ($\lambda = 4.2 \times 10^{-9}$ m, **Fig. 4.5**e). Thus, the spinodal decomposition predominantly yields a misfit strengthening effect of ~140 MPa and a modulus strengthening effect of ~141 MPa, resulting in a total increase in strength ($\Delta\sigma$) of ~281 MPa. Using a conversion factor between hardness and yield strength of $\Delta HV0.2 \approx 3 \cdot \Delta\sigma$ [223, 224], an increment in hardness is thus predicted to be 84.3 HV0.2. The measured value of the hardness increased by 91 HV0.2 agrees well with this predicted value. Moreover, the hardness is further enhanced with prolonged heat treatment in H_2 associated with the intensified composition fluctuation (**Fig. 4.6**d).

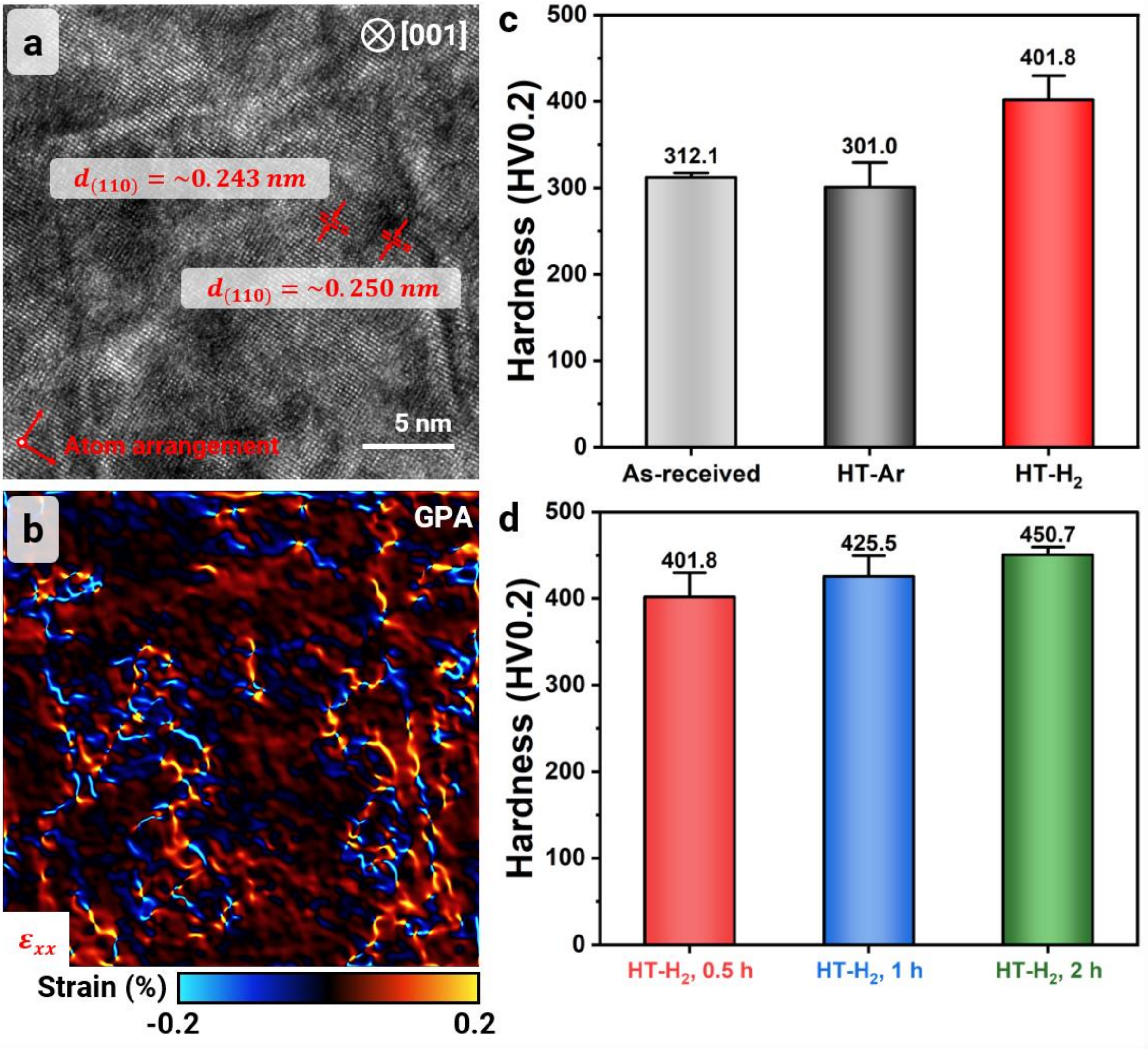

Fig. 4.6 (a) Image-corrected high-resolution transmission electron microscopy (HR-TEM) image of the HT-H$_2$ specimen along [001] zone axis. (b) Map of strain distribution (ε_{xx}) of the HT-H$_2$ specimen determined by geometric phase analysis (GPA) of HR-TEM image from the same area in (a). (c) Hardness (HV0.2) of as-received, HT-Ar, and HT-H$_2$ specimens after the heat treatment (hardness measurements were conducted one week after the heat treatment). (d) Hardness (HV0.2) evolution of specimens treated in H$_2$ at 500 °C for 0.5 h (HT-H$_2$), 1 h (HT-H$_2$-1h), and 2 h (HT-H$_2$-2h).

The wear behavior of the as-received and HT-H$_2$-2h samples was also studied by scratch tests. As revealed by the three-dimensional morphology of the wear surfaces using confocal microscopy (Fig. 4.7a-c), the HT-H$_2$-2h sample reveals a narrow (2.38 μm in width) and shallow (210 nm in depth) wear track, which is profoundly different from the wide (3.54 μm) and deep (278 nm) wear track of the as-received sample. A much higher steady-state friction coefficient of 14.23±0.58 is detected for the HT-H$_2$-2h sample compared with that of the as-received sample (1.66±0.42, Fig. 4.7d), which is primarily attributed to the spinodal decomposition [225, 226]. It is worth noting that such a higher steady-state coefficient for the

$HT-H_2-2h$ sample is independent of crystallographic orientation (Fig. 4.7e). Moreover, yield strength and plastic properties are evaluated based on scratch tests (see Supplementary Note 4.2) [227, 228]. Compared with the estimated yielding strength of the as-received sample (929 MPa), an increase in yield strength by 401 MPa is observed in the $HT-H_2-2h$ sample. Additionally, the $HT-H_2-2h$ sample possesses a higher strain hardening exponent of 0.153 than that of the as-received sample of 0.146. Such a higher strain hardening exponent implies a stronger work-hardening effect in the $HT-H_2-2h$ sample. These two examples (*i.e.,* enhancement in hardness and wear resistance) demonstrate that the hydrogen-assisted spinodal decomposition is an effective tool to tailor the mechanical properties of TiNbZrHfTa CCAs.

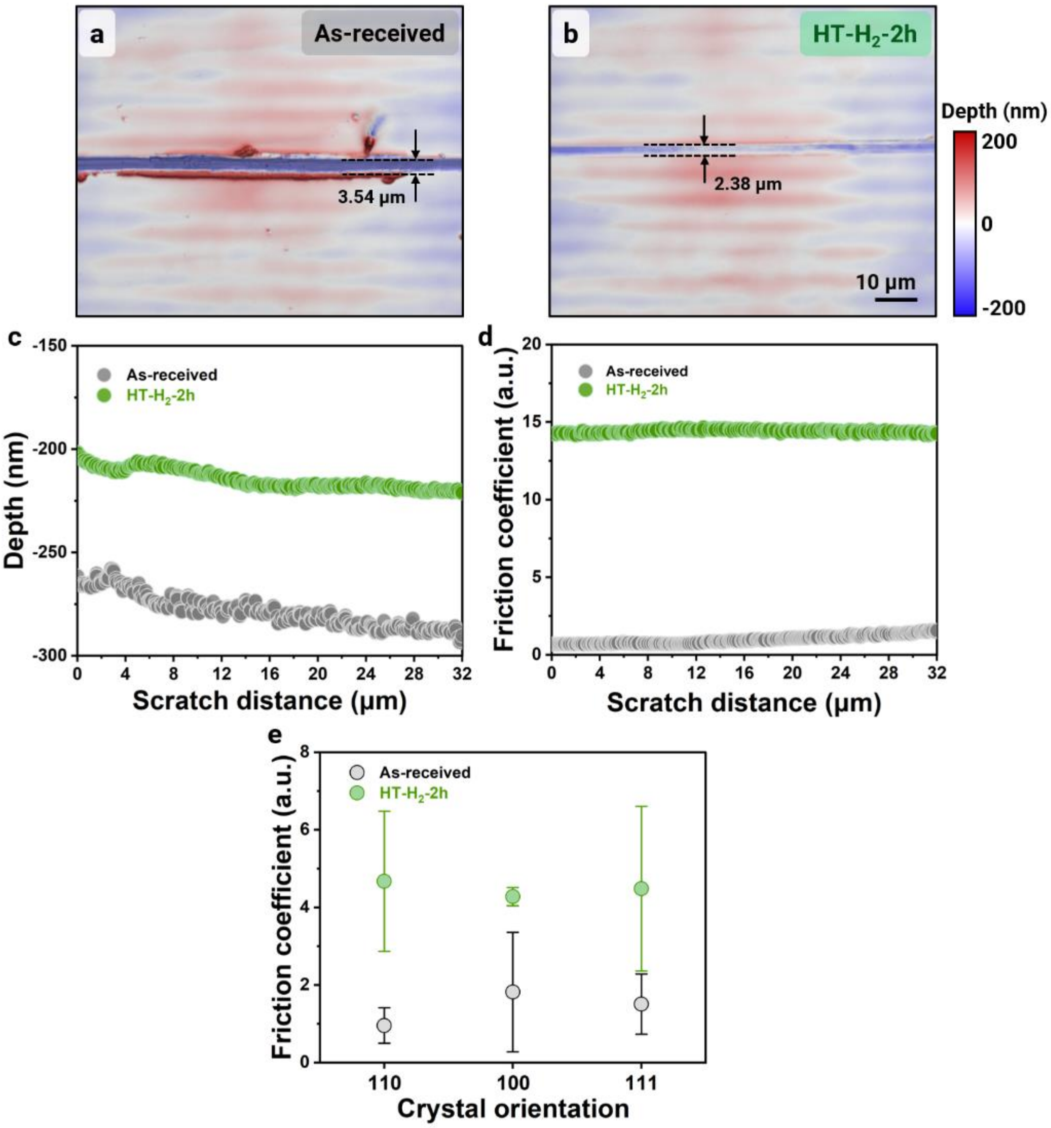

Fig. 4.7 Three-dimensional profiles of the wear surface of (a) the as-received and (b) $HT-H_2-2h$ samples. (c) The corresponding two-dimensional cross-sectional depth profiles and (d) friction coefficients as a function of the scratch distance. (e) Averaged friction coefficients of the as-received and $HT-H_2-2h$ samples, primarily from the (110), (100), and (111) crystallographic planes.

4.4. Discussion

The preferential spinodal decomposition in specimens treated in a hydrogen atmosphere poses one intriguing question regarding the role of hydrogen in this phase decomposition process. To unravel the underlying mechanisms of hydrogen-assisted spinodal decomposition, we next assess the role of hydrogen from both the thermodynamic and kinetic perspectives. Thermodynamically, Gibbs free energy was calculated by adopting a sub-regular solution model considering the chemical complexity of the present system (see Supplementary Note 4.3) [4, 229]:

$$G = G^{id} + G^{\mathrm{ex}} \tag{4.2}$$

where, G^{id} and G^{ex} represent the ideal Gibbs free energy and excess Gibbs free energy, respectively. Here, G^{id} takes the form of a weighted average of all the alloying elements:

$$G^{id} = \sum_{i} x_i G_i \tag{4.3}$$

where, x_i and G_i are referred to as the atomic percentage of i element in the alloy system including hydrogen (which satisfies $\sum_i x_i = 1$) and the corresponding ideal Gibbs free energy respectively. For the sake of simplicity, we assume $x_{Zr} = x_{Ti} = x_{Hf}$, and $x_{Ta} = x_{Nb}$, according to the elemental separation tendency. For hydrogen, its content (x_H) is fixed either 0 at.% (for as-received condition) or a constant of 8.60 at.% (for HT-H_2 condition), consistent with the total hydrogen content measured by TDS in the HT-H_2 sample. The G^{ex} is the excess Gibbs free energy contribution due to the mutual interaction of binary, ternary, quaternary, and quinary elements as well as the senary interactive contribution:

$$G^{\mathrm{ex}} = G^{ex}_{binary} + G^{ex}_{ternary} + G^{ex}_{quaternary} + G^{ex}_{quinary} + G^{ex}_{\mathrm{senary}} \tag{4}$$

To avoid redundancy in the main text, the analytical details regarding the calculation of Gibbs free energy as well as the corresponding interaction parameters are all summarized in Supplementary Note 4.3. As illustrated in the Gibbs free energy landscape as a function of Zr composition (**Fig. 4.8**a and b), the incorporation of hydrogen into the alloy changes the free energy landscape of the TiNbZrHfTa alloy, revealing a characteristic double-well potential with a region of negative curvature in between the local free energy minima, which are delineated by the chemical spinodal points $\partial^2 G/\partial x^2 = 0$. The equiatomic TiNbZrHfTa composition falls in between the spinodal point. Moreover, the eigenvalues (λ_1) of the Hessian matrix were calculated to assess the extent of the thermodynamic effect of hydrogen on spinodal decomposition in this multicomponent alloy system (**Fig. 4.8**c) [230]. A positive λ_1 indicates a stable configuration, while the phase instability is reflected by a negative λ_1. The results suggest that spinodal decomposition can occur in the TiNbZrHfTa alloy system without the presence of hydrogen below the critical temperature point (~500 °C), implying that the single BCC phase is unstable. A single solid solution is prone to be stabilized by the entropy effect at high temperatures, while it becomes unstable at low temperatures, decomposing into multiple phases [189, 231, 232]. The stability of a solid solution with multiple elements, particularly those exceeding three, remains a topic of ongoing debate [231, 232]. The stability of the initial TiNbZrHfTa alloy system is not the main topic in this study. We, however, note that the addition of hydrogen expands the spinodal region to a high-temperature region, with a critical temperature of 570 °C. The lower λ_1 value with the incorporation of hydrogen (**Fig. 4.8**c) suggests a larger driving force for spinodal decomposition as compared with the TiNbZrHfTa alloy system. Thus, spinodal decomposition is prone to occur at 500 °C in the TiNbZrHfTa alloy system in the presence of hydrogen, supporting the experimental observations. Such a change in the spinodal region can also be triggered by a small amount of other interstitials, for instance, 2 at.% of oxygen can control the formation of the spinodal structure by influencing the spinodal gap of the Ti-V-Hf-Nb system [52].

Hydrogen, in this regard, contributes saliently to the activation of spinodal decomposition from a thermodynamic perspective by expanding the spinodal region. This is probably ascribed to the intensively negative mixing enthalpy between hydrogen and the principal elements (<-40 kJ/mol) [35]. The more negative mixing enthalpy of Zr-H (ΔH_{ZrH}^{mix} = -69 kJ/mol) and Ti-H (ΔH_{TiH}^{mix} = -54 kJ/mol) pairs as compared with that of Nb-H (ΔH_{NbH}^{mix} = -46 kJ/mol) and Ta-H (ΔH_{TaH}^{mix} = -46 kJ/mol) pairs predominantly drives the separation between Zr/Ti and Nb/Ta [35]. These results suggest that hydrogen can result in a significant thermodynamic modification in the TiNbZrHfTa alloy system.

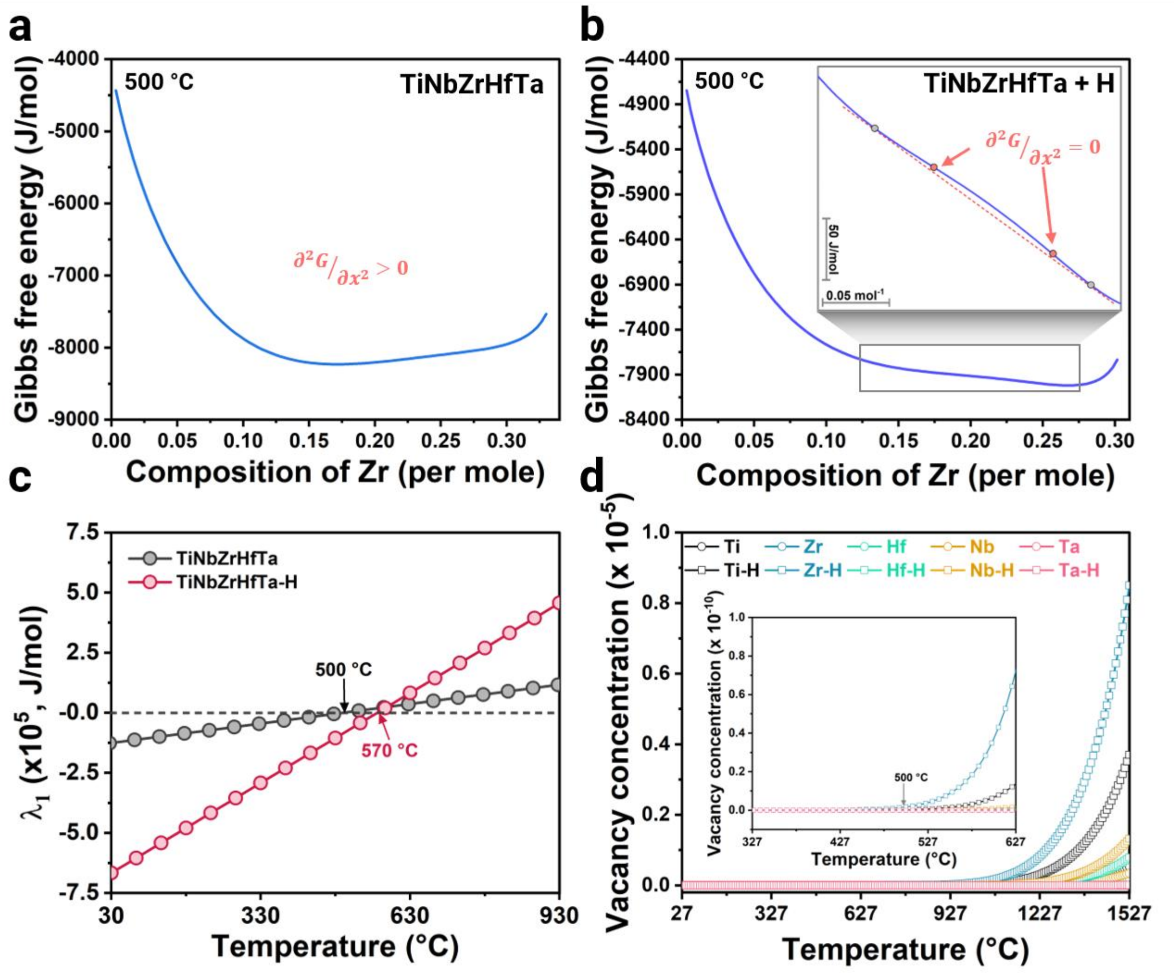

Fig. 4.8 Zr composition dependence of Gibbs free energy in the TiZrHf-NbTa pseudo-binary system (a) without and (b) with the presence of hydrogen. Insert in (b) showing the existence of miscibility gap, indicated by the points where the second derivative of Gibbs free energy with respect to Zr composition is 0. (c) Eigenvalues (λ_1) as a function of temperature for TiNbZrHfTa with and without the incorporation of hydrogen. (d) Calculated vacancy concentration as a function of temperature.

From the kinetic perspective, the introduction of hydrogen increases the vacancy concentration via the reduction of vacancy formation enthalpy, on the one hand, thus facilitating substitutional diffusion via vacancies [233, 234]. On the other hand, the formation of hydrogen-vacancy clusters can significantly impede vacancy migration, leading to opposing effects on diffusion [114, 235, 236]. Since the stagnation in atomic diffusion (*e.g.*, principle elements) does not contribute positively to spinodal decomposition, here we could first focus on the vacancy concentration to evaluate the kinetic effect caused by hydrogen on spinodal decomposition. Therefore, vacancy concentration (C_v^a) was calculated to evaluate the kinetic influence of hydrogen on the activation of spinodal decomposition:

$$C_v^a = \exp\left(-\frac{G_f^v}{kT}\right) \approx \exp\left(-\frac{H_f^v}{kT}\right) \tag{5}$$

where, H_f^v, k, and T denote the formation enthalpy for vacancy, gas constant, and absolute temperature, respectively. The calculation details and corresponding vacancy formation enthalpies of the individual principle elements with and without incorporating hydrogen are summarized in Supplementary Note 4.4 and **Table S4.5**. As seen in **Fig. 4.8**d, there is little difference in vacancy concentration with and without the presence of hydrogen at 500 °C, demonstrating a negligible kinetic effect caused by hydrogen on spinodal decomposition. Thus, the hydrogen-assisted spinodal decomposition is predominantly rationalized by the thermodynamic effect of hydrogen in the TiNbZrHfTa alloy system, which modifies the local thermodynamic landscape of the system and promotes phase separation.

4.5. Conclusions

In summary, we show that hydrogen can be introduced as an effective tool to modify the local thermodynamics in an equimolar TiNbZrHfTa compositional complex alloy at 500 °C, facilitating spinodal decomposition. A periodically modulated chemical pattern forms with a wavelength of ~13 nm and consists of one phase enriched in Ti and Zr and the other enriched in Nb and Ta. The needle-like spinodal features are preferentially aligned along <001> directions, to minimize the elastic strain energy of the system. Such a hydrogen-assisted spinodal decomposition is rationalized by the modification of the local thermodynamic landscape by hydrogen, rendering an expanded spinodal region. Moreover, we exemplarily demonstrate that this hydrogen-assisted spinodal decomposition improves the hardness and wear resistance in the alloy system. Thus, we show here a novel strategy to trigger spinodal decomposition by introducing hydrogen as an acquired alloying element from the heat treatment environment, opening up alternative avenues for designing metastable alloys and improving mechanical properties.

4.6. Supplementary materials

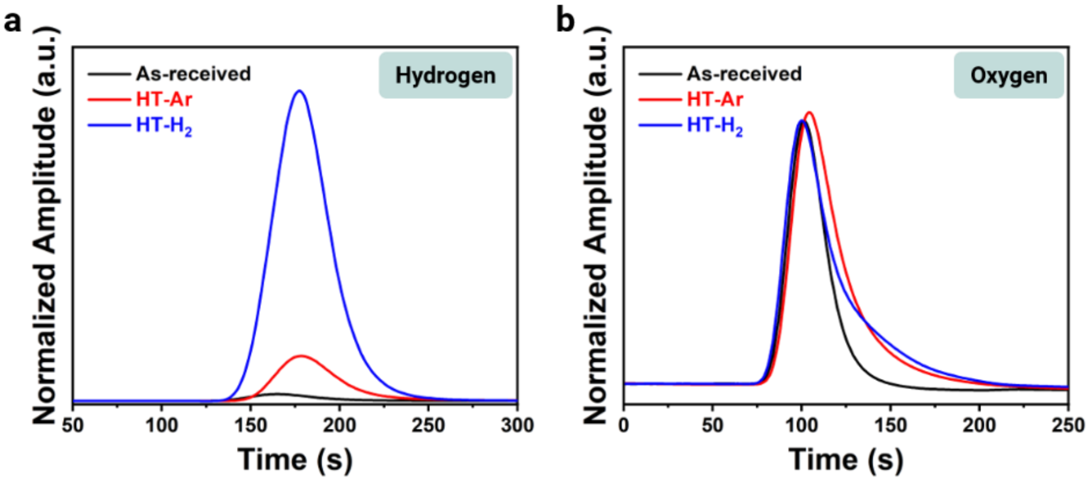

Fig. S4.1 Normalized voltage amplitude when measuring hydrogen (a) and oxygen (b) as a function of time of as-received, HT-Ar, and HT-H_2 samples. Normalization was calculated over the individual weight of samples, Normalized amplitude. = $V_{\mathrm{samples}}/m_{\mathrm{samples}}$, where V_{samples} is the voltage during measurement, and m_{samples} is the weight of the individual measured sample.

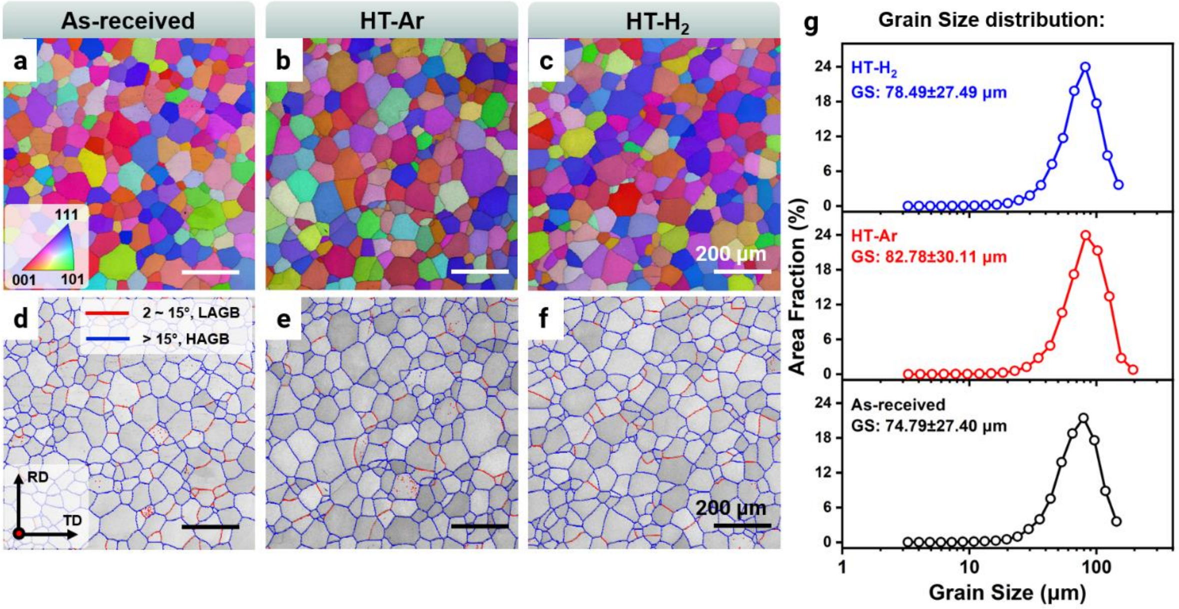
As-received
HT-Ar
HT-H2
a
b
c
111
001
101
200 μm
d
e
f
2 ~ 15°, LAGB
> 15°, HAGB
RD
TD
200 μm
g
Grain Size distribution:
HT-H2
GS: 78.49±27.49 μm
HT-Ar
GS: 82.78±30.11 μm
As-received
GS: 74.79±27.40 μm
Area Fraction (%)
0
6
12
18
24
1
10
100
Grain Size (μm)

Fig. S4.2 (a-c) Inverse pole figure (IPF + IQ) and (d-f) grain boundaries (GB + IQ) overlaid with the image quality of as-received, HT-Ar and HT-H_2 samples probed by the electron backscatter diffraction (EBSD), respectively. (g) Distribution of grain sizes of different samples. The pristine microstructure of TiNbZrHfTa exhibits randomly oriented grains. All the results indicate that heat treatments (500 °C) in pure Ar and H_2 have negligible effects on grain orientation, low / high-angle grain boundary fractions, and grain size.

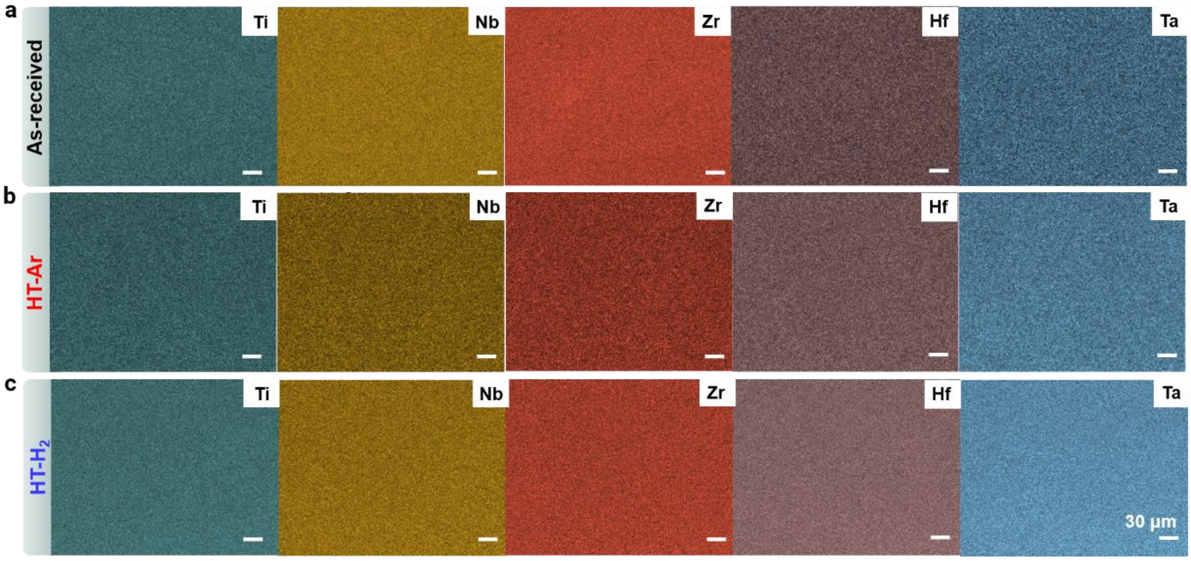

Fig. S4.3 Individual elemental maps of Ti, Nb, Zr, Hf, and Ta of the (a) as-received, (b) HT-Ar, and (HT-H_2) samples probed by electron dispersive spectroscopy (EDS). All of the principal elements are evenly distributed without obvious partitioning or segregation phenomena.

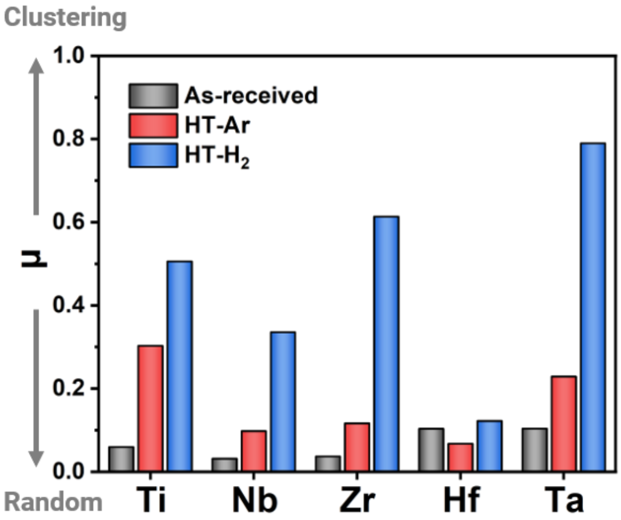

Fig. S4.4 μ values determined from the frequency distribution analysis (FDA)[207] of each principal element in as-received, HT-Ar, and HT-H_2 specimens.

The presence of Ti clustering is verified from the μ values after the normalization of the chi-squared coefficient (χ^2) extracted from the APT dataset. μ value reflects the local clustering of each element, where it is indicative of element clustering when μ closes to 1, while it means random distortion of elements when μ closes to 0 [207, 208]. The μ values for each principle element of the HT-H_2 specimen are larger than those of the other two specimens. Ta exhibits the highest μ value of 0.7899, at least three times larger than those of as-received and HT-Ar specimens (**Table S2**). The discrepancy of the μ value for Zr is even bigger, with a gap of 0.4973 and 0.5677 to HT-Ar and as-received specimens, respectively. Similar trends are also observed for Ti and Nb elements among these three specimens. Hence, all of the principal elements except Hf favorably tend to cluster after heat treatment in H_2.

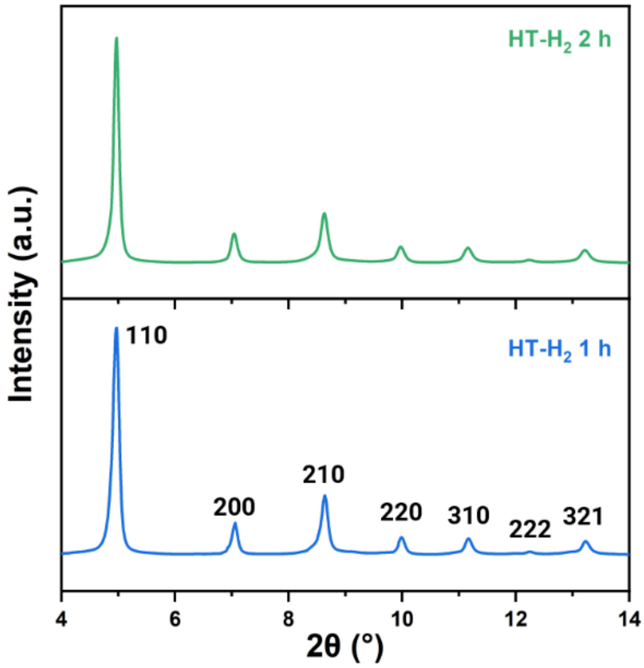

Fig. S4.5 High-energy X-ray diffraction (HEXRD) profiles of specimens after heat treatment in H_2 for 1 h (HT-H_2-1h) and 2 h (HT-H_2-2h). Both two specimens exhibit a single body-centered cubic crystal structure without the formation of secondary phases, such as hydride.

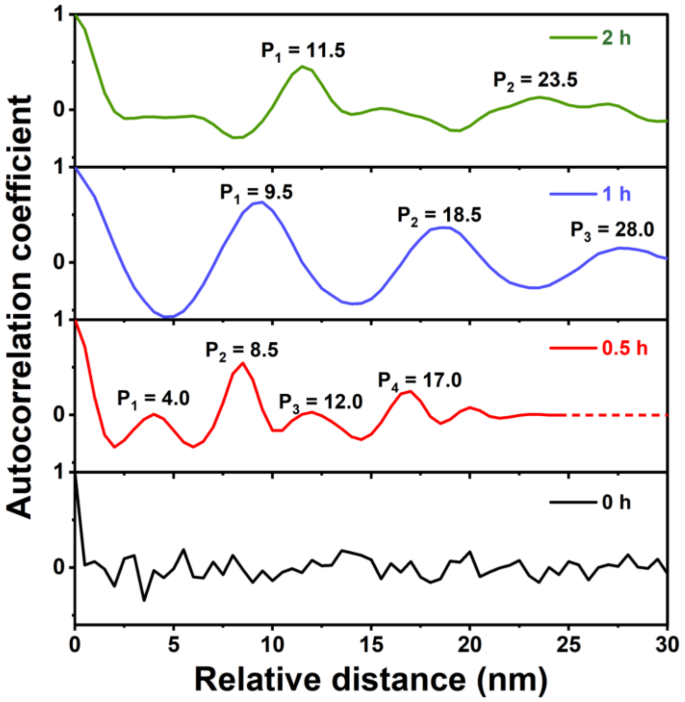

Fig. S4.6 Representative autocorrelation coefficient profiles of Zr for comparison.

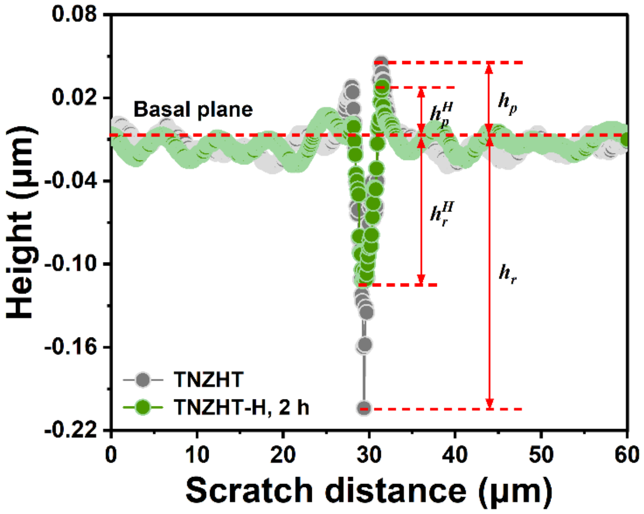

Fig. S4.7 Residual cross-sectional profiles for the as-received TiNbZrHfTa and HT-H_2, 2 h alloys. h_p^H, and h_r^H represent the pile-up height and residual height for the HT-H_2, 2h sample respectively, while h_p and h_r represent the pile-up height and residual height for the as-received TiNbZrHfTa alloy respectively. These values will be used in the calculation for the strain hardening exponent (n) and yield strength (σ_y).

Table S4.1 The hydrogen content and oxygen content measured by thermo desorption spectrometer (TDS) of the as-received, HT-Ar, and HT-H_2 specimens, respectively. Three individual specimens were used for the TDS measurements.

	Hydrogen content (wppm)	Oxygen content (wppm)
As-received	45.32±26.68 (0.45±0.32 at.%)	280.24±50.45 (0.21±0.04 at.%)
HT-Ar	88.96±44.65 (1.03±0.52 at.%)	223.59±37.54 (0.16±0.03 at.%)
HT-H_2	803.07±34.93 (8.60±0.41 at.%)	200.03±54.85 (0.13±0.04 at.%)

Table S4.2 The concentrations and μ values of each principal element of the as-received, HT-Ar, and HT-H_2 specimens, respectively. The concentrations and μ values shown here are calculated from the whole APT tip. The concentrations were analyzed on the basis of three individual tips.

	As-received		HT-Ar		HT-H_2	
Element	Con. (at.%)	μ	Con. (at.%)	μ	Con. (at.%)	μ
Ti	20.32±0.16	0.0595	21.39±0.02	0.3027	19.66±0.91	0.5056
Nb	20.13±0.65	0.0314	21.379±0.32	0.0977	21.02±0.91	0.3354
Zr	20.62±0.29	0.0367	21.20±0.22	0.1161	19.08±0.90	0.6134
Hf	18.76±0.18	0.1032	18.14±0.23	0.0673	19.05±0.06	0.1220
Ta	19.51±0.40	0.1034	17.91±0.11	0.2289	19.46±0.33	0.7899

Note 4.1 The determinization of the orientation dependence of spinodal features

When considering the Gibbs free energy under a general stress field [202]:

$$G = U - \sum_{\mathrm{i},j} \epsilon_{ij}\sigma_{\mathrm{i}j} - TS \tag{S4.1}$$

In Eq. S1, U is the internal energy, T is the temperature, S is the entropy, ϵ_{ij} and $\sigma_{\mathrm{i}j}$ represent the strain tensor and stress tensor of the substance respectively. Then, we take the differential form of G:

$$\mathrm{d}G = \mathrm{d}U - \sum_{i,j} \epsilon_{ij}\,\mathrm{d}\sigma_{ij} - \sum_{i,j} \sigma_{ij} d\epsilon_{ij} - T\,\mathrm{d}S - S\,\mathrm{d}T \tag{S4.2}$$

At constant temperature (dT = 0), using the first law of thermodynamics ($\Delta U = Q - W$) to cancel some terms:

$$\mathrm{d}G = -\sum_{i,j} \epsilon_{ij}\,\mathrm{d}\sigma_{ij} \tag{S4.3}$$

The stress tensor in the former equation can be written as the product of a scalar magnitude and a tensor with a constant trace of order unity:

$$G = -\sum_{i,j} \epsilon_{ij}\hat{\sigma}_{ij}\,\mathrm{d}\sigma = -\sum_{i,j,k,l} s_{ijkl}\hat{\sigma}_{ij}\hat{\sigma}_{kl}\sigma\,\mathrm{d}\sigma \tag{S4.4}$$

where s_{ijkl} represents the elastic compliance tensor. To determine the Gibbs free energy under a general stress σ, we integrate the stress from 0 to σ:

$$G = G_0 + \int_0^{\sigma} \mathrm{d}G = G_0 - \frac{1}{2}\sigma^2\Big(\sum_{i,j,k,l} s_{ijkl}\hat{\sigma}_{ij}\hat{\sigma}_{kl}\Big) \tag{S4.5}$$

G_0 is the Gibbs free energy at a datum condition, which the status with 0 stress is chosen in the above equation. Using matrix to replace the compliance tensor:

$$G = G_0 - \frac{1}{2}\sigma^2[\hat{\boldsymbol{\sigma}}\mathbf{S}\hat{\boldsymbol{\sigma}}^T] \tag{S4.6}$$

Since the TiNbZrHfTa CCA system has the BCC crystal structure, the compliance tensor **S** is

$$\begin{pmatrix} s_{11} & s_{12} & s_{12} & & & \\ s_{12} & s_{11} & s_{12} & & 0 & \\ s_{12} & s_{12} & s_{11} & & & \\ & & & s_{44} & 0 & 0 \\ & 0 & & 0 & s_{44} & 0 \\ & & & 0 & 0 & s_{44} \end{pmatrix}$$

in Eq. S6, while ^{T} denotes the transpose. For a general orientation of the stress relative to the crystallographic axes, $\hat{\sigma}$ is satisfied in eight different ways, corresponding to the eight-symmetry equivalent stresses,

$$\hat{\boldsymbol{\sigma}} = \left[\sigma_1, \sigma_2, \sigma_3, \pm\sqrt{\sigma_1\sigma_2}, \pm\sqrt{\sigma_1\sigma_3}, \pm\sqrt{\sigma_2\sigma_3}\right] \tag{S4.7}$$

where σ_i are the diagonal components of matrix $\hat{\sigma}$. Thus, G has the value:

$$G = G_0 - \frac{1}{2}\sigma^2\left[s_{11}({\sigma_1}^2 + {\sigma_2}^2 + {\sigma_3}^2) - 2\left(s_{11} - s_{12} - \frac{1}{2}s_{44}\right)(\sigma_1\sigma_2 + \sigma_1\sigma_3 + \sigma_2\sigma_3)\right] \tag{S4.8}$$

Since G keeps the same value for each of the eight possible choices of sign for the last three entries in Eq. S8, and the trace of the stress tensor is invariant under rotation and is equal to unity:

$$G = G_0 - \frac{1}{2}\sigma^2\left[s_{11} - 2\left(s_{11} - s_{12} - \frac{1}{2}s_{44}\right)(\sigma_1\sigma_2 + \sigma_1\sigma_3 + \sigma_2\sigma_3)\right] \tag{S4.9}$$

The Eq. S9 can be written as a sum of orientation-independent and orientation-dependent terms:

$$G = G_0' + \sigma^2\left(s_{11} - s_{12} - \frac{1}{2}s_{44}\right)(\sigma_1\sigma_2 + \sigma_1\sigma_3 + \sigma_2\sigma_3) \tag{S4.10}$$

The quantity $\sigma_1\sigma_2 + \sigma_1\sigma_3 + \sigma_2\sigma_3$ contains the orientation dependence, which shows a minimum value of 0 when the stress is aligned with a ⟨100⟩ direction, while exhibits a maximum of $\frac{1}{3}$ when aligned at ⟨111⟩ direction. Since the term $s_{11} - s_{12} - \frac{1}{2}s_{44}$ is always positive calculated according to the values in **Table S4.3**, G is minimized when the spinodal features are aligned with ⟨100⟩ directions.

Table S4.3 Elastic compliance tensors of the pure β-Ti or Ti alloys with a BCC crystal structure adopted for the calculation of Gibbs free energy.

Alloy systems	s_{11} (GPa)	s_{12} (GPa)	s_{44} (GPa)	Ref
β-Ti	134	110	36	[222]
Ti-40Nb	141.3	117.0	32.1	[237]
Ti–36Nb–5Zr	142.8	108.6	25.4	[238]
Ti-30Nb-10Ta-5Zr	67.1	39.9	29.8	[239]
Ti–36Nb–2Ta–3Zr–0.3O	125	93	28	[240]

Note 4.2 Predictive methodology for strain hardening exponent (*n*) and yield strength (σ_y)

The prediction of strain hardening exponent (*n*) and yield strength (σ_y) is based on the results obtained from the scratch test [227, 228]. The independent functions (like the scratch hardness H_S, the pile-up height h_p, the residual height h_r, and the friction coefficient μ_a) can be written for independent quantities, which subsequently can be evaluated numerically and used for any specific material condition within the solution space by making the quantities dimensionless and using the Π theorem [227, 228]:

$$\Pi_\alpha = \left(\frac{H_s}{\sigma_y}\right) = [\alpha 1(n) + n\Gamma_{\alpha 1}(\mu_a)]\left(\frac{\sigma_y}{E^*}\right)^{[\alpha_2(n)+\Gamma_{\alpha 2}(u_a)]} \qquad \text{S4.11}$$

$$\Pi_\beta = \frac{h_p}{h_r} = r_p = \Pi_{\beta,RP}(n)\Gamma_{\beta,RP}(\mu_a) \,/\, \left[1 + \left(\frac{\sigma_y}{X_\beta(n)\Gamma_{X\beta}(\mu_a)E^*}\right)^{p_\beta(n)}\right] \qquad \text{S4.12}$$

where E^*, and r_p represent the reduced elastic modulus and the normalized pile-up height obtained from the scratch test respectively, the subscript *RP* indicates the value of the function at the limit of rigid plastic properties. All the numerical closed-form solutions to these sub-functions are listed below:

$$\alpha 1(n) = 3.32 - 5.79n + 2.8n^2 \qquad \text{S4.13}$$

$$\Gamma_{\alpha 1}(\mu_a) = 0.12 - 0.64/[1 + e^{30(\mu_a - 0.1)}] \qquad \text{S4.14}$$

$$\alpha_2(n) = 0.07 - 1.283n + 0.248n^2 \qquad \text{S4.15}$$

$$\Gamma_{\alpha 2}(u_a) = 0.006 - 0.0278/[1 + e^{25(\mu_a - 0.1)}] \qquad \text{S4.16}$$

$$\Pi_{\beta,RP}(n) = 0.904 - 1.684n + 1.987n^2 - 2.722n^3 \qquad \text{S4.17}$$

$$\Gamma_{\beta,RP}(\mu_a) = 0.909 + 0.627\mu_a \qquad \text{S4.18}$$

$$X_\beta(n) = 0.0378 - 0.2129n + 1.145n^2 - 3.34n^3 + 3.54n^4 \qquad \text{S4.19}$$

$$\Gamma_{X\beta}(\mu_a) = 0.651 + 1.21\mu_a + 7.61{\mu_a}^2 \qquad \text{S4.20}$$

$$p_\beta(n) = 0.681\ln(n + 0.02) \qquad \text{S4.21}$$

There are some assumptions before this method is valid: a. incremental theory of plasticity is valid; b. the material plastic flow behavior is isotropic.

Therefore, the above dimensionless functions can be rewritten:

$$\Pi'_\alpha(H_s, E^*, n, u_a) = \left(\frac{\sigma_y}{E^*}\right) = \left[\left(\frac{H_s}{E^*}\right)/(\alpha 1(n) + n\Gamma_{\alpha 1}(\mu_a))\right]^{[1/(1+\alpha_2(n)+\Gamma_{\alpha 2}(u_a))]} \qquad \text{S4.22}$$

$$\Pi'_\beta(\Pi'_\alpha, n, u_a) = \frac{h_p}{h_r} = r_p = \Pi_{\beta,RP}(n)\Gamma_{\beta,RP}(\mu_a) \,/\, \left[1 + \left(\frac{\Pi'_\alpha}{X_\beta(n)\Gamma_{X\beta}(\mu_a)}\right)^{p_\beta(n)}\right] \qquad \text{S4.23}$$

To solve this system numerically, Π'_α is inserted into Π'_β to obtain *n*. Then the obtained value *n* is inserted in Π'_β to determine $\frac{\sigma_y}{E^*}$.

Note 4.3 Thermodynamic calculation for Gibbs free energy of TiNbZrHfTa CCA system

The Gibbs free energy in the TiNbZrHfTa CCA with and without heat treatment under H2 is calculated via a sub-regular model [4, 229]:

$$G = G^{id} + G^{\mathrm{ex}} \tag{S4.24}$$

In Eq. S11, G^{id} represents the ideal Gibbs free energy:

$$G^{id} = \sum_i x_i G_i = \sum_i RTx_i lnx_i \tag{S4.25}$$

where R is the gas constant, T is the temperature, and x_i represents the atomic percentage of i element in the alloy system. Since Ti and Zr show the tendency to accumulate together from the experimental results, we assume that the content of Zr (x_{Zr}) remains the same as that of Ti (x_{Ti}) and Hf (x_{Hf}) for the sake of simplicity. Similarly, x_{Ta} is assumed to be the same as x_{Nb}:

$$x_{Zr} = x_{Ti} = x_{Hf} \text{ and } x_{Ta} = x_{Nb} \tag{S4.26}$$

where the sum of the contents of all the elements is 1 ($x_{Zr} + x_{Ti} + x_{Hf} + x_{Ta} + x_{Nb} = 1$). In the case of hydrogen, we maintain the similar assumption. However, the hydrogen content (x_H) is fixed at a constant of 8.60 at.% according to the total hydrogen content measured by TDS. One additional condition is incorporated into the calculation of the Gibbs free energy of the TiNbZrHfTa CCA system coupled hydrogen:

$$x_{Zr} + x_{Ti} + x_{Hf} + x_{Ta} + x_{Nb} + x_H = 1 \text{ and } x_H = 0.086 \tag{S4.27}$$

The excess free energy term G^{ex} is calculated considering the binary, ternary, quaternary, quinary and even the senary interaction terms:

$$G^{\mathrm{ex}} = G^{ex}_{binary} + G^{ex}_{ternary} + G^{ex}_{quaternary} + G^{ex}_{quinary} + G^{ex}_{\mathrm{senary}} \tag{S4.28}$$

Specifically, the binary interaction term G^{ex}_{binary} is expressed as:

$$G^{ex}_{binary} = \sum_{i,j} G^{SD}_{ij} = \sum_{i,j} x_i x_j \Omega^{SD}_{ij} \tag{S4.29}$$

where Ω^{SD}_{ij} is the binary interaction parameter, and the exact forms of Ω^{SD}_{ij} available for the calculation are summarized in **Table S4.4.** Similarly, the ternary, quaternary, quinary, and senary excess free energy are modeled respectively via:

$$G^{ex}_{ternary} = \sum_{i,j,k} G^{SD}_{ijk}, \quad G^{ex}_{quaternary} = \sum_{i,j,k,l} G^{SD}_{ijkl},$$

$$G^{ex}_{quinary} = \sum_{i,j,k,l,m} G^{SD}_{ijklm}, \quad G^{ex}_{\mathrm{senary}} = \sum_{i,j,k,l,m,n} G^{SD}_{ijklmn} \tag{S4.30}$$

Table S4.4 Thermodynamic parameters adopted for binary and ternary excess free-energy calculation. The quantities shown here are all the available parameters to the best of our literature search. Part of the ternary interaction parameters, all of the quaternary, quinary and senary interaction parameters are not available.

Term		Equations or values	Ref
Binary interaction parameter	$\Omega^{BCC}_{T_iNb}$, J/mol	$-9166.70xNb + 9552.67$	[241]
	$\Omega^{BCC}_{T_iTa}$, J/mol	$-9938.63xTa + 9938.63$	[241]
	$\Omega^{BCC}_{T_iZr}$, J/mol	$-4346 + 5.489 \cdot T$	[242]
	$\Omega^{BCC}_{T_iHf}$, J/mol	$+3003.24 - 7.4114 \cdot T$	[242]
	Ω^{BCC}_{ZrHf}, J/mol	-838.6	[242]

	Ω_{ZrNb}^{BCC}, J/mol	$+15911 + 3.35 \cdot T + (3919 - 1.091T) \cdot (xNb - xZr)$	[243]
	Ω_{ZrTa}^{BCC}, J/mol	$-4396.2 + 4.4302 \cdot T$	[244]
	Ω_{HfNb}^{BCC}, J/mol	$+22713.5$	[245]
	Ω_{HfTa}^{BCC}, J/mol	$+22945.8$	[246]
	Ω_{NbTa}^{BCC}, J/mol	$+1298.3$	[247]
	$\Omega_{T_iH}^{BCC}$, J/mol	$2970.28 - 6.5847 \cdot T$	[234]
	Ω_{ZrH}^{BCC}, J/mol	$-474971 + 359 \cdot T$	[248]
	Ω_{NbH}^{BCC}, J/mol	52413	[248]
	Ω_{TaH}^{BCC}, J/mol	33700	[233]
Ternary interaction parameter	$\Omega_{T_iNbZr}^{BCC}$, J/mol	37.46	[249]
	$\Omega_{T_iNbTa}^{BCC}$, J/mol	-136602.7	[250]
	Ω_{NbZrH}^{BCC}, J/mol	15247.30	[248]
	Ω_{TiZrH}^{BCC}, J/mol	$+50800 - 54 \cdot T$ *	[251]

Note 4.4 Calculation for vacancy concentration of TiNbZrHfTa CCA system

The calculation of vacancy concentration is modeled via [12]:

$$C_v^a = \exp\left(-\frac{G_f^v}{kT}\right) = \exp\left(-\frac{H_f^v - TS_f^v}{kT}\right) \approx \exp(-\frac{H_f^v}{kT}) \tag{S4.31}$$

The corresponding vacancy formation enthalpy (H_f^v) available for the calculation of vacancy concentration before and after heat treatment under H_2 are summarized in **Table S4.5.**

Table S4.5 Vacancy formation enthalpy (H_f^v) adopted for the calculation of vacancy concentration change.

Element	H_f^v, eV	H_f^v with H, eV
Ti	2.24[252]	1.94[55, 253]
Zr	2.34[252]	1.81[55, 254]
Hf	2.39[252]	2.18[55]
Nb	2.31[255]	2.10[255]
Ta	3.08[256]	2.87[55]

5. Role of boron in yield strength softening and plastic deformation mechanisms in a refractory high-entropy alloy

This chapter is a modified version based on the paper entitled "*Role of boron in yield strength softening and plastic deformation mechanisms in a refractory high-entropy alloy*" (Ready for submission)

5.1. Introduction

Refractory complex concentrated alloys (CCAs) composed of multiple (five or more) elements offer renowned advantages over the dilute counterparts in optimizing mechanical and functional properties within the seemingly infinite compositional space [2, 24, 96]. Although these refractory CCAs have the intrinsic high strength (*e.g.*, ~1200 MPa for TiNbZrHfTa) due to the significant Peierls barrier, the relatively poor ductility (~10%) at room temperature is detrimental to the potential applications of this new class of alloys [13, 20, 21, 257]. This limitation is mainly attributed to the subtle difference between the ideal ultimate tensile strength and the strength for cleavage inception, which arises from the presence of less densely packed atomic planes in body-centered cubic (BCC) alloys [12, 14]. This subtle difference means that refractory CCAs are more likely to fail in a brittle manner before significant plastic deformation occurs. As a consequence, the reported tensile ductility of refractory CCAs is usually below 15%, and most researches are concentrating on ductility observed during compression tests [21, 258-262]. Additionally, the poor processability at atmospheric temperature make it difficult to eliminate the as-cast defects in refractory CCAs including porosity, dendrite microstructure and elemental inhomogeneity that are susceptible to stochastic premature failure [20, 263]. Therefore, the design of refractory CCAs with large room-temperature tensile ductility and processability, while maintaining high strength remains challenging.

High-temperature homogenization (above $0.7T_m$, where T_m is the absolute melting point) is one common method to achieve the desirable ductility by obtaining a uniform microstructure [96, 264]. This processing routine is usually time and energy intensive due to the sluggish diffusion of these refractory elements as well as being accompanied with a sacrifice of yield strength [21, 265]. Significant efforts including reducing grain size, introducing heterogeneous microstructure or inducing phase transformation have also been devoted to improving the ductility of refractory CCAs [263, 266, 267]. These methods mainly contribute to enhanced working hardening capacity, thus increasing the formability. However, tensile ductility has only been reported in a limited number of refractory CCA systems, as implementing these approaches (*e.g.*, inducing phase transformation) requires specific alloy compositions to be effective. An emerging alternative strategy for improving the ductility of refractory CCAs is grain boundary (GB) segregation engineering, altering interface properties by atomic-scale fine-tuning of the GB excess quantity [42, 43, 268]. As derived from classical thermodynamics, a solute element may preferentially reside in GBs driven by the reduction of Gibbs free energy [44, 46, 269]. Among the various dopants, boron (B) has garnered significant attention for its ability to enhance the mechanical properties of polycrystalline materials, which serves as a cost-effective method to improve the strength and ductility as compared with the alloying elements [32, 270-274]. For example, in an as-cast NbMoTaW solid solution, the addition of metalloid B was revealed to mitigate the oxygen contaminant at GBs, thereby alleviating the room-temperature brittleness [32]. On the other hand, the enhanced GB drag effect and reduced Gibbs-Thomson force caused by B segregation impede grain coarsening during recrystallization of polycrystalline refractory CCAs [271, 272].

In the present work, we report a counter-intuitive phenomenon in the B-doped equiatomic TiNbZrHfTa refractory CCA, where a yield strength softening behavior (a reduction by ~6.2±0.7%) is observed despite a decrease in grain size. To explore the underlying mechanisms for this softening behavior, the site-specific atom probe tomography (APT) was conducted to measure the GB chemistry upon B doping and the associated deformation behavior was evaluated by integrating EBSD/SEM correlative characterization, crystallographic analysis, and subsequent quantitative assessments on micro-deformation events related to GBs. Hence, we reveal that: (1) B addition significantly alters the GB chemistry, where B and Zr co-segregation is observed; (2) The reduction in yield strength is mainly due to a reduction in Hall-Petch coefficient caused by segregation of B as well as Zr at GB, thus compromising the strengthening effect induced by grain refinement; (3) GBs tend to accommodate higher strain upon B doping as compared with the B-free sample; (4) The inception of slip transfer can be mitigated by GB shear localization, where active slip transfer is significantly confined to lower misalignments for both slip planes and directions when B segregation is present.

5.2. Experimental section

5.2.1. Materials

The equimolar TiNbZrHfTa refractory CCAs without B addition, and with the addition of 0.003 at.% (30 ppm) B were cast using arc-melting under Ar atmosphere. The pure metals

(>99.95 wt%) were used for the base alloy. B doping was conducted by adding high-purity TiB_2. The as-casted samples were cold-rolled with a thickness reduction of 80%, followed by homogenization annealing in the BCC solid solution domain at 1100 °C for 5 h under a helium atmosphere, to rejuvenate the recrystallized microstructure. The annealed materials were then quenched in water. Hereafter, the TiNbZrHfTa CCAs with 0 ppm B and 30 ppm B were denoted as B-free and B-doped specimens, respectively. We also note that the overall oxygen content of the specimens is below 0.30 at.% as measured atom probed tomography (APT), which is supposed to not alter the mechanical properties of this class of alloys [275].

5.2.2. Microstructure characterization

The metallographic specimens were ground from 220 grit up to 4000 grit SiC sandpaper and subsequently polished with 50 nm colloidal silica oxide particle suspension to obtain a mirror-finished surface. A combination of secondary electron, backscatter electron (BSE) imaging, energy-dispersive X-ray spectroscopy (EDS), and electron backscatter diffraction (EBSD) techniques was used for microstructure characterization (Zeiss Sigma 500, Germany). The EBSD scans were carried out at an acceleration energy of 15 kV and a current of 2 nA, and a scanning step size of 1.0 μm was set for the scans. The post-processing of the EBSD data and the extraction of corresponding crystallographic information for further theoretical analysis were accomplished in commercial OIM software (version 8.0). Surface slip trace analysis and slip transfer quantification were carried out in a home-built STrCryst software package (https://github.com/shaolouwei/STrCryst).

To quantitatively explore the effect of GB chemistry on the plastic deformation mechanisms, we employ the crystallographic orientation data and slip line morphology to determine the activated slip modes by slip trace analysis. This technique has been applied in the investigation of deformation mechanisms for both single- and dual-phase metallic alloys [17, 276, 277]. However, three potential sources of inaccuracies should be mentioned: (1) the slip trace observation can be interfered with by the surface quality; (2) the identification of slip variants is complicated by the curvature of the slip traces, especially at the regions with high local strains; (3) the present work primarily focuses on slip configurations at the meso-scale (i.e., the scale of grain size), while composite slip may admittedly develop at the microscopic level [16, 72, 73, 278]. To mitigate the potential artifact generated during specimen preparation, the specimens were tilted to ±10° to verify the occurrence of slip steps before imaging. Considering the geometric relation between the crystal orientations and slip lines, the active slip modes can be calculated via the following equation,

$$\mathbf{t} = (\mathrm{g}^{-1} \cdot \mathbf{n}) \times \mathbf{N} \tag{5.1}$$

where **t** represents the unit directional vector corresponding to the slip plane. **n**, and **N** are the unit outer normal directions of the slip plane (crystal frame) and sample surface (sample frame), respectively. g denotes the coordinate transformation matrix [279],

$$\mathrm{g} = \begin{bmatrix} \cos\varphi_1\cos\varphi_2 - \sin\varphi_1\sin\varphi_2\cos\Phi & \sin\varphi_1\cos\varphi_2 + \cos\varphi_1\sin\varphi_2\cos\Phi & \sin\varphi_2\sin\Phi \\ -\cos\varphi_1\sin\varphi_2 - \sin\varphi_1\cos\varphi_2\cos\Phi & -\sin\varphi_1\sin\varphi_2 + \cos\varphi_1\cos\varphi_2\cos\Phi & \cos\varphi_2\sin\Phi \\ \sin\varphi_1\sin\Phi & -\cos\varphi_1\sin\Phi & \cos\Phi \end{bmatrix} \quad (5.2)$$

where $(\varphi_1, \Phi, \varphi_2)$ are the Euler angles following Bunge's convention, which can be obtained from the EBSD measurements [279]. For the slip trace analysis, $\{110\}\langle 1\bar{1}1\rangle$, $\{112\}\langle 11\bar{1}\rangle$, and $\{123\}\langle 11\bar{1}\rangle$ slip systems are all taken into consideration due to the similar packing density of the $\{110\}$, $\{112\}$, and $\{123\}$ planes in a BCC crystal structure [73]. The angle (φ) between the slip line and the loading axis can then be calculated via,

$$\varphi = \arccos\left|\frac{\mathbf{t}\cdot\mathbf{f}}{|\mathbf{t}|\cdot|\mathbf{f}|}\right| \quad (5.3)$$

In this equation, $\mathbf{f} = [010]^{\mathrm{T}}$, denotes the far-field uniaxial loading direction. Theoretical slip traces are determined by applying a ±10° (φ) deviation tolerance as compared with the experimental observations. The corresponding Schmid factors (m) specific to the activated slip systems are calculated through [280],

$$m = [(\mathrm{g}\cdot\mathbf{f})\cdot\mathbf{n}]\cdot[(\mathrm{g}\cdot\mathbf{f})\cdot\mathbf{s}] \quad (5.4)$$

Here, **n** and **s** represent the unit slip plane normal and the unit slip direction.

Synchrotron high-energy X-ray diffraction (HEXRD) experiments were conducted in a transmission mode at the Powder Diffraction and Total Scattering Beamline P02.1 of PETRA III at Deutsches Elektronen-Synchrotron (DESY) in Hamburg, Germany [70]. A beam with a fixed energy at 60 keV was employed to obtain a monochromatic X-ray with a wavelength of ~0.207 Å. The acquired diffraction peaks were integrated and subsequently post-analyzed using GSAS-II software [76]. Based on the XRD line broadening, the modified Williamson-Hall method was used to evaluate the dislocation density (ρ) of the specimens [281]:

$$\beta\cos\theta = 4\varepsilon\sin\theta + \frac{k\lambda}{D} \quad (5.5)$$

where β was the full width of half maximum (FWHM) of the diffraction peak at θ. ε, λ, and D represent the microstrain, the wavelength of the X-ray beamline, and the crystallite size, respectively. k is a constant for different materials, where 0.94 is usually used for BCC-type alloys [].

Then, the dislocation density was calculated as follows [282]:

$$\rho = \frac{2\sqrt{3}\varepsilon}{D|b|} \quad (5.6)$$

Atom probe tomography (APT) was employed to analyze the local chemistry at GBs down to near-atomic resolution. The APT tips were prepared using the site-specific lift-out method with the aid of the EBSD technique (to identify GBs prior to lift-out) using an FEI Helios NanoLab 660i dual-beam SEM/FIB instrument. The APT measurements were conducted in a LEAP 5000XR instrument (a reflectron mode) to ensure high mass resolution. Laser mode was employed for the measurements with a tip temperature, laser energy, pulse rate, and detection rate of 70 K, 60 pJ, 100 kHz, and 0.5 % (5 ions per 10000 pulses), respectively. The reconstruction and post-analysis of APT data were carried out using the AP suite software (version 6.1).

5.2.3. Uniaxial tensile testing

Rectangular dog bone-shaped tensile specimens with a gauge geometry of $4.0\times2.0\times1.0$ mm^3 were prepared using electrical discharge machining. The specimens were ground with a series of SiC sandpaper (from 200 grit to 4000 grit), followed by fine-polishing with 50 nm colloidal silica oxide particle suspension before tensile tests. A Kammrath and Weiss stage (strain rate: 1.25×10^{-3} s^{-1}) equipped with an optical camera (every 1 s) for digital image correlation (DIC) analysis was employed for the tensile test. A virtual extensometer (speckle patterns) was adopted to measure the local strains, and the data was processed using the Aramis GOM Correlate 2020 software (V6.3.0, GOM GmbH). Three tests were repeated for each microstructural condition to achieve reasonable statistics.

5.3. Results

5.3.1. Microstructure and GB segregation

Both B-free and B-doped TiNbZrHfTa refractory CCAs exhibit an equiaxed grain microstructure (**Fig. 5.1**a and b), showing a random orientation distribution with negligible texture (**Fig. S5.1**). High-angle GBs (> 75%) constitute the major type of GBs in both specimens, implying complete recrystallization after homogenization. The grain sizes of B-free and B-doped specimens are 69.9±27.2 μm and 53.9±23.5 μm, respectively (inserts in **Fig. 5.1**a and b). Compared with the B-free specimen, the reduction in grain size of the B-doped specimen probably originates from the B addition and its possible segregation at GBs, increasing the activation energy for GB migration and thereby leading to grain refinement [272], which will be discussed in **Section 4.1**. The corresponding EDS elemental distribution maps across the magnified regions marked in **Fig. 5.1**a and b show a homogeneous distribution of all elements. Additionally, the compositions for the B-free and B-doped specimens are determined to be $Ti_{19.77}Nb_{18.75}Zr_{21.27}Hf_{20.70}Ta_{19.51}$ and $Ti_{19.21}Nb_{18.74}Zr_{20.66}Hf_{20.86}Ta_{20.52}$ (in at.%), respectively (**Table S5.1**), consistent with the nominal equiatomic composition.

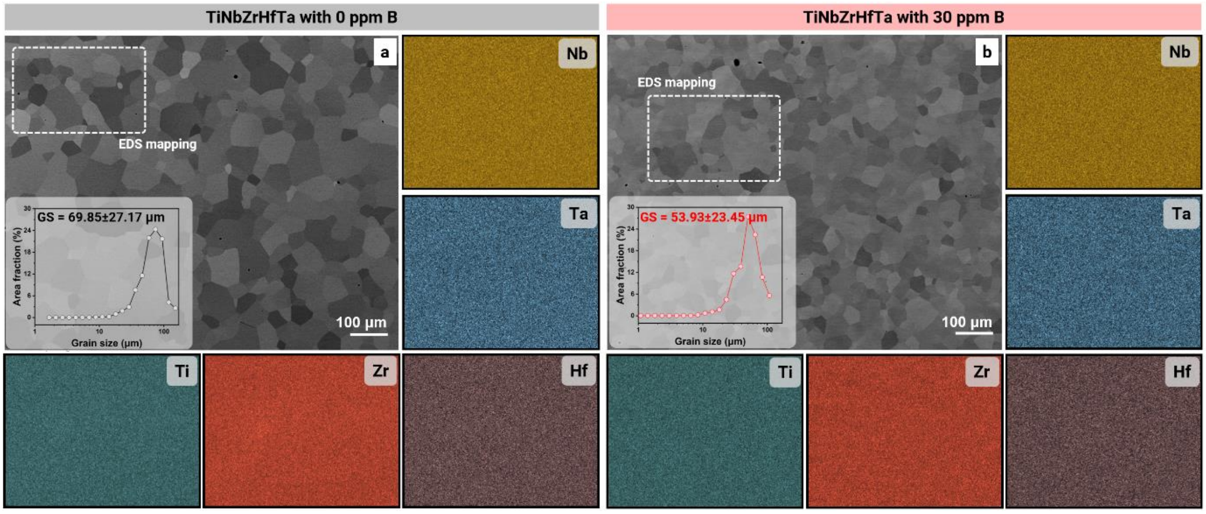
TiNbZrHfTa with 0 ppm B
TiNbZrHfTa with 30 ppm B
a
EDS mapping
GS = 69.85±27.17 μm
Area fraction (%)
Grain size (μm)
100 μm
b
EDS mapping
GS = 53.93±23.45 μm
Area fraction (%)
Grain size (μm)
100 μm
Nb
Ta
Ti
Zr
Hf
Nb
Ta
Ti
Zr
Hf

Fig. 5.1 Representative scanning electron microscopy (SEM) images of the (a) B-free and (b) B-doped TiNbZrHfTa CCAs, and their corresponding energy-dispersive X-ray spectroscopy (EDS) mapping of individual principal elements. The regions for EDS mapping are indicated by white dashed lines. The inserts represent the grain size distribution obtained over 50 grains from (a) and (b), respectively.

The HEXRD profiles confirm that (**Fig. 5.2**a) both specimens reveal a single-phase microstructure with a body-centered cubic (BCC) crystal structure. The lattice parameters are 3.406 Å and 3.398 Å (**Fig. S5.2**) for the B-free and B-doped specimens, respectively. No additional diffraction peaks of a boride phase are observed in the B-doped specimen. From the linear fitting curves of $\beta \cos\theta$ as a function of $4 \sin\theta$ (**Fig. 5.2**b), the microstrain (ε) and crystalline size (D) can be extracted from the slopes and intercepts, respectively, to calculate the dislocation density (Equations (5) and (6)). As revealed in **Fig. 5.2**c, both specimens possess a similar level of dislocation density, 1.77×10^{14} m^{-2} and 1.72×10^{14} m^{-2} in the B-free and B-doped specimens, respectively. These results suggest that the small addition of B (30 ppm) does not cause obvious changes in microstructure features, such as grain morphology, phase constituent, chemistry at the microscopic scale, and initial dislocation density, except grain size.

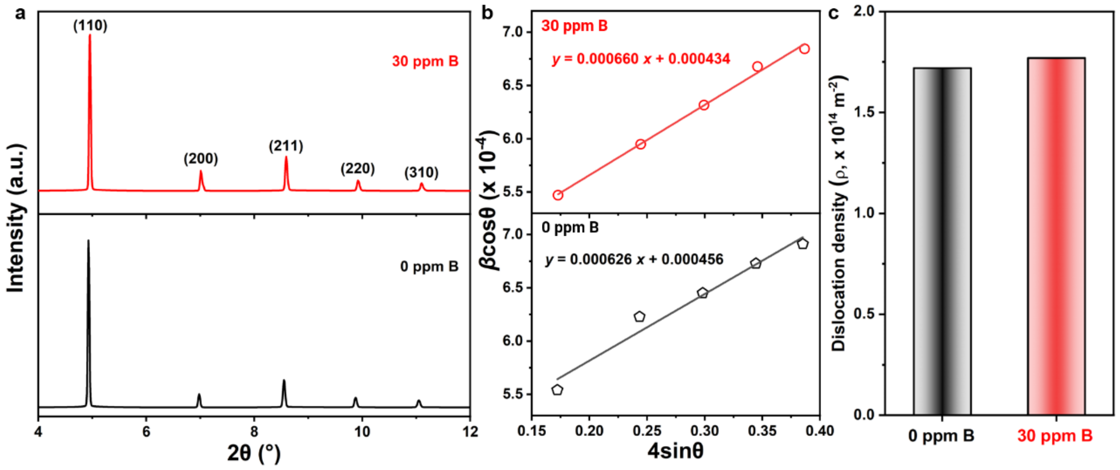

Fig. 5.2 (a) Synchrotron high-energy X-ray diffraction (HEXRD) profiles of the TiNbZrHfTa CCAs without and with 30 ppm B. (b) Plots of $\beta\cos\theta$ versus $4\sin\theta$ and their corresponding linear-fitted curves. β represents the full width of half maximum (FWHM) while θ is the diffraction angle. (c) Calculated dislocation density of the TiNbZrHfTa CCAs without and with 30 ppm B.

Although the observed grain refinement signifies the potential B segregation at GBs, it remains crucial to identify the actual distribution of B in the specimens. B is widely recognized to be located at GBs due to the minimization of the free energy at the GB [271, 272]. Three-dimensional APT analyses were employed to quantitatively investigate the GB chemistry of both specimens (Fig. 5.3). The misorientations of the probed GBs are determined to be 44.57° and 47.10° using EBSD for the B-free and B-doped specimens (Fig. S5.3), respectively. The GBs in APT datasets are identified by the decoration of B atoms (marked by blue dots). The B-free specimen exhibits a slight enrichment of B (max. 0.10 at.%) at the GB as highlighted by the iso-concentration surface of B (0.08 at.%, Fig. 5.3b). This subtle contamination of B in the B-free specimen is perhaps due to the metallurgical impurity introduced in the raw materials or during sample preparation. Additionally, a co-segregation of Zr at the GB is detected up to 24.08 at.%, as shown by the iso-concentration surface containing 22.00 at.% Zr, in contrast to the bulk concentration in the matrix, *i.e.*, 20.77 at.%. Subtle depletion of Nb and Ta (Fig. 5.3c and d) by 1.92 at.% and 1.52 at.% from the equiatomic composition is determined at the GB, as shown in the 1D concentration profiles. The lowest mixing enthalpy between B and Zr (-71 kJ/mol) predominantly contributes to such a co-segregation behavior as compared with the other principle elements [35]. The depletion of Nb and Ta is mainly ascribed to their high mixing enthalpy with B (both are -54 kJ/mol) [35]. In the B-doped specimen, the quantity of B at GBs is intensified as highlighted by a set of isosurfaces delineating regions containing more than 0.80 at.% B (Fig. 5.3f). An enrichment of up to 1.98 at.% B is found at the GB, whereas the concentration of B in the matrix is less than 0.10 at.% (Fig. 5.3h), demonstrating that B is mainly accumulated at the GBs. Similar to B-free specimen, co-segregation of Zr at the GB is observed in the B-doped specimen (Fig. 5.3g), but with a higher concentration, reaching up to 28.20 at.% (Fig. 5.3h). Additionally, depletion of Nb and Ta is observed with a stronger extent (a reduction of 3.27 at.% and 3.36 at.% for Nb and Ta, respectively). These changes in GB chemistry between the B-free and B-doped TiNbZrHfTa CCAs can significantly affect not only the microstructure (*e.g.*, grain refinement) but also the mechanical responses, particularly those associated with GB properties (GB strengthening, GB shear localization, slip transfer across the GB, etc.), which will be elaborated in the **Discussion** section.

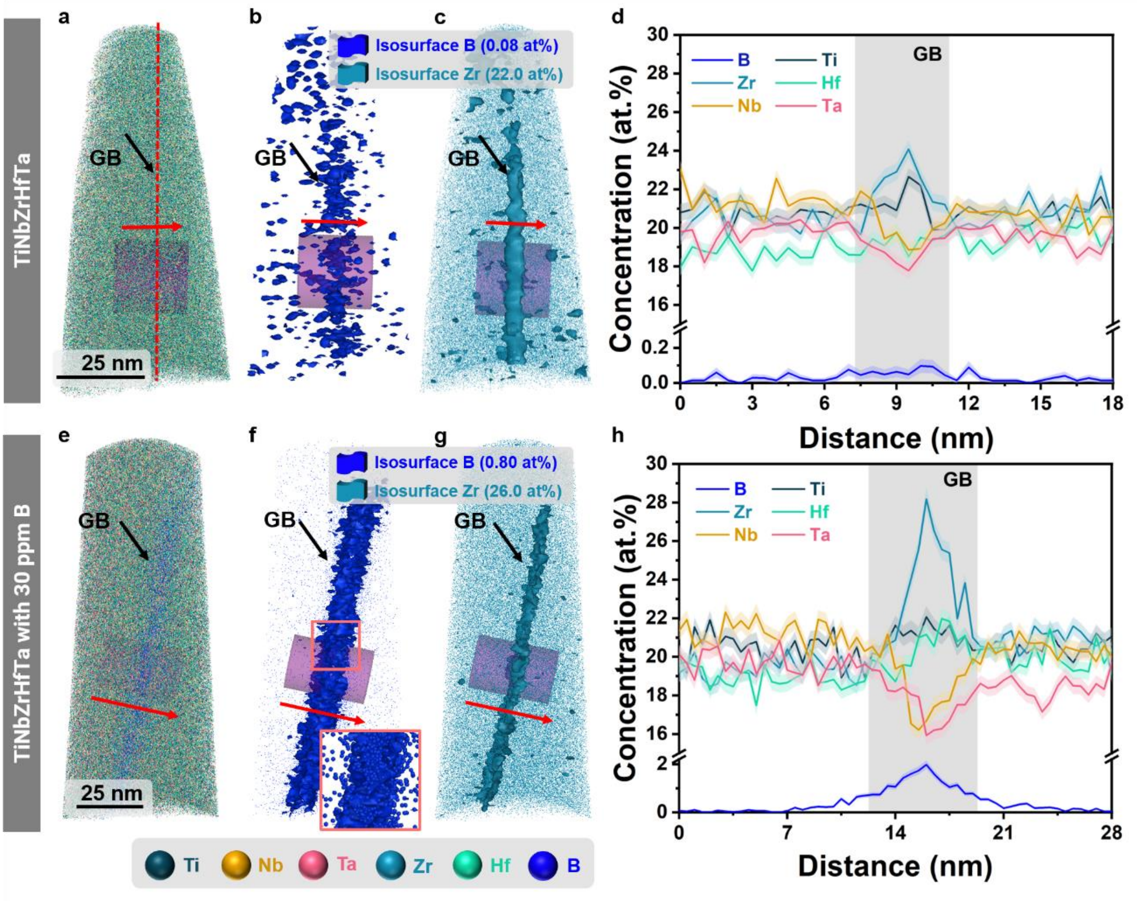

Fig. 5.3 Atom probe tomography (APT) analysis for the grain boundary of TiNbZrHfTa CCAs with (a-d) 0 ppm B and (e-h) 30 ppm B. Grain boundaries are indicated by black arrows. B atomic distribution (in blue) with a 0.08 at.% and 0.80 at.% B isosurface for TiNbZrHfTa CCAs containing (b) 0 ppm B and (f) 30 ppm B, respectively. Insert in (f) shows the enrichment of B atoms (depicted in spheres) within the grain boundary. 1D concentration profiles of B, Ti, Zr, Hf, Nb, and Ta across the grain boundary of the TiNbZrHfTa CCAs containing (d) 0 ppm B and (h) 30 ppm B as highlighted with a 25-nm cylinder of purple cylinders. Red arrows indicate the direction of the cylinders.

5.3.2. Tensile properties

Fig. 5.4a presents the uniaxial tensile properties of the TiNbZrHfTa refractory CCAs without and with the B addition (with three repeated tests). The B-free specimen yields at 920.70±3.69

MPa, followed by a modest strain hardening process, reaching an ultimate tensile strength of 940.35±15.15 MPa at a uniform elongation of 3.80%. In contrast, a lower yield strength of 869.78±10.41 MPa is observed for the B-doped specimens (insert in Fig. 5.4a), with a reduction by 6.2±0.7% compared with the B-free specimens. As B addition in other alloys often results in an enhancement in strength [270, 272, 273], such yield strength softening in the TiNbZrHfTa alloy necessitates the fundamental understanding of the underlying mechanisms, which will be discussed in **Section 4.1**. Both alloys exhibit similar fracture elongation values (22.24±0.20% and 20.91±1.14% for B-free and B-doped specimens, respectively), and strain-hardening rates (Fig. 5.4b).

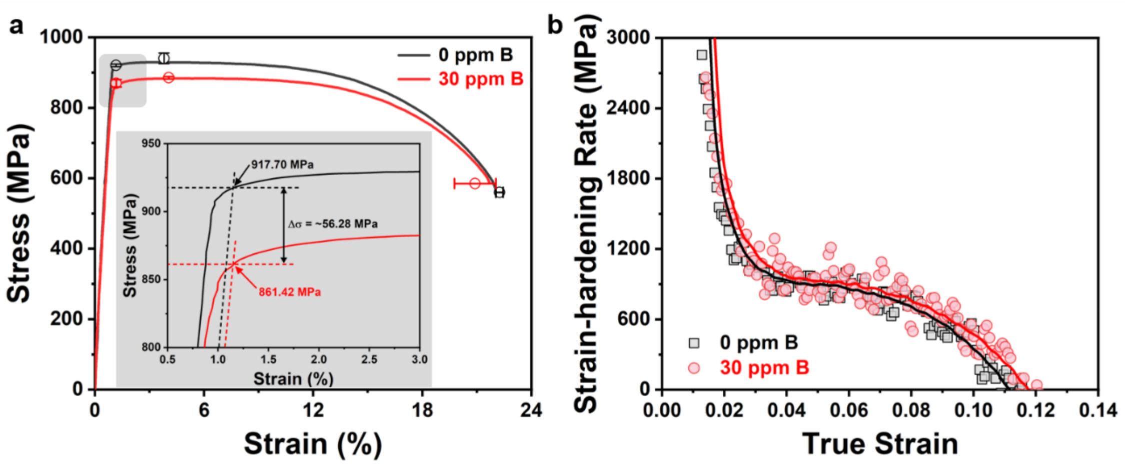

Fig. 5.4 (a) Engineering stress-strain curves of the TiNbZrHfTa CCAs with 0 and 30 ppm B. The mean values (shown as open circles) and corresponding scale bars are obtained over three repeated tests. Insert is the enlarged view of the strain range from 0.5 % to 3.0 %, revealing the yield strength softening after the addition of 30 ppm B. (b) Strain-hardening rates as a function of true strain.

5.3.3. Slip trace assessments

Apart from the single slip occurring inside the grains (Fig. S5 and Fig. S5.6), Fig. 5.5a and b show the experimental and theoretical results for the two regions of interest that underwent multiple slip and cross slip, respectively, in the B-doped specimen. The determination of different slip activities was conducted using fast-Fourier transform patterns, and the corresponding details were revealed in Fig. S5.5. In the multiple slip example, two types of straight slip traces (with different Burgers vector) with an intersecting angle of 45.66° are found. These two slip traces are recognized to be the activated $(121)[1\bar{1}1]$ (m = 0.381) and $(2\bar{3}1)[111]$ (m = 0.326) slip systems via the comparison of the actual slip traces and the calculated ones (Fig. 5.5a). For the cross slip case, curved slip traces (with the same Burgers vector) with activated $(1\bar{2}3)[\bar{1}11]$ (m = 0.468) and $(1\bar{1}2)[\bar{1}11]$ (m = 0.448) slip systems are identified (Fig. 5.5b), implying the change in slip planes during dislocation slip. These results suggest that the activated slip systems do not strictly obey the Schmid law, where the slip systems with the highest Schmid factors will tend to be activated before those with lower Schmid factors. This characteristic is primarily ascribed to the non-linear glide behavior of dislocations in the BCC alloys [13, 14]. In addition to the common slip activities, the presence of GB shear localization is revealed by an out-of-plane offset between adjacent grains (**Fig. 5.5**c, **Fig. S5.5** and **Fig. S5.6**). In this case, plasticity is accommodated by the GB sliding. A sharp increase in gray value in secondary electron image (by ~101) is detected across the GB region (**Fig. 5.5**d). Therefore, we adopted the first derivative of gray value (the absolute value above 20) as an indicator to identify the shear localization at the GB instead of milling all the GBs for side-view observations (**Fig. S5.10**) for subsequent quantitative assessments on the slip modes accommodating plasticity.

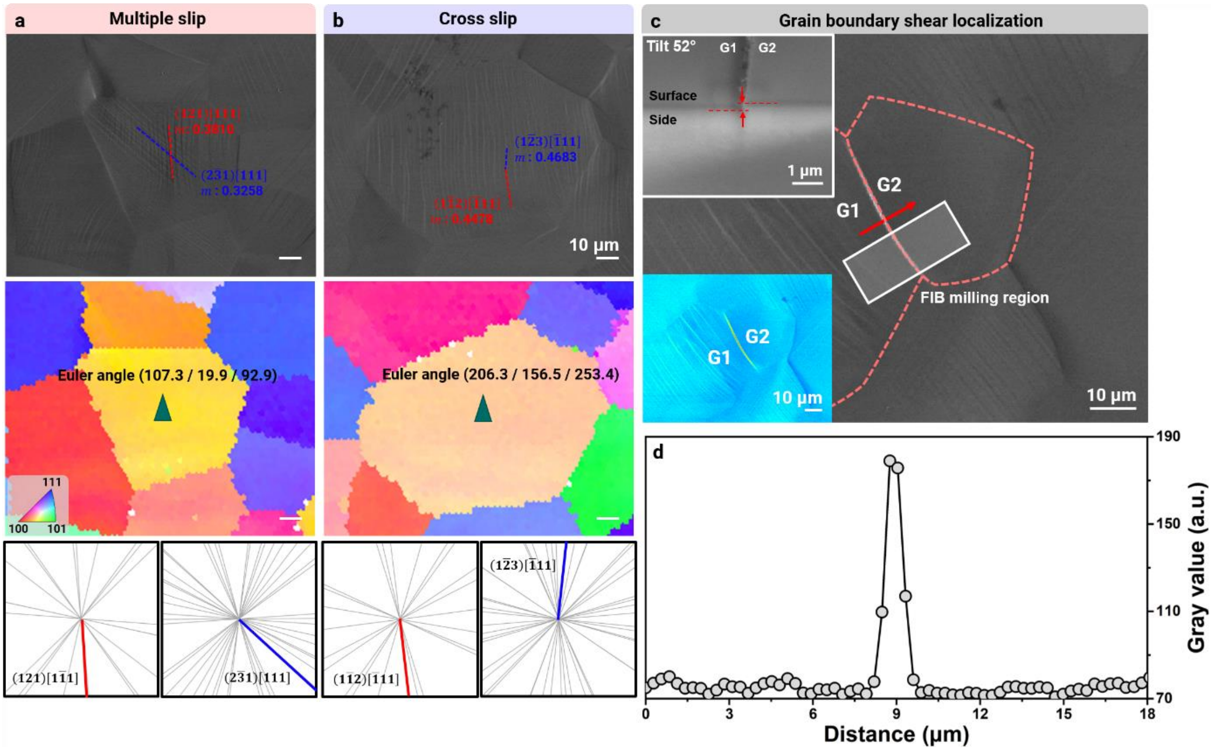
a
Multiple slip
$(121)[1\bar{1}1]$
m: 0.3810
$(2\bar{3}1)[111]$
m: 0.3258
b
Cross slip
$(1\bar{2}3)[\bar{1}11]$
m: 0.4683
$(1\bar{1}2)[\bar{1}11]$
m: 0.4478
10 μm
Euler angle (107.3 / 19.9 / 92.9)
Euler angle (206.3 / 156.5 / 253.4)
111
100
101
$(121)[1\bar{1}1]$
$(2\bar{3}1)[111]$
$(1\bar{1}2)[\bar{1}11]$
$(1\bar{2}3)[\bar{1}11]$
c
Grain boundary shear localization
Tilt 52°
G1
G2
Surface
Side
1 μm
G2
G1
FIB milling region
G2
G1
10 μm
10 μm
d
190
150
110
70
Gray value (a.u.)
0
3
6
9
12
15
18
Distance (μm)

Fig. 5.5 Representative B-doped grains at a global strain of 2% with (a) multiple-slip activity and (b) cross-slip activity and the corresponding inverse pole figure (IPF) maps as well as the slip trace analysis for identifying the operating slip systems, respectively. (c) Observation of grain boundary shear localization acquired at an incident plastic deformation (2% strain). The top insert in (c) is the SEM image of the cross-sectional view of the grain couple with a tilt angle of 52°, showing the height misfit between the adjacent two grains (marked with G1 and G2). The bottom insert in (c) is the post-processed SEM image with a color transform using blue lookup table, revealing the sharp increase in contrast at the grain boundary region. (d) The gray values across the grain boundary as highlighted by a red arrow in (c).

5.4. Discussion

5.4.1. Competitive effect between Hall-Petch coefficient (K_y) and grain size (d) on the change of yield strength

A decrease in yield strength was observed in the B-doped specimen compared with the B-free counterpart (**Fig. 5.4**a). This yield strength softening behavior is contradictory to most of the observations on the simultaneous increase in both yield strength and ductility by B addition in other metallic materials, *e.g.*, steels, Ti-based alloys and metal matrix composite [270, 272-274]. Generally, yield strength (σ_{ys}) of the metallic alloys can be expressed as follows [6],

$$\sigma_{\mathrm{ys}} = \sigma_{\mathrm{gb}} + \sigma_{\mathrm{dislo}} + \sigma_{\mathrm{P}} + \sigma_{\mathrm{ss}} \tag{5.7}$$

where, σ_{gb}, σ_{dislo}, σ_{P}, and σ_{ss} denote the strengthening effects from GB, dislocation density, precipitate, and solid solution (dilute and concentrated), respectively. In this study, negligible changes in the σ_{dislo} (identical dislocation densities at the initial state, **Fig. 5.2**c), σ_{P} (no formation of secondary phases, **Fig. 5.2**a), and σ_{ss} (similar alloy composition as well as the ppm-level addition of B) are found upon B doping. Therefore, the decrease in yield strength in the sample with B addition is mainly ascribed to the contribution from GBs (σ_{gb}). This hypothesis also aligns with the experimental observations that the major differences in microstructure in these two specimens are the grain size and the elemental segregation at GBs (**Fig. 5.1** and **Fig. 5.5**). The strengthening effect from GB is generally expressed by the Hall-Petch relationship [283-285],

$$\sigma_{\mathrm{gb}} = {K_y}/{\sqrt{d}} \tag{5.8}$$

In the above equation, K_y is a material-dependent constant, while d is the mean grain size. These two factors will be discussed in detail individually to explore the plausible mechanisms causing the yield strength softening.

***On grain refinement* (*d*).** For the term grain size d in the Hall-Petch equation, GB segregation of B and Zr in the B-doped CCA can lead to an enhanced GB solute drag effects, thus refining the grain size as compared with the B-free one [271, 272]. Such grain refinement can be reflected by the classical mean-field grain growth kinetics [271],

$$D_t^n - D_0^n = C \times t \tag{5.9}$$

where D_t, D_0, and n are the measured mean grain size at annealing time t, initial grain size (assumed to be 1 μm [271]), kinetic exponent quantifying the grain growth behavior, respectively. C represents the kinetic constant $C = C_0 \times \exp\left(-{Q}/{RT}\right)$ [286], where C_0, Q, R, and T denote the pre-exponential factor, activation energy for grain growth, gas constant and annealing temperature, respectively. Then, we can obtain,

$$ln\{(D_f^n - D_0^n)/t\} = \ln C_0 - \left({}^{Q}/_{RT}\right) \tag{5.10}$$

For n, generally, it is in the range from 2 (for uniform grain growth) to 4 (indicating the abnormal grain growth) [287]. Here, $n = 3$ is selected for the calculation considering the broad grain size distribution (**Fig. 5.1** and **Fig. S5.11**) in the investigated CCAs. With $n = 3$, $D_f = \frac{9}{8}D_t$ can be obtained, representing the final grain size [288, 289]. Therefore, the activation energies for grain growth (Q) are calculated to be 273.17 kJ/mol, and 282.02 kJ/mol for the B-free and B-doped CCAs. The addition of B (and Zr co-segregation) leads to an increase in Q, thus resulting in the reduction in grain size d, which is consistent with the grain refinement observed after B doping (**Fig. 5.1**). However, instead of an expected increase in yield strength, an opposite change, yield strength softening, was revealed in the investigated B-doped CCA. Such an intriguing phenomenon suggests that changes in GB chemistry will also have a non-negligible effect on K_y.

***On the effect of grain boundary chemistry on K_y*.** As for the Hall-Petch slope, K_y, the effect of B segregation as well as the associated alternation in GB chemistry can be demonstrated based on the selection of yielding models (*i.e.* the pile-up model, and the GB ledge mode) [290-292]. In this study, as shown in **Fig. S5.12**, massive dislocation segments and the formation of dislocation channels are observed near the GB, while no visible dislocation can be detected inside the grain at the initial stage of plastic deformation (with a global strain of around 1.2%). These behaviors suggest that GBs can serve as dislocation sources for the B-doped CCAs [292]. In this case, K_y is adopted according to the GB ledge model,

$$K_y = \alpha M G^{\mathrm{GB}} b\sqrt{3m} \tag{5.11}$$

where, α, G^{GB}, and m represent a material-dependent constant, shear modulus of the GB, and the ledge density. From the EBSD mapping (**Fig. S5.1**), the types of GBs are similar in composition for B-free and B-doped CCAs, where high-angle GBs account for more than 75%. The ledge density, which is a function of the misorientation angle, is thereby assumed to be identical for these two cases [293]. A change in G^{GB} can be deduced due to more intensive segregation of Zr and depletion of Nb/Ta at the GB in the B-doped specimen as compared with the B-free case (**Fig. 5.3**). Zr (BCC) possesses the lowest shear modulus (18 GPa), while Nb and Ta have comparably higher ones (38 GPa for Nb and 68 GPa for Ta) among these metallic elements, thus leading to a reduction in G^{GB} [294, 295]. Taken a linear approximation of G^{GB}

to the GB composition, $G^{\mathrm{GB}} = \sum_1^n x_i G_i$, where x_i represents the atomic percentage of i element, it is revealed that the G^{GB} (32.1 GPa) of the B-doped specimen is lower than the vicinal values (~35.2 GPa) in the matrix and the G^{GB} (~33.5 GPa) for the B-free one (**Fig. 5.6**b). A simple relationship between grain chemistry composition and Hall-Petch coefficient can thus be evaluated via $\frac{K_{\mathrm{y}}^{\mathrm{B}}}{K_{\mathrm{y}}^{\mathrm{noB}}} \propto \frac{G_{\mathrm{B}}^{\mathrm{GB}}}{G_{\mathrm{noB}}^{\mathrm{GB}}} \propto \frac{\sum x_{\mathrm{B}}^{\mathrm{GB}}}{\sum x_{\mathrm{noB}}^{\mathrm{GB}}}$, where K_y decreases with the increasing Zr concentration (**Fig. 5.6**c). Hence, the GB ledge model also supports the observed yield strength softening in this study.

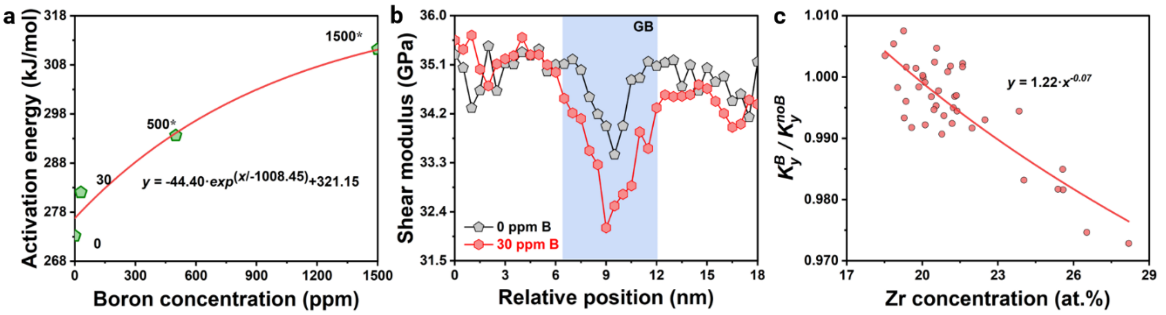

Fig. 5.6 (a) Calculated activation energy for grain growth as a function of B concentration. *: data used in the calculation is shown in **Fig. S11**. (b) Calculated shear modulus across the GB with the composition obtained from APT analysis. (c) Hall-Petch constant of non-B sample over Hall-Petch constant of B-containing sample (K_y^B / K_y^{noB}) plotted against Zr concentration.

A competition effect between K_y and d on the change of yield strength caused by the alternation in GB chemistry (B, and Zr segregation) can then be assessed according to the above results. The overall yield behavior is determined by the magnitude and balance between the size effect and segregation-induced softening. Thus, three scenarios are summarized: (a) The strengthening effect caused by grain refinement plays the dominant role, which can even offset the softening effect induced by the reduction of K_y. In this case, a continuous increase in yield strength can be determined from the combination effect of B and Zr (**Fig. 5.7**a). (b) A crossover point exists when the strengthening effect from the reduction of d is comparable with the softening effect caused by the decreasing K_y. Hence, there will be a critical segregation concentration of B/Zr where the strengthening effect from grain refinement will be predominant on the change of yield strength (**Fig. 5.7**b). (c) K_y plays a dominant role, demonstrating that the combination effect from B and Zr always results in a reduction of yield strength (**Fig. 5.7**c). The reduction in yield strength observed in the present study implies the possibility of case (b) or (c) in the investigated CCAs. To clarify the actual case, additional studies are required in the future. Such findings suggest the non-negligible role of the co-segregation elements (here, Zr) in the mechanical properties. When deploying GB segregation engineering of doping elements, co-segregation behavior of other alloying elements is necessary to be considered.

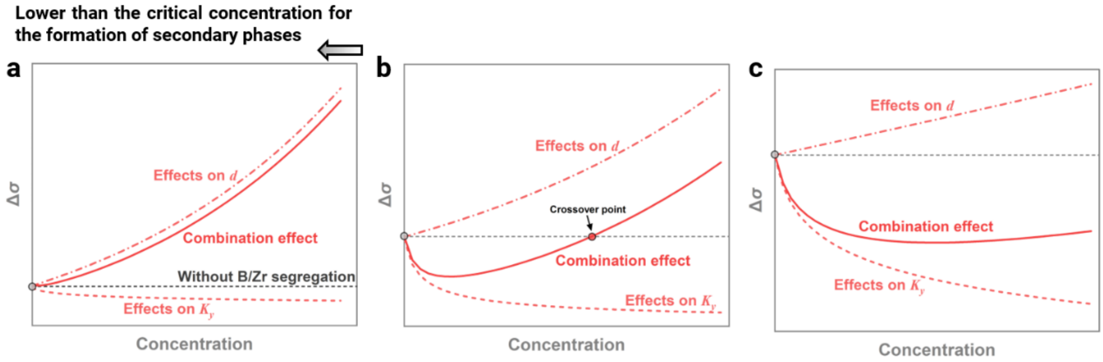

Fig. 5.7 Scheme diagrams showing the competition effect between B and Zr on yield strength: (a) The strengthening effect of B is the dominant part, contributing to the continuous increment of yield strength; (b) The strengthening effect from B and the weakening effect from Zr is comparable, so there exists a crossover point from the combination effect. (c) The weakening effect from Zr is dominant, thus leading to a drop of yield strength as compared to the non-B sample.

5.4.2. Activation of grain boundary shear localization upon B doping

In addition to the yield strength softening characteristic, the plastic deformation behavior with and without B doping is also evaluated to verify whether the change in GB chemistry will affect subsequent plastic deformation behaviors. In the TiNbZrHfTa refractory CCA, dislocation slip accounts for the primary deformation mechanism to accommodate plastic deformation. Generally, plasticity of BCC metals and alloys is controlled by the mobility a/2<111> screw dislocations whose core structure is a non-planar and gliding in {110}, {112}, and {123} planes or in composite mode (pencil glide) [12-14]. To clarify the slip behavior of the polycrystalline refractory CCA, a large region (500×500 μm^2) with a global strain of approximately 2% was captured for the quantitative assessment of activated slip traces (Fig. 5.8a and b, Table S5.3 and Table S5.4). Most of the grains exhibit slip traces following low-indexed slip planes, such as {110}, {112} and {123}. The $\{112\}(11\bar{1})$ system is determined to be the favorable slip system for plastic deformation in both the B-free and B-doped systems (Fig. 5.8c), suggesting that B addition has a negligible effect on the types of slip systems activated for plastic accommodation. Apart from the activated slip systems, comparison results of the plastic accommodation modes (multiple slip, cross slip, GB shear localization and slip transfer) were also acquired. Since the total plastic deformation gradient caused by plasticity micro-mechanisms that can be considered as affine shear (*e.g.*, conservative motion of dislocations and mechanical twinning) takes the form of $\sum_{\alpha} \gamma^{\alpha} (\boldsymbol{s}^{\alpha} \otimes \boldsymbol{m}^{\alpha})$, where $\boldsymbol{s}^{\alpha}$, and $\boldsymbol{m}^{\alpha}$ denote the constant orthonormal unit vectors of each plastic deformation mode α [296].γ^{α} represents the scalar shear strain, which defines the plastic strain theoretically. However, deriving this value experimentally is challenging. Here, instead of acquiring the shear rate, here we mainly focus on the counts for the sake of simplicity. As revealed in **Fig. 5.8**d, GB shear localization becomes one new mechanism for accommodating plasticity in the B-doped CCA as compared with the B-free CCA. In the latter case, single-mode dislocation slip (not shown in the figure) is the main mechanism for plastic accommodation. GBs are usually considered as the origin of strain localization and damage initiation once dislocations approach and concentrate on them, serving as a barrier against dislocation motion and thus resulting in stress concentration [297-299]. This associated forward stress concentration can be mitigated via Rachinger-type GB sliding, *i.e.*, a highly localized shear deformation along or at the vicinity of the GB planes [300-303]. Therefore, this increase in the amount of GB shear localization cases (from the count of 8 to 27) after the addition of B suggests that GBs tend to become another deformation mode to accommodate plasticity in addition to grain interiors, potentially relating to the detected alternation in GB chemistry. Furthermore, it is found that the GB shear localization occurs more frequently at high-angle GBs, particularly those with a misorientation angle above 30° (**Fig. 5.8**e and **Fig. S5.15**). This characteristic is primarily due to the larger free volume within the high-angle GB (as free volume increases with the misorientation angle between grains), thus resulting in a stronger enrichment of B and Zr [304, 305]. The magnitude of the GB shear localization can be evaluated via the sliding rate ($\dot{\gamma}_{\mathrm{gbs}}$) between two grains (the corresponding details are shown in supplementary Note 5.1) [306],

$$\dot{\gamma}_{\mathrm{gbs}} = \frac{\beta b^2 \sigma^2}{d G^{\mathrm{GB}} k T} D_l \tag{5.12}$$

In this equation, β and D_l represent a constant depending on materials and lattice self-diffusion coefficient. Taking all the known values from the experiments (σ, d, and G^{GB} (the shear modulus at the GB is taken into consideration since this behavior is sensitive to the change in local chemistry)), then, we can obtain, $\frac{\dot{\gamma}_{\mathrm{gbs}}^{\mathrm{noB}}}{\dot{\gamma}_{\mathrm{gbs}}^{\mathrm{B}}} = \frac{\sigma^{\mathrm{noB}^2} d^{\mathrm{B}} G_{\mathrm{B}}^{\mathrm{GB}}}{\sigma^{\mathrm{B}^2} d^{\mathrm{noB}} G_{\mathrm{noB}}^{\mathrm{GB}}} \approx 0.837 < 1$. Therefore, the B-doped TiNbZrHfTa refractory CCA exhibits a higher GB sliding rate than that of the B-free CCA, suggesting that the enrichment of B as well as Zr at GBs can modulate the mechanical behavior of GBs under applied stress. In stark contrast to the increase in the frequency of the GB shear localization upon B addition, another plastic deformation mode at GBs, slip transfer, is suppressed from 36 cases to 28 cases. Such an opposing effect on the activation of plastic deformation modes at GBs suggests a mutual competition between these two mechanisms (slip transfer across GB versus GB shear localization), which will be discussed in detail in the following section.

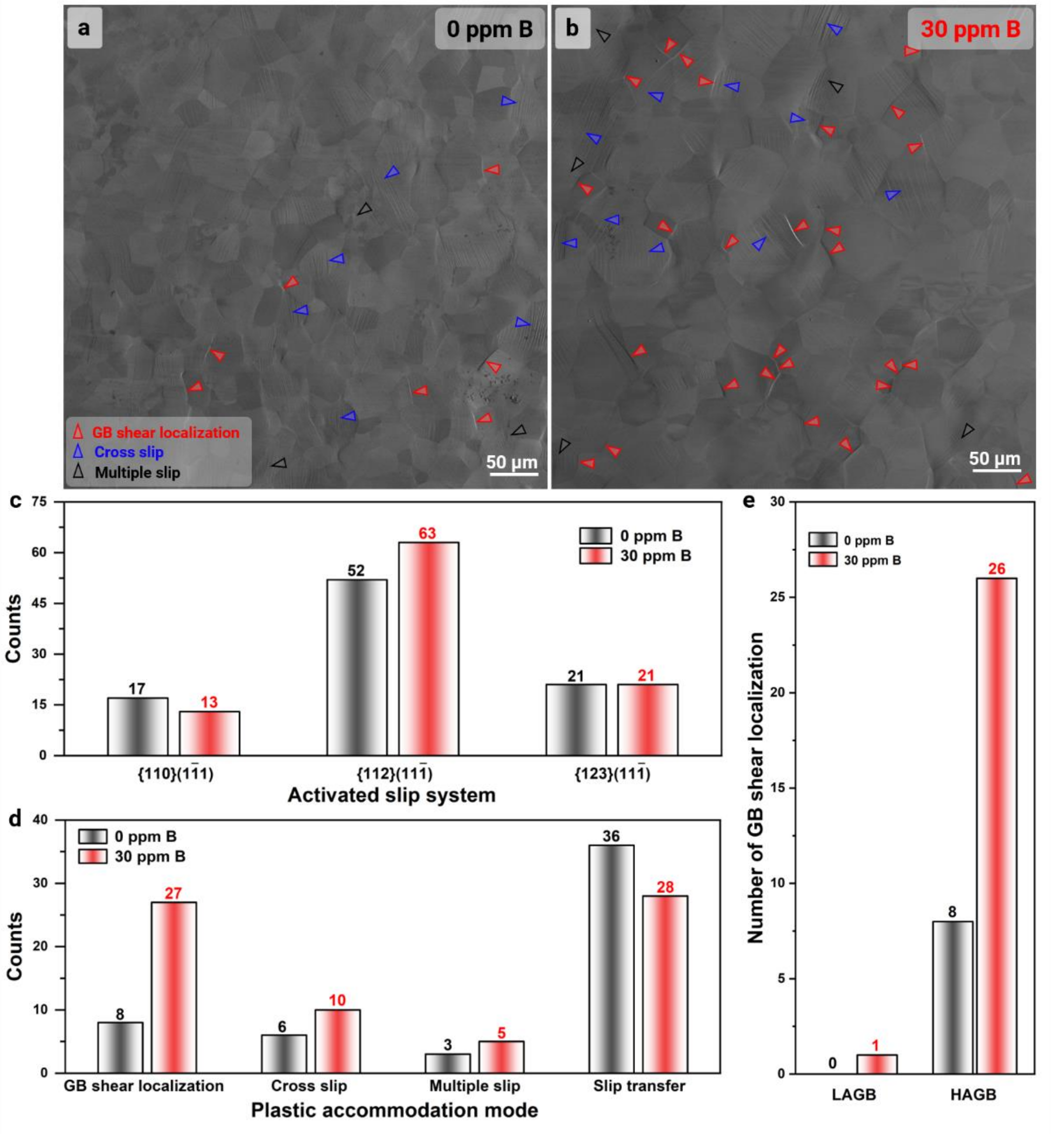

Fig. 5.8 Statistical analysis of plastic accommodation modes of TiNbZrHfTa CCAs with (a) 0 ppm B, and (b) 30 ppm B at a strain of 2%. Quantitative assessments of the (c) activated slip systems and (d) plastic accommodation modes of both the TiNbZrHfTa CCAs with 0 ppm B and 30 ppm B. (e) Further assessment of the GB shear localization frequency versus the types of GBs. LAGB and HAGB represent the low-angle GB and high-angle GB, respectively.

Two accommodation processes associated with GB shear localization have been demonstrated, one is the diffusive motion of atoms in the GB, while the other one is the dislocation slip [307, 308]. Dislocation slip is likely expected for refractory CCAs at room temperature, while vacancy diffusion, as well as the sluggish diffusion of refractory atoms, will become predominant at higher temperatures [265, 306]. It was revealed that lattice dislocations activated from grain interior could dissociate into GB structural dislocations, following by moving along the GB to cause GB shear localization [309]. Such a characteristic of slip-mediated GB shear localization will then intensify the localized plastic deformation.

Upon B doping, the GB shear localization becomes a new plastic accommodation mechanism, where GBs behave as the accommodation sites for plastic deformation as compared with the B-free CCA. The kernel average misorientation (KAM) maps of the B-free and B-doped CCAs were then collected for verifying the regions for strain localization (**Fig. 5.9**). To semi-quantitatively determine the strain partitioning behavior between grain interiors and GBs, we segment the KAM maps into two parts (GB (with a width of around 11 pixels) and grain interior), and then extracted the individual KAM value from each pixel. For the grain interior, the B-free specimen exhibits a broad KAM distribution with an average KAM value of 0.757±0.023°, significantly higher than that (0.543±0.012°) for the B-doped one (**Fig. 5.9**g). In comparison, as revealed in **Fig. 5.9**h, a higher averaged KAM value (0.828±0.038°) can be determined at the GB of the B-doped case as compared with the specimen without B addition (0.734±0.029°), indicating the enhanced strain localization at GBs upon B doping. It is also worth noting that two distribution histograms of KAM values can be deconvoluted in the GB region of the B-doped specimen, where one with an averaged KAM value of 0.828±0.038° constitutes the major part (61.3%), while the other exhibits an averaged KAM value of 2.082±0.178°, accounting for 38.7%, implying that strain localization tends to occur at specific types of GBs. These stain partitioning behaviors suggest that strain tends to be redistributed between grain interiors and boundaries due to B addition, where GBs can accommodate higher strain than those of the B-free case. Such findings demonstrate that in addition to yield strength softening, B segregation alters the mechanisms for plastic accommodation, rendering GBs a new manner for accommodating plastic deformation.

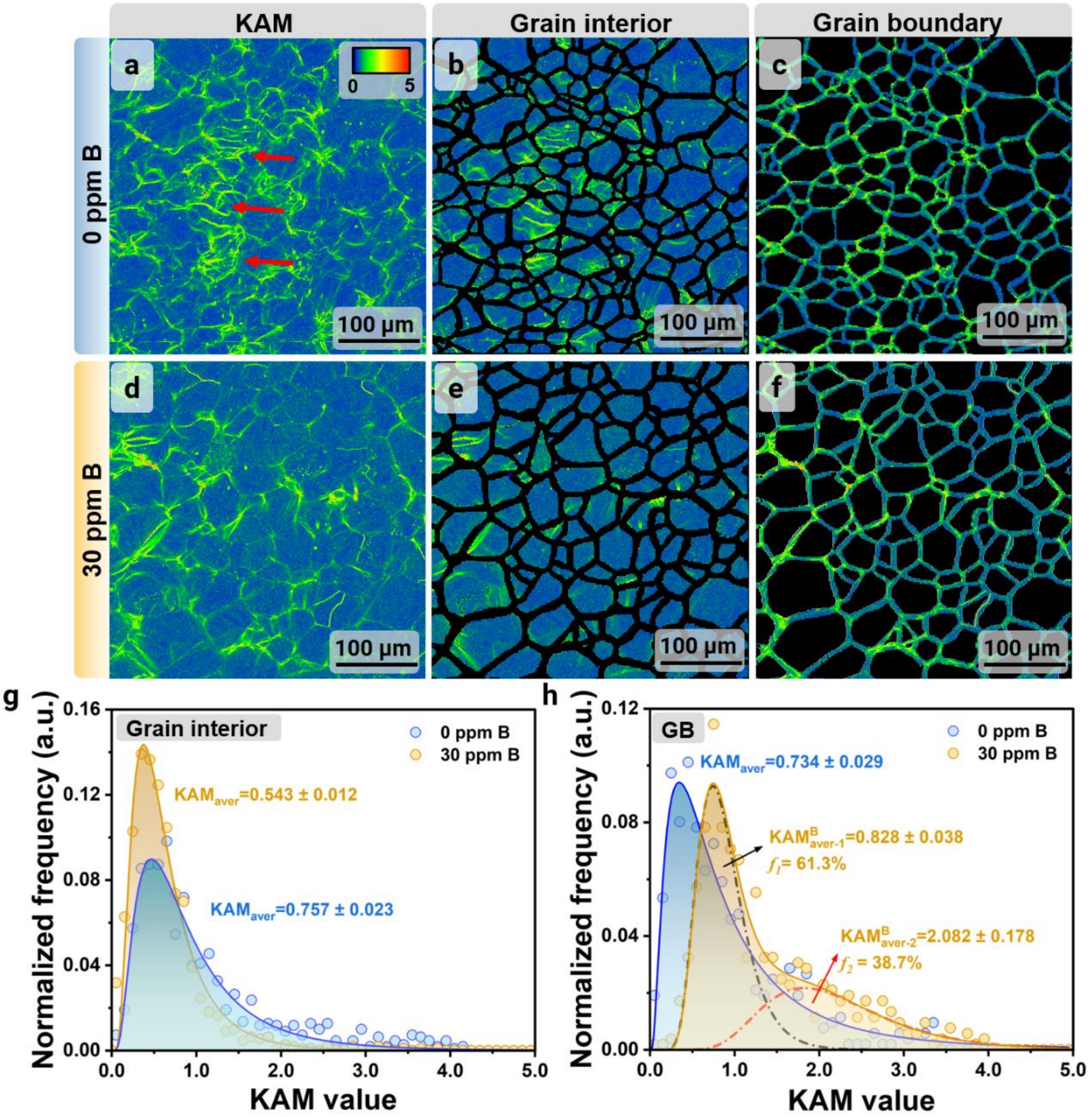

Fig. 5.9 Kernel average misorientation (KAM) maps of the TiNbZrHfTa CCAs with (a) 0 ppm B and (d) 30 ppm B, and the corresponding exemplary KAM maps of the (b, e) grain interior regions and (c, f) GB regions subjected to the regression analysis, respectively. Lognormal regression analysis for the corresponding KAM maps of the (g) grain interior regions and (h) GB regions.

5.4.3. Competition between grain boundary shear localization and slip transfer

In addition to GB shear localization, slip transfer across GBs is recognized as another common deformation mechanism at GBs (**Fig. 5.10**c) [300, 301]. Here, the relationship between GB shear localization and slip transfer through GBs is evaluated to unravel the potential competition between these two accommodating mechanisms associated with GBs (**Fig. 5.10**). The drop in the amount of slip transfer cases for the B-doped specimen (with a count of 28) as compared with the B-free one (with a count of 36) demonstrates a phenomenological retardation effect on slip transfers due to B segregation. The Luster-Morris geometric compatibility factor (m') was employed to quantify the condition for slip transfer micro-events [310],

$$m' = [(g_1^{-1} \cdot \mathbf{s}_1) \cdot (g_2^{-1} \cdot \mathbf{s}_2)] \cdot [(g_1^{-1} \cdot \mathbf{n}_1) \cdot (g_2^{-1} \cdot \mathbf{n}_2)] \tag{5.13}$$

which considers the misalignment between slip directions at the individual grain ($\mathbf{s}_1$ and $\mathbf{s}_2$) together with the misalignment of these corresponding slip plane normals ($\mathbf{n}_1$ and $\mathbf{n}_2$). When m' closes to 1, it indicates a high tendency for slip transfer across the GB. Otherwise, the slip transfer is suppressed for an m' value close to 0. Furthermore, the misalignment angle between the slip directions (κ) and the misalignment angle between the slip normals (ψ) can also be determined through:

$$\kappa = \arccos[(g_1^{-1} \cdot \mathbf{s}_1) \cdot (g_2^{-1} \cdot \mathbf{s}_2)] \tag{5.14}$$

$$\psi = \arccos[(g_1^{-1} \cdot \mathbf{n}_1) \cdot (g_2^{-1} \cdot \mathbf{n}_2)] \tag{5.15}$$

To ensure the statistical reliability, at least 20 grains exhibiting slip transfer events were surveyed for analysis and the corresponding crystallographic details were summarized in **Table S5.5**, **Table S5.6** and **Table S5.7**. Almost all the m' datum points exhibit inverse correlation with the increase of the misorientation angle, suggesting a strong geometrical dependency for the inception of slip transfer (**Fig. 5.10**d), *i.e.* slip transfer favors GBs with low angles. This sort of dependency is consistent with the literature reported on single-phase BCC alloys and even pure metals like Al, Ni, or Ta [72, 300, 311, 312]. A closer inspection of **Fig. 5.10**d substantiates that the unambiguous role of B in altering the slip transfer response: much more datum points tend to aggregate to the lower misorientation angle (*i.e.* high m') in the B-doped CCA as compared with the B-free one, suggesting a more stringent local geometric confinement of slip transfer, despite the similar global deformation level (the pre-strain level has been kept identical as ~2.0% for both cases). The mechanical revelation of **Fig. 5.10**d also lies in the fact that the capability of GB-aided forward stress alleviation via slip transfer is somewhat impaired due to B addition, which instead necessitate alternative deformation pathway at or in the vicinity of GBs, rationalizing the observed immense shear localization revealed in the preceding discussion. Instead, the GB shear localization is prone to happen at GBs where adjacent grains exhibit slip traces with a high intersecting angle or are even parallel to GBs in the B-doped CCA, acting as an alternative way to accommodate plastic deformation (**Fig. S5.15**). For a more precise quantification, we also computed the ψ versus κ diagram, assessing the respective contributions from slip direction misalignment and slip plane misalignment. A greater tolerance to geometrical alignments including both the slip direction ($0° < \kappa < 76°$) and slip plane ($0° < \psi < 83°$) misalignments can be revealed for the B-free specimen as compared to the B-doped one where geometrical alignments are constrained to be lower than 56° and 48° for κ and ψ respectively. Upon B doping, the sensitivity of the slip transfer to ψ is lower than κ, which may be due to the change in GB chemistry, as it quantifies the possibility of local GB plane distortion to accommodate the imposed stress/tractions. Additionally, the frequency of slip transfer occurring within the contour line with an iso-value of 0.9 (shown in blue lines) of the B-doped CCA is 53.8%, significantly higher than that of the B-free CCA (29.0%), confirming a stronger geometrical dependence for slip transfer in the B-doped case. Such a correlation indicates that upon B doping, the B and Zr co-segregation tend to facilitate the relative movement of the GB instead of the slip transfer across GBs. A rational mechanism can be that the pile-up dislocations at the GB are mainly absorbed and driven to glide along the GB [312]. The slip transfer and GB shear localization observed in this system are anti-compatible and primarily determined by the misorientation of the GB. GBs with low misorientations (< 30°) facilitates slip transfer with a frequency of 75.0%, while the GB shear localization preferably occurs at high-misorientation GBs (> 30°), accounting for 85.1%. These results demonstrate that there exists a competitive effect between slip transfer and GB shear localization, with crystallographic and geometrical orientations playing a crucial role in the determination of the types for plastic deformation at GBs. More importantly, the GB chemistry in this alloy is proved to be important on the alternation of accommodation mechanisms for plastic deformation, where B addition leads to an increase on the presence of GB shear localization.

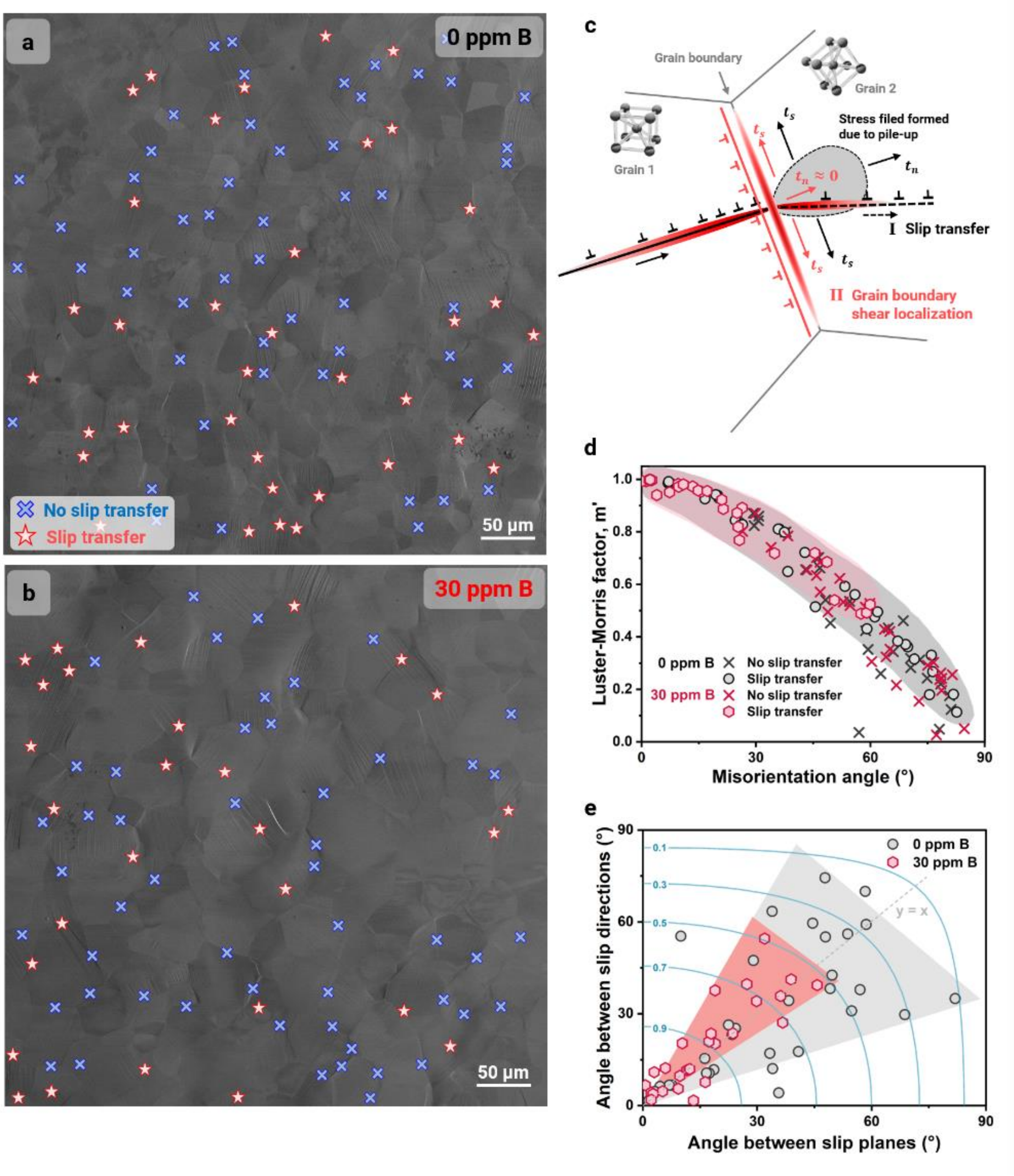

Fig. 5.10 Statistical analysis of slip transfer activities of TiNbZrHfTa CCAs with (a) 0 ppm B, and (b) 30 ppm B at a strain of 2%. (c) Scheme diagram demonstrating the competition between slip transfer and GB shear localization. (d) Luster-Morris factor (m') versus misorientation angle for all surveyed grain couples. (e) Geometric correlation chart concerning the angles between slip directions and slip planes for all the surveyed grain couples with slip transfer.

5.5. Conclusions

In this study, the mechanical behavior in a polycrystalline TiNbZrHfTa refractory complex concentrated alloy (CCA) with the addition of 30 ppm boron (B) was systematically and quantitatively investigated and compared with the B-free reference sample. The major findings are summarized as follows:

(1) The ppm-level addition of B (here, 30 ppm) could result in a reduction in grain size from 69.9 μm to 53.9 μm due to the solute drag effect of B on grain growth. The grain boundary (GB) chemistry was significantly altered upon B doping, where the co-segregation of B (1.98 at.%) and Zr (up to 28.20 at.%) accompanied with the depletion of Ta (by 3.36 at.%) and Nb (by 3.27 at.%) was revealed with the aid of atom probe tomography. The lower mixing enthalpy between B and Zr primarily contributed to the co-segregation behavior.

(2) Yield strength softening with a decrease by ~6.2±0.7% was revealed upon B addition. This softening is mainly due to a reduction in Hall-Petch coefficient caused by a change in GB chemistry (B/Zr co-segregation), thus reducing the critical shear stress (from GB pile-up model) or the shear modulus at the GB (from GB ledge mode) for dislocation emission or transmission. Such a reduction in yield strength even surpass the strengthening effect induced by grain refinement.

(3) Upon plastic deformation, GBs actively accommodate plastic deformation in the B-doped refractory CCA, exhibiting as slip-mediated GB shear localization, which was identified via the quantitative assessment of the plastic deformation modes. This change in plastic accommodation mechanisms suggested the predominant role of the local chemistry at GBs in the plastic deformation mechanisms in the CCAs. Additionally, the slip direction misalignment (κ) and slip normal misalignment (ψ) relationships of the surveyed slip traces revealed a more stringent local geometric confinement of slip transfer upon B doping as compared with the B-free case. Such a constrain suggested a competition between slip transfer and GB shear localization, further confirming the unambiguous role of elemental segregation in altering the slip transfer response.

These findings highlight the profound impact of ppm-level B doping on the macroscopic mechanical performance of the polycrystalline TiNbZrHfTa refractory CCAs. The observed changes in microscopic deformation modes illuminate the intricate interplay between GB chemistry and plasticity mechanisms, offering valuable insights into the design of advanced materials. Thus, this work shed lights on the development and application of GB segregation engineering strategies aimed at optimizing the mechanical performance of complex alloys.

5.6. Supplementary materials

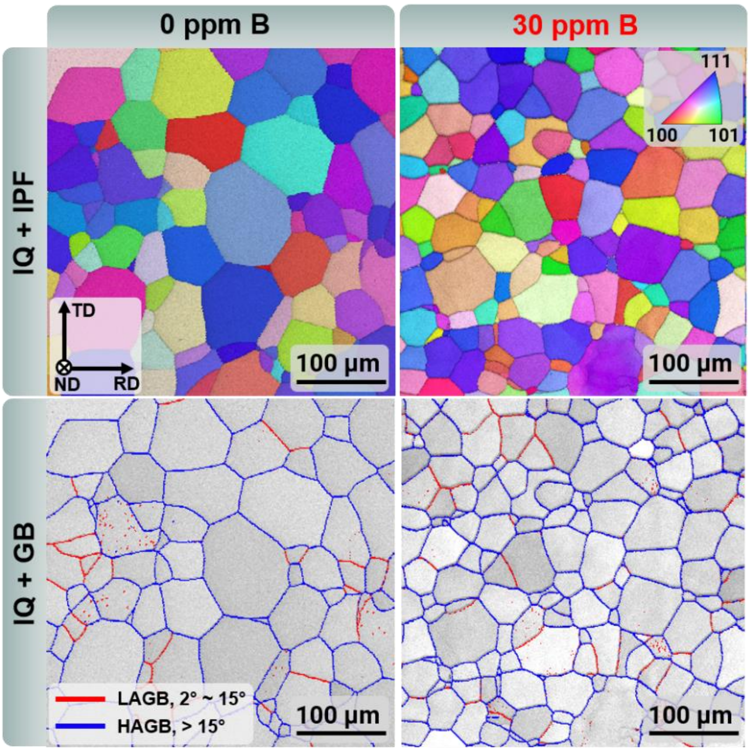

Fig. S5.1 EBSD image quality (IQ) overleid with inverse pole figure (IPF) maps and grain boundary (GB) maps of the TiNbZrHfTa CCAs with 0 ppm B and 30 ppm B, respectively. The EBSD scans were acquired at the undeformed regions.

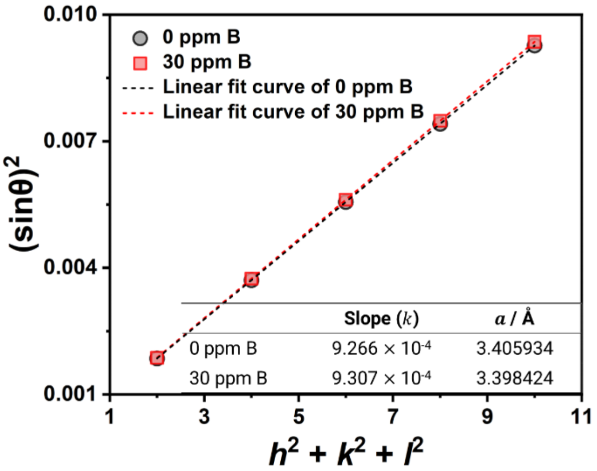

	Slope (k)	a / Å
0 ppm B	9.266×10^{-4}	3.405934
30 ppm B	9.307×10^{-4}	3.398424

Fig. S5.2 Calculated (sinθ)^2 as a function of $h^2+k^2+l^2$ for the determination of lattice parameters. The typical Bragg's equation is used: $(sin\,\theta)^2 = \frac{\lambda^2}{4a^2}(h^2 + k^2 + l^2)$, where θ, λ, and a represent the diffraction angle, wavelength and lattice parameter respectively, while h, k, l is the Miller indices of the crystallographic plane. Through the slope (S_k) from the linear fitting curve, we can solve the lattice parameter, $a = \sqrt{\frac{\lambda^2}{4S_k}}$.

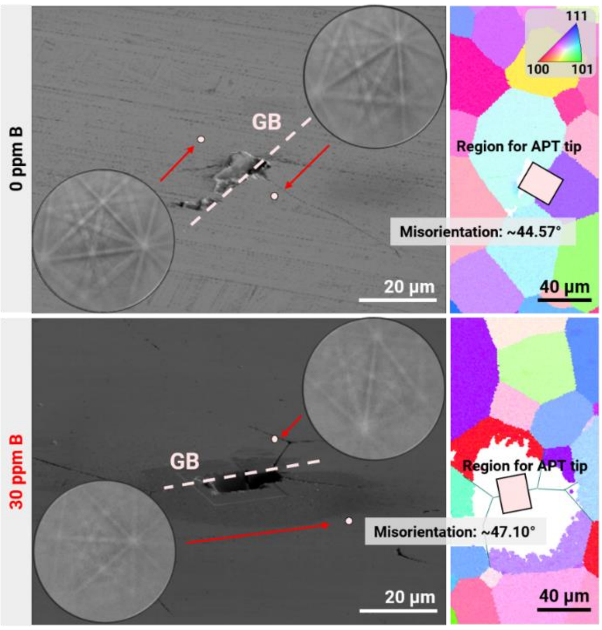
0 ppm B
GB
20 µm
111
100
101
Region for APT tip
Misorientation: ~44.57°
40 µm
30 ppm B
GB
20 µm
Region for APT tip
Misorientation: ~47.10°
40 µm

Fig. S5.3 Left: SEM images showing the lift-out position of the lamellar for APT tips with targeted grain boundaries and the corresponding Kikuchi patterns for the adjacent grains. Right: EBSD scans of the same regions shown on the left revealing the misorientation angle of the grain boundaries. The white regions shown in the EBSD maps are due to the contamination of the Ga$^+$ source during the lift-out of the lamellar. Both the grain boundaries are high-angle grain boundaries with an identical misorientation angle of 44.57° and 47.10° for the 0 ppm B and 30 ppm B samples, respectively.

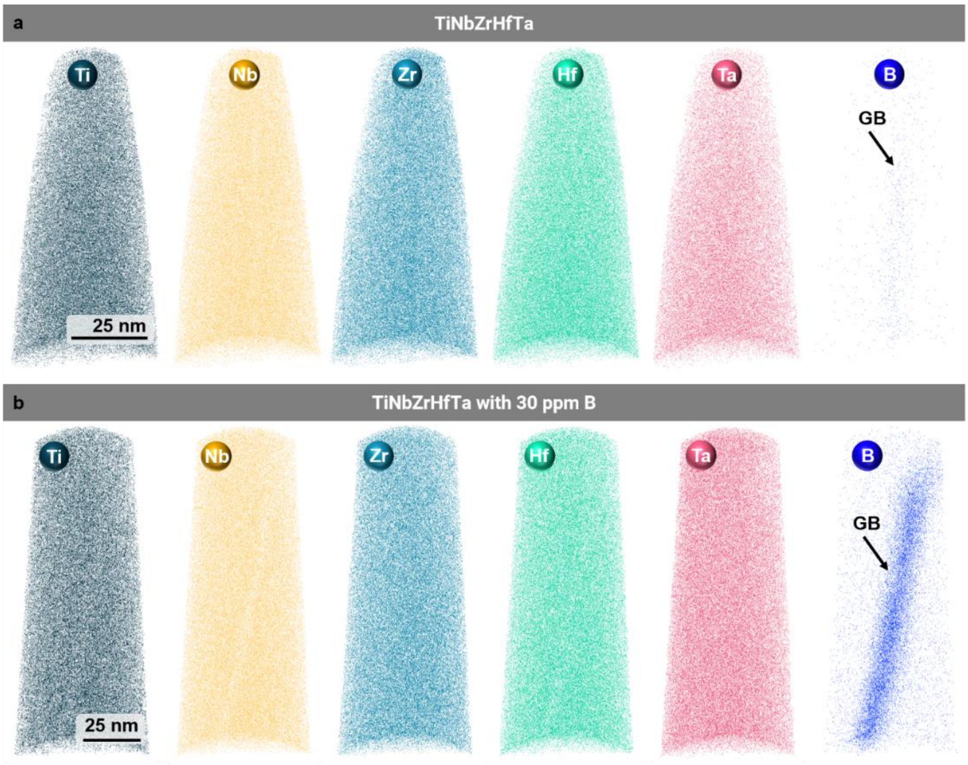
a
TiNbZrHfTa
Ti
Nb
Zr
Hf
Ta
B
GB
25 nm
b
TiNbZrHfTa with 30 ppm B
Ti
Nb
Zr
Hf
Ta
B
GB
25 nm

Fig. S5.4 3D dimensional atomic distribution including all the principle elements (Ti, Nb, Zr, Hf, Ta) as well as boron (B) of the TiNbZrHfTa CCAs with 0 ppm B and 30 ppm B. Grain boundaries in both cases are marked with black arrows.

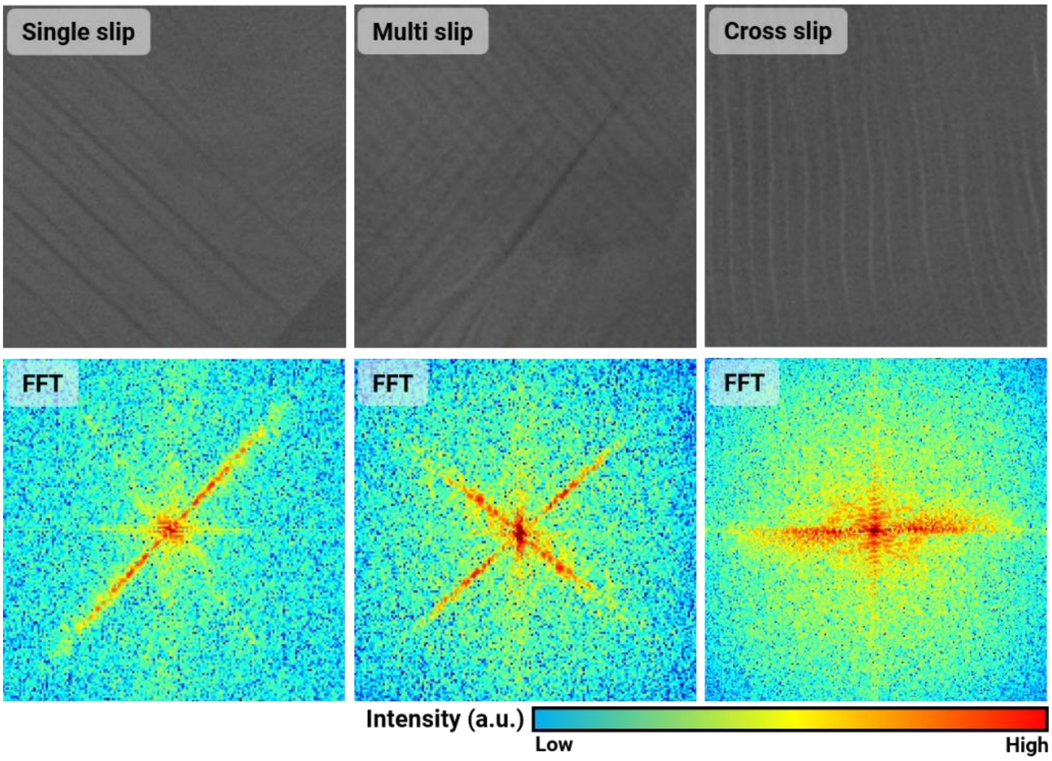
Single slip
Multi slip
Cross slip
FFT
FFT
FFT
Intensity (a.u.)
Low
High

Fig. S5.5 The standards used for the determination of different slip activities. For the single slip activity, the fast-Fourier transform (FFT) shows a single-line pattern, while a two-line FFT pattern (intersected with a certain degree) is revealed for the multi slip activity. As for the cross slip, the FFT pattern is diffuse without sharp lines.

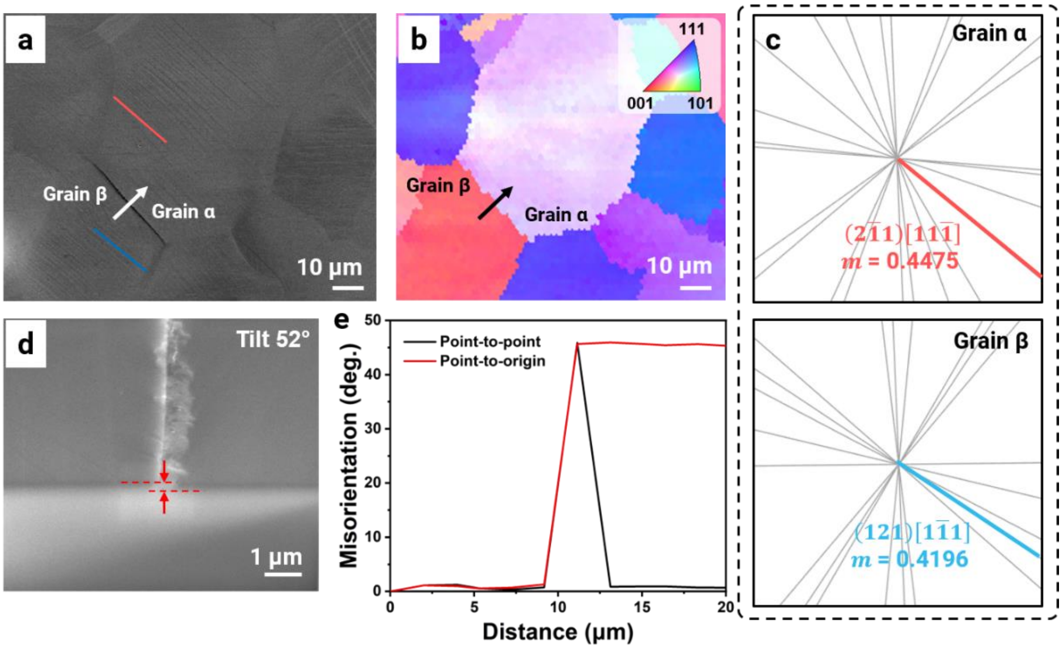

Fig. S5.6 Typical grain with grain boundary shear localization activity (with a high-angle grain boundary), and the corresponding crystallographic assessment of the slip traces on both grains.

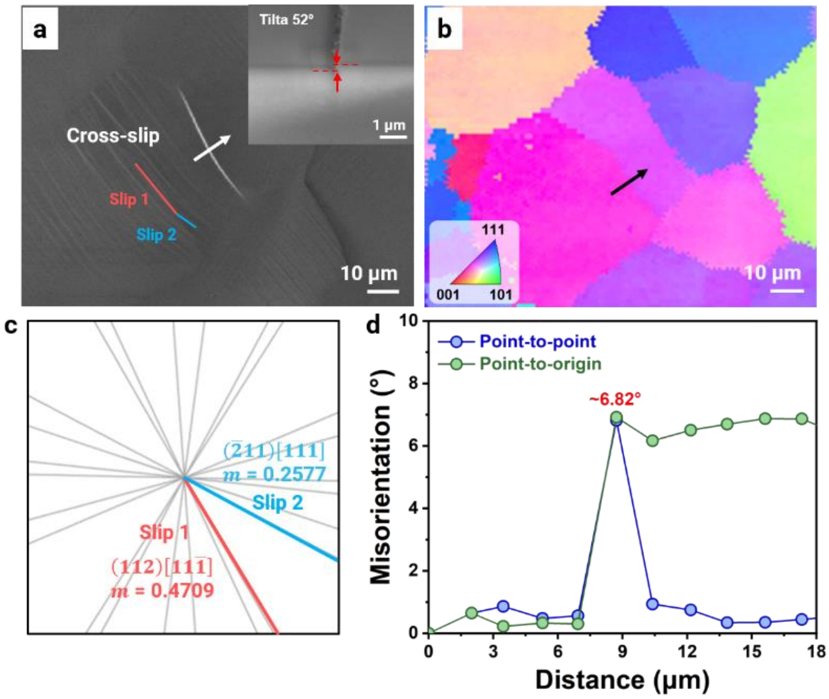

Fig. S5.7 Typical grain with grain boundary shear localization activity (with a low-angle grain boundary), and the corresponding crystallographic assessment of the slip trace.

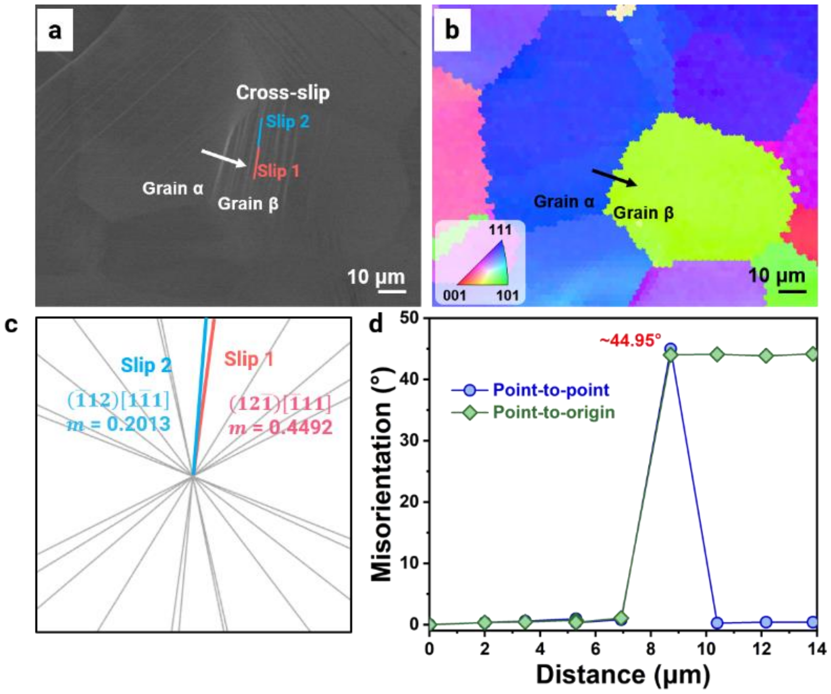

Fig. S5.8 Typical grain with grain boundary shear localization activity (with a high-angle grain boundary), and the corresponding crystallographic assessment of the slip trace.

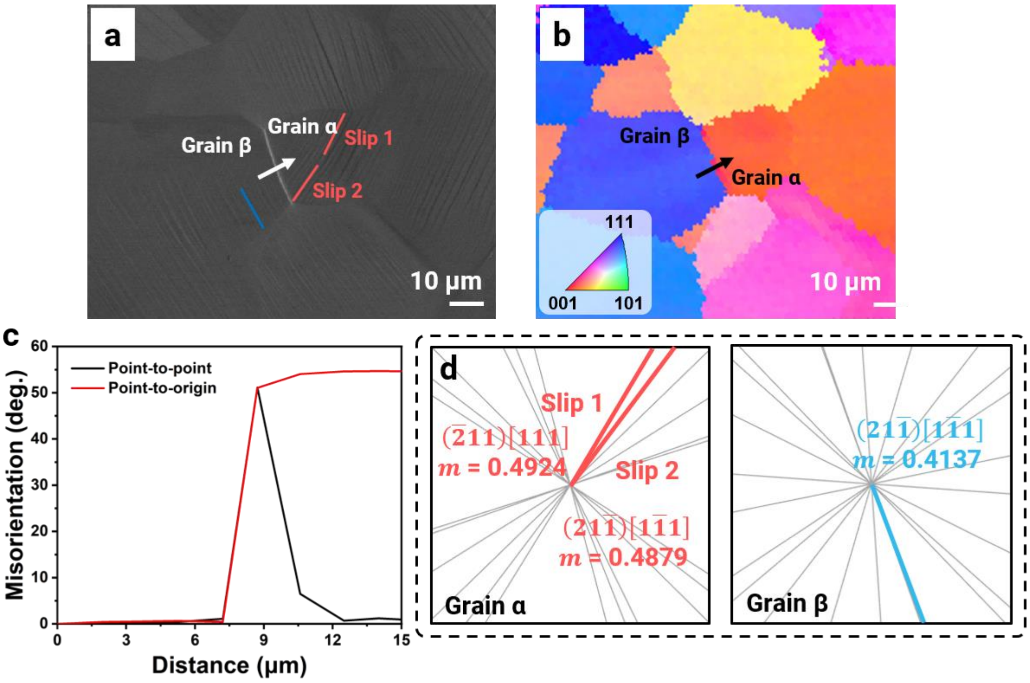

Fig. S5.9 Typical grain with grain boundary shear localization activity (with a high-angle grain boundary), and the corresponding crystallographic assessment of the slip traces on both grains.

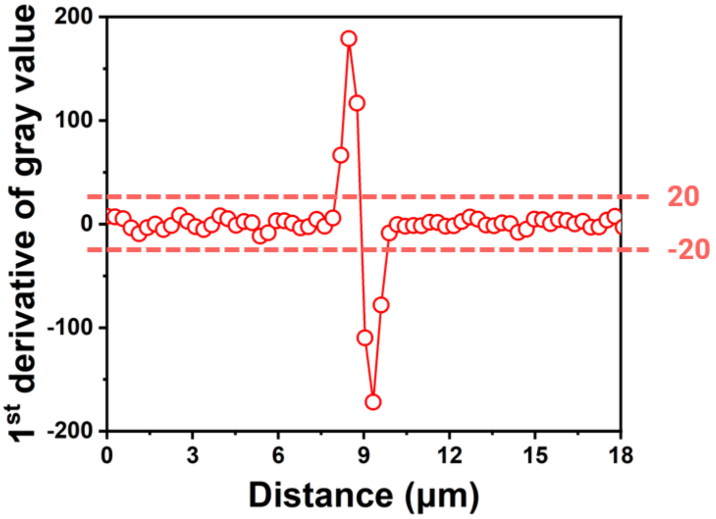

Fig. S5.10 1st derivative of the gray value obtained in Fig. 5.7d. In our study, we utilize the first derivative of the gray value as a standard to detect the presence of grain boundary shear localization within the grain boundary region. When the absolute value of the first derivative exceeds 20, we identify it as grain boundary shear localization.

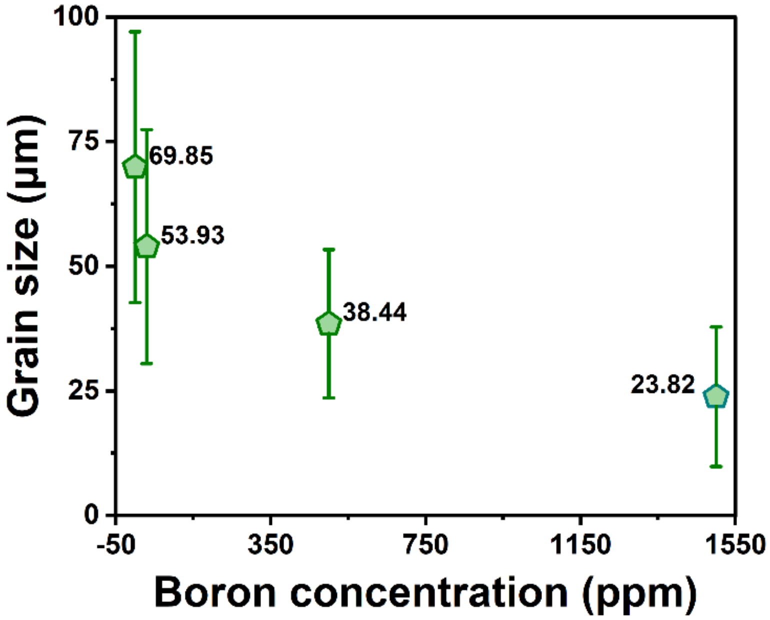

Fig. S5.11 Grain size as a function of boron concentration. For the 500 ppm and 1500 ppm cases, the potential formation of borides could also exert the Zener pining effects on the growth of grain boundaries.

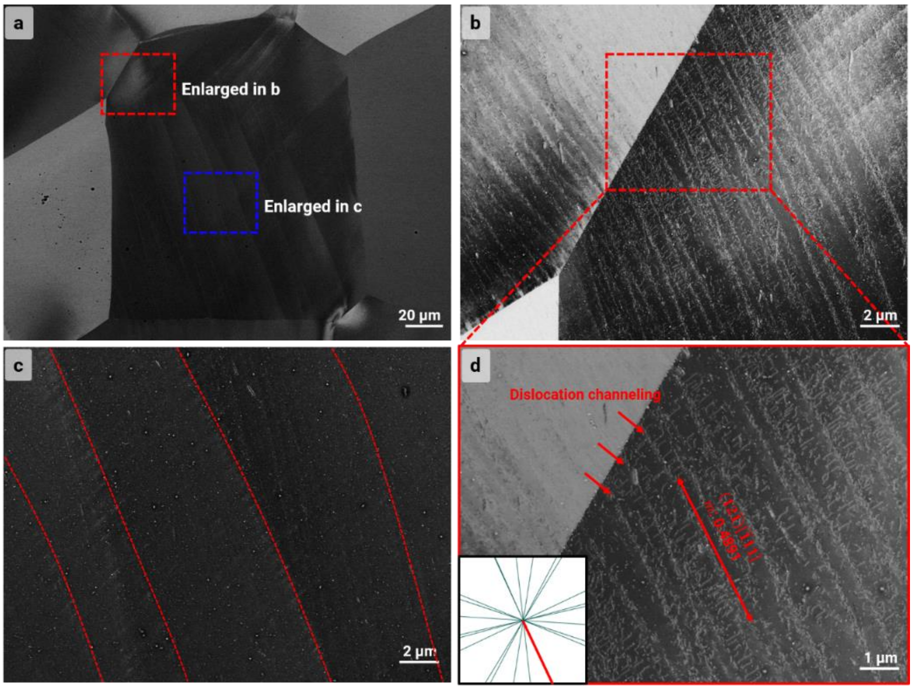
a
Enlarged in b
Enlarged in c
20 μm
b
2 μm
c
2 μm
d
Dislocation channeling
(121)[111]
m: 0.4891
1 μm

Fig. S5.12 Representative SEM images of the B-doped TiNbZrHfTa sample showing the dislocation behavior with a global strain of approximately 1.2% (after yielding). (a) The whole grain that we are interested in, where the grain boundary region and grain interior region are enlarged in (b) and (c) respectively to investigate the origin for dislocation emission. (d) Enlarged view of the rectangle region in (b). Dislocation channeling behavior can be observed, while the $(12\bar{1})[\bar{1}11]$ slip system is activated with a Schimid factor (m) of 0.4891.

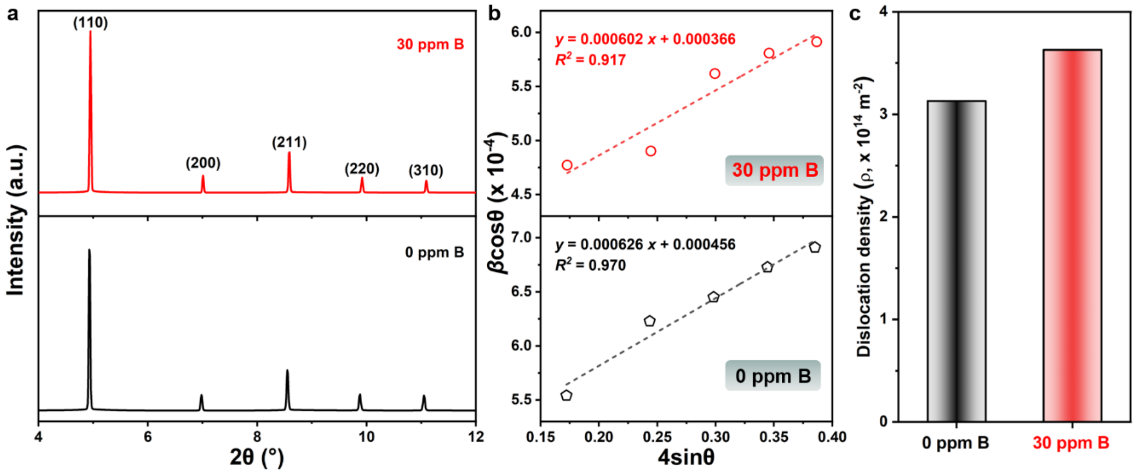

Fig. S5.13 (a) Synchrotron high-energy X-ray diffraction (SHEXRD) profiles of the TiNbZrHfTa CCAs with 0 ppm B and 30 ppm B at deformed region (0.5 mm away from fracture). No formation of secondary phases is found after the tensile test. (b) $\beta\cos\theta$ versus $4\sin\theta$ and the corresponding linear fitting curves for the determination of dislocation density. (c) Calculated dislocation density of the TiNbZrHfTa CCAs with 0 ppm B and 30 ppm B at the deformed region.

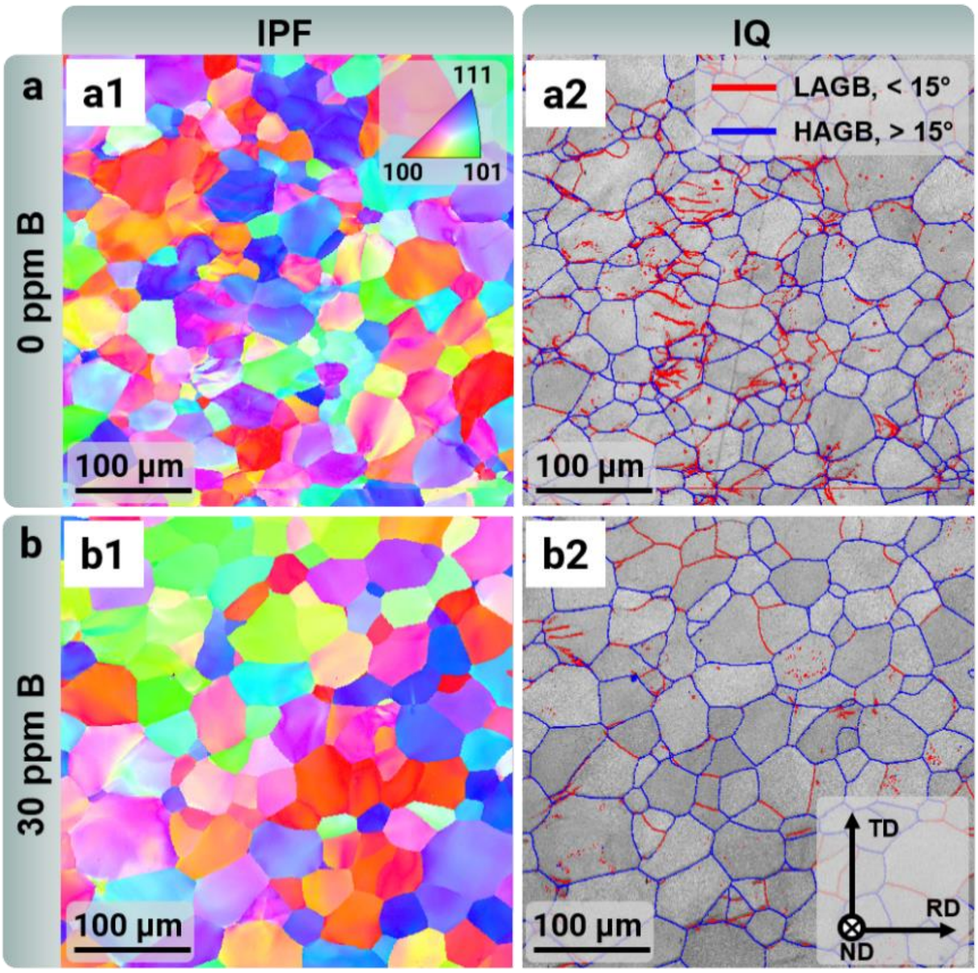
IPF
IQ
a
0 ppm B
a1
111
100
101
100 µm
a2
LAGB, < 15°
HAGB, > 15°
100 µm
b
30 ppm B
b1
100 µm
b2
100 µm
TD
RD
ND

Fig. S5.14 EBSD IQ + IPF maps and IQ + GB maps of the TiNbZrHfTa CCAs with 0 ppm B and 30 ppm B at the deformed region (0.5 mm away from the fracture), respectively.

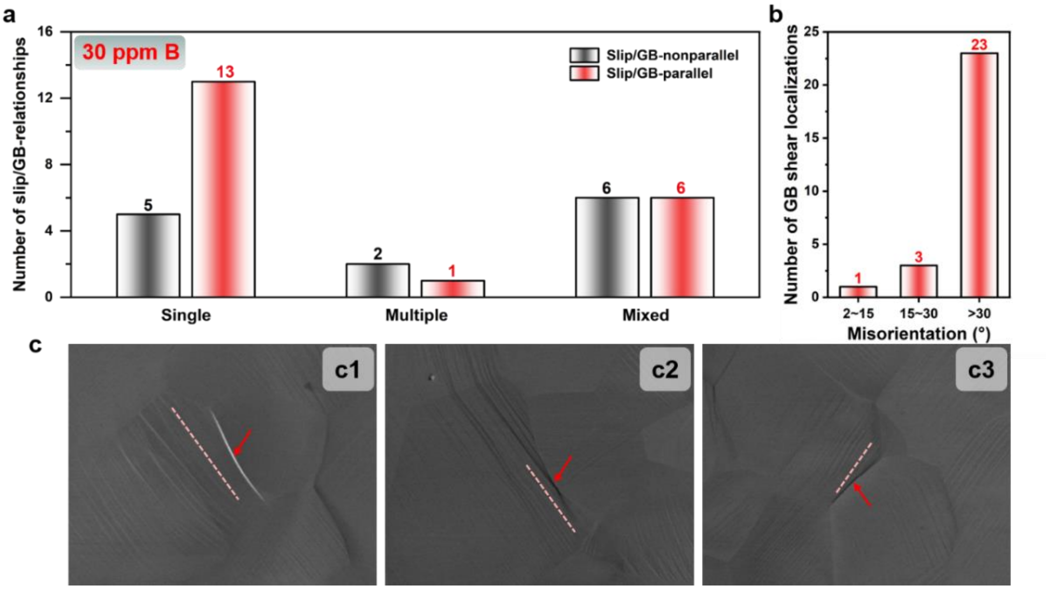

Fig. S5.15 (a) Quantitative assessment of the slip trace direction with the grain boundary for the grain boundary shear localization cases in the TiNbZrHfTa CCA with 30 ppm B. Single: slip is activated on only one grain; Multiple: slips are activated on both two grains and they are all parallel or non-parallel with the grain boundary. Mixed: slips are activated on both two grains. In this case, slip is parallel to grain boundary in one grain while slip is non-parallel to grain boundary in the other grain. (b) Frequency of the GB shear localization versus the misorientation between two grains in the TiNbZrHfTa CCA with 30 ppm B. (c1-c3) Some representative grain couples with grain boundary shear localization activity, where the slip traces on either side of the grains are parallel with the grain boundary.

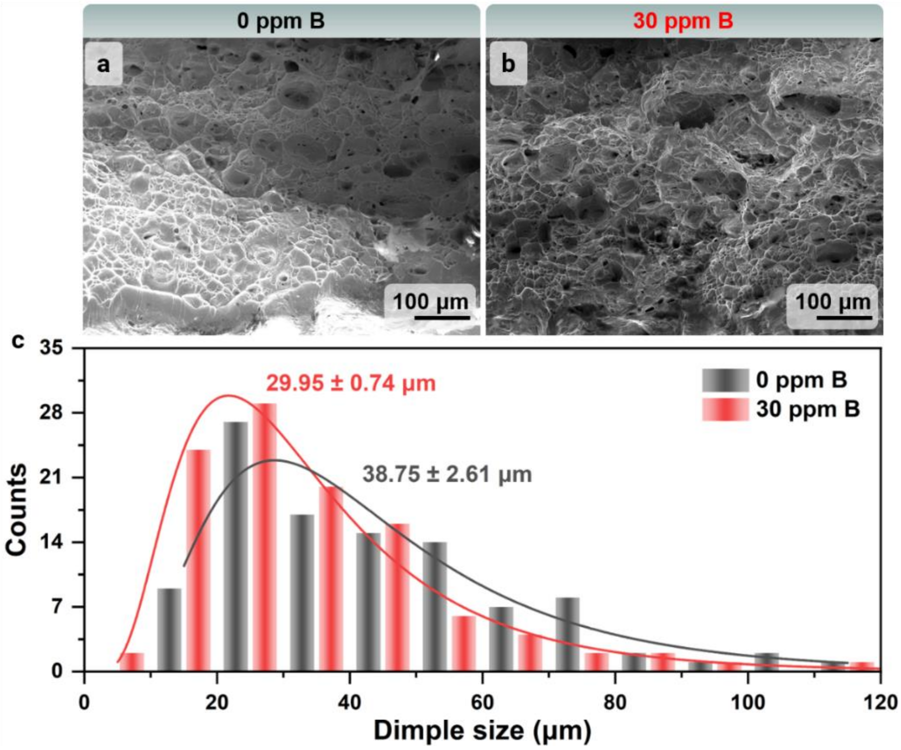

Fig. S5.16 Fractography analysis of the TiNbZrHfTa CCAs with (a) 0 ppm B and (b) 30 ppm B. (c) Dimple size distribution of the TiNbZrHfTa CCAs with 0 ppm B and 30 ppm B. Over 100 dimples were used for statistical

analysis, and we noted both cases exhibited a ductile fracture behavior with micro-size dimples, and no significant change on dimple sizes was found between two cases.

Table S5.1 Principle element composition obtained from energy-dispersive X-ray spectroscopy (EDS) analysis.

Element	**0 ppm B (at.%)**	**30 ppm B (at.%)**
Ti	19.77	19.21
Zr	21.27	20.66
Nb	18.75	18.74
Hf	20.70	20.86
Ta	19.51	20.52

Table S5.2 Shear modulus (G) of each principle elements [294, 295].

	Ti	**Nb**	**Zr**	**Hf**	**Ta**
***G* (GPa)**	21	38	18	30	69

Table S5.3 Summary of all the grain couples with grain boundary shear localization activity observed in the TiNbZrHfTa CCA with 0 ppm B as well as the corresponding crystallographic assessment of the observed slip traces.

Grain 1 / SF* / relationship	**Grain 2 / SF* / relationship**	**Misorientation (°)**
$(11\bar{2})[111]$ / 0.4034 / parallel	$(21\bar{1})[1\bar{1}1]$ / 0.3525 / parallel	46.52
$(231)[1\bar{1}1]$ / 0.3904 / parallel	-	53.61
$(\bar{2}11)[111]$ / 0.4201 / parallel	-	59.44
$(1\bar{1}1)[\bar{1}11]$ / 0.3660 / parallel	-	40.14
$(\bar{1}21)[11\bar{1}]$ / 0.4492/ nonparallel	-	36.26
$(2\bar{1}1)[11\bar{1}]$ / 0.3194 / parallel	(211)[-111] / 0.4821 / parallel	41.61
$(121)[1\bar{1}1]$ / 0.3968 / parallel	(132)[-111] / 0.4579 / nonparallel	33.11
$(1\bar{1}0)[11\bar{1}]$ / 0.4382 / parallel	-	51.76

* Schmid Factor

Table S5.4 Summary of all the grain couples with grain boundary shear localization activity observed in the TiNbZrHfTa CCA with 30 ppm B as well as the corresponding crystallographic assessment of the observed slip traces.

Grain 1 / SF* / relationship	**Grain 2 / SF* / relationship**	**Misorientation (°)**
$(110)[1\bar{1}1]$ / 0.3654 / parallel	-	43.63
$(\bar{1}21)[11\bar{1}]$ / 0.3271 / parallel		54.72
$(123)[11\bar{1}]$ / 0.3066 / parallel	$(\bar{1}21)[11\bar{1}]$ / 0.3271 / nonparallel	49.05

$(12\bar{1})[\bar{1}11]$ / 0.4492 / parallel	-	44.95
$(121)[\bar{1}11]$ / 0.4772 / parallel	-	26.49
$(132)[1\bar{1}1]$ / 0.4401 / nonparallel		
$(011)[\bar{1}1\bar{1}]$ / 0.3273 / parallel	$(1\bar{2}1)[111]$ / 0.3371 / nonparallel	57.97
$(211)[\bar{1}11]$ / 0.4000 / parallel	-	50.25
$(121)[1\bar{1}1]$ / 0.3805 / parallel	-	40.06
$(\bar{2}13)[1\bar{1}1]$ / 0.3926 / nonparallel	-	40.27
$(\bar{1}12)[1\bar{1}1]$ / 0.3109 / parallel	-	51.49
$(\bar{1}12)[1\bar{1}1]$ / 0.3109 / parallel	-	42.04
$(\bar{1}12)[1\bar{1}1]$ / 0.3109 / nonparallel	-	40.56
$(\bar{1}12)[1\bar{1}1]$ / 0.3109 / nonparallel	$(\bar{1}21)[11\bar{1}]$ / 0.2971 / nonparallel	38.99
$(110)[1\bar{1}\bar{1}]$ / 0.4597 / parallel	-	48.09
$(10\bar{1})[111]$ / 0.4265 / parallel	$(12\bar{1})[\bar{1}11]$ / 0.3408 / nonparallel	48.99
$(112)[11\bar{1}]$ / 0.2605 / parallel		36.62
$(211)[\bar{1}11]$ / 0.3976 / parallel	$(112)[11\bar{1}]$ / 0.2605 / nonparallel	45.24
$(211)[\bar{1}11]$ / 0.3976 / nonparallel	-	50.64
$(121)[1\bar{1}1]$ / 0.4332 / parallel	-	56.58
$(112)[11\bar{1}]$ / 0.4709 / parallel	-	6.85
$(\bar{1}21)[11\bar{1}]$ / 0.3552 / parallel	$(110)[1\bar{1}\bar{1}]$ / 0.3298 / nonparallel	39.23
$(110)[1\bar{1}\bar{1}]$ / 0.3298 / nonparallel	-	35.44
$(01\bar{1})[111]$ / 0.3331 / parallel	-	59.4
$(21\bar{3})[111]$ / 0.3996 / parallel	-	49.47
$(1\bar{1}2)[\bar{1}11]$ / 0.4780 / parallel	$(1\bar{1}2)[\bar{1}11]$ / 0.4842 / parallel	16.91
$(2\bar{3}1)[111]$ / 0.4687 / nonparallel	-	55.65
$(112)[11\bar{1}]$ / 0.4936 / nonparallel	$(2\bar{3}1)[111]$ / 0.3615 / nonparallel	25.98

* Schmid Factor

Table S5.5 Summary of all the grain couples where slip traces intersect with the grain boundaries in the TiNbZrHfTa CCA with 0 ppm B as well as the corresponding misorientation angle between two grains and the Luster-Morris *m'* factor. Cases with or without slip transfer are surveyed over 20 sets of grain couples.

Orientation of grain 1	Orientation of grain 2	Misorientation angle	*m'*	Slip transfer
(184.6°, 117.5°, 338.8°)	(113.6°, 42.3°, 270.6°)	57.03	0.0359	No
(144.5°, 12.5°, 238.5°)	(211.8°, 46.0°, 120.8°)	68.62	0.4615	No
(211.8°, 46.0°, 120.8°)	(206.2°, 28.5°, 158.8°)	37.66	0.7988	No
(211.8°, 46.0°, 120.8°)	(305.1°, 28.4°, 50.3°)	54.54	0.535	No
(83.3°, 20.8°, 238.5°)	(109.9°, 34.1°, 283.1°)	70.54	0.318	No
(59.1°, 41.9°, 256.8°)	(88.7°, 31.8°, 274.9°)	46.43	0.702	No
(161.0°, 22.6°, 221.2°)	(306.0°, 15.6°, 31.4°)	58.75	0.4233	No
(306.0°, 15.6°, 31.4°)	(291.3°, 9.6°, 104.7°)	59.39	0.5057	No
(154.5°, 41.9°, 236.0°)	(291.3°, 9.6°, 104.7°)	49.51	0.4522	No
(263.3°, 20.9°, 70.4°)	(43.0°, 53.6°, 302.9°)	70.61	0.2823	No
(43.0°, 53.6°, 302.9°)	(227.3°, 23.1°, 134.8°)	78.48	0.2198	No

(244.9°, 43.0°, 138.6°)	(55.8°, 37.2°, 315.8°)	80.78	0.1752	No
(244.9°, 43.0°, 138.6°)	(109.9°, 34.187, 283.1°)	72.95	0.312	No
(284.8°, 16.3°, 39.8°)	(54.2°, 50.2°, 302.4°)	65.98	0.344	No
(68.0°, 44.2°, 276.6°)	(53.7°, 16.8°, 298.0°)	29.52	0.8232	No
(53.7°, 16.8°, 298.0°)	(9.8°, 26.2°, 357.4°)	25.76	0.8601	No
(287.7°, 17.4°, 78.1°)	(9.8°, 26.2°, 357.4°)	29.31	0.8708	No
(272.5°, 40.3°, 55.4°)	(309.5°, 43.6°, 45.6°)	30.74	0.8596	No
(228.5°, 25.7°, 92.0°)	(71.4°, 34.390, 254.4°)	59.38	0.3517	No
(139.4°, 53.4°, 223.0°)	(104.7°, 24.6°, 226.03°)	43.05	0.6558	No
(112.9°, 45.9°, 220.1°)	(94.8°, 25.0°, 306.4°)	74.89	0.2424	No
(314.0°, 21.7°, 62.2°)	(137.7°, 55.7°, 227.6°)	78.11	0.0485	No
(306.6°, 51.7°, 43.3°)	(91.7°, 20.4°, 309.6°)	81.18	0.1232	No
(306.6°, 51.7°, 43.3°)	(290.9°, 16.4°, 89.6°)	48.25	0.5403	No
(247.1°, 48.7°, 113.4°)	(242.2°, 24.4°, 77.2°)	46.75	0.6623	No
(110.4°, 38.2°, 229.6°)	(242.2°, 24.4°, 77.2°)	62.71	0.2601	No
(228.5°, 25.7°, 92.0°)	(71.4°, 34.3°, 254.4°)	59.38	0.352	No
(81.0°, 8.1°, 239.4°)	(56.7°, 30.5°, 282.6°)	30.59	0.8423	No
(93.9°, 27.0°, 253.5°)	(70.3°, 45.6°, 303.9°)	37.87	0.7998	No
(245.0°, 20.8°, 80.7°)	(248.2°, 32.9°, 141.4°)	64.7	0.434	No
(262.09°, 42.74°, 87.43°)	(203.3°, 62.1°, 319.7°)	12.59	0.5142	Yes
(59.11°, 41.93°, 256.84°)	(305.17°, 28.4°, 50.34°)	75.5	0.1797	Yes
(256.9°, 11.5°, 92.70°)	(307.7°, 29.1°, 51.62°)	24.57	0.8433	Yes
(266.67°, 2.84°, 65.29°)	(233.1°, 20.9°, 106.63°)	20.26	0.9281	Yes
(259.47°, 14.76°, 136.57°)	(233.1°, 20.9°, 106.63°)	55.93	0.5604	Yes
(190.6°, 121.9°, 49.4°)	(189.2°, 122.6°, 47°)	2.15	0.9992	Yes
(111.26°, 24.79°, 292.85°)	(94.8°, 25.0°, 306.94°)	7.002	0.9859	Yes
(258.72°, 18.6°, 64.85°)	(216.9°, 46.1°, 113.85°)	36.13	0.8102	Yes
(44.81°, 47.7°, 326.66°)	(44.16°, 6.99°, 340.49°)	42.81	0.7214	Yes
(66.20°, 51.30°, 321.91°)	(70.0°, 47.9°, 313.98°)	7.11	0.9909	Yes
(258.9°, 41.2°, 82.14°)	(157.8°, 11.35°, 234.15°)	69.78	0.3616	Yes
(299.0°, 14.7°, 31.18°)	(70.7°, 22.4°, 322.86°)	69.23	0.3708	Yes
(58.3°, 6.9°, 72.7°)	(259.1°, 171.6°, 213.9°)	2.22	0.9953	Yes
(222.2°, 10.9°, 173.87°)	(90.331°, 8.1°, 295.29°)	19.99	0.9381	Yes
(267.7°, 39.7°, 49.65°)	(90.3°, 8.145°, 295.29°)	81.77	0.1809	Yes
(260.3°, 23.5°, 131.86°)	(251.0°, 39.5°, 129.87°)	19.44	0.9416	Yes
(253.0°, 27.7°, 66.69°)	(38.8°, 24.3°, 321.28°)	61.17	0.4757	Yes
(82.3°, 16.0°, 257.74°)	(274.898°, 22.43°, 66.78°)	38.34	0.6487	Yes
(60.4°, 38.9°, 263.12°)	(198.9°, 49.8°, 128.01°)	82.65	0.1129	Yes
(211.5°, 10.5°, 109.70°)	(67.5°, 44.9°, 306.81°)	75.99	0.3301	Yes
(248.7°, 38.5°, 76.78°)	(88.1°, 20.9°, 286.15°)	76.39	0.2672	Yes
(248.7°, 38.5°, 76.78°)	(217.9°, 18.4°, 113.16°)	25.81	0.8246	Yes
(258.8°, 33.3°, 89.66°)	(217.9°, 18.4°, 113.16°)	26.45	0.8277	Yes
(69.2°, 27.6°, 255.01°)	(261.7°, 20.6°, 109.90°)	67.17	0.3836	Yes
(69.2°, 27.6°, 255.01°)	(227.5°, 30.5°, 116.17°)	59.11	0.4303	Yes
(15.9°, 26.6°, 301.92°)	(227.5°, 30.5°, 116.17°)	61.88	0.4949	Yes
(245.6°, 12.1°, 140.47°)	(253.1°, 47.63°, 137.87°)	35.87	0.8106	Yes
(309.2°, 15.5°, 82.71°)	(226.7°, 26.96°, 116.27°)	53.33	0.5922	Yes
(288.7°, 41.2°, 63.50°)	(292.7°, 25.0°, 56.56°)	16.61	0.9258	Yes
(232.8°, 39.2°, 91.62°)	(292.7°, 25.0°, 56.56°)	37.45	0.7985	Yes
(236.4°, 38.1°, 124.38°)	(56.75°, 30.5°, 282.67°)	71.55	0.3154	Yes

Table S5.6 Summary of all the grain couples where slip traces intersect with the grain boundaries in the TiNbZrHfTa CCA with 30 ppm B as well as the corresponding misorientation angle between two grains and the Luster-Morris *m'* factor. Cases with or without slip transfer are surveyed over 20 sets of grain couples.

Orientation of grain 1	Orientation of grain 2	Misorientation angle	*m'*	Slip transfer
(35.25°, 56.2°, 308.3°)	(315.5°, 32.4°, 44.51°)	65.08	0.4204	No
(35.2°, 56.2°, 308.31°)	(93.6°, 30.4°, 268.71°)	45.88	0.6338	No
(337.7°, 31.8°, 30.20°)	(21.3°, 8.1°, 347.24°)	26.47	0.8017	No

(80.1°, 27.6°, 265.29°)	(110.1°, 9.4°, 293.21°)	59.86	0.5273	No
(73.3°, 9.3°, 245.21°)	(33.1°, 35.4°, 355.31°)	76.58	0.3029	No
(33.1°, 35.4°, 355.31°)	(306.3°, 26.6°, 54.88°)	45.85	0.7013	No
(33.1°, 35.4°, 355.32°)	(137.0°, 24.2°, 198.66°)	75.03	0.2916	No
(160.4°, 24.63°, 163.92°)	(275.2°, 15.3°, 48.94°)	33.96	0.7407	No
(292.5°, 9.0°, 43.25°)	(217.6°, 52.4°, 126.28°)	51.97	0.6222	No
(275.2°, 15.3°, 48.94°)	(41.4°, 54.3°, 300.95°)	65.15	0.3534	No
(275.2°, 15.3°, 48.95°)	(25.8°, 23.9°, 17.20°)	81.49	0.256	No
(25.8°, 23.9°, 17.20°)	(149.1°, 43.7°, 218.53°)	72.76	0.1545	No
(25.8°, 23.9°, 17.21°)	(306.0°, 10.9°, 19.44°)	78.51	0.2624	No
(75.3°, 46.6°, 317.25°)	(83.3°, 44.13°, 265.16°)	46.81	0.6836	No
(135.9°, 42.3°, 236.53°)	(78.8°, 43.2°, 320.14°)	54.67	0.5198	No
(269.0°, 13.3°, 131.42°)	(89.1°, 25.0°, 313.30°)	38.35	0.784	No
(22.93°, 24.6°, 339.86°)	(89.1°, 25.01°, 313.31°)	43.39	0.6545	No
(41.7°, 53.9°, 301.77°)	(176.2°, 31.3°, 191.46°)	78.66	0.1955	No
(48.4°, 27.2°, 322.62°)	(176.2°, 31.3°, 191.47°)	52.92	0.5329	No
(48.49°, 27.2°, 322.63°)	(312.9°, 36.8°, 50.81°)	46.84	0.5705	No
(15.3°, 45.1°, 1.60°)	(344.5°, 40.1°, 45.59°)	29.86	0.8703	No
(101.3°, 26.2°, 283.15°)	(245.9°, 35.5°, 141.68°)	58.69	0.513	No
(246.9°, 23.2°, 128.81°)	(322.1°, 46.9°, 44.86°)	48.85	0.4944	No
(246.9°, 23.2°, 128.82°)	(215.3°, 49.3°, 131.95°)	66.81	0.2161	No
(246.9°, 23.2°, 128.83°)	(302.2°, 54.55°, 35.29°)	64.12	0.3235	No
(302.2°, 54.5°, 35.29°)	(219.5°, 61.8°, 126.43°)	78.72	0.2415	No
(261.3°, 21.0°, 74.38°)	(76.3°, 38.7°, 250.37°)	60.35	0.3057	No
(234.1°, 39.6°, 94.05°)	(172.45°, 21.4°, 203.58°)	63.7	0.429	No
(329.1°, 18.8°, 359.48°)	(73.6°, 48.9°, 320.63°)	78.18	0.2372	No
(35.2°, 56.2°, 308.30°)	(315.5°, 32.4°, 44.51°)	77.3	0.0261	No
(35.2°, 56.2°, 308.31°)	(93.63°, 30.4°, 268.71°)	84.61	0.0499	No
(31.2°, 51.4°, 318.77°)	(295.5°, 21.9°, 33.41°)	57.54	0.4887	Yes
(316.3°, 40.3°, 61.70°)	(275.1°, 16.1°, 80.86°)	34.87	0.7183	Yes
(275.1°, 16.1°, 80.86°)	(304.9°, 31.3°, 43.37°)	21.43	0.8872	Yes
(295.56°, 21.9°, 33.41°)	(304.9°, 31.3°, 43.38°)	21.04	0.9222	Yes
(21.3°, 8.1°, 347.24°)	(234.9°, 9.9°, 153.22°)	26.4	0.8915	Yes
(234.9°, 9.9°, 153.22°)	(228.2°, 37.1°, 118.75°)	48.63	0.685	Yes
(83.7°, 63.4°, 313.5°)	(257.8°, 127.0°, 302.5°)	3.996	0.94	Yes
(275.1°, 16.1°, 80.86°)	(306.2°, 18.34°, 49.00°)	9.571	0.9822	Yes
(329.4°, 48.9°, 36.52°)	(336.5°, 51.2°, 44.07°)	15.65	0.9532	Yes
(316.3°, 156.5°, 340.2°)	(23.0°, 24.7°, 249.1°)	26.65	0.5682	Yes
(25.8°, 23.96°, 17.20°)	(83.3°, 44.1°, 365.16°)	45.45	0.7191	Yes
(104.6°, 17.8°, 229.28°)	(106.4°, 27.63°, 228.10°)	9.736	0.9717	Yes
(113.4°, 26.7°, 235.50°)	(74.8°, 13.9°, 254.57°)	25.04	0.8719	Yes
(319.7°, 14.1°, 6.32°)	(74.8°, 13.9°, 254.58°)	25.32	0.8188	Yes
(267.3°, 149.9°, 310.5°)	(89.1°, 25.0°, 313.30°)	1.161	0.9925	Yes
(231.46°, 33.0°, 151.03°)	(246.90°, 23.2°, 128.81°)	14.84	0.9572	Yes
(246.9°, 23.29°, 128.81°)	(245.9°, 35.5°, 141.68°)	17.19	0.9558	Yes
(244.92°, 13.5°, 86.37°)	(105.36°, 20.5°, 274.64°)	59.04	0.4921	Yes
(100.3°, 18.0°, 289.89°)	(105.3°, 20.5°, 274.65°)	10.97	0.9806	Yes
(76.33°, 38.7°, 250.37°)	(58.6°, 52.9°, 321.17°)	59.93	0.5228	Yes
(39.0°, 60.1°, 283.7°)	(219.5°, 120.5°, 339.9°)	0.1455	0.9932	Yes
(280.2°, 137.5°, 320.8°)	(94.4°, 46.7°, 44.6°)	5.833	0.0244	Yes
(325.1°, 116.6°, 119.8°)	(142.7°, 63.0°, 147.5°)	1.984	0.9965	Yes
(100.4°, 36.0°, 231.94°)	(211.9°, 18.6°, 148.39°)	50.58	0.5394	Yes
(121.1°, 52.70°, 210.80°)	(100.7°, 53.5°, 50.6°)	7.331	0.951	Yes
(234.5°, 146.0°, 310.0°)	(59.3°, 33.9°, 318.7°)	2.68	0.9967	Yes
(53.3°, 76.9°, 9.3°)	(53.1°, 79.1°, 9.6°)	2.224	0.9987	Yes

Table S5.7 Summary of the slip direction misalignments and slip plane misalignments of all the cases with slip transfer in both the non-boron and boron-doped TiNbZrHfTa CCAs alloys.

0 ppm B		30 ppm B	
Slip direction misalignment (°)	Slip plane misalignment (°)	Slip direction misalignment (°)	Slip plane misalignment (°)
2.701	87.54	56.69	27.12
58.33	69.97	29.81	34.1
23.43	23.2	18.99	20.25
18.63	11.74	10.35	20.37
9.968	55.32	17.35	20.95
1.523	1.667	27.29	39.66
6.947	6.679	11.54	11.54
34.05	12.08	9.311	5.545
40.8	17.64	5.907	12.29
4.513	6.304	38.89	41.22
44.56	59.57	36.13	35.8
33.92	63.46	9.727	9.742
3.124	4.634	17.9	23.51
17.38	10.6	23.63	23.63
47.79	74.38	5.167	4.696
16.69	10.68	12.14	11.74
49.65	42.61	12.31	11.97
38.27	34.28	31.94	54.56
81.9	34.98	2.992	10.92
53.75	56.07	18.94	57.63
58.56	59.15	0.6607	6.653
24.3	25.21	5.847	88.59
22.5	26.37	2.179	4.271
47.9	55.09	45.73	39.39
56.97	37.87	16.38	7.701
54.77	30.93	2.682	3.792
35.63	4.195	2.209	1.921

29	47.39
16.24	15.38
33.33	17.07
68.7	29.74

Note 1. Evaluation of grain boundary shear localization via the sliding rate of grains

Grain boundary sliding usually occurs by the climb and glide of dislocation, where the rate of sliding is primarily dominated by climb rate since this is a slower process as compared to glide [306]. Then, the frequency of climb can be expressed as [306],

$$\nu_c = p_j \nu (z-1) \exp\left({}^{S_d}/_{k}\right) \exp\left(-{}^{U_d}/_{kT}\right) \{\exp(\tau_x\, \Omega / k\, T) - 1\} \qquad \text{(S5.1)}$$

where p_j, ν, z, S_d, U_d, τ_x, and Ω denote the probability of finding a jog on a dislocation, the vibrational frequency of an atom, the coordination number, the entropy of activation for diffusion, the energy of activation for diffusion, the stress required to induce climb along the boundary, and the activation volume, respectively.

The rate of climb along the grian boundary can be written as,

$$\dot{s} = Nb\nu_c \qquad \text{(S5.2)}$$

Here, N is the number of grain boundary dislocations per unit length, while b represents the Burgers vector. Given that dislocations are uniformly distributed along the grain boundary and the dislocation spacing is determined by a stress field around a single-edge dislocation, gives:

$$N \propto {}^{2\pi(1-\mu)\tau}/_{Gb} \qquad \text{(S5.3)}$$

where μ, τ, and G are Poisson's's ratio, shear stress, and shear modulus, respectively. Assuming the dislocations move in a zone adjacent to the boundary, then $U_{gbs} \propto U_{sd}$, the first equation can be simplified using the lattice self-diffusion coefficient, D_l:

$$D_l \propto b^2 \nu \exp\left({}^{S_d}/_{k}\right) \exp\left(-{}^{U_d}/_{kT}\right) \qquad \text{(S5.4)}$$

with $U_d \equiv U_{sd}$. The shear strain rate in a climb-glide process $\dot{\gamma}_{gbs}$, controlled by the rate of climb but producing strain through glide, is

$$\dot{\gamma}_{gbs} = MAb\dot{s} \qquad \text{(S5.5)}$$

where M and A are the number of boundaries per unit volume and the total area swept out by dislocations moving along a boundary. Dislocations sink into the grain boundaries through slip on either side of the boundary, so M and A can be addressed as ${}^{6}/_{\pi d^3}$ and πd^2, where d is the average grain diameter. Together with taking b^3 for Ω, $\tau = \tau_x = {}^{\sigma}/_{2}$, and $\dot{\gamma}_{gbs} = \frac{3\dot{\epsilon}_{gbs}}{4}$ for $\tau_x \Omega << kT$, gives:

$$\dot{\gamma}_{gbs} \sim \dot{\epsilon}_{gbs} \sim \frac{4\pi p_j b^2 (1-\mu)(z-1)\sigma^2}{dGkT} D_l \qquad \text{(S5.6)}$$

To make use of the above equation, an assumption is necessary concerning p_j. Since dislocations in BCC-type alloys don't dissociate into partials, particularly in the boundary, p_j is probably close to the equilibrium value given by $p_j = exp(\frac{U_j}{kT})$, where U_j is the jog energy. Taking $p_j \sim 10^{-2}$, $\mu \sim 0.3$, and putting $z = 8$ for BCC materials, gives:

$$\dot{\gamma}_{gbs} = \frac{\beta b^2 \sigma^2}{dGkT} D_l \qquad \text{(S5.7)}$$

where β is a constant depending on the materials.

6. Ductilization of a TiNbZr refractory complex concentrated alloy via the strain delocalization by nanoscale chemical heterogeneity

This chapter is a modified version based on the paper entitled "*Ductilization of a TiNbZr refractory complex concentrated alloy via the strain delocalization by nanoscale chemical heterogeneity*" (In preparation)

6.1. Introduction

Refractory complex concentrated alloys (RCCAs) have gained increasing attention as a promising class of high-performance materials designed for extreme environments, such as aerospace applications, nuclear reactors, and hydrogen storage systems [24, 54, 57, 313]. Unlike traditional alloys that rely on a single principal element, RCCAs comprise multiple refractory elements (typically three or more) with concentrations ranging from 5 to 35 at.%, significantly expanding the compositional space for alloy design [2, 314]. Due to the observed four core effects (*i.e.*, high entropy, lattice distortion, sluggish diffusion, and cocktail effects) in RCCAs, these materials can be tailored to exhibit exceptional mechanical properties, thermal stability, and corrosion resistance, making them versatile for a wide range of applications [315-318]. Among RCCAs, TiNbZr-based alloys with a body-centered cubic (BCC) have garnered particular interest due to their excellent corrosion/oxidation resistance, biocompatibility, and tunable mechanical properties [319-323]. For example, TiNbZr RCCAs exhibit lower density (*e.g.*, ~5.1 $g{\cdot}cm^{-3}$ for Ti-10Nb-10Zr) compared to other refractory systems, making them also ideal for lightweight structural applications [323]. Additionally, in biomedical fields, TiNbZr alloys are also considered as next-generation implant materials due to their low elastic modulus (40~60 GPa), which closely matches that of human bone, thereby mitigating stress-shielding effects [320].

Despite their promising attributes, achieving a synergistic enhancement of both strength and ductility in BCC RCCAs remains a challenge. In contrast to face-centered cubic (FCC) alloys, where the planar nature of dislocation cores facilitates relatively easy dislocation glide on the $\{111\}$ family of crystallographic planes, the non-planar core structure of screw dislocations in BCC alloys limits the availability of easily activated slip systems [12, 324, 325]. Dislocation glide predominantly occurs in the $\langle 111 \rangle$ directions without well-defined slip planes [12]. While the $\{110\}$ family of planes serves as the primary slip planes, additional slip can be activated on the $\{112\}$ and $\{123\}$ families of crystallographic planes, particularly under high strain rates, contributing to the complexity of slip behavior in BCC alloys [18, 324, 325]. BCC alloys also feature less densely packed atomic planes, resulting in high Peierls barriers that impede dislocation motion [12, 324]. These characteristics primarily contribute to the inherent susceptibility of BCC alloys to strain localization (*e.g.*, necking) and premature failure due to the limited strain-hardening capability [6, 326]. When strain localization appears, BCC alloys typically experience rapid strain softening, which accelerates damage accumulation and reduces their ability to sustain further plastic deformation [12, 326, 327]. Additionally, the intrinsically high stacking fault energy of refractory elements (*e.g.*, ~400 mJ/m^2 for pure Ti) further suppresses the tendency for twinning, reducing the capacity for plastic deformation [328]. Addressing this strength-ductility trade-off in BCC alloys necessitates the development of microstructural design strategies that can enhance strain hardening while preserving strength. Various strategies have been explored to overcome the restricted strain-hardening capacity. Grain refinement through severe plastic deformation or rapid solidification processing has been demonstrated to improve strength while maintaining moderate ductility [329-331]. Precipitation strengthening has also been employed to enhance mechanical performances; however, strain incompatibility between the matrix and secondary phases often leads to embrittlement [315, 332, 333]. More recently, nanoscale compositional heterogeneity has been introduced as a means to manipulate local mechanical responses, improve strain hardening, and enhance damage tolerance [52]. Although these approaches provide insights into increasing yield strength, the sacrifice of ductility remains inevitable. Therefore, finding a strategy to enhance strain-hardening behavior without compromising ductility is critical for the advancement of BCC RCCAs.

In this study, we investigate the effect of a short-term induction treatment on the mechanical behavior of a TiNbZr RCCA, with a particular emphasis on its influence on ductility and strain-hardening mechanisms. Our findings reveal that: (1) The short-term induction treatment leads to an increase in oxygen content, which intensifies Ti concentration fluctuations, promoting localized compositional heterogeneity. These Ti-rich nanofeatures exhibit an ellipsoidal morphology. (2) The Ti-rich nanoscale heterogeneities significantly strongly pin dislocations, enhancing strain-hardening capacity. Concurrently, an increase in strain rate sensitivity is observed, contributing to improved ductility while maintaining yield strength comparable to that of the homogenized sample. (3) The refinement of deformation bands, along with a reduction in the density of geometrically necessary dislocations (GNDs), is observed in the induction-treated sample, leading to a more homogeneous strain distribution. By elucidating the underlying mechanisms governing the enhanced mechanical performance, this study provides valuable insights into the role of nanoscale chemical heterogeneity in tuning the deformation behavior of a TiNbZr RCCA. Our findings highlight the potential of induction treatment as an effective processing strategy for optimizing the strength-ductility synergy in TiNbZr-based alloys.

6.2. Experimental sections

6.2.1. Materials

The pure metals with a purity of 99.99 wt.% were used as the base alloy. The equiatomic TiNbZr RCCA was cast using arc-melting under the Ar atmosphere. During the arc-melting process, the RCCA ingots were remelted at least five times to ensure a homogeneous distribution of all the principle elements. A piece of Ti getter was employed to prevent potential oxygen contamination. The as-casted samples were cold-rolled with a thickness reduction of 80% and then homogenized at 1000 °C for 5 h, followed by air quenching to ambient temperature (**Fig. 6.1**). The as-homogenized samples were further induction-treated in an induction heated tube furnace with a powder density of 45%. The gas pipeline was purged three times with high-purity N_2 (99.999%) and evacuated after each purge before the induction treatment. Five cycles of induction treatment were conducted (approximately 5 s for isothermal holding) under a mixed gas atmosphere (N_2 with ~1 vol.% O_2).

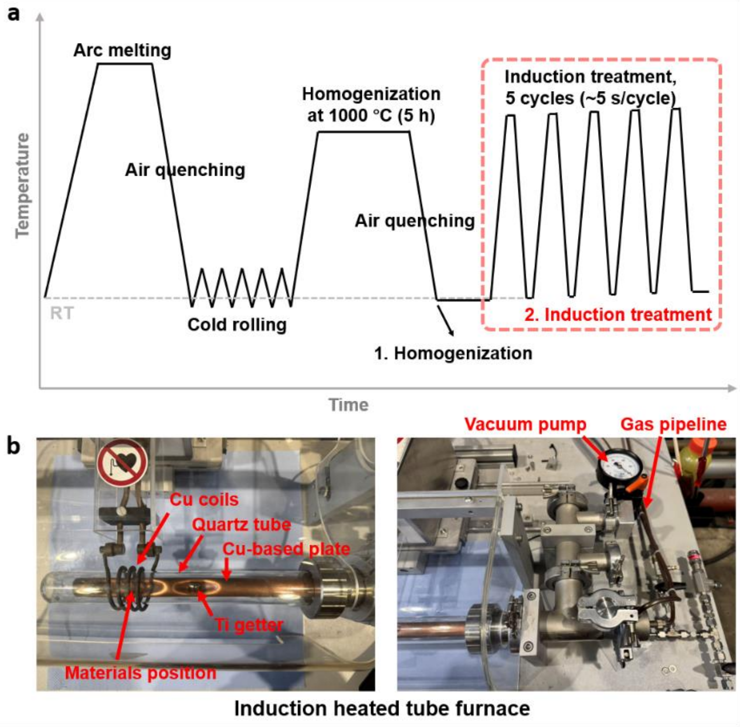
a
Arc melting
Temperature
Air quenching
Homogenization
at 1000 °C (5 h)
Air quenching
Induction treatment,
5 cycles (~5 s/cycle)
RT
Cold rolling
2. Induction treatment
1. Homogenization
Time
b
Vacuum pump
Gas pipeline
Cu coils
Quartz tube
Cu-based plate
Ti getter
Materials position
Induction heated tube furnace

Fig. 6.1 (a) Scheme depicting the processing of equiatomic TiNbZr complex concentrated alloys (CCAs) after homogenization and induction treatment. (b) The induction heated tube furnace used for induction treatment in this study.

6.2.2. Microstructure characterization and uniaxial tensile test

Thermal-desorption spectroscopy (TDS, Burker GALILEO G8) was employed to determine the dissolved oxygen and nitrogen contents of the homogenization and induction treatment samples. The samples were ground successively from 400-grit to 4000-grit SiC paper to remove the potential surface oxide layer prior to the measurements. The oxygen and nitrogen contents were determined using a melt extraction method with a thermal conductivity detector (carrying gas: helium).

Synchrotron high-energy X-ray diffraction (HEXRD) experiments were conducted at the Powder Diffraction and Total Scattering Beamline, P02.1, of PETRA III at Deutsches Elektronen-Synchrotron (DESY, Hamburg) to evaluate the phase compositions. HEXRD profiles were acquired with a wavelength (λ) of 0.2074 Å (60 keV) and post-analyzed employing GSAS-II software [334]. Additionally, small-angle X-ray scattering (SAXS) experiments were performed at the Diffraction & Imaging at the Swedish Beamline, P21.2 to identify the geometric size of the nanofeatures inside the samples. SAXS profiles were acquired with a fixed beam energy of 70 keV ($\lambda = 0.1756$ Å) and processed using SasView software.

A combination of backscattered electron (BSE) imaging, energy dispersive X-ray spectroscopy (EDS), and electron backscatter diffraction (EBSD) techniques were employed to characterize the microstructure of samples after homogenization and induction treatment (Zeiss Sigma 500). Samples were mechanically ground with SiC papers from 400 to 4000 grits, followed by polishing with 30 vol.% H_2O_2-contained colloidal silica suspension solution before SEM characterization. EBSD data was acquired at an acceleration voltage of 15 kV (high current mode). The step size of the EBSD scans was 5 μm, and 1 μm for the underformed, and deformed regions, respectively. The EBSD datasets were processed using the OIM Analysis 9 software.

Atom probe tomography (APT, CAMECA LEAP 5000XR) was employed to investigate the elemental distribution at a near-atomic scale. The sharp-tip specimens were prepared by standard lift-out and subsequent annular milling procedures using the FEI Helios NanoLab 660i dual-beam SEM/FIB instrument. APT measurements were conducted under laser mode with a base temperature, laser energy, pulse rate, and detection rate of 60 K, 40 pJ, 200 kHz, and 0.5%, respectively. The reconstruction and post-processing of APT datasets were performed employing the commercial AP Suite software (version 6.3).

Dog bone-shaped tensile specimens with a gauge geometry of $4.0\times2.0\times1.0$ mm^3 were used for the uniaxial tensile testing. The tensile specimens were fabricated by electrical discharge machining, followed by grinding to remove the surficial oxide layer. A Kammrath and Weiss stage was employed for tensile tests with a strain rate of 2.5×10^{-4} s^{-1}. During the tensile test, an optical camera was further used for digital image correlation (DIC) analysis. The surface of the tensile specimen was sprayed with a speckle pattern (a virtual extensometer) to acquire local strains, and the Aramis GOM Correlate 2020 software (V6.3.0, GOM GmbH) was adopted for the data analysis. Three independent tests were conducted for each microstructural condition to achieve reasonable statistics.

6.3. Results

6.3.1. Microstructure

As indicated by the HEXRD profile in **Fig. 6.2**a, the as-homogenized TiNbZr sample exhibits a single BCC crystal structure with a lattice parameter of 3.3902 Å. After the induction treatment, the TiNbZr alloy absorbs a substantial amount of oxygen, quantified as 2.55±0.12 at.% by TDS measurement (**Fig. 6.2**b and **Table S6.1**). This oxygen content is significantly higher than that of the homogenized sample (0.37±0.04 at.%), while the nitrogen contents (0.07±0.01 at.%) remain consistent between the homogenized and induction-treated samples. This behavior is mainly attributed to the facts that, (1) all the constituent elements have a higher tendency towards oxygen as compared with nitrogen (*i.e.*, for Zr, the formation enthalpy of Zr oxide (-973 kJ/mol) is significantly lower than that of Zr nitride (-365.3 kJ/mol)) [335, 336]; (2) the dissolution of oxygen requires less energy (498 kJ/mol) than that for nitrogen (945 kJ/mol) [337, 338]. It is worth noting that the induction-treated sample remains BCC structure, with a slightly increased lattice parameter of 3.3909 Å. This result is consistent with the previous literature, where the increment in lattice parameter of Ti-30Zr-14Nb (and Ti-30Zr-26Nb) is around 0.03 Å by the addition of 2 at.% of oxygen [62].

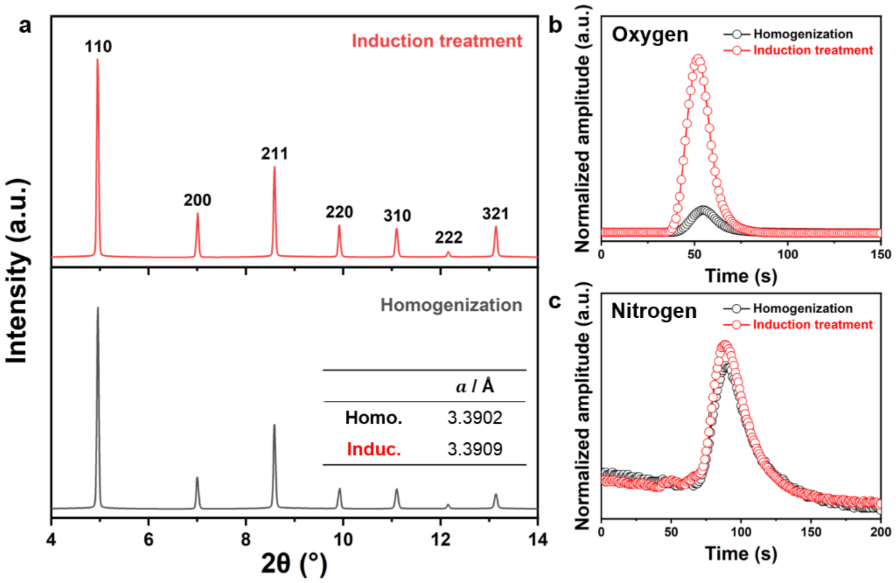

Fig. 6.2 (a) High-energy X-ray diffraction (HEXRD) profiles of the samples after homogenization and induction treatment. The inserted table in (a) shows the measured lattice parameters (*a*). (b) Normalized voltage amplitude when measuring oxygen (a) and nitrogen (c) as a function of the time of the samples after homogenization and induction treatment.

The TiNbZr alloys after homogenization and induction treatment both display an equiaxed grain microstructure (**Fig. 6.3**a and b), with a random grain orientation (**Fig. S6.1**). A homogeneous distribution of all the principle elements is observed as suggested by the corresponding EDS elemental distribution maps. The compositions are $Ti_{33.19\pm3.53}Nb_{33.33\pm4.12}Zr_{33.48\pm3.85}$ and $Ti_{33.26\pm3.52}Nb_{33.35\pm4.12}Zr_{33.39\pm3.84}$ (in at.%) for the as-homogenized and induction-treated samples (**Table S6.2**), which are consistent to the nominated equiatomic concentrations. Additionally, the grain sizes of the samples after homogenization and induction treatment are determined to be 259.12±82.7 μm and 257.22±112.9 μm, respectively(**Fig. 6.3**c). These results suggest that the short-term induction treatment has negligible effects on both microstructure and elemental distribution since such a short time, despite the high temperature, is tough for these constituent refractory elements to diffuse over long distances [339, 340].

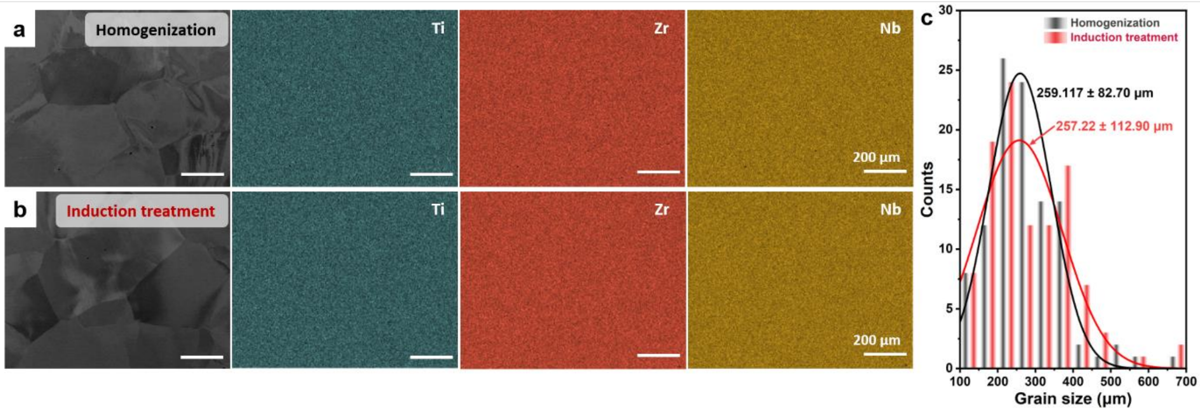

Fig. 6.3 Backscattered electron (BSE) images and the corresponding energy dispersive X-ray spectroscopy (EDS) mapping of the principle elements of the samples after homogenization (a) and induction treatment (b). (c) The distribution of grain sizes of the homogenization and induction treatment samples. The distribution is fitted with a Lognormal function to obtain the mean and standard deviation values.

6.3.2. Mechanical properties

The tensile properties of the samples after homogenization and induction treatment are presented in Fig. 6.4a. The sample after homogenization yields at 715.5±3.8 MPa, followed by a moderate strain hardening process until an ultimate strength (UTS) of 758.3±8.7 MPa is reached. Similar behavior is observed for the sample after induction treatment, yielding at 742.7±10.8 MPa and subsequently reaching a UTS of 762.1±7.4 MPa. Compared to the continuous drop in flow stress after the UTS point observed in the as-homogenized sample, the induction-treated sample exhibits a more gradual decline in flow stress. More specifically, the sample after induction treatment exhibits a larger fraction elongation (28.4±1.5%) than that of as-homogenized one (18.9±2.1%). The inserts in Fig. 6.4a also suggest that the sample after induction treatment can endure greater deformation after necking, as evidenced by the narrower width before fracture compared to that after homogenization. Additionally, in contrast to the continuous and fast decline in the strain-hardening rate (Θ) of the homogenized sample, the strain-hardening behavior can be divided into three distinct stages for the induction-treated sample (Fig. 6.4b). The change of strain-hardening rate in stage I is identical for both samples after homogenization and induction treatment. However, an increase and a prolonged decline in strain-hardening rate are observed for the induction-treated sample in stages II and III, respectively. The maintenance of a moderate strain-hardening rate during the whole tensile deformation primarily contributes to the enhanced ductility in the induction-treated sample [12, 341]. These distinct behaviors and the associated mechanisms during stages II and III of the induction-treated sample will be elaborated in the Discussion sections.

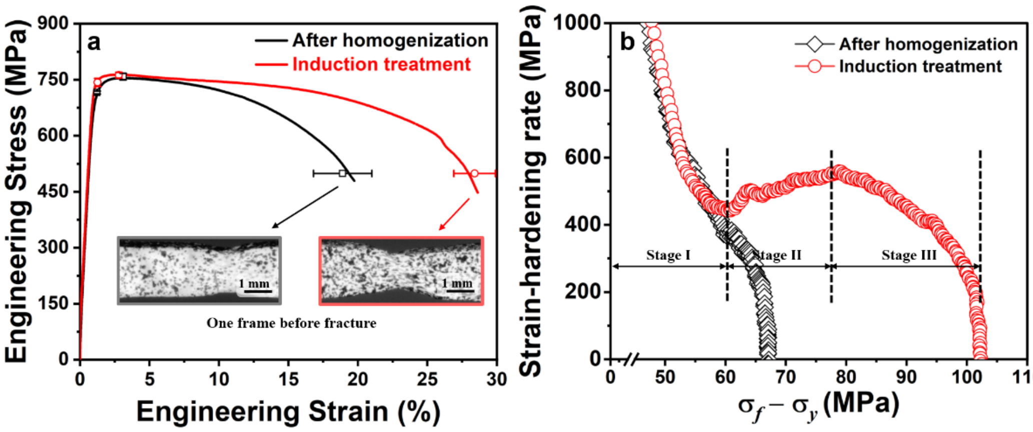

Fig. 6.4 (a) Engineering stress-strain curves and the corresponding (b) Kocks-Mecking plots (strain-hardening rate as a function of $\sigma_f - \sigma_y$) of the samples after homogenization and induction treatment. Inserts in (a) show the corresponding deformation behaviors acquired one frame prior to fracture. σ_f, and σ_y denote the flow stress and the yield stress, respectively.

6.3.3. Deformation behaviors

Fig. 6.5 demonstrates the dislocation behaviors of the homogenized and induction-treated samples at the regions with a local strain of ~30%. In the homogenized sample, dense dislocations are randomly distributed, with long and flat dislocation structures observed (**Fig. 6.5**a). However, after induction treatment, the dislocation structure changes dramatically, with pinning points appearing along the dislocation lines, causing them to curve (**Fig. 6.5**b). This change in dislocation behavior suggests the formation of nanofeatures that significantly hinder dislocation motion in the induction-treated sample. As illustrated in **Fig. 6.5**c, dislocations in the homogenized sample move smoothly with negligible resistance, where deformation formation appears as a single large bump. In contrast, in the induction-treated sample, the presence of pinning points introduces substantial resistance to dislocation movement, leading to the formation of segregated kinks. Additionally, the distance in between two pinning points (λ') of the induction-treated sample is significantly smaller than that of the homogenized sample (λ).

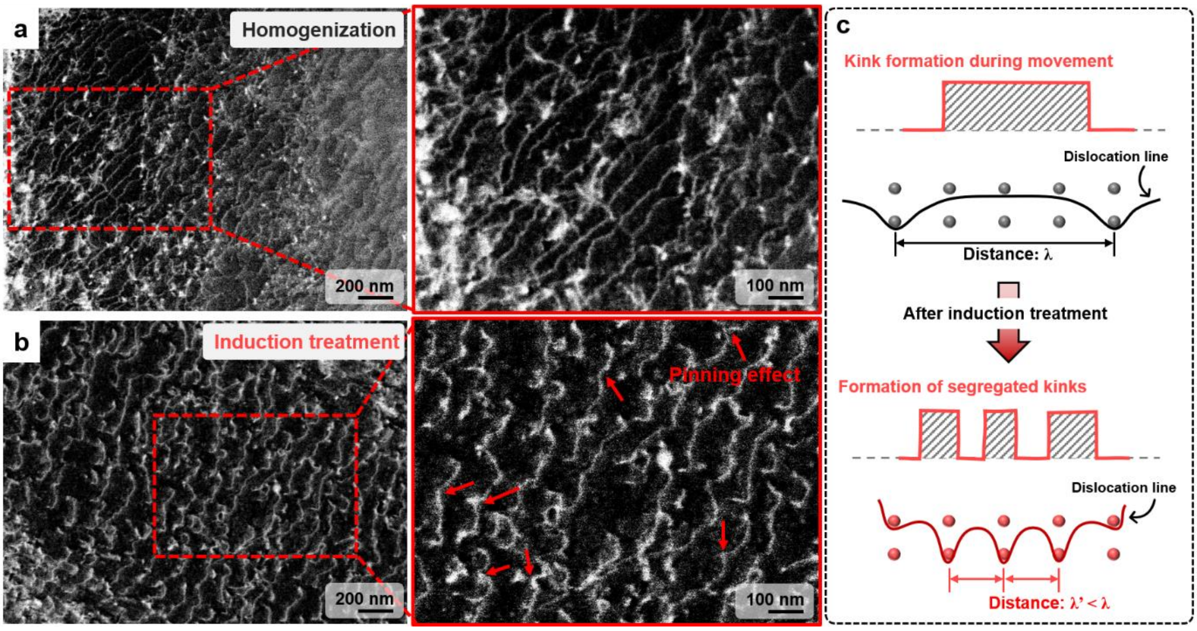
a
Homogenization
200 nm
100 nm
b
Induction treatment
200 nm
Pinning effect
100 nm
c
Kink formation during movement
Dislocation line
Distance: λ
After induction treatment
Formation of segregated kinks
Dislocation line
Distance: λ' < λ

Fig. 6.5 Electron channeling contrast imaging (ECCI) of the dislocation behaviors and the corresponding magnified ECC images of the samples after (a) homogenization and (b) induction treatment. Note that the obvious pinning points are marked by red arrows. (c) Scheme diagram illustrating the change of dislocation behaviors after induction treatment.

To determine what serves as the pinning points along the curved dislocation line, APT was employed to reveal the elemental distribution at a near-atomic scale. Homogeneous elemental distributions are observed for all principle elements in both the homogenized and induction-treated samples (**Fig. 6.6**a and d). However, the 1D concentration profile of the induction-treated sample shows small fluctuations in Ti concentration compared to the homogenized sample (**Fig. 6.6**b and e), indicating the formation of Ti-enriched regions after induction treatment. These Ti-rich regions have an average width of approximately 2 nm, with the maximum local Ti concentration reaching 39.6 at.% in the induction-treated sample (compared to 36.2 at.% in the homogenized sample). To further identify these regions, isocomposition surfaces containing more than 38.5 at.% Ti was generated (**Fig. 6.6**c and f), revealing that the Ti-rich regions are randomly distributed in both samples. After induction treatment, their density increases significantly to 1.96±0.14 vol.%**,** compared to 1.15±0.05 vol.% in the homogenized sample. This increased density of Ti-enriched regions after induction treatment suggests that they act as pinning points, halting dislocation motion and thereby contributing to work hardening [10, 342]. The formation of these Ti-enriched regions is primarily attributed to the incorporation of oxygen interstitials within the matrix (the tendency of oxygen to attract Ti), which has also been reported in other refractory CCAs, *e.g.*, Ti30Zr14Nb and TiZrHfNb [33, 62].

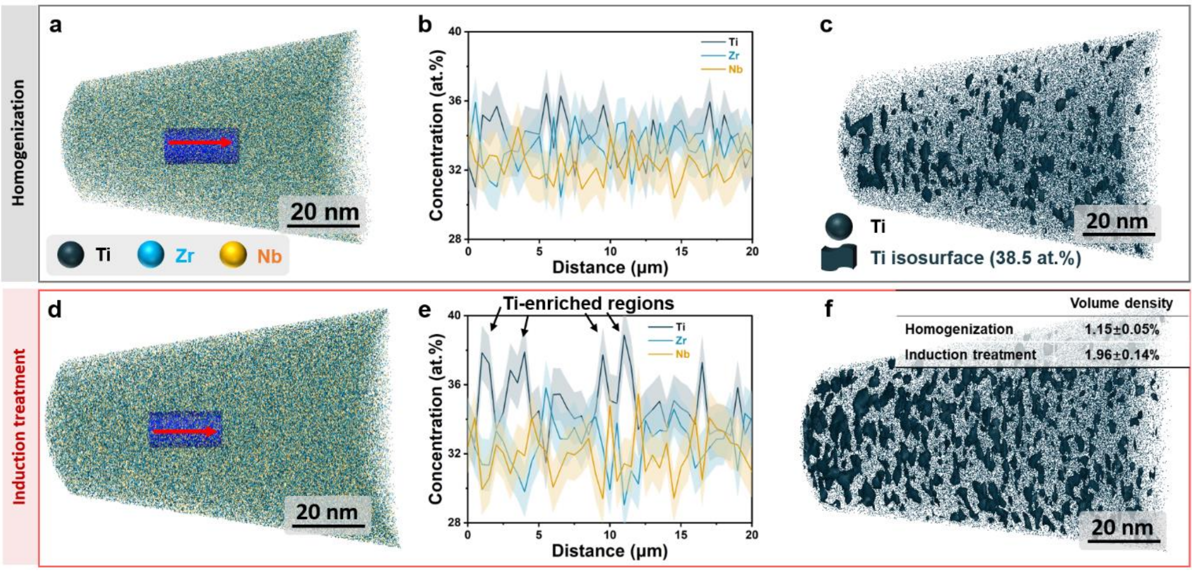

Fig. 6.6 Three-dimensional elemental distributions of the principle elements, and the corresponding 1D concentration profiles for the samples after (a, b) homogenization, and (d, e) induction treatment, respectively. The 1D concentration profiles are obtained following the blue columns (10 nm in diameter) in (a) and (d) with a binning size of 0.5 nm. Ti distribution and the Ti-enriched regions delineated by iso-concentration surfaces containing 38.5 at.% of Ti for the samples after (c) homogenization, and (f) induction treatment. Insert is a table showing the volume density of the Ti-enrich features.

The SAXS technique was further employed to quantitatively extract the morphological information of Ti-rich regions [77]. The high scattering intensity at low scattering vectors (<0.2 Å^{-1}) in both the homogenized and induction-treated samples suggests the formation of nanofeatures, consistent with the previous APT results (**Fig. 6.7**a). A plate-like 2D SAXS pattern is observed in the homogenized sample, whereas after induction treatment, the SAXS pattern transforms into a more anisotropic, star-like shape. These anisotropic SAXS patterns indicate that the nanofeatures are directionally dependent, with a stronger anisotropy observed after induction treatment. Therefore, in combination with the APT data, as demonstrated in a small region delineated by an isosurface containing more than 38.5 at.% Ti, an ellipsoidal morphology was assumed for the Ti-rich regions (**Fig. 6.7**b). The ellipsoid model adopted for curve fitting to obtain the morphological information can be expressed as [343, 344],

$$I(q,\alpha) = \frac{1}{V} F^2(q,\alpha) + \mathrm{B} \tag{6.1}$$

where,

$$F(q,\alpha) = \Delta\rho V \frac{3(\sin qr - qr\cos qr)}{(qr)^2} \tag{6.2}$$

for,

$$r = \left[R_e^2 \sin^2\alpha + R_p^2 \cos^2\alpha\right]^{\frac{1}{2}} \tag{6.3}$$

In the above equations, $V = (\frac{4}{3})\pi R_p R_e^2$, is the volume of the ellipsoid. α is the angle between the axis of the ellipsoid and $\vec{q}$. $\Delta\rho$ is the scattering length density difference between two phases. R_e and R_p denote the equatorial and polar radius of the ellipsoid model, respectively. SAXS profile fitting analysis reveals that the Ti-rich nanofeatures in the homogenized sample exhibit an ellipsoidal morphology, with a R_e of 4.1 nm and a R_p of 1.6 nm (**Fig. 6.7**b). After induction treatment, in addition to the increment in local Ti concentration and density (**Fig. 6.6**), the morphological anisotropy of the Ti-rich nanofeatures also increases, with R_e and R_p reaching 4.5 nm and 1.1 nm, respectively. Notably, Ti atoms tend to redistribute along specific crystallographic planes. This orientation-dependent behavior of the Ti-rich nanofeatures is primarily attributed to a reduction in elastic strain energy [182, 345].

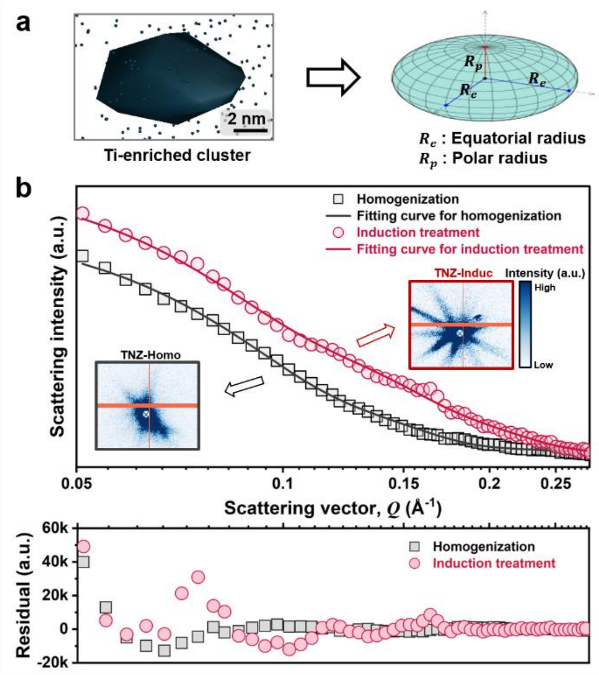

Fig. 6.7 (a) A highly magnified view of a single particle from the APT results in **Fig. 6.6**f, along with its approximate geometric shape. (b) Small-angle X-ray diffraction (SAXS) profiles of the samples after homogenization and induction treatment, and the corresponding fitting curves using an ellipsoid model. Inserts are the two-dimensional SAXS patterns.

The comparison of the deformed regions (with similar local strain, ~70%) in the homogenized and induction-treated samples reveals significant differences in deformation behaviors and misorientation distributions. In the homogenized sample (**Fig. 6.8**a and b), the deformation is characterized by a broad distribution of highly deformation bands, as indicated by the point-to-origin misorientation profiles in **Fig. 6.8**c and d. The average misorientation angle is approximately 40°, with the misorientation zone extending up to ~15 μm near the fracture surface and ~30 μm within the grain. Additionally, the local Kernel average misorientation (KAM) value at this deformation band can reach values up to 4.55°. These characteristics indicate highly localized strain distribution due to the accumulation of geometrically necessary dislocations (GND), leading to the softening and the potential pre-fracture of materials [346-348]. The density of GND can be approximately determined using the equation, $\rho = \frac{3 \cdot \mathrm{KAM}}{b \cdot \Delta x}$ [145], where b and Δx denote the magnitude of the Burgers vector and step size used for the EBSD scan, respectively. The GND density then is calculated to be 5.41×10^{14} m^{-2} around the deformation band in the homogenized samples. Conversely, after induction treatment (**Fig. 6.8**e and f), the deformation band appears more refined, with a significant reduction in the size of the deformation band. The corresponding misorientation profiles (**Fig. 6.8**g and h) show a decrease in the characteristic length of deformation bands to ~3 μm and ~10 μm, demonstrating a more homogenous strain distribution as compared with the sample after homogenization [349, 350]. The local KAM value around the deformation band is approximately 3.10°, giving rise to a GND density of 3.68×10^{14} m^{-2}, which is significantly lower than that of the homogenized sample. The observed refinement in deformation bands, along with the reduction in GND density, suggests a more homogeneous strain distribution after induction treatment. This behavior can be attributed to increased dislocation interactions and strain localization, which are predominantly influenced by the Ti-enriched nanofeatures induced during the induction treatment [13, 351]. The number and width of these deformation bands were further statistically analyzed across the tensile specimens to evaluate the deformation behavior (**Fig. S6.2**). It is found that deformation bands begin to form (with a number of ~5) in regions with low local strains (<20%) in the homogenized sample, and their number (~17) increases significantly as the local strain reaches ~30%. The width of these deformation bands exceeds 10 μm. In the case of the sample after induction treatment, only a few observable deformation bands (~2) appear in regions with local strain below 30%. The formation of deformation bands in regions with low local strain indicates strain inhomogeneity during early-stage plastic deformation, leading to strain localization and the pre-softening of the homogenized sample [352, 353].

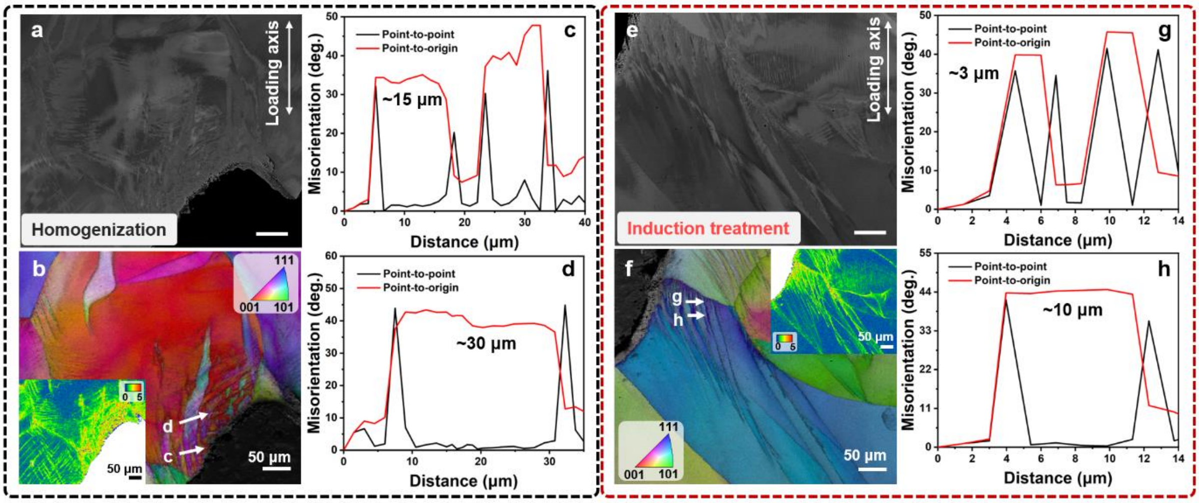

Fig. 6.8 BSE images and the corresponding inverse pole figures overlaid with image quality (IPF + IQ) maps of the samples after (a, b) homogenization and (e, f) induction treatment. The images are captured both at the regions close to fracture with a similar local strain of ~70%. Inserts in (b) and (f) are the kernel average misorientation (KAM) maps. (c, d, g, h) Quantitative misorientation line profiles excerpted from (b) and (f).

In addition to the deformation bands appearing in regions with local strain below 70%, it is worth noting that, at the necking region of the induction-treated sample, ~35 deformation bands appear with an average bandwidth of 4 μm are observed (**Fig. S6.2**). As revealed in **Fig. 6.9**, deformation in the necking region is characterized by finer deformation bands (ranging from 2.5 μm to 6.5 μm), compared to those in regions with local strain below 70%. They are evenly distributed along the fracture surface. Additionally, the misorientation angle of these fine deformation bands is approximately 24° near the fracture surface, gradually decreasing to 20° as one moves toward the interior of the grain. The local KAM value around these refined deformation bands is ~2.61°, accompanied by a GND density of 3.10×10^{14} m^{-2}, which is lower than the values observed in regions with local strains of ~70% in both the homogenized and induction-treated samples. These fine and evenly distributed deformation bands with low GND density in the necking region are often associated with more ductile and fracture-resistant behavior, as they facilitate homogenous strain distribution [349, 351]. This deformation characteristic also influences the fracture behavior, where a larger ductile region (~48.9%) with dimpled structures is observed in the induction-treated sample as compared with the homogenized sample (~26.1%, **Fig. S6.3**).

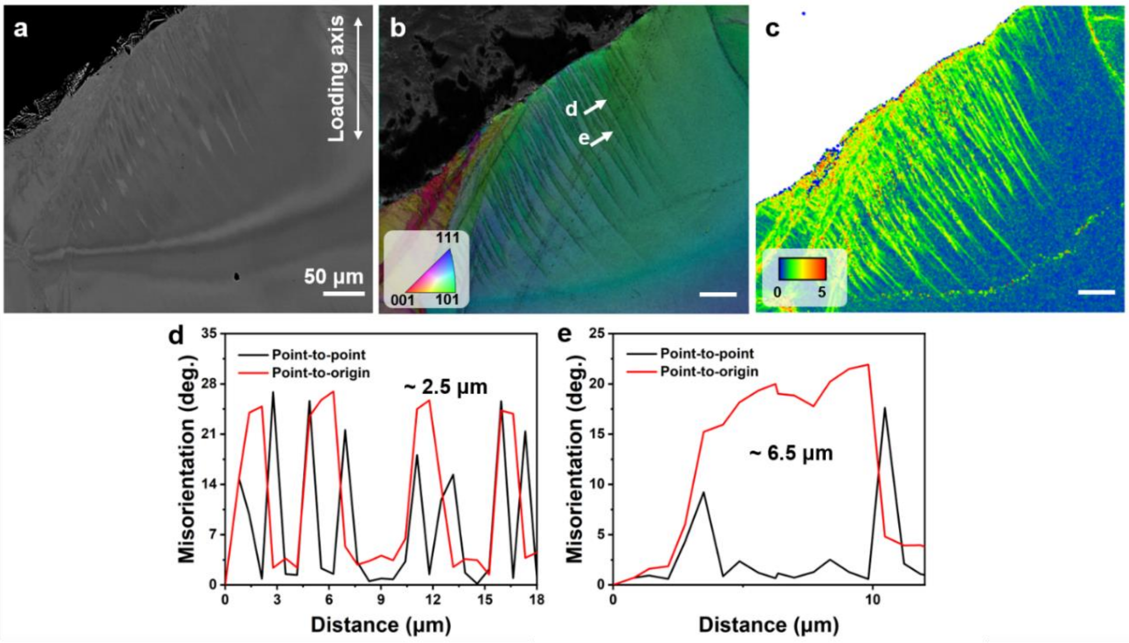

Fig. 6.9 (a) BSE image, and the corresponding (b) IPF + IQ and (c) KAM maps of the induction-treated sample at the necking region. (d, e) Quantitative misorientation line profiles following the direction of arrows in (b).

6.4. Discussion

6.4.1. Increased strain-hardening rate during stage II

Generally, an increase in strain-hardening rate is primarily attributed to the enhanced dislocation density, dislocation pinning, or the transformation-induced plasticity (TRIP) effect [12, 13]. The formation of secondary phases (*e.g.*, precipitate) and secondary boundaries (*e.g.*, twin boundary) can act as pinning points to restrict dislocation motion, thereby resulting in enhanced work hardening [13]. As indicated by the HEXRD results (**Fig. 6.1**a), both the homogenized and induction-treated samples exhibit a single BCC phase. The spot scans conducted near the fracture region also demonstrate that no secondary phase formation in the deformed samples (**Fig. S6.5**). Nevertheless, β-Ti alloys are known to undergo a reversible phase transformation under mechanical loading and unloading [354, 355]. More specifically, the original BCC phase will transform into α'' martensite upon mechanical loading, while the transformed α'' phase reverts to BCC when the force is withdrawn This reversible phase transformation makes it challenging to capture the formation of secondary phases using *ex-situ* HEXRD technique, as stress relaxation occurs in the deformed samples. To address this issue, *in-situ* tensile tests were performed to monitor potential phase transformations during deformation (**Fig. S6.6**). The results suggest that only a single BCC phase is present throughout the deformation process, with no evidence of martensite (α'') transformation. We next calculated the dislocation density in deformed regions (with a local strain of ~70%) based on the modified Williamson-Hall equation to assess its influence on the strain-hardening rate [281, 282]. The homogenized sample has a dislocation density of 9.6×10^{14} m^{-2}, similar to that of the induction-treated sample (10.2×10^{14} m^{-2}). These identical dislocation densities indicate that dislocation density is also not a major factor contributing to the enhanced strain-hardening rate in the induction-treated sample. As for the possibility of twin boundary formation, no observable twin systems (*i.e.*, $\{112\}\langle111\rangle$ twin system with a misorientation angle of ~70°, and $\{332\}\langle111\rangle$ twin system with a misorientation angle of ~60°) can be identified via the EBSD results shown in **Fig. 6.8** and **Fig. 6.9**. This behavior is mainly ascribed to the high stacking fault energy exhibited by the principal elements (*e.g.*, ~400 mJ/m² for pure Ti), which significantly reduces their tendency to undergo twinning [328]. Consequently, the increased strain-hardening rate after induction treatment is predominantly associated with the formation of anisotropic Ti-enriched nanofeatures that impede dislocation motion.

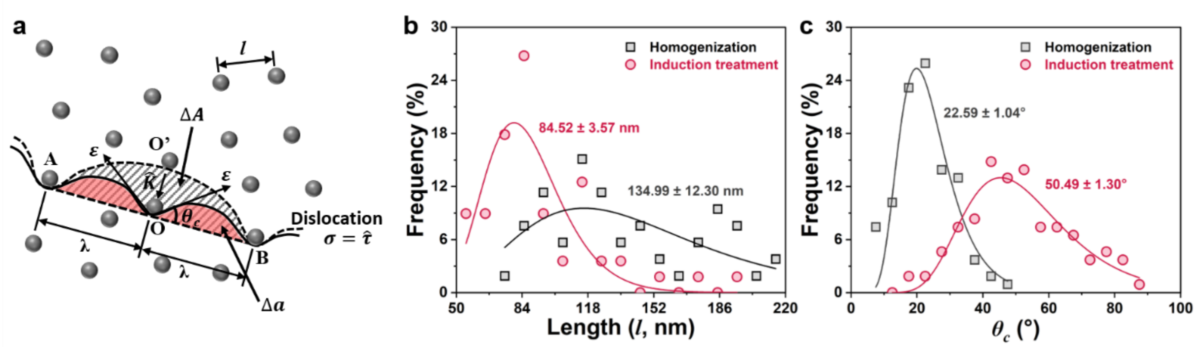

Fig. 6.10 (a) Schematic detailing a dislocation advancing in a field of pointlike slip obstacles (equilibrium state: $\sigma = \hat{\tau}$, where σ and $\hat{\tau}$ indicate the applied stress and shear strength, respectively). (b) The interspacing (l) of the obstacles and (c) the bowing angle (θ_c) of the dislocations statistically analyzed over 50 dislocations for the samples after homogenization and induction treatment.

To assess the influence of Ti-enriched nanofeatures on dislocation movement, an analytical model was adopted on the basis of the interaction between dislocations and contact points (**Fig. 6.10**a). For the sake of simplicity, three assumptions were made: (1) all the contact points are spherical with similar radius, (2) dislocation moves in a steady state, and (3) the interspacing between two clusters (l) can be approximated as the interspacing between two pinning points (λ) [13]. To reduce the reductance in the manuscript, more details associated with the analytical mode can be seen in Supplementary Materials Note 1. Therefore, the critical shear stress ($\hat{\tau}$) to advance steady-state dislocation motion can be expressed as [13],

$$\hat{\tau} \propto \frac{(\theta_c)^{3/2}}{l} \tag{6.4}$$

where θ_c and l denote the bowed-out angle for dislocation and interspacing bewteen two pinning points, respectively. Here, more than 50 dislocations in both of the homogenized and the induction-treated samples were statistically analyzed for the θ_c and l parameters to ensure reliable results (**Fig. 6.10**b and c). The parameter l exhibits a broad distribution in the sample after homogenization, with an average value of 134.99±12.30 nm, while the induction-treated sample shows a smaller l value (84.52±3.57 nm) and a relatively narrow distribution. For θ_c, the homogenized and induction-treated samples possess values of 22.59±1.04° and 50.49±1.30°, respectively. By substituting these values into equation (4), we can obtain,

$$\frac{\hat{\tau}_{Induc}}{\hat{\tau}_{Homo}} = \frac{(\theta_c^{Induc}/\theta_c^{Homo})^{3/2}}{(l_{Induc}/l_{Homo})} = 5.34 > 1 \tag{6.5}$$

This comparison demonstrates that after induction treatment, a higher shear stress is required to keep continuous dislocation movement within the sample, thus resulting in an enhanced strain-hardening rate.

6.4.2. Increase in total elongation during the stage III

The increase in total elongation, particularly after necking, is dependent on the damage tolerance (*i.e.*, suppress crack initiation and propagation) of the investigated materials [303, 356]. To evaluate the role of damage tolerance in post-necking elongation, cross-sectional fractography was performed. No observable voids or microcracks can be detected in either the homogenized or induction-treated samples, suggesting that fracture did not occur through conventional void growth mechanisms. This observation indicates that damage tolerance exhibits a negligible effect on the increase in post-necking elongation.

According to the nonlinear instability analyses by Hutchinson and Neale, strain rate sensitivity (m) is another critical factor that significantly influences the post-necking elongation of metallic alloys [357]. Understanding the effect of m on post-necking elongation differences between the homogenized and induction-treated samples can provide insights into the underlying deformation mechanisms. To evaluate strain rate sensitivity, strain rate jump tests (alternating jumps between 2.5×10^{-3} and 2.5×10^{-5} s^{-1}) were conducted, with the corresponding results presented in **Fig. 6.11**a. The m at a given temperature (T, room temperature for this study) can be defined as [358, 359],

$$m = \left.\frac{\partial \ln \sigma}{\partial \ln \dot{\varepsilon}}\right|_T \tag{6}$$

where σ and $\dot{\varepsilon}$ denote the flow stress and strain rate, respectively. Throughout the plastic elongation regime, the induction-treated sample exhibits a significantly higher m than the homogenized sample, indicating a greater capacity for strain-hardening after the onset of localized deformation (necking). This characteristic contributes to the larger post-necking elongation observed in the induction-treated sample [357]. Since m is mathematically related to the apparent activation volume ($V_{\text{app.}}$) through $m \propto \frac{1}{V_{\text{app.}}}$, a lower $V_{\text{app.}}$ corresponds to a higher strain rate sensitivity [358, 359]. By definition, $V_{\text{app.}}$ signifies the characteristic volume associated with an elementary plastic deformation event [13]. $V_{\text{app.}}$ is highly sensitive to microstructural features such as solutes, precipitates, and second-phase particles. A lower $V_{\text{app.}}$ often suggests stronger interactions between dislocations and these obstacles, thereby leading to increased strain rate sensitivity. Consequently, variations in $V_{\text{app.}}$ provide a direct indication on the evolution of strain rate sensitivity during deformation and its connection to underlying microstructural changes. $V_{\text{app.}}$ can be determined with respect to a certain temperature (T) and miscrostructural state (μ_S) as follows,

$$V_{\text{app.}} = M k_B T \frac{\partial \ln \dot{\varepsilon}}{\partial \sigma}\bigg|_{T,\,\mu_S} \tag{7}$$

where M represents the Taylor factor (here, 2.75 was adopted since the investigated alloy is polycrystalline with a BCC crystal structure [360]), and k_B is the Boltzman constant. The $V_{\text{app.}}$ values at initial states of plastic flow provide insights into dislocation interactions with solutes and microstructure heterogeneities (*e.g.*, precipitates, grain boundaries, etc.) [96]. At a plastic strain of ~1.9%, the induction-treated sample exhibits a significantly lower $V_{\text{app.}}$ value of ~55.8 b^3, as compared with the homogenized sample (~67.1 b^3), suggesting stronger pinning effects on dislocations (**Fig. 6.11**b). These findings are in line with the microstructural observations revealed by SEM (**Fig. 6.5**), where curved dislocations with segregated kinks along individual dislocation lines are observed. As discussed in Section 4.1, the formation of Ti-enriched nanofeatures after induction treatment plays a dominant role in the strong dislocation pinning effects, thus leading to a reduction in $V_{\text{app.}}$, and the associated increase in m. Additionally, the measured $V_{\text{app.}}$ decreases with increasing plastic strain, consistent with trends reported for other BCC concentrated alloys (*e.g.*, TiNbZrHfTa) [361, 362]. This reduction in $V_{\text{app.}}$ during deformation is ascribed to the strong dislocation-dislocation interactions, stemming from the decreasing dislocation spacing ($l = \sqrt{\rho}$, ρ is the dislocation density) as a result of the continuous generation and multiplication of dislocations [13]. A more quantitative analysis employing the Hassen plot (**Fig. 6.11**c) is further presented to reveal the dependency of the flow stress ($\sigma_f - \sigma_{ys}$) on the quantity ($M k_B T / V_{\text{app.}}$) [358]. A larger positive offset at the y-axis

(6.79) for the induction-treated sample suggests a stronger combined effect of solute and precipitation strengthening compared to the homogenized sample, although further systematic experiments are required to separate these contributions. While the identical slopes of the two samples (0.077 *vs.* 0.071) indicate a similar forest hardening behavior.

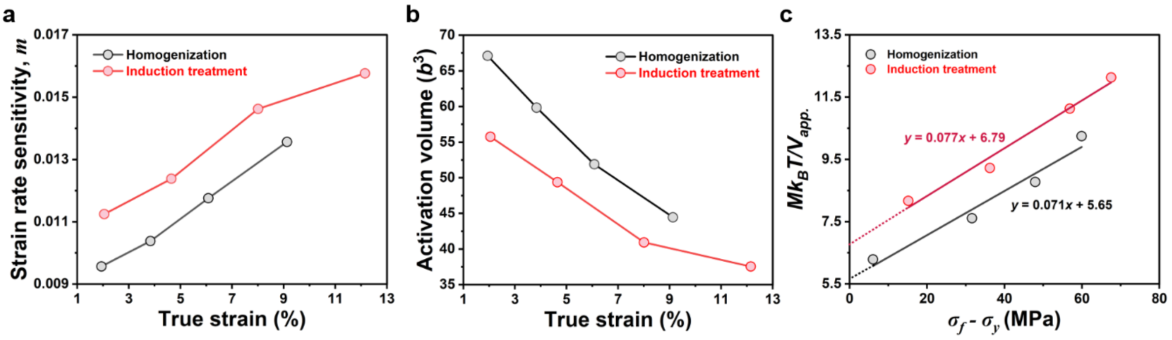

Fig. 6.11 (a) Measured strain rate sensitivities (*m*) and (b) apparent activation volumes ($V_{app.}$) of the samples after homogenization and induction treatment with respect to increasing true plastic strain. (c) Haasen plots of the samples after homogenization and induction treatment

6.5. Conclusions

In the present study, an increase in ductility (especially post-necking elongation) while maintaining comparable strength after a short-term induction treatment was achieved in a TiNbZr CCA. The influence of the induction treatment on the microstructure and the associated deformation mechanisms was evaluated. The major findings are summarized as follows:

(1) After induction treatment, the concentration fluctuation of Ti increased, with the maximum Ti concentration reaching 39.6 at.% as compared to that of the homogenized sample (36.2 at.%). This intensified Ti fluctuation was primarily attributed to the incorporated oxygen interstitials (2.55±0.12 at.%), acting as strong attractors for Ti and thereby promoting localized compositional heterogeneity. Alongside compositional changes, an increase in structural anisotropy was observed for these Ti-rich regions. An ellipsoid shape was identified for these Ti-enriched regions with the induction-treated sample as quantified by SAXS results, with an equatorial radius of 4.6 nm and a polar radius of 1.1 nm. This morphological change was primarily driven by the elastic anisotropy of the samples, which promoted the formation of orientation-dependent nanofeatures to minimize the elastic strain energy.

(2) The induction-treated sample demonstrated a better fracture elongation (28.4±1.5%) without the sacrifice in yield strength than that of the homogenized sample (18.9±2.1%), with a significant increase in post-necking elongation. As indicated by the strain rate jump tests, the increase in total elongation was primarily attributed to the increase in strain rate sensitivity. Additionally, the refinement of deformation bands observed in the induction-treated sample,

characterized by the reduction in both bandwidth and GND density, also suggested improved fracture tolerance by mitigating strain localization and facilitating more uniform deformation behavior. In the necking region, even finer deformation bands (~3 μm) with an average misorientation angle of ~20° were detected, further promoting homogeneous strain distribution and delaying failure.

(3) Compared to the continuous decline in strain-hardening rate observed in the homogenized sample, the induction-treated sample exhibited an initial increase followed by a prolonged decrease in strain-hardening rate. This behavior was primarily attributed to the strong pinning effects of Ti-rich nanofeatures, which impeded dislocation motion and necessitated higher critical shear stress for steady-state dislocation movement. The pronounced dislocation pinning effect was further evidenced by the presence of curved dislocations in the induction-treated sample, indicating restricted glide and enhanced work-hardening capacity.

6.6. Supplementary materials

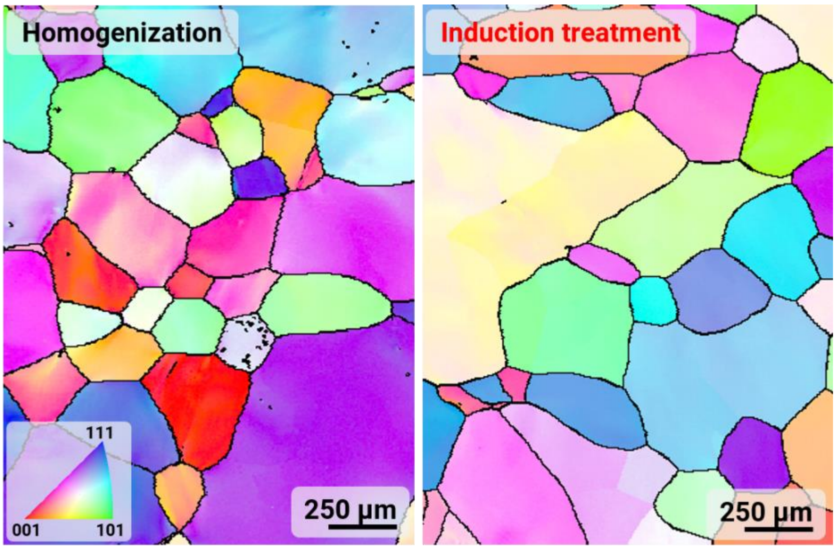

Fig. S6.1 EBSD scans of the samples after (left) homogenization and (right) induction treatment.

The EBSD measurements were conducted at the undeformed regions with a step size of 5 μm. Both homogenized and induction-treated samples exhibit equiaxed grains, with a random grain orientation (negligible texture).

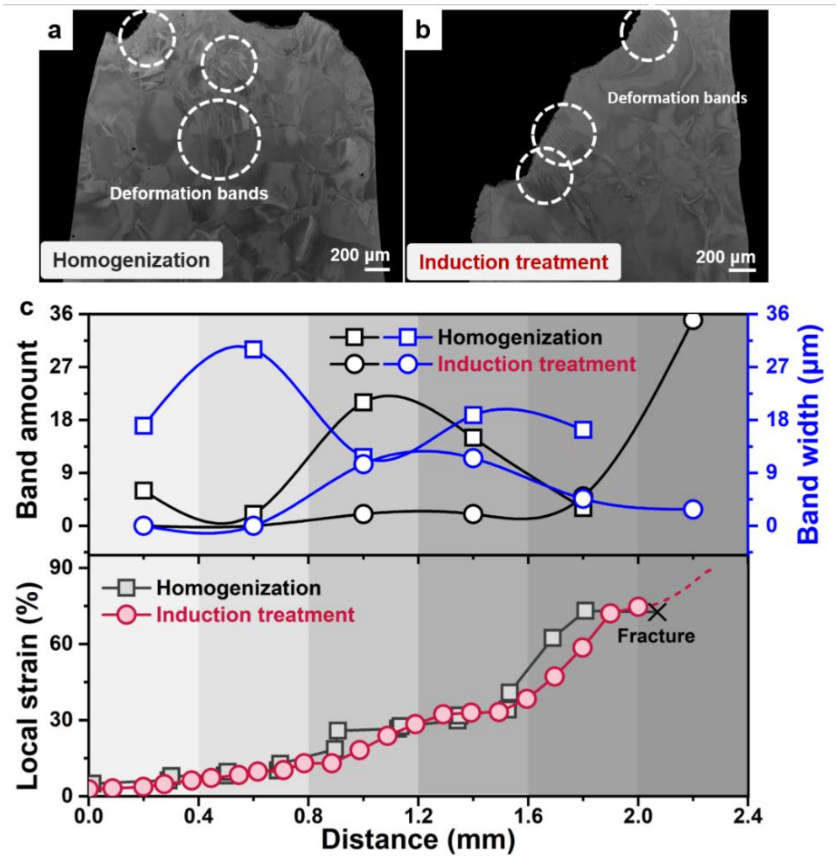

Fig. S6.2 Cross-sectional views of the tensile samples after (a) homogenization and (b) induction treatment. (c) Statistical analysis of the amount and width of deformation bands from the regions with identical local strains.

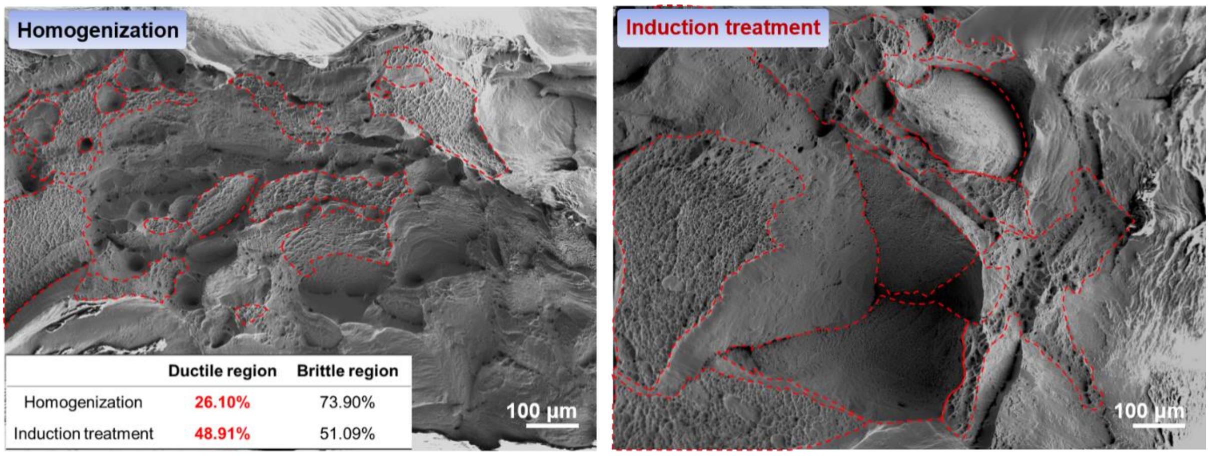

	Ductile region	Brittle region
Homogenization	**26.10%**	73.90%
Induction treatment	**48.91%**	51.09%

Fig. S6.3 Fractography of the samples after homogenization and induction treatment. The ductile regions with dimple structures are indicated by red dash lines. Insert table shows the fraction of the ductile and brittle regions. The sample after induction treatment displays larger ductile region as compared with that of homogenized one, suggesting a good ductility.

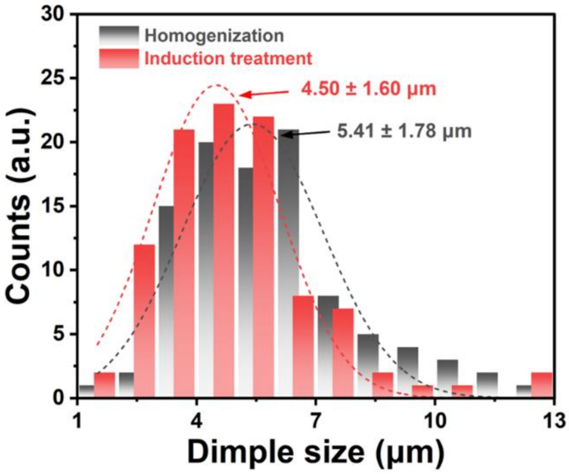

Fig. S6.4 The distributions of dimple size of the samples after homogenization and induction treatment. The dimple sizes are 5.41±1.78 µm and 4.50±1.60 µm for the homogenized and induction-treated samples, respectively.

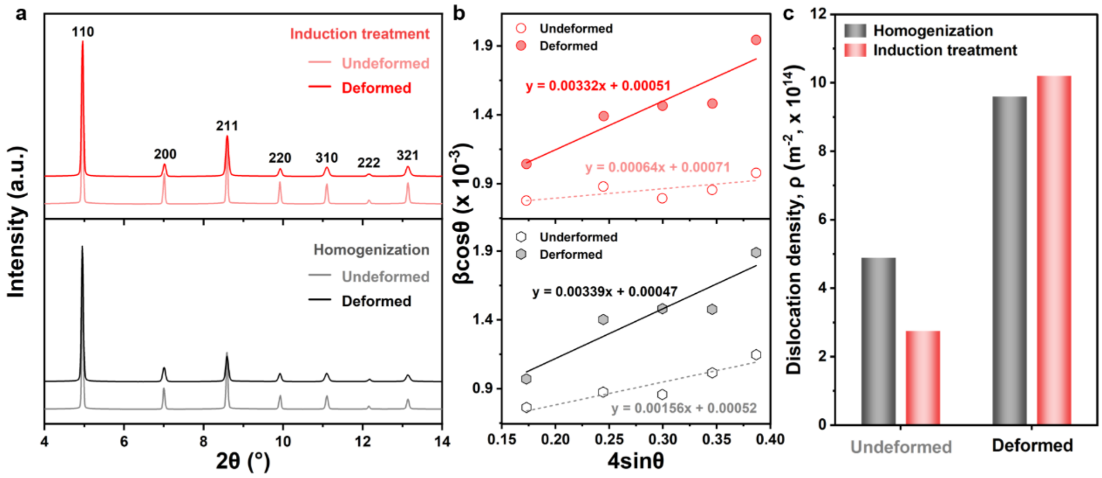

Fig. S6.5 (a) High-energy X-ray diffraction (HEXRD) profiles of the homogenized and induction-treated samples captured at the undeformed and derformed (close to fracture) regions. (b) Plots of $\beta \cos \theta$ as a function of $4 \sin \theta$ and their corresponding linear-fitted curves. β represents the full width of half maximum (FWHM) while θ is the diffraction angle. (c) Calculated dislocation density (ρ) at the undeformed and derformed (close to fracture) regions for samples after homogenization and induction treatment.

The determination of ρ is based on the modified Williamson-Hall equation [281, 282],

$$\beta \cos \theta = 4\varepsilon \sin \theta + \frac{k\lambda}{D} \tag{S6.1}$$

$$\rho = \frac{2\sqrt{3}\varepsilon}{D|b|} \tag{S6.2}$$

where ε, k, λ, D, and b represent the microstrain, a constant (0.94 is usually used for BCC-type alloys) [363], the wavelength of the X-ray beamline, the crystallite size, and the Burgers vector respectively.

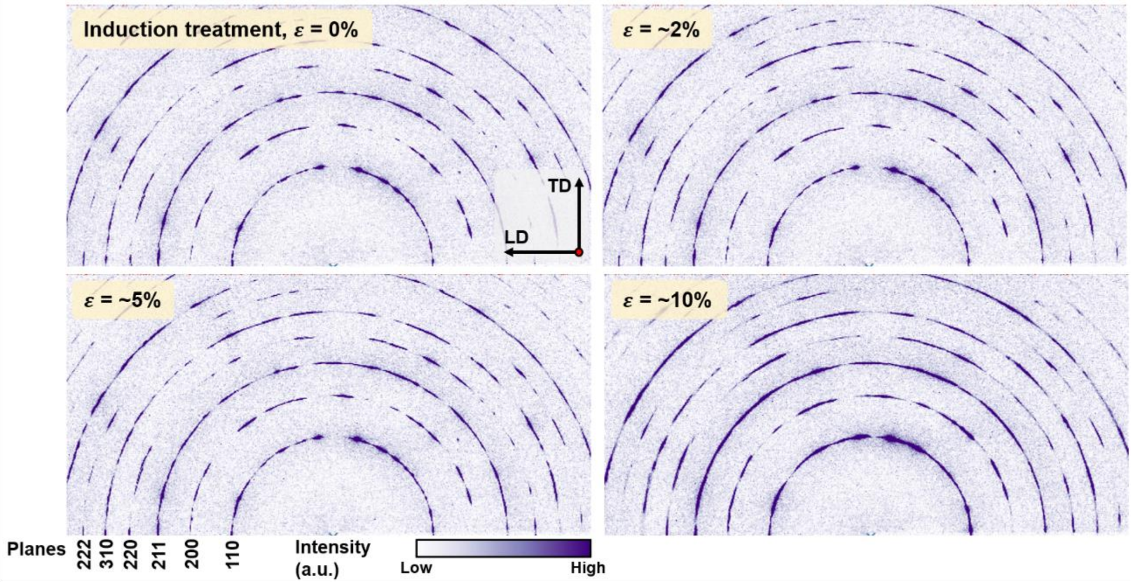

Fig. S6.6 Debye-Scherrer rings of the induction-treated sample during in-situ tensile tests. The snapshots of the two-dimensional diffractograms with a global strain (ε) of 0, ~2, ~5, and ~10% are shown here. Only single BCC crystal structure is observed during the deformation, without the occurrence of martensite transformation (α'').

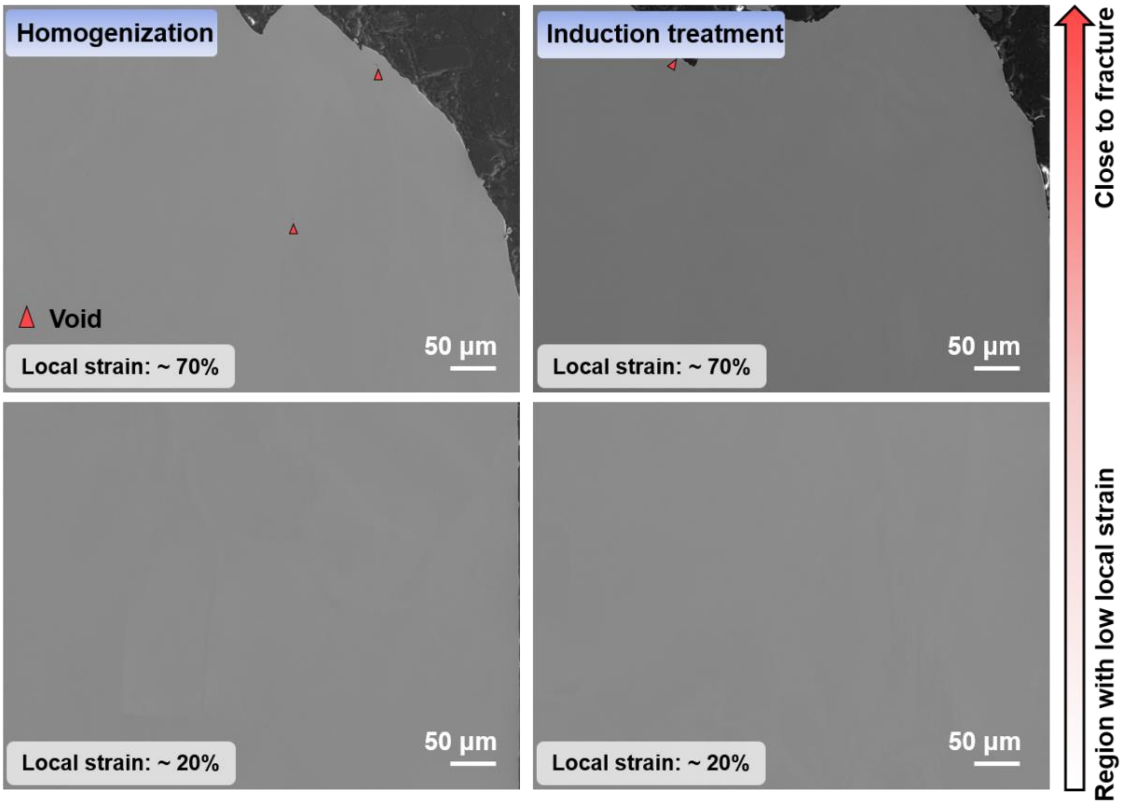
Homogenization
Induction treatment
Void
Local strain: ~ 70%
Local strain: ~ 70%
Local strain: ~ 20%
Local strain: ~ 20%
50 μm
50 μm
50 μm
50 μm
Close to fracture
Region with low local strain

Fig. S6.7 Cross-sectional SEM images of the tensile samples after fracture to evaluate the damage tolerance of the samples after homogenization and induction treatment. No obvious voids can be observed for both samples after homogenization and induction treatment, suggesting that damage tolerance is not the predominant reason for the increase in toal elongation.

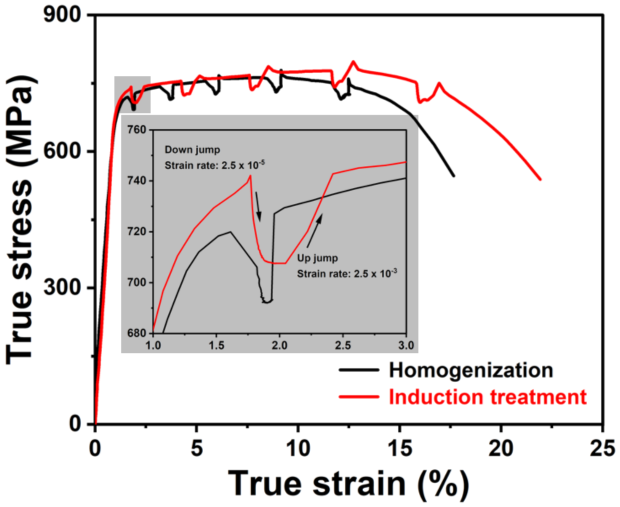

Fig. S6.8 Strain rate jump test of the as-homogenized and induction-treated samples. Insert is the enlarged image of the first jump during the tensile test. A strain rate of 2.5×10^{-5} s^{-1} was used for the down jump, while the strain rate of the up jump is 2.5×10^{-3} s^{-1}. More details regarding the strain rate jump test can be found in the main text.

Table S6.1 The dissolved oxygen and nitrogen contents of the samples after homogenization and induction treatment.

	Homogenization	Induction treatment
Oxygen content	773.17±83.52 wppm (0.37±0.04 at.%)	5410.04±242.71 wppm (2.55±0.12 at.%)
Nitrogen content	107.19±18.68 wppm (0.06±0.01 at.%)	130.53±10.80 wppm (0.07±0.01 at.%)

Table S6.2 The element composition of the samples after homogenization and induction treatment.

Element	Homogenization	Induction treatment
Ti	33.19±3.53 at.%	33.26±3.52 at.%
Zr	33.48±3.85 at.%	33.39±3.84 at.%
Nb	33.33±4.12 at.%	33.35±4.12 at.%

Table S6.3 The morphological information of the formed Ti-rich regions in the samples after homogenization and induction treatment.

	Homogenization	Induction treatment
Radius-polar, R_p	1.6 nm	1.1 nm
Radius-equatorial, R_e	4.1 nm	4.5 nm
Contrast difference, q	17.3	20.7

Note 6.1. Assessment of the force on the dislocation

At a typical contact point between dislocation and clusters (**Fig. 10**a), force equilibrium (f) is reached [13],

$$f = 2\varepsilon \sin\theta_c = \widehat{K} \tag{S6.3}$$

where ε, θ_c, and $\widehat{K}$ represent the line tension acting on the dislocation, the bow-out angle, and the peak resistive force acting on the contact point, respectively. Given at steady flow, the area AOBO' must be on average equal to l^2 (l is the distance between two clusters),

$$\mathrm{Area}_{\mathrm{AOBO'}} = l^2 = \Delta A - 2\Delta a \tag{S6.4}$$

where ΔA and Δa denote the area of the regions highlighted by gray diagonal lines and red color, respectively. When θ_c is small, we can have,

$$\Delta a = \frac{(2R\theta_c)^2}{12R} = \frac{\lambda_c^3}{12R} \tag{S6.5}$$

and,

$$\Delta A = \frac{8\lambda_c^3}{12R} \tag{S6.6}$$

where $\frac{1}{R} = \frac{\hat{\tau}b}{\varepsilon}$ indicates the curvature of the bowed-out segments ($\hat{\tau}$ and b are the critical shear stress and Burgers vector). Combing equations (S3)-(S6),

$$\frac{\lambda_c}{l} = \left(\frac{2\varepsilon}{\hat{\tau}bl}\right)^{1/3} = \frac{1}{(\widehat{K}/2\,\varepsilon)^{1/2}} \tag{S6.7}$$

Move $\hat{\tau}$ to the left-hand side of the equation,

$$\hat{\tau} = \left(\frac{\widehat{K}}{2\varepsilon}\right)^{3/2}\left(\frac{2\varepsilon}{bl}\right) \tag{S6.8}$$

Since θ_c is assumed to be small, we can also have $2\varepsilon \cong Gb^2$ and $\frac{\widehat{K}}{2\varepsilon} \cong \theta_c$ (G indicates the shear modulus). Combing these into equation (S8),

$$\hat{\tau} \cong (\theta_c)^{3/2}\left(\frac{Gb}{l}\right) \tag{S6.9}$$

It is found that $\hat{\tau}$ is positivley proportional to $(\theta_c)^{3/2}$, while inversely proportional to l,

$$\hat{\tau} \propto \frac{(\theta_c)^{3/2}}{l} \tag{S6.10}$$

7. Summary and outlooks

7.1. Summary

This thesis was dedicated to unraveling the unignorable role of interstitial atoms in determining the microstructure, phase stability, and mechanical properties of refractory complex concentrated alloys (RCCAs). Through a combination of experimental techniques and computational modeling, key mechanisms such as hydrogen-induced lattice transformations, hydrogen-assisted spinodal decomposition, and boron-induced modifications in grain boundary chemistry were elucidated. These findings not only highlight the influence of small interstitial atoms on the macroscopic performance of RCCAs but also provide critical insights into developing advanced alloys capable of withstanding extreme conditions.

(1) **Hydrogen accommodation and its influence on lattice symmetry**. In the first part of this study, hydrogen-induced lattice isotropic expansion, structural transformation, and interstitial ordering of hydrogen solutes were revealed and analyzed via a combination of *in-situ* synchrotron high-energy X-ray diffraction and density functional theory. More specifically, during the heating process, a linear expansion of the lattice was found due to the thermal expansion, while a significant increase in lattice parameters induced by the uptake of hydrogen was observed during the isothermal heat treatment. Additionally, a transition in crystal structure from BCC to BCT was detected. The ordering distribution of hydrogen interstitials (tetrahedral site) primarily contributed to the presence of tetragonality of the lattice. Results in this part revealed hydrogen's preference for tetrahedral sites, its higher affinity for Ti/Zr-rich regions, and its role (*i.e.*, ordering distribution) in promoting lattice symmetry breaking and distortion. These findings explore the interaction between hydrogen and RCCAs at a near-atomic scale, offering insights into the development of potential RCCAs for hydrogen storage.

(2) **Hydrogen-assisted spinodal decomposition via the modulation on the free energy landscape**. In addition to the lattice symmetry, hydrogen was shown to facilitate spinodal decomposition in a TiNbZrHfTa RCCA at 500 °C, modulating nanoscale compositional modulations aligned along <001> directions. Atom probe tomography results revealed that Ti and Zr tended to accumulate together, while Nb exhibited a preference for enrichment with Ta. This preference was mainly ascribed to the lower mixing enthalpies between these elements, which thermodynamically favor their segregation and clustering. The orientation dependence of these formed spinodal features was mainly attributed to the reduction in elastic strain energy. A statistical thermodynamical model further suggested that hydrogen modulates the Gibbs free energy landscape via the expansion of the spinodal region, while exhibiting negligible effects

on the kinetic part. This decomposition process enhanced hardness and wear resistance, demonstrating the potential of hydrogen as a functional alloying element for tailoring metastable microstructures and enhancing mechanical properties.

(3) **Boron segregation induces yield strength softening and the change in plastic deformation mechanisms**. For the third part, we demonstrated that a small addition of boron (30 ppm) in a TiNbZrHfTa RCCA reduced grain size, altered grain boundary chemistry through the co-segregation of both B and Zr, and influenced macroscopic mechanical behavior. Although grain refinement was achieved after the addition of B, a reduction of yield strength was observed. This B-induced yield strength softening was linked to the change (*i.e.*, a decrease in grain boundary shear modulus) in grain boundary properties. Additionally, the alternation of grain boundary chemistry led to an enhanced slip-mediated grain boundary shear localization, highlighting the interplay between grain boundary chemistry and plastic deformation mechanisms. A competition between grain boundary shear localization and slip transfer through the grain boundary was also revealed, wherein the addition of B hindered slip transfer, making its occurrence more difficult. This work sheds light on the development and application of grain boundary segregation engineering strategies aimed at optimizing the mechanical performance of refractory complex concentrated alloys.

(4) **Ductilization of a TiNbZr RCCA while preserving yield strength via the oxygen-induced nanoscale chemical heterogeneity.** In the fourth part, oxygen uptake was observed in a TiNbZr RCCA after a short-term induction treatment. As indicated by atom probe tomography and small-angle X-ray diffraction results, the incorporated oxygen interstitials induced a nanoscale chemical heterogeneity (*i.e.*, the formation of Ti-rich nanofeatures with an ellipsoid shape). These nanofeatures strongly pinned dislocations, significantly increasing the critical shear stress required for steady-state dislocation movement. This change in dislocation behavior led to an enhanced strain-hardening rate, thereby increasing the strain-hardening capacity. An increase in strain rate sensitivity was suggested by strain rate jump tests, resulting in increased total elongation, particularly the post-necking elongation. Furthermore, a refinement of deformation bands was found, contributing to a more homogeneous strain distribution, which could also be associated with enhanced ductility.

7.2. Outlooks

7.2.1. On advancing techniques for detecting small interstitial atoms

The detection and characterization of small interstitial atoms (particularly H) remain challenging due to their low atomic numbers, small scattering cross-sections, and dynamic behavior within materials. Advancements in analytical techniques are crucial to enhance our quantitative understanding of their roles in determining the properties of RCCAs (*i.e.*, contents, spatial distribution, *etc.*). In this thesis, *ex-situ* detection of interstitial atoms by a thermal conductivity detector was utilized. Only the total contents of these interstitial atoms can be obtained, offering limited insight into interactions between RCCAs and interstitials. APT has emerged as a promising technique, enabling near-atomic scale mapping and precise quantification of the spatial distribution of light elements, such as interstitial atoms. To overcome environmental contamination and accurately capture interstitial distributions, future studies should combine advanced methods such as cryogenic focused ion beam (FIB) for sample preparation, reaction hub (filled with isotope-labeled gases, like D_2, D_2O, $^{18}O_2$, $^{15}NH_3$, *etc.*) for *in-situ* charging, and cryogenic ultra-high vacuum modules for contamination-free sample transportation. These approaches will enable deeper insights into interstitial behaviors and guide the design of RCCAs with optimized performance under demanding conditions.

7.2.2. On understanding time-resolved microstructural changes induced by interstitials

Although APT provides quantitative spatial distribution of interstitial atoms, its destructive nature limits its ability to capture time-resolved information on microstructural evolutions induced by interstitials. As demonstrated in this thesis, interstitial atoms often drive significant changes in materials, such as elemental partitioning, phase separation, and defect formation—phenomena effectively probed by SAXS. This perspective highlights the potential of leveraging SAXS for deeper insights into the role of interstitial atoms in microstructural evolution. For instance, as shown in **Fig. 7.1**, significant differences in SAXS signals were observed in TiNbZrHfTa RCCAs subjected to heat treatments with and without H incorporation, indicating nanoscale structural changes. Detailed SAXS fitting and analysis can quantify nucleation and growth rates of these features, revealing the kinetics of structural evolution driven by interactions between RCCAs and interstitials. Extending this method to RCCAs incorporating other interstitials (*e.g.*, N and O) allows for comparative analysis of their kinetic effects. Moreover, integrating SAXS with computational modeling, complementary characterization techniques, and advanced *in-situ* experimental setups (*e.g.*, high-pressure or high-temperature environments) can provide a comprehensive understanding of microstructural evolution. These quantitative and time-resolved insights enhance our understanding of the kinetic effects of interstitial atoms, offering fundamental guidance for designing materials (*i.e.*, insights on the parameters for heat treatment or the longevity under reactive atmospheric species) optimized for extreme conditions where interstitials critically influence mechanical performance.

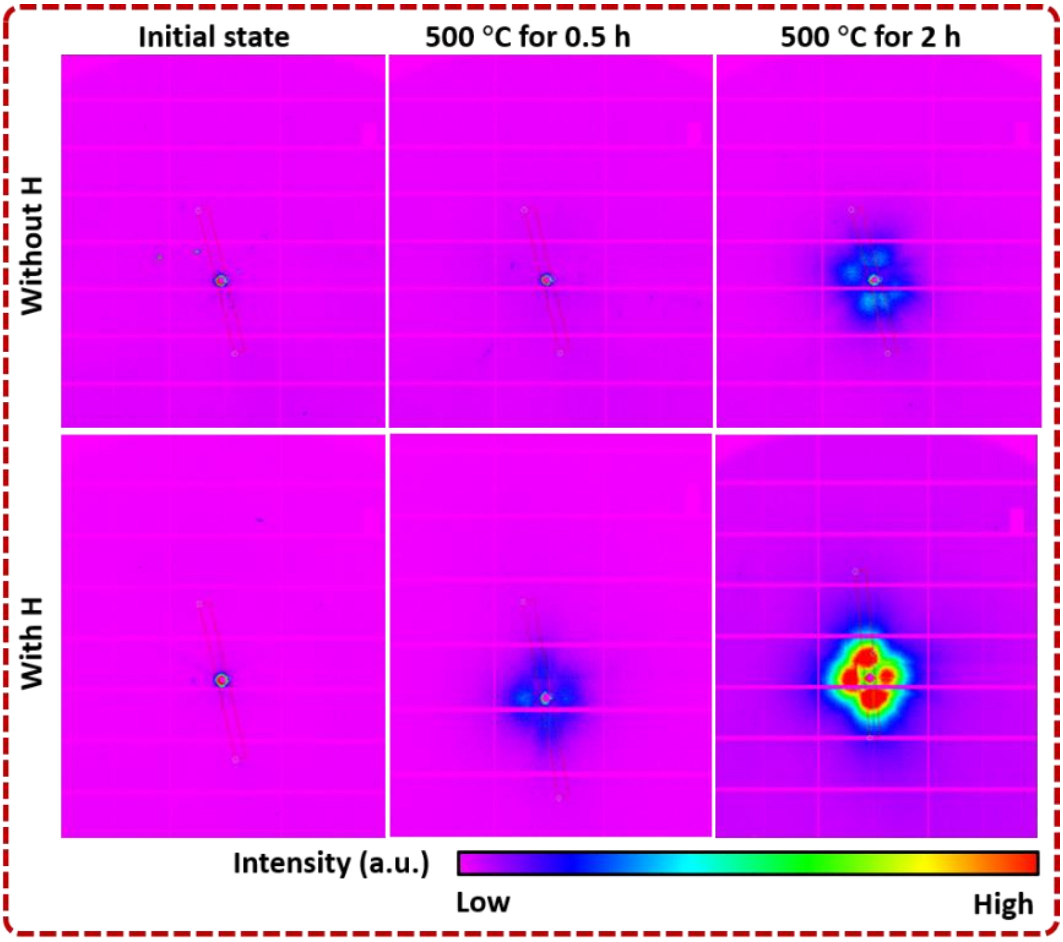

Fig. 7.1 Preliminary results: *In-situ* SAXS data of the TiNbZrHfTa RCCA during the heat treatment (at 500 °C) with and without H.

7.2.3. Perspectives on understanding the effects of the incorporated interstitial atoms on mechanical/functional properties

Interstitial atoms have profound effects on the mechanical properties of materials, particularly in RCCAs due to their strong affinity with refractory elements. These effects are often multifaceted, arising from their interactions with microstructure, phase stability, and defects. While embrittlement induced by the interstitial atoms (such as H and O) has long been a concern, recent studies, including this thesis, highlight the potential of interstitials as both a challenge and a tool for tailoring material properties. The influence of interstitial atoms stems from their ability to alter atomic bonding, promote phase transformations, and interact with defects such as dislocations and grain boundaries. Taking H as an example, H was shown to induce nanoscale spinodal decomposition in TiNbZrHfTa RCCAs, enhancing hardness and wear resistance (see Chapter 4). Conversely, H can exacerbate embrittlement of this RCCA through mechanisms like decohesion at GBs (a transition in fracture mode from transgranular to intergranular, Fig. 7.2a). A key challenge in understanding the mechanical effects of interstitials lies in their mobility and complex interactions within materials. Techniques like APT provide valuable insights into interstitial distribution and its role in microstructural evolution. As shown in Fig. 7.2b, APT reveals the 3D elemental distribution of TiNbZrHfTa RCCA including features at the GB after interacting with H. A notable segregation of Zr along GBs is observed, which can be attributed to the influence of H segregation (not directly detectable) that attracts Zr.

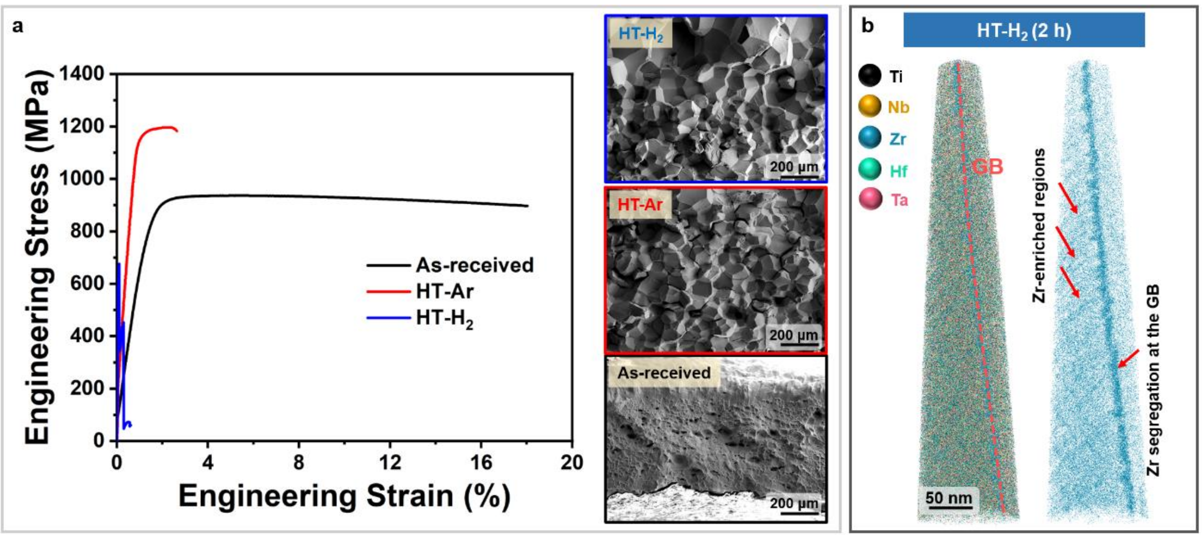

Fig. 7.2 Preliminary results on TiNbZrHfTa RCCAs: (a) Engineering stress-strain curves of the as-received, HT-Ar, and HT-H_2 samples, and the corresponding images illustrating the fracture surfaces. (b) Three-dimensional reconstruction of the elemental distribution of the sample after heat treatment in H_2 for 2 h, showing a Zr segregation behavior at GB.

More intriguingly, entirely different phenomena can be observed when RCCAs are exposed to various gases. This thesis has demonstrated a BCC-to-BCT crystal structure transition in TiNbZr RCCA induced by H solutes under H_2, leading to the formation of low-angle grain boundaries (see Chapter 3). In contrast, exposure to atmospheric conditions resulted in the formation of an interfacial oxide layer and GB secondary phases, while nano-scale features were observed upon exposure to NH_3 (Fig. 7.3). These diverse microstructural responses to different interstitial atoms further expand the potential for designing RCCAs with tailored microstructures. However, looking forward, systematic studies are still needed to decouple the beneficial and detrimental effects of interstitial atoms:

(1) A comprehensive understanding and thorough exploration of phase diagrams in complex systems to aid in predicting phase stability and guiding the rational design of RCCAs;

(2) To investigate how interstitials interact with specific sites, such as GBs, dislocations, or precipitates, to clarify their roles in embrittlement versus strengthening;

(3) To employ *in-situ* deformation techniques under relevant conditions (*e.g.*, temperature, pressure, or specific gaseous atmosphere) to study the dynamic effects of interstitials on deformation mechanisms.

Leveraging the insights gained from interstitial atom behavior could inspire novel alloy design strategies, such as tailoring segregation at grain boundaries, modifying microstructures with specific interstitials, and exploring the synergistic effects of multiple interstitial species (*i.e.*, B co-addition helps strengthen the GB) to shape material properties. By incorporating the kinetic effects of interstitials gleaned from SAXS data (*i.e.*, insights on heat treatment parameters), a further understanding of the dual effects of interstitials can advance the design of materials with optimized performance in extreme environments, such as those encountered in H-rich atmosphere, aerospace, and energy. This perspective underscores the transformative potential of harnessing interstitial atoms to refine and enhance both the mechanical and functional properties of RCCAs.

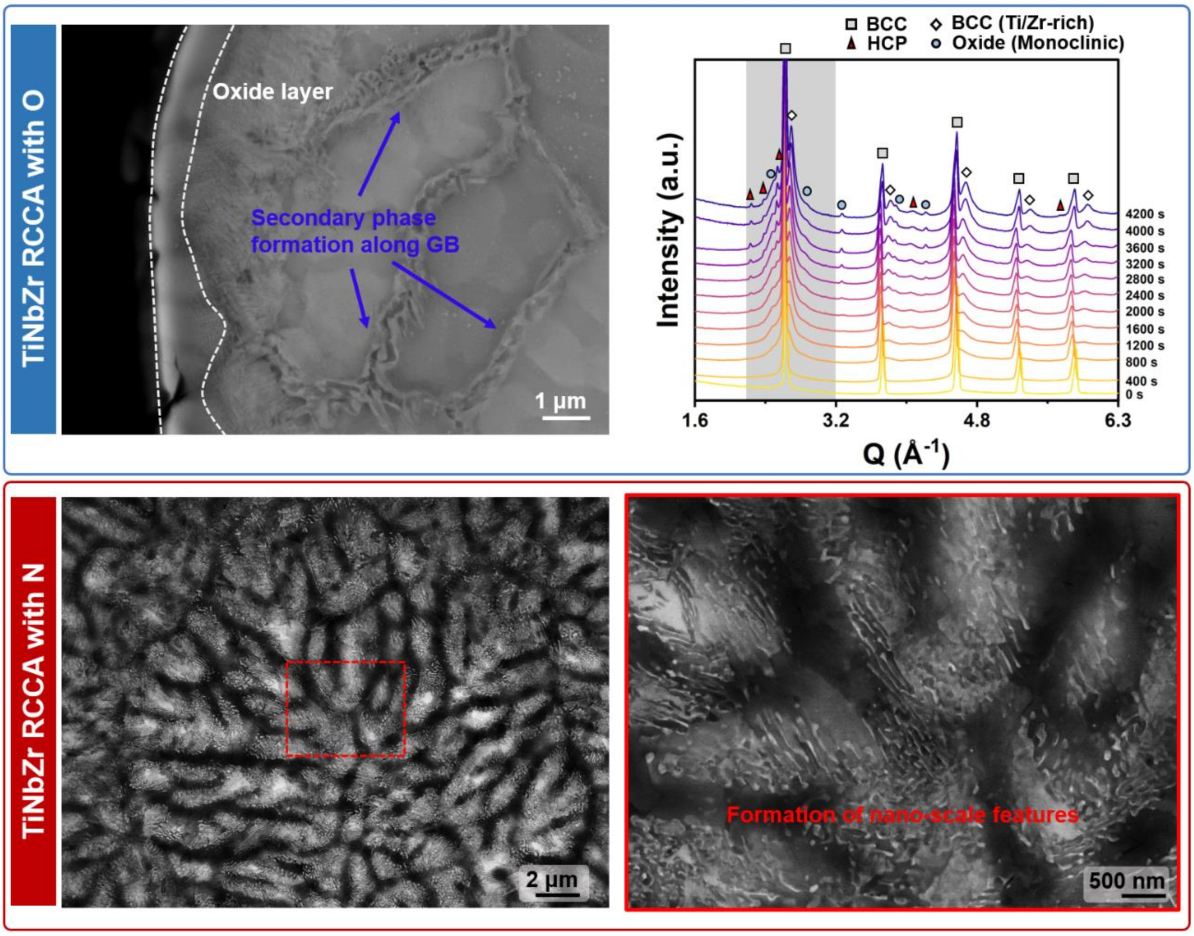

Fig. 7.3 Preliminary results: (Top) After exposure TiNbZr RCCA to the atmospheric environment (at ~740 °C), the formation of GB secondary phases can be observed. The *in-situ* HEXRD data reveals a complex reaction, where two BCC phases enriched in different constituent elements are found, while the formation of HCP and oxide phases is also detected during the heating process. (Bottom) The consequent microstructure after the interaction with N (NH_3, at 700 °C) is shown, where the formation of nanoscale features can be found.

Reference

[1] Ö. Özgün, X. Lu, Y. Ma, D. Raabe, How much hydrogen is in green steel?, npj Materials Degradation 7(1) (2023) 78.

[2] E.P. George, D. Raabe, R.O. Ritchie, High-entropy alloys, Nature reviews materials 4(8) (2019) 515-534.

[3] J.W. Yeh, S.K. Chen, S.J. Lin, J.Y. Gan, T.S. Chin, T.T. Shun, C.H. Tsau, S.Y. Chang, Nanostructured high-entropy alloys with multiple principal elements: novel alloy design concepts and outcomes, Advanced engineering materials 6(5) (2004) 299-303.

[4] C.H. Lupis, Chemical thermodynamics of materials, Elsevier Science Publishing Co., Inc.1983.

[5] D.B. Miracle, O.N. Senkov, A critical review of high entropy alloys and related concepts, Acta materialia 122 (2017) 448-511.

[6] E.P. George, W.A. Curtin, C.C. Tasan, High entropy alloys: A focused review of mechanical properties and deformation mechanisms, Acta Materialia 188 (2020) 435-474.

[7] Y. Jien-Wei, Recent progress in high entropy alloys, Ann. Chim. Sci. Mat 31(6) (2006) 633-648.

[8] B. Gault, A. Chiaramonti, O. Cojocaru-Miredin, P. Stender, R. Dubosq, C. Freysoldt, S.K. Makineni, T. Li, M. Moody, J.M. Cairney, Atom probe tomography, Nat Rev Methods Primers 1(51) (2021).

[9] G. Laplanche, A. Kostka, O. Horst, G. Eggeler, E. George, Microstructure evolution and critical stress for twinning in the CrMnFeCoNi high-entropy alloy, Acta Materialia 118 (2016) 152-163.

[10] D. Utt, S. Lee, Y. Xing, H. Jeong, A. Stukowski, S.H. Oh, G. Dehm, K. Albe, The origin of jerky dislocation motion in high-entropy alloys, Nature communications 13(1) (2022) 4777.

[11] Z. Li, K.G. Pradeep, Y. Deng, D. Raabe, C.C. Tasan, Metastable high-entropy dual-phase alloys overcome the strength–ductility trade-off, Nature 534(7606) (2016) 227-230.

[12] G. Gottstein, Physical foundations of materials science, Springer2004.

[13] A. Argon, Strengthening mechanisms in crystal plasticity, OUP Oxford2007.

[14] D. Hull, D.J. Bacon, Introduction to dislocations, Elsevier2011.

[15] F. Maresca, D. Dragoni, G. Csányi, N. Marzari, W.A. Curtin, Screw dislocation structure and mobility in body centered cubic Fe predicted by a Gaussian Approximation Potential, npj Computational Materials 4(1) (2018) 69.

[16] C. Marichal, H. Van Swygenhoven, S. Van Petegem, C. Borca, {110} Slip with {112} slip traces in bcc Tungsten, Scientific Reports 3(1) (2013) 2547.

[17] Q. He, S. Yoshida, S. Okajo, M. Tanaka, N. Tsuji, Characteristic dislocation slip behavior in polycrystalline HfNbTiZr refractory medium entropy alloy, Journal of Materials Science & Technology 210 (2025) 29-39.

[18] D. Caillard, B. Bienvenu, E. Clouet, Anomalous slip in body-centred cubic metals, Nature 609(7929) (2022) 936-941.

[19] D.B. Miracle, O.N. Senkov, C. Frey, S. Rao, T.M. Pollock, Strength vs temperature for refractory complex concentrated alloys (RCCAs): A critical comparison with refractory BCC elements and dilute alloys, Acta Materialia 266 (2024) 119692.

[20] O. Senkov, G. Wilks, D. Miracle, C. Chuang, P. Liaw, Refractory high-entropy alloys, Intermetallics 18(9) (2010) 1758-1765.

[21] O.N. Senkov, D.B. Miracle, K.J. Chaput, J.-P. Couzinie, Development and exploration of refractory high entropy alloys—A review, Journal of materials research 33(19) (2018) 3092-3128.

[22] D. Xu, X. Wang, Y. Lu, Heterogeneous-Structured Refractory High-Entropy Alloys: A Review of State-of-the-Art Developments and Trends, Advanced Functional Materials 34(49) (2024) 2408941.

[23] C.H. Belcher, B.E. MacDonald, D. Apelian, E.J. Lavernia, The role of interstitial constituents in refractory complex concentrated alloys, Progress in Materials Science 137 (2023) 101140.

[24] S. Eswarappa Prameela, T.M. Pollock, D. Raabe, M.A. Meyers, A. Aitkaliyeva, K.-L. Chintersingh, Z.C. Cordero, L. Graham-Brady, Materials for extreme environments, Nature Reviews Materials 8(2) (2023) 81-88.

[25] R.I. Jaffee, A brief review of refractory metals, (1959).

[26] J. Wadsworth, T. Nieh, J. Stephens, Recent advances in aerospace refractory metal alloys, International materials reviews 33(1) (1988) 131-150.

[27] D.R. Askeland, P.P. Phulé, W.J. Wright, D. Bhattacharya, The science and engineering of materials, (2003).

[28] R.W. Balluffi, S.M. Allen, W.C. Carter, Kinetics of materials, John Wiley & Sons2005.

[29] T. Leveau, L. Ventelon, E. Clouet, Interaction of C, N and O interstitial solute atoms with screw dislocations in HfNbTaTiZr high entropy alloy, Acta Materialia (2024) 120062.

[30] R. Wang, Y. Tang, Z. Lei, Y. Ai, Z. Tong, S. Li, Y. Ye, S. Bai, Achieving high strength and ductility in nitrogen-doped refractory high-entropy alloys, Materials & Design 213 (2022) 110356.

[31] Y. Cui, Q. Zhu, G. Xiao, W. Yang, Y. Liu, G.-H. Cao, Z. Ren, Interstitially carbon-alloyed refractory high-entropy alloys with a body-centered cubic structure, Science China Materials 65(2) (2022) 494-500.

[32] Z. Wang, H. Wu, Y. Wu, H. Huang, X. Zhu, Y. Zhang, H. Zhu, X. Yuan, Q. Chen, S. Wang, Solving oxygen embrittlement of refractory high-entropy alloy via grain boundary engineering, Materials Today 54 (2022) 83-89.

[33] Z. Lei, X. Liu, Y. Wu, H. Wang, S. Jiang, S. Wang, X. Hui, Y. Wu, B. Gault, P. Kontis, Enhanced strength and ductility in a high-entropy alloy via ordered oxygen complexes, Nature 563(7732) (2018) 546-550.

[34] R. Poulain, M. Rajkowski, Y. Zhao, P. Gemagami, B. Appolaire, S. Laube, A. Kauffmann, L. Perrière, J.-P. Couzinié, T. Li, Oxygen-induced decomposition of the body-centered cubic HfNbTaTiZr high-entropy alloy, Acta Materialia 280 (2024) 120295.

[35] A. Takeuchi, A. Inoue, Classification of bulk metallic glasses by atomic size difference, heat of mixing and period of constituent elements and its application to characterization of the main alloying element, Materials transactions 46(12) (2005) 2817-2829.

[36] W. Lengauer, A. Eder, Nitrides: Transition metal solid-state chemistry, na2005.

[37] J.H. Park, H.S. Seo, K.Y. Kim, Alloy design to prevent intergranular corrosion of low-Cr ferritic stainless steel with weak carbide formers, Journal of The Electrochemical Society 162(8) (2015) C412.

[38] A. Earnshaw, N.N. Greenwood, Chemistry of the Elements, Butterworth-Heinemann Oxford1997.

[39] A. Züttel, Materials for hydrogen storage, Materials today 6(9) (2003) 24-33.

[40] J. Völkl, G. Alefeld, Diffusion of hydrogen in metals, Hydrogen in Metals I: Basic Properties (2005) 321-348.

[41] N. Peterson, Diffusion in refractory metals, Advanced Metals Research Corp Somerville MA, 1960.

[42] D. Raabe, M. Herbig, S. Sandlöbes, Y. Li, D. Tytko, M. Kuzmina, D. Ponge, P.-P. Choi, Grain boundary segregation engineering in metallic alloys: A pathway to the design of interfaces, Current Opinion in Solid State and Materials Science 18(4) (2014) 253-261.

[43] M. Seah, E. Hondros, Grain boundary segregation, Proceedings of the Royal Society of London. A. Mathematical and Physical Sciences 335(1601) (1973) 191-212.

[44] M. Seah, Adsorption-induced interface decohesion, Acta Metallurgica 28(7) (1980) 955-962.

[45] I. Langmuir, The adsorption of gases on plane surfaces of glass, mica and platinum, Journal of the American Chemical society 40(9) (1918) 1361-1403.

[46] P. Lejček, S. Hofmann, Thermodynamics and structural aspects of grain boundary segregation, Critical Reviews in Solid State and Material Sciences 20(1) (1995) 1-85.

[47] S. Xin, X. Shen, C. Du, J. Zhao, B. Sun, H. Xue, T. Yang, X. Cai, T. Shen, Bulk nanocrystalline boron-doped VNbMoTaW high entropy alloys with ultrahigh strength, hardness, and resistivity, Journal of Alloys and Compounds 853 (2021) 155995.

[48] P.-H. Ko, Y.-J. Lee, J.-H. Wang, C.-Y. Tsai, S.-Y. Chang, Boron Interstitials Strengthening Grain Boundary for Toughening HfxMo0. 5NbTaxTiV1. 5-xZrx Refractory High-Entropy Alloys, Materials Science and Engineering: A (2024) 147694.

[49] C. Liu, W. Lu, W. Xia, C. Du, Z. Rao, J.P. Best, S. Brinckmann, J. Lu, B. Gault, G. Dehm, G. Wu, Z. Li, D. Raabe, Massive interstitial solid solution alloys achieve near-theoretical strength, Nat Commun 13(1) (2022) 1102.

[50] C. Zhang, Y. Wu, L. You, W. Qiu, Y. Zhang, Y. Yuan, Z. Lu, X. Song, Nanoscale phase separation of TiZrNbTa high entropy alloy induced by hydrogen absorption, Scripta Materialia 178 (2020) 503-507.

[51] C. Wu, L.S. Aota, J. Rao, X. Zhang, L. Perrière, M.J. Duarte, D. Raabe, Y. Ma, Hydrogen-assisted spinodal decomposition in a TiNbZrHfTa complex concentrated alloy, Acta Materialia (2025) 120707.

[52] D. Cui, Y. Zhang, L. Liu, Y. Li, L. Wang, Z. Wang, J. Li, J. Wang, F. He, Oxygen-assisted spinodal structure achieves 1.5 GPa yield strength in a ductile refractory high-entropy alloy, Journal of Materials Science & Technology 157 (2023) 11-20.

[53] Y. Wan, Y. Cheng, Y. Chen, Z. Zhang, Y. Liu, H. Gong, B. Shen, X. Liang, A Nitride-Reinforced NbMoTaWHfN Refractory High-Entropy Alloy with Potential Ultra-High-Temperature Engineering Applications, Engineering 30 (2023) 110-120.

[54] L. Han, S. Zhu, Z. Rao, C. Scheu, D. Ponge, A. Ludwig, H. Zhang, O. Gutfleisch, H. Hahn, Z. Li, D. Raabe, Multifunctional high-entropy materials, Nature Reviews Materials 9(12) (2024) 846-865.

[55] C. Moore, J. Wilson, M. Rushton, W. Lee, J. Astbury, S. Middleburgh, Hydrogen accommodation in the TiZrNbHfTa high entropy alloy, Acta Materialia 229 (2022) 117832.

[56] X. Wang, W. Guo, Y. Fu, High-entropy alloys: emerging materials for advanced functional applications, Journal of Materials Chemistry A 9(2) (2021) 663-701.

[57] F. Marques, M. Balcerzak, F. Winkelmann, G. Zepon, M. Felderhoff, Review and outlook on high-entropy alloys for hydrogen storage, Energy & Environmental Science 14(10) (2021) 5191-5227.

[58] Y. Ma, Y. Ma, Q. Wang, S. Schweidler, M. Botros, T. Fu, H. Hahn, T. Brezesinski, B. Breitung, High-entropy energy materials: challenges and new opportunities, Energy & Environmental Science 14(5) (2021) 2883-2905.

[59] D. Ouyang, Z.-j. Chen, H.-b. Yu, K. Chan, L. Liu, Oxidation behavior of the Ti38V15Nb23Hf24 refractory high-entropy alloy at elevated temperatures, Corrosion Science 198 (2022) 110153.

[60] S. Sheikh, M.K. Bijaksana, A. Motallebzadeh, S. Shafeie, A. Lozinko, L. Gan, T.-K. Tsao, U. Klement, D. Canadinc, H. Murakami, Accelerated oxidation in ductile refractory high-entropy alloys, Intermetallics 97 (2018) 58-66.

[61] H. Luo, Z. Li, W. Lu, D. Ponge, D. Raabe, Hydrogen embrittlement of an interstitial equimolar high-entropy alloy, Corrosion Science 136 (2018) 403-408.

[62] M. Jiao, Z. Lei, Y. Wu, J. Du, X.-Y. Zhou, W. Li, X. Yuan, X. Liu, X. Zhu, S. Wang, Manipulating the ordered oxygen complexes to achieve high strength and ductility in medium-entropy alloys, Nature Communications 14(1) (2023) 806.

[63] L. Ventelon, D. Caillard, B. Lüthi, E. Clouet, D. Rodney, F. Willaime, Mobility of carbon-decorated screw dislocations in bcc iron, Acta Materialia 247 (2023) 118716.

[64] G. Hachet, D. Caillard, L. Ventelon, E. Clouet, Mobility of screw dislocation in BCC tungsten at high temperature in presence of carbon, Acta Materialia 222 (2022) 117440.

[65] S. Marchetti, In situ tests by flat dilatometer, Journal of the geotechnical engineering division 106(3) (1980) 299-321.

[66] T.A. Kop, J. Sietsma, S. Van Der Zwaag, Dilatometric analysis of phase transformations in hypo-eutectoid steels, Journal of Materials Science 36 (2001) 519-526.

[67] D. Hömberg, N. Togobytska, M. Yamamoto, On the evaluation of dilatometer experiments, Applicable Analysis 88(5) (2009) 669-681.

[68] A.K. Mukhopadhyay, C.-S. Shon, D.G. Zollinger, Activation energy of alkali–silica reaction and dilatometer method, Transportation research record 1979(1) (2006) 1-11.

[69] J. James, J. Spittle, S. Brown, R. Evans, A review of measurement techniques for the thermal expansion coefficient of metals and alloys at elevated temperatures, Measurement science and technology 12(3) (2001) R1.

[70] A.-C. Dippel, H.-P. Liermann, J.T. Delitz, P. Walter, H. Schulte-Schrepping, O.H. Seeck, H. Franz, Beamline P02. 1 at PETRA III for high-resolution and high-energy powder diffraction, Journal of synchrotron radiation 22(3) (2015) 675-687.

[71] Y. Ma, B. Sun, A. Schökel, W. Song, D. Ponge, D. Raabe, W. Bleck, Phase boundary segregation-induced strengthening and discontinuous yielding in ultrafine-grained duplex medium-Mn steels, Acta Materialia 200 (2020) 389-403.

[72] S. Wei, J. Kim, C.C. Tasan, In-situ investigation of plasticity in a Ti-Al-V-Fe (α+ β) alloy: Slip mechanisms, strain localization, and partitioning, International Journal of Plasticity 148 (2022) 103131.

[73] S. Wei, G. Zhu, C.C. Tasan, Slip-twinning interdependent activation across phase boundaries: An in-situ investigation of a Ti-Al-V-Fe (α+ β) alloy, Acta Materialia 206 (2021) 116520.

[74] C.Y. Ho, R.W. Powell, P.E. Liley, Thermal conductivity of the elements, Journal of Physical and Chemical Reference Data 1(2) (1972) 279-421.

[75] J.A. Kaduk, S.J.L. Billinge, R.E. Dinnebier, N. Henderson, I. Madsen, R. Černý, M. Leoni, L. Lutterotti, S. Thakral, D. Chateigner, Powder diffraction, Nature Reviews Methods Primers 1(1) (2021).

[76] B.H. Toby, R.B. Von Dreele, GSAS-II: the genesis of a modern open-source all purpose crystallography software package, Journal of Applied Crystallography 46(2) (2013) 544-549.

[77] C.M. Jeffries, J. Ilavsky, A. Martel, S. Hinrichs, A. Meyer, J.S. Pedersen, A.V. Sokolova, D.I. Svergun, Small-angle X-ray and neutron scattering, Nature Reviews Methods Primers 1(1) (2021) 70.

[78] Z. Hegedüs, T. Müller, J. Hektor, E. Larsson, T. Bäcker, S. Haas, A. Conceiçao, S. Gutschmidt, U. Lienert, Imaging modalities at the Swedish Materials Science beamline at PETRA III, IOP Conference Series: Materials Science and Engineering, IOP Publishing, 2019, p. 012032.

[79] S. Zaefferer, G. Habler, Scanning electron microscopy and electron backscatter diffraction, (2017).

[80] W. Zhou, R. Apkarian, Z.L. Wang, D. Joy, Fundamentals of scanning electron microscopy (SEM), Scanning microscopy for nanotechnology: techniques and applications (2007) 1-40.

[81] S. Zaefferer, N.-N. Elhami, Theory and application of electron channelling contrast imaging under controlled diffraction conditions, Acta Materialia 75 (2014) 20-50.

[82] N.K. Lassen, D.J. Jensen, K. Conradsen, Image processing procedures for analysis of electron back scattering patterns, Scanning microscopy 6 (1992) 115-121.

[83] Y.H. Chen, S.U. Park, D. Wei, G. Newstadt, M.A. Jackson, J.P. Simmons, M. De Graef, A.O. Hero, A dictionary approach to electron backscatter diffraction indexing, Microscopy and Microanalysis 21(3) (2015) 739-752.

[84] W. Lenthe, S. Singh, M. De Graef, A spherical harmonic transform approach to the indexing of electron back-scattered diffraction patterns, Ultramicroscopy 207 (2019) 112841.

[85] D.B. Williams, C.B. Carter, D.B. Williams, C.B. Carter, The transmission electron microscope, Springer1996.

[86] E. Muller, Experiments of the theory of electron emission under the influence of high field strength, Physikalische Zeitschrift 37 (1936) 838-842.

[87] A.A. El-Zoka, S.-H. Kim, S. Deville, R.C. Newman, L.T. Stephenson, B. Gault, Enabling near-atomic–scale analysis of frozen water, Science Advances 6(49) (2020) eabd6324.

[88] S.M. Das, P. Harrison, S. Kiranbabu, X. Zhou, W. Ludwig, E.F. Rauch, M. Herbig, C.H. Liebscher, Correlating grain boundary character and composition in 3-dimensions using 4D-scanning precession electron diffraction and atom probe tomography, arXiv preprint arXiv:2409.01753 (2024).

[89] X. Chen, W. Gonçalves, Y. Hu, Y. Gao, P. Harrison, S.M. Das, G. Dehm, B. Gault, W. Ludwig, E. Rauch, Secondary Grain Boundary Dislocations Alter Segregation Energy Spectra, arXiv preprint arXiv:2411.10350 (2024).

[90] P. Geerlings, F. De Proft, W. Langenaeker, Conceptual density functional theory, Chemical reviews 103(5) (2003) 1793-1874.

[91] C. Wu, Y. Gong, C. Liu, X. Li, G. Gizer, C. Pistidda, F. Körmann, Y. Ma, J. Neugebauer, D. Raabe, Hydrogen accommodation and its role in lattice symmetry in a TiNbZr medium-entropy alloy, Acta Materialia 288 (2025).

[92] D. Raabe, The Materials Science behind Sustainable Metals and Alloys, Chemical Reviews 123(5) (2023) 2436-2608.

[93] M.D. Allendorf, V. Stavila, J.L. Snider, M. Witman, M.E. Bowden, K. Brooks, B.L. Tran, T. Autrey, Challenges to developing materials for the transport and storage of hydrogen, Nat Chem 14(11) (2022) 1214-1223.

[94] C. Pistidda, Solid-state hydrogen storage for a decarbonized society, Hydrogen 2(4) (2021) 428-443.

[95] A. Zuttel, Hydrogen storage methods, Naturwissenschaften 91(4) (2004) 157-72.

[96] S. Wei, S.J. Kim, J. Kang, Y. Zhang, Y. Zhang, T. Furuhara, E.S. Park, C.C. Tasan, Natural-mixing guided design of refractory high-entropy alloys with as-cast tensile ductility, Nature Materials 19(11) (2020) 1175-1181.

[97] M. Yan, W. Xu, M.S. Dargusch, H.P. Tang, M. Brandt, M. Qian, Review of effect of oxygen on room temperature ductility of titanium and titanium alloys, Powder Metallurgy 57(4) (2014) 251-257.

[98] O.N. Senkov, J.M. Scott, S.V. Senkova, D.B. Miracle, C.F. Woodward, Microstructure and room temperature properties of a high-entropy TaNbHfZrTi alloy, Journal of Alloys and Compounds 509(20) (2011) 6043-6048.

[99] C. Yang, S. Yang, L. Chen, H. Dong, X. Duan, C. Yu, W. Zhang, L. Liu, Low modulus Ti-rich biocompatible TiNbZrTaHf concentrated alloys with exceptional plasticity, Materials Research Letters 11(7) (2023) 604-612.

[100] C. Zlotea, M.A. Sow, G. Ek, J.P. Couzinié, L. Perrière, I. Guillot, J. Bourgon, K.T. Møller, T.R. Jensen, E. Akiba, M. Sahlberg, Hydrogen sorption in TiZrNbHfTa high entropy alloy, Journal of Alloys and Compounds 775 (2019) 667-674.

[101] M. Sahlberg, D. Karlsson, C. Zlotea, U. Jansson, Superior hydrogen storage in high entropy alloys, Sci Rep 6 (2016) 36770.

[102] X. Ma, X. Ding, R. Chen, W. Cao, Q. Song, Study on hydrogen storage property of (ZrTiVFe) xAly high-entropy alloys by modifying Al content, International Journal of Hydrogen Energy 47(13) (2022) 8409-8418.

[103] J. Hu, J. Zhang, H. Xiao, L. Xie, H. Shen, P. Li, J. Zhang, H. Gong, X. Zu, A Density Functional Theory Study of the Hydrogen Absorption in High Entropy Alloy TiZrHfMoNb, Inorg Chem 59(14) (2020) 9774-9782.

[104] B. Sun, W. Krieger, M. Rohwerder, D. Ponge, D. Raabe, Dependence of hydrogen embrittlement mechanisms on microstructure-driven hydrogen distribution in medium Mn steels, Acta Materialia 183 (2020) 313-328.

[105] S. Jothi, T. Croft, S. Brown, Influence of grain boundary misorientation on hydrogen embrittlement in bi-crystal nickel, International journal of hydrogen energy 39(35) (2014) 20671-20688.

[106] L. Huang, D. Chen, D. Xie, S. Li, Y. Zhang, T. Zhu, D. Raabe, E. Ma, J. Li, Z. Shan, Quantitative tests revealing hydrogen-enhanced dislocation motion in α-iron, Nature Materials 22(6) (2023) 710-716.

[107] B. Sun, W. Lu, B. Gault, R. Ding, S.K. Makineni, D. Wan, C.-H. Wu, H. Chen, D. Ponge, D. Raabe, Chemical heterogeneity enhances hydrogen resistance in high-strength steels, Nature Materials 20(12) (2021) 1629-1634.

[108] H. Zhao, P. Chakraborty, D. Ponge, T. Hickel, B. Sun, C.-H. Wu, B. Gault, D. Raabe, Hydrogen trapping and embrittlement in high-strength Al alloys, Nature 602(7897) (2022) 437-441.

[109] C.A. Wert, Trapping of hydrogen in metals, in: G. Alefeld, J. Völkl (Eds.), Hydrogen in Metals II: Application-Oriented Properties, Springer Berlin Heidelberg, Berlin, Heidelberg, 1978, pp. 305-330.

[110] M.B. Djukic, G.M. Bakic, V. Sijacki Zeravcic, A. Sedmak, B. Rajicic, The synergistic action and interplay of hydrogen embrittlement mechanisms in steels and iron: Localized plasticity and decohesion, Engineering Fracture Mechanics 216 (2019) 106528.

[111] H. Luo, W. Lu, X. Fang, D. Ponge, Z. Li, D. Raabe, Beating hydrogen with its own weapon: Nano-twin gradients enhance embrittlement resistance of a high-entropy alloy, Materials Today 21(10) (2018) 1003-1009.

[112] H. Luo, Z. Li, D. Raabe, Hydrogen enhances strength and ductility of an equiatomic high-entropy alloy, Scientific reports 7(1) (2017) 9892.

[113] H. Luo, S.S. Sohn, W. Lu, L. Li, X. Li, C.K. Soundararajan, W. Krieger, Z. Li, D. Raabe, A strong and ductile medium-entropy alloy resists hydrogen embrittlement and corrosion, Nature communications 11(1) (2020) 3081.

[114] Y. Fukai, The metal-hydrogen system: basic bulk properties, Springer Science & Business Media2006.

[115] C. Zhang, A. Song, Y. Yuan, Y. Wu, P. Zhang, Z. Lu, X. Song, Study on the hydrogen storage properties of a TiZrNbTa high entropy alloy, International Journal of Hydrogen Energy 45(8) (2020) 5367-5374.

[116] M.M. Nygård, G. Ek, D. Karlsson, M. Sahlberg, M.H. Sørby, B.C. Hauback, Hydrogen storage in high-entropy alloys with varying degree of local lattice strain, International Journal of Hydrogen Energy 44(55) (2019) 29140-29149.

[117] S. Wei, J. Kang, C.C. Tasan, An in situ synchrotron X-ray study of reverse austenitic transformation in a metastable FeMnCo alloy, Journal of Materials Research 38(2) (2022) 281-296.

[118] Y. Ma, W. Song, W. Bleck, Investigation of the Microstructure Evolution in a Fe-17Mn-1.5Al-0.3C Steel via In Situ Synchrotron X-ray Diffraction during a Tensile Test, Materials 10(10) (2017).

[119] M.W. Davids, T. Martin, M. Lototskyy, R. Denys, V. Yartys, Study of hydrogen storage properties of oxygen modified Ti- based AB2 type metal hydride alloy, International Journal of Hydrogen Energy 46(25) (2021) 13658-13663.

[120] S. Yamanaka, T. Tanaka, M. Miyake, Effect of oxygen on hydrogen solubility in zirconium, Journal of nuclear materials 167 (1989) 231-237.

[121] D. Peterson, B. Schlader, Solubility and diffusion of hydrogen in vanadium-oxygen alloys, Metallurgical Transactions A 19 (1988) 67-72.

[122] G. Welsch, R. Boyer, E. Collings, Materials properties handbook: titanium alloys, ASM international1993.

[123] U. Bösenberg, C. Pistidda, M. Tolkiehn, N. Busch, I. Saldan, K. Suarez-Alcantara, A. Arendarska, T. Klassen, M. Dornheim, Characterization of metal hydrides by in-situ XRD, international journal of hydrogen energy 39(18) (2014) 9899-9903.

[124] C. Pistidda, A. Santoru, S. Garroni, N. Bergemann, A. Rzeszutek, C. Horstmann, D. Thomas, T. Klassen, M. Dornheim, First direct study of the ammonolysis reaction in the most common alkaline and alkaline earth metal hydrides by in situ SR-PXD, The Journal of Physical Chemistry C 119(2) (2015) 934-943.

[125] P.E. Blöchl, Projector augmented-wave method, Physical Review B 50(24) (1994) 17953-17979.

[126] G. Kresse, J. Furthmüller, Efficient iterative schemes for ab initio total-energy calculations using a plane-wave basis set, Physical review B 54(16) (1996) 11169.

[127] G. Kresse, J. Furthmüller, Efficiency of ab-initio total energy calculations for metals and semiconductors using a plane-wave basis set, Computational materials science 6(1) (1996) 15-50.

[128] G. Kresse, D. Joubert, From ultrasoft pseudopotentials to the projector augmented-wave method, Physical review b 59(3) (1999) 1758.

[129] J.P. Perdew, K. Burke, M. Ernzerhof, Generalized gradient approximation made simple, Physical review letters 77(18) (1996) 3865.

[130] A. Baldereschi, Mean-value point in the Brillouin zone, Physical Review B 7(12) (1973) 5212.

[131] H.J. Monkhorst, J.D. Pack, Special points for Brillouin-zone integrations, Physical review B 13(12) (1976) 5188.

[132] A. Zunger, S.-H. Wei, L. Ferreira, J.E. Bernard, Special quasirandom structures, Physical review letters 65(3) (1990) 353.

[133] C. Zhang, Y. Wu, L. You, X. Cao, Z. Lu, X. Song, Investigation on the activation mechanism of hydrogen absorption in TiZrNbTa high entropy alloy, Journal of Alloys and Compounds 781 (2019) 613-620.

[134] J. Jin, M. Liu, P. Lin, T. Fu, Y. Hao, H. Jin, Ultrahigh temperature processing by concentrated solar energy with accurate temperature measurement, Applied Thermal Engineering 150 (2019) 1337-1344.

[135] A.K. Swarnakar, O. Van der Biest, B. Baufeld, Thermal expansion and lattice parameters of shaped metal deposited Ti–6Al–4V, Journal of Alloys and Compounds 509(6) (2011) 2723-2728.

[136] Q. Li, K. Lin, Z. Liu, L. Hu, Y. Cao, J. Chen, X. Xing, Chemical Diversity for Tailoring Negative Thermal Expansion, Chemical Reviews 122(9) (2022) 8438-8486.

[137] R. Feenstra, R. Griessen, D. De Groot, Hydrogen induced lattice expansion and effective HH interaction in single phase PdHc, Journal of Physics F: Metal Physics 16(12) (1986) 1933.

[138] M. Khanuja, B. Mehta, P. Agar, P. Kulriya, D. Avasthi, Hydrogen induced lattice expansion and crystallinity degradation in palladium nanoparticles: Effect of hydrogen concentration, pressure, and temperature, Journal of Applied Physics 106(9) (2009) 093515.

[139] G.K. Pálsson, A. Bliersbach, M. Wolff, A. Zamani, B. Hjörvarsson, Using light transmission to watch hydrogen diffuse, Nature communications 3(1) (2012) 892.

[140] E. Galindo-Nava, B. Basha, P. Rivera-Díaz-del-Castillo, Hydrogen transport in metals: Integration of permeation, thermal desorption and degassing, Journal of Materials Science & Technology 33(12) (2017) 1433-1447.

[141] M. Yashima, K. Morimoto, N. Ishizawa, M. Yoshimura, Diffusionless tetragonal–cubic transformation temperature in zirconia–ceria solid solutions, Journal of the American Ceramic Society 76(11) (1993) 2865-2868.

[142] L. Delaey, Diffusionless transformations, Phase Transformations in Materials (2001) 583-654.

[143] Y. Fukai, Site preference of interstitial hydrogen in metals, Journal of the Less Common Metals 101 (1984) 1-16.

[144] H. Pfeiffer, H. Peisl, Lattice expansion of niobium and tantalum due to dissolved hydrogen and deuterium, Physics Letters A 60(4) (1977) 363-364.

[145] P.J. Konijnenberg, S. Zaefferer, D. Raabe, Assessment of geometrically necessary dislocation levels derived by 3D EBSD, Acta Materialia 99 (2015) 402-414.

[146] E. Breitbarth, S. Zaefferer, F. Archie, M. Besel, D. Raabe, G. Requena, Evolution of dislocation patterns inside the plastic zone introduced by fatigue in an aged aluminium alloy AA2024-T3, Materials Science and Engineering: A 718 (2018) 345-349.

[147] Z.-H. Sung, M. Wang, A. Polyanskii, C. Santosh, S. Balachandran, C. Compton, D. Larbalestier, T. Bieler, P. Lee, Development of low angle grain boundaries in lightly deformed superconducting niobium and their influence on hydride distribution and flux perturbation, Journal of Applied Physics 121(19) (2017) 193903.

[148] D.-G. Xie, L. Wan, Z.-W. Shan, Hydrogen enhanced cracking via dynamic formation of grain boundary inside aluminium crystal, Corrosion Science 183 (2021) 109307.

[149] T. Ishimoto, M. Koyama, Theoretical study of tetrahedral site occupation by hydrogen in Pd nanoparticles, J Chem Phys 148(3) (2018) 034705.

[150] J. Li, B. Li, X. Yu, H. Zhao, H. Shao, Geometrical effect in Mg-based metastable nano alloys with BCC structure for hydrogen storage, International Journal of Hydrogen Energy 44(55) (2019) 29291-29296.

[151] Y. Ikeda, I. Tanaka, J. Neugebauer, F. Körmann, Impact of interstitial C on phase stability and stacking-fault energy of the CrMnFeCoNi high-entropy alloy, Physical Review Materials 3(11) (2019) 113603.

[152] Y.A. Du, L. Ismer, J. Rogal, T. Hickel, J. Neugebauer, R. Drautz, First-principles study on the interaction of H interstitials with grain boundaries in α-and γ-Fe, Physical Review B—Condensed Matter and Materials Physics 84(14) (2011) 144121.

[153] D. Westlake, Hydrides of intermetallic compounds: A review of stabilities, stoichiometries and preferred hydrogen sites, Journal of the Less Common Metals 91(1) (1983) 1-20.

[154] Y. Lu, H. Yu, R.D. Sisson, The effect of carbon content on the c/a ratio of as-quenched martensite in Fe-C alloys, Materials Science and Engineering: A 700 (2017) 592-597.

[155] M. Cadeville, J. Friedt, C. Lerner, Structural, electronic and magnetic properties of splat-quenched FeCx alloys (x⩽ 0.05), Journal of Physics F: Metal Physics 7(1) (1977) 123.

[156] T. Tanaka, N. Maruyama, N. Nakamura, A.J. Wilkinson, Tetragonality of Fe-C martensite – a pattern matching electron backscatter diffraction analysis compared to X-ray diffraction, Acta Materialia 195 (2020) 728-738.

[157] G. Nolze, A. Winkelmann, G. Cios, T. Tokarski, Tetragonality mapping of martensite in a high-carbon steel by EBSD, Materials Characterization 175 (2021).

[158] S. Zaefferer, A critical review of orientation microscopy in SEM and TEM, Crystal Research and Technology 46(6) (2011) 607-628.

[159] J. Mayer, L.A. Giannuzzi, T. Kamino, J. Michael, TEM sample preparation and FIB-induced damage, MRS bulletin 32(5) (2007) 400-407.

[160] X. Zhang, H. Wang, T. Hickel, J. Rogal, Y. Li, J. Neugebauer, Mechanism of collective interstitial ordering in Fe–C alloys, Nature Materials 19(8) (2020) 849-854.

[161] G. Ek, M.M. Nygård, A.F. Pavan, J. Montero, P.F. Henry, M.H. Sørby, M. Witman, V. Stavila, C. Zlotea, B.C. Hauback, Elucidating the effects of the composition on hydrogen sorption in TiVZrNbHf-based high-entropy alloys, Inorganic Chemistry 60(2) (2020) 1124-1132.

[162] D. Karlsson, G. Ek, J. Cedervall, C. Zlotea, K.T. Møller, T.C. Hansen, J. Bednarcik, M. Paskevicius, M.H. Sørby, T.R. Jensen, Structure and hydrogenation properties of a HfNbTiVZr high-entropy alloy, Inorganic chemistry 57(4) (2018) 2103-2110.

[163] L. Beavis, Characteristics of some binary transition metal hydrides, Journal of the Less Common Metals 19(4) (1969) 315-328.

[164] A. San-Martin, F. Manchester, The H− Ti (hydrogen-titanium) system, Bulletin of alloy phase diagrams 8(1) (1987) 30-42.

[165] E. Zuzek, J. Abriata, A. San-Martin, F. Manchester, The H-Zr (hydrogen-zirconium) system, Bulletin of alloy phase diagrams 11(4) (1990) 385-395.

[166] Y. Ye, Q. Wang, J. Lu, C. Liu, Y. Yang, High-entropy alloy: challenges and prospects, Materials Today 19(6) (2016) 349-362.

[167] S. Weissmann, M. Hirabayashi, H. Fujita, On the Mechanical and Thermal Stability of Low‐Angle Boundaries in Zinc Single Crystals, Journal of Applied Physics 32(6) (1961) 1156-1164.

[168] H. Guo, Y. Zhao, Y. Sun, J. Tian, H. Hou, K. Qi, X. Tian, Phase field crystal study of grain boundary structure and annihilation mechanism in low-angle grain boundary, Superlattices and Microstructures 129 (2019) 163-175.

[169] J.F. Smith, The H−Nb (Hydrogen-Niobium) and D−Nb (Deuterium-Niobium) systems, Bulletin of Alloy Phase Diagrams 4(1) (1983) 39-46.

[170] S. Yang, F. Yang, C. Wu, Y. Chen, Y. Mao, L. Luo, Hydrogen storage and cyclic properties of (VFe) 60 (TiCrCo) 40-xZrx (0≤ x≤ 2) alloys, Journal of Alloys and Compounds 663 (2016) 460-465.

[171] M.M. Nygård, G. Ek, D. Karlsson, M.H. Sørby, M. Sahlberg, B.C. Hauback, Counting electrons-a new approach to tailor the hydrogen sorption properties of high-entropy alloys, Acta Materialia 175 (2019) 121-129.

[172] R. Floriano, G. Zepon, K. Edalati, G.L. Fontana, A. Mohammadi, Z. Ma, H.-W. Li, R.J. Contieri, Hydrogen storage in TiZrNbFeNi high entropy alloys, designed by thermodynamic calculations, International Journal of Hydrogen Energy 45(58) (2020) 33759-33770.

[173] P. Edalati, R. Floriano, A. Mohammadi, Y. Li, G. Zepon, H.-W. Li, K. Edalati, Reversible room temperature hydrogen storage in high-entropy alloy TiZrCrMnFeNi, Scripta Materialia 178 (2020) 387-390.

[174] J. Montero, G. Ek, L. Laversenne, V. Nassif, G. Zepon, M. Sahlberg, C. Zlotea, Hydrogen storage properties of the refractory Ti–V–Zr–Nb–Ta multi-principal element alloy, Journal of Alloys and Compounds 835 (2020) 155376.

[175] J. Montero, C. Zlotea, G. Ek, J.-C. Crivello, L. Laversenne, M. Sahlberg, TiVZrNb multi-principal-element alloy: synthesis optimization, structural, and hydrogen sorption properties, Molecules 24(15) (2019) 2799.

[176] I. Kunce, M. Polanski, J. Bystrzycki, Microstructure and hydrogen storage properties of a TiZrNbMoV high entropy alloy synthesized using Laser Engineered Net Shaping (LENS), International Journal of Hydrogen Energy 39(18) (2014) 9904-9910.

[177] H. Shen, J. Zhang, J. Hu, J. Zhang, Y. Mao, H. Xiao, X. Zhou, X. Zu, A novel TiZrHfMoNb high-entropy alloy for solar thermal energy storage, Nanomaterials 9(2) (2019) 248.

[178] H. Shen, J. Hu, P. Li, G. Huang, J. Zhang, J. Zhang, Y. Mao, H. Xiao, X. Zhou, X. Zu, Compositional dependence of hydrogenation performance of Ti-Zr-Hf-Mo-Nb high-entropy alloys for hydrogen/tritium storage, Journal of Materials Science & Technology 55 (2020) 116-125.

[179] J. Montero, G. Ek, M. Sahlberg, C. Zlotea, Improving the hydrogen cycling properties by Mg addition in Ti-V-Zr-Nb refractory high entropy alloy, Scripta Materialia 194 (2021) 113699.

[180] M. Witman, G. Ek, S. Ling, J. Chames, S. Agarwal, J. Wong, M.D. Allendorf, M. Sahlberg, V. Stavila, Data-driven discovery and synthesis of high entropy alloy hydrides with targeted thermodynamic stability, Chemistry of Materials 33(11) (2021) 4067-4076.

[181] G. Zepon, B.H. Silva, C. Zlotea, W.J. Botta, Y. Champion, Thermodynamic modelling of hydrogen-multicomponent alloy systems: Calculating pressure-composition-temperature diagrams, Acta Materialia 215 (2021) 117070.

[182] C. Wu, L.S. Aota, J. Rao, X. Zhang, L. Perrière, M.J. Duarte, D. Raabe, Y. Ma, Hydrogen-assisted spinodal decomposition in a TiNbZrHfTa complex concentrated alloy, Acta Materialia 285 (2025) 120707.

[183] S.E. Hosseini, M.A. Wahid, Hydrogen production from renewable and sustainable energy resources: Promising green energy carrier for clean development, Renewable and Sustainable Energy Reviews 57 (2016) 850-866.

[184] A. Kovač, M. Paranos, D. Marciuš, Hydrogen in energy transition: A review, International Journal of Hydrogen Energy 46(16) (2021) 10016-10035.

[185] J.O. Abe, A.P.I. Popoola, E. Ajenifuja, O.M. Popoola, Hydrogen energy, economy and storage: Review and recommendation, International Journal of Hydrogen Energy 44(29) (2019) 15072-15086.

[186] J.C. Zhao, J.H. Westbrook, Ultrahigh-Temperature Materials for Jet Engines, MRS Bulletin 28(9) (2003) 622-630.

[187] C. Zlotea, M. Sow, G. Ek, J.-P. Couzinié, L. Perrière, I. Guillot, J. Bourgon, K. Møller, T. Jensen, E. Akiba, Hydrogen sorption in TiZrNbHfTa high entropy alloy, Journal of Alloys and Compounds 775 (2019) 667-674.

[188] O.N. Senkov, S. Gorsse, D.B. Miracle, High temperature strength of refractory complex concentrated alloys, Acta Materialia 175 (2019) 394-405.

[189] F. Sun, G. Miyamoto, Y. Liu, Y. Hayasaka, T. Furuhara, Phase separation with ordering in aged Fe-Ni-Mn medium entropy alloy, Acta Materialia 223 (2022) 117487.

[190] P.T. Hung, M. Kawasaki, J.-K. Han, J.L. Lábár, J. Gubicza, Thermal stability of a nanocrystalline HfNbTiZr multi-principal element alloy processed by high-pressure torsion, Materials Characterization 168 (2020) 110550.

[191] Y. Guo, J. He, W. Lu, L. Jia, Z. Li, The evolution of compositional and microstructural heterogeneities in a TaMo0.5ZrTi1.5Al0.1Si0.2 high entropy alloy, Materials Characterization 172 (2021) 110836.

[192] Y. Cao, W. Zhang, B. Liu, Y. Liu, M. Du, A. Fu, Phase decomposition behavior and its effects on mechanical properties of TiNbTa0.5ZrAl0.5 refractory high entropy alloy, Journal of Materials Science & Technology 66 (2021) 10-20.

[193] H.-J. Christ, M. Decker, S. Zeitler, Hydrogen diffusion coefficients in the titanium alloys IMI 834, Ti 10-2-3, Ti 21 S, and alloy C, Metallurgical and Materials Transactions A 31 (2000) 1507-1517.

[194] K. Hirata, S. Iikubo, M. Koyama, K. Tsuzaki, H. Ohtani, First-Principles Study on Hydrogen Diffusivity in BCC, FCC, and HCP Iron, Metallurgical and Materials Transactions A 49(10) (2018) 5015-5022.

[195] S. Trasatti, Electronegativity, work function, and heat of adsorption of hydrogen on metals, Journal of the Chemical Society, Faraday Transactions 1: Physical Chemistry in Condensed Phases 68 (1972) 229-236.

[196] S.K. Dwivedi, M. Vishwakarma, Hydrogen embrittlement in different materials: A review, International Journal of Hydrogen Energy 43(46) (2018) 21603-21616.

[197] I.M. Robertson, P. Sofronis, A. Nagao, M.L. Martin, S. Wang, D. Gross, K. Nygren, Hydrogen embrittlement understood, Metallurgical and Materials Transactions A 46 (2015) 2323-2341.

[198] P. Cotterill, The hydrogen embrittlement of metals, Progress in Materials Science 9(4) (1961) 205-301.

[199] L. Luo, L. Chen, L. Li, S. Liu, Y. Li, C. Li, L. Li, J. Cui, Y. Li, High-entropy alloys for solid hydrogen storage: a review, International Journal of Hydrogen Energy 50 (2024) 406-430.

[200] T.R. Somo, M.V. Lototskyy, V.A. Yartys, M.W. Davids, S.N. Nyamsi, Hydrogen storage behaviours of high entropy alloys: A Review, Journal of Energy Storage 73 (2023) 108969.

[201] M. Hÿtch, E. Snoeck, R. Kilaas, Quantitative measurement of displacement and strain fields from HREM micrographs, Ultramicroscopy 74(3) (1998) 131-146.

[202] D.R. McKenzie, Y. Yin, W.D. McFall, N.H. Hoang, The orientation dependence of elastic strain energy in cubic crystals and its application to the preferred orientation in titanium nitride thin films, Journal of Physics: Condensed Matter 8(32) (1996) 5883.

[203] D. Seol, S. Hu, Y. Li, J. Shen, K. Oh, L. Chen, Computer simulation of spinodal decomposition in constrained films, Acta materialia 51(17) (2003) 5173-5185.

[204] A. Shariq, T. Al-Kassab, R. Kirchheim, Studying nearest neighbor correlations by atom probe tomography (APT) in metallic glasses as exemplified for Fe40Ni40B20 glassy ribbons, Journal of Alloys and Compounds 512(1) (2012) 270-277.

[205] T. Philippe, F. De Geuser, S. Duguay, W. Lefebvre, O. Cojocaru-Mirédin, G. Da Costa, D. Blavette, Clustering and nearest neighbour distances in atom-probe tomography, Ultramicroscopy 109(10) (2009) 1304-1309.

[206] D.E. Perea, I. Arslan, J. Liu, Z. Ristanović, L. Kovarik, B.W. Arey, J.A. Lercher, S.R. Bare, B.M. Weckhuysen, Determining the location and nearest neighbours of aluminium in zeolites with atom probe tomography, Nature Communications 6(1) (2015) 7589.

[207] M.P. Moody, L.T. Stephenson, A.V. Ceguerra, S.P. Ringer, Quantitative binomial distribution analyses of nanoscale like-solute atom clustering and segregation in atom probe tomography data, Microscopy Research and Technique 71(7) (2008) 542-550.

[208] R. Hu, S. Jin, G. Sha, Application of atom probe tomography in understanding high entropy alloys: 3D local chemical compositions in atomic scale analysis, Progress in Materials Science 123 (2022) 100854.

[209] T. Philippe, P.W. Voorhees, Ostwald ripening in multicomponent alloys, Acta Materialia 61(11) (2013) 4237-4244.

[210] T. Philippe, D. Blavette, P. Voorhees, Critical nucleus composition in a multicomponent system, The Journal of Chemical Physics 141(12) (2014).

[211] Z. Rao, B. Dutta, F. Körmann, W. Lu, X. Zhou, C. Liu, A.K. da Silva, U. Wiedwald, M. Spasova, M. Farle, Beyond solid solution high‐entropy alloys: tailoring magnetic properties via spinodal decomposition, Advanced Functional Materials 31(7) (2021) 2007668.

[212] M. Hetherington, M. Miller, On the statistical analysis of atom probe data, Le Journal de Physique Colloques 48(C6) (1987) C6-559-C6-564.

[213] D. Blavette, F. Vurpillot, P. Pareige, A. Menand, A model accounting for spatial overlaps in 3D atom-probe microscopy, Ultramicroscopy 89(1-3) (2001) 145-153.

[214] W.M. Haynes, CRC handbook of chemistry and physics, CRC press2016.

[215] T. Xin, Y. Zhao, R. Mahjoub, J. Jiang, A. Yadav, K. Nomoto, R. Niu, S. Tang, F. Ji, Z. Quadir, Ultrahigh specific strength in a magnesium alloy strengthened by spinodal decomposition, Science advances 7(23) (2021) eabf3039.

[216] B.G. Yuan, C.F. Li, H.P. Yu, D.L. Sun, Influence of hydrogen content on tensile and compressive properties of Ti–6Al–4V alloy at room temperature, Materials Science and Engineering: A 527(16) (2010) 4185-4190.

[217] W.R. Kerr, The effect of hydrogen as a temporary alloying element on the microstructure and tensile properties of Ti-6Al-4V, Metallurgical Transactions A 16 (1985) 1077-1087.

[218] H.J. Christ, A. Senemmar, M. Decker, K. Prü\ner, Effect of hydrogen on mechanical properties of β -titanium alloys, Sadhana 28(3) (2003) 453-465.

[219] W. Soboyejo, Mechanical properties of engineered materials, CRC press2002.

[220] J. Waisman, G. Sines, L. Robinson, Diffusion of hydrogen in titanium alloys due to composition, temperature, and stress gradients, Metallurgical transactions 4 (1973) 291-302.

[221] M. Kato, Hardening by spinodally modulated structure in bcc alloys, Acta Metallurgica 29(1) (1981) 79-87.

[222] W. Petry, A. Heiming, J. Trampenau, M. Alba, C. Herzig, H. Schober, G. Vogl, Phonon dispersion of the bcc phase of group-IV metals. I. bcc titanium, Physical Review B 43(13) (1991) 10933.

[223] D. Tabor, The physical meaning of indentation and scratch hardness, British Journal of Applied Physics 7(5) (1956) 159.

[224] Y. Luo, Q. Pan, Y. Sun, S. Liu, Y. Sun, L. Long, X. Li, X. Wang, M. Li, Hardening behavior of Al-0.25Sc and Al-0.25Sc-0.12Zr alloys during isothermal annealing, Journal of Alloys and Compounds 818 (2020) 152922.

[225] R. Rachbauer, S. Massl, E. Stergar, D. Holec, D. Kiener, J. Keckes, J. Patscheider, M. Stiefel, H. Leitner, P.H. Mayrhofer, Decomposition pathways in age hardening of Ti-Al-N films, Journal of Applied Physics 110(2) (2011).

[226] Z. An, S. Mao, T. Yang, C.T. Liu, B. Zhang, E. Ma, H. Zhou, Z. Zhang, L. Wang, X. Han, Spinodal-modulated solid solution delivers a strong and ductile refractory high-entropy alloy, Materials Horizons 8(3) (2021) 948-955.

[227] S. Bellemare, M. Dao, S. Suresh, A new method for evaluating the plastic properties of materials through instrumented frictional sliding tests, Acta materialia 58(19) (2010) 6385-6392.

[228] A. Prasad, M. Dao, S. Suresh, Steady-state frictional sliding contact on surfaces of plastically graded materials, Acta Materialia 57(2) (2009) 511-524.

[229] S. Wei, C.C. Tasan, Deformation faulting in a metastable CoCrNiW complex concentrated alloy: a case of negative intrinsic stacking fault energy?, Acta Materialia 200 (2020) 992-1007.

[230] K. Kadirvel, S.R. Koneru, Y. Wang, Exploration of spinodal decomposition in multi-principal element alloys (MPEAs) using CALPHAD modeling, Scripta Materialia 214 (2022) 114657.

[231] S. Wei, F. He, C.C. Tasan, Metastability in high-entropy alloys: A review, Journal of Materials Research 33(19) (2018) 2924-2937.

[232] S.A. Kube, J. Schroers, Metastability in high entropy alloys, Scripta Materialia 186 (2020) 392-400.

[233] E. Veleckis, R.K. Edwards, Thermodynamic properties in the systems vanadium-hydrogen, niobium-hydrogen, and tantalum-hydrogen, The Journal of Physical Chemistry 73(3) (1969) 683-692.

[234] K. Wang, X. Kong, J. Du, C. Li, Z. Li, Z. Wu, Thermodynamic description of the Ti–H system, Calphad 34(3) (2010) 317-323.

[235] H.-X. Huang, Y.-H. Li, Z.-Z. Li, P.-W. Hou, F.-F. Ma, Q.-Y. Ren, H.-B. Zhou, G.-H. Lu, Role of hydrogen in stability and mobility of vacancy clusters in tungsten, Tungsten 4(3) (2022) 219-230.

[236] L. Ismer, M.S. Park, A. Janotti, C.G. Van de Walle, Interactions between hydrogen impurities and vacancies in Mg and Al: A comparative analysis based on density functional theory, Physical Review B 80(18) (2009) 184110.

[237] H.W. Jeong, Y.S. Yoo, Y.T. Lee, J.K. Park, Elastic softening behavior of Ti–Nb single crystal near martensitic transformation temperature, Journal of Applied Physics 108(6) (2010).

[238] Q. Meng, Q. Liu, S. Guo, Y. Zhu, X. Zhao, Effect of thermo-mechanical treatment on mechanical and elastic properties of Ti–36Nb–5Zr alloy, Progress in Natural Science: Materials International 25(3) (2015) 229-235.

[239] E. Obbard, Y. Hao, T. Akahori, R. Talling, M. Niinomi, D. Dye, R. Yang, Mechanics of superelasticity in Ti–30Nb–(8–10) Ta–5Zr alloy, Acta Materialia 58(10) (2010) 3557-3567.

[240] R. Talling, R. Dashwood, M. Jackson, S. Kuramoto, D. Dye, Determination of (C11-C12) in Ti–36Nb–2Ta–3Zr–0.3 O (wt.%)(Gum metal), Scripta Materialia 59(6) (2008) 669-672.

[241] R. Chinnappan, B. Panigrahi, A. van de Walle, First-principles study of phase equilibrium in Ti–V, Ti–Nb, and Ti–Ta alloys, Calphad 54 (2016) 125-133.

[242] G. Cacciamani, P. Riani, F. Valenza, Equilibrium between MB2 (M= Ti, Zr, Hf) UHTC and Ni: a thermodynamic database for the B–Hf–Ni–Ti–Zr system, Calphad 35(4) (2011) 601-619.

[243] T. Tokunaga, S. Matsumoto, H. Ohtani, M. Hasebe, Thermodynamic analysis of the phase equilibria in the Nb-Ni-Zr system, Materials transactions 48(9) (2007) 2263-2271.

[244] C. Guo, C. Li, S. Shang, Z. Du, Thermodynamic description of the Ta–W–Zr system, International Journal of Materials Research 105(11) (2014) 1048-1056.

[245] Y. Yang, Y. Chang, J.-C. Zhao, B. Bewlay, Thermodynamic modeling of the Nb–Hf–Si ternary system, Intermetallics 11(5) (2003) 407-415.

[246] Y. Pan, P. Zhou, Y. Peng, Y. Du, F. Luo, A thermodynamic description of the C–Hf–Ta system over the whole composition and temperature ranges, Calphad 53 (2016) 1-9.

[247] W. Xiong, Y. Du, Y. Liu, B. Huang, H. Xu, H. Chen, Z. Pan, Thermodynamic assessment of the Mo–Nb–Ta system, Calphad 28(2) (2004) 133-140.

[248] M. Dottor, J.-C. Crivello, J.-M. Joubert, Critical reassessment of the H–Nb system and experimental investigation and thermodynamic modeling of the H–Nb–Zr system, Calphad 83 (2023) 102617.

[249] M. Liao, Y. Liu, P. Cui, N. Qu, F. Zhou, D. Yang, T. Han, Z. Lai, J. Zhu, Modeling of alloying effect on elastic properties in BCC Nb-Ti-V-Zr solid solution: From unary to quaternary, Computational Materials Science 172 (2020) 109289.

[250] C. Marker, S.-L. Shang, J.-C. Zhao, Z.-K. Liu, Thermodynamic description of the Ti-Mo-Nb-Ta-Zr system and its implications for phase stability of Ti bio-implant materials, Calphad 61 (2018) 72-84.

[251] S. Ukita, H. Ohtani, M. Hasebe, Thermodynamic Analysis of the Ti-Zr-H Ternary Phase Diagram, Advanced Materials Research 26 (2007) 989-992.

[252] O. Le Bacq, F. Willaime, A. Pasturel, Unrelaxed vacancy formation energies in group-IV elements calculated by the full-potential linear muffin-tin orbital method: Invariance with crystal structure, Physical Review B 59(13) (1999) 8508.

[253] X. Han, Q. Wang, D. Sun, H. Zhang, First-principles study of the effect of hydrogen on the Ti self-diffusion characteristics in the alpha Ti–H system, Scripta materialia 56(1) (2007) 77-80.

[254] L.A. Svyatkin, Y.M. Koroteev, I.P. Chernov, Mutual influence of hydrogen and vacancies in α-zirconium on the energy of their interaction with metal, Physics of the Solid State 60 (2018) 10-19.

[255] A.-Y. Gao, Y.-L. Liu, Z.-H. Dai, C. Duan, Elucidating hydrogen assisting vacancy formation in metals: Mo and Nb as examples, The European Physical Journal B 86 (2013) 1-8.

[256] A. Satta, F. Willaime, S. de Gironcoli, First-principles study of vacancy formation and migration energies in tantalum, Physical Review B 60(10) (1999) 7001.

[257] O. Senkov, S. Semiatin, Microstructure and properties of a refractory high-entropy alloy after cold working, Journal of Alloys and Compounds 649 (2015) 1110-1123.

[258] Y. Zou, S. Maiti, W. Steurer, R. Spolenak, Size-dependent plasticity in an Nb25Mo25Ta25W25 refractory high-entropy alloy, Acta Materialia 65 (2014) 85-97.

[259] O.N. Senkov, C. Woodward, D.B. Miracle, Microstructure and Properties of Aluminum-Containing Refractory High-Entropy Alloys, JOM 66(10) (2014) 2030-2042.

[260] C. Lee, Y. Chou, G. Kim, M.C. Gao, K. An, J. Brechtl, C. Zhang, W. Chen, J.D. Poplawsky, G. Song, Y. Ren, Y.-C. Chou, P.K. Liaw, Lattice-Distortion-Enhanced Yield Strength in a Refractory High-Entropy Alloy, Advanced Materials 32(49) (2020) 2004029.

[261] Z.D. Han, N. Chen, S.F. Zhao, L.W. Fan, G.N. Yang, Y. Shao, K.F. Yao, Effect of Ti additions on mechanical properties of NbMoTaW and VNbMoTaW refractory high entropy alloys, Intermetallics 84 (2017) 153-157.

[262] W. Guo, B. Liu, Y. Liu, T. Li, A. Fu, Q. Fang, Y. Nie, Microstructures and mechanical properties of ductile NbTaTiV refractory high entropy alloy prepared by powder metallurgy, Journal of Alloys and Compounds 776 (2019) 428-436.

[263] C. Zhang, H. Wang, X. Wang, Y.T. Tang, Q. Yu, C. Zhu, M. Xu, S. Zhao, R. Kou, X. Wang, B.E. MacDonald, R.C. Reed, K.S. Vecchio, P. Cao, T.J. Rupert, E.J. Lavernia, Strong and ductile refractory high-entropy alloys with super formability, Acta Materialia 245 (2023) 118602.

[264] R. Huang, W. Wang, T. Li, L. Zhang, A. Amar, X. Chen, Z. Ren, Y. Lu, A novel AlMoNbHfTi refractory high-entropy alloy with superior ductility, Journal of Alloys and Compounds 940 (2023) 168821.

[265] N. Peterson, Diffusion in refractory metals, Wright Air Development Division, Air Research and Development Command …1960.

[266] H. Huang, Y. Wu, J. He, H. Wang, X. Liu, K. An, W. Wu, Z. Lu, Phase-Transformation Ductilization of Brittle High-Entropy Alloys via Metastability Engineering, Advanced Materials 29(30) (2017) 1701678.

[267] C.-C. Juan, M.-H. Tsai, C.-W. Tsai, W.-L. Hsu, C.-M. Lin, S.-K. Chen, S.-J. Lin, J.-W. Yeh, Simultaneously increasing the strength and ductility of a refractory high-entropy alloy via grain refining, Materials Letters 184 (2016) 200-203.

[268] M. Seah, Interface adsorption, embrittlement and fracture in metallurgy: A review, Surface Science 53(1) (1975) 168-212.

[269] M. Seah, Segregation and the strength of grain boundaries, Proceedings of the Royal Society of London. A. Mathematical and Physical Sciences 349(1659) (1976) 535-554.

[270] Y. Tan, R. Chen, H. Fang, Y. Liu, H. Cui, Y. Su, J. Guo, H. Fu, Enhanced strength and ductility in Ti46Al4Nb1Mo alloys via boron addition, Journal of Materials Science & Technology 102 (2022) 16-23.

[271] J. Pang, H. Zhang, L. Zhang, Z. Zhu, H. Fu, H. Li, A. Wang, Z. Li, H. Zhang, Simultaneous enhancement of strength and ductility of body-centered cubic TiZrNb multi-principal element alloys via boron-doping, Journal of Materials Science & Technology 78 (2021) 74-80.

[272] J.B. Seol, J.W. Bae, Z. Li, J.C. Han, J.G. Kim, D. Raabe, H.S. Kim, Boron doped ultrastrong and ductile high-entropy alloys, Acta Materialia 151 (2018) 366-376.

[273] Y. Qi, T. Cao, H. Zong, Y. Wu, L. He, X. Ding, F. Jiang, S. Jin, G. Sha, J. Sun, Enhancement of strength-ductility balance of heavy Ti and Al alloyed FeCoNiCr high-entropy alloys via boron doping, Journal of Materials Science & Technology 75 (2021) 154-163.

[274] L. Ma, X. Zhang, B. Pu, D. Zhao, C. He, N. Zhao, Achieving the strength-ductility balance of boron nitride nanosheets/Al composite by designing the synergistic transition interface and intragranular reinforcement distribution, Composites Part B: Engineering 246 (2022) 110243.

[275] S. Wei, K.S. Kim, J. Foltz, C.C. Tasan, Discovering Pyramidal Treasures: Multi‐scale Design of High Strength‐Ductility Titanium Alloys, Advanced Materials (2024) 2406382.

[276] G. Zhu, L. Wang, H. Zhou, J. Wang, Y. Shen, P. Tu, H. Zhu, W. Liu, P. Jin, X. Zeng, Improving ductility of a Mg alloy via non-basal< a> slip induced by Ca addition, International Journal of Plasticity 120 (2019) 164-179.

[277] P.M. Anderson, J.P. Hirth, J. Lothe, Theory of dislocations, Cambridge University Press2017.

[278] L. Wang, Y. Yang, P. Eisenlohr, T. Bieler, M. Crimp, D. Mason, Twin nucleation by slip transfer across grain boundaries in commercial purity titanium, Metallurgical and Materials Transactions A 41(2) (2010) 421-430.

[279] H.-J. Bunge, Texture analysis in materials science: mathematical methods, Elsevier2013.

[280] S. Wei, J. Kim, C.C. Tasan, Boundary micro-cracking in metastable Fe45Mn35Co10Cr10 high-entropy alloys, Acta Materialia 168 (2019) 76-86.

[281] G. Williamson, W. Hall, X-ray line broadening from filed aluminium and wolfram, Acta metallurgica 1(1) (1953) 22-31.

[282] G. Williamson, R. Smallman, III. Dislocation densities in some annealed and cold-worked metals from measurements on the X-ray debye-scherrer spectrum, Philosophical magazine 1(1) (1956) 34-46.

[283] E. Hall, The deformation and ageing of mild steel: III discussion of results, Proceedings of the Physical Society. Section B 64(9) (1951) 747.

[284] N.J. Petch, The cleavage strength of polycrystals, J. Iron Steel Inst. 174 (1953) 25-28.

[285] N. Hansen, Hall–Petch relation and boundary strengthening, Scripta materialia 51(8) (2004) 801-806.

[286] J. Burke, D. Turnbull, Recrystallization and grain growth, Progress in metal physics 3 (1952) 220-292.

[287] H. Atkinson, Overview no. 65: Theories of normal grain growth in pure single phase systems, Acta Metallurgica 36(3) (1988) 469-491.

[288] H. Adrian, F. Pickering, Effect of titanium additions on austenite grain growth kinetics of medium carbon V–Nb steels containing 0· 008–0· 018% N, Materials Science and Technology 7(2) (1991) 176-182.

[289] M. Hillert, On the theory of normal and abnormal grain growth, Acta metallurgica 13(3) (1965) 227-238.

[290] R. Armstrong, I. Codd, R. Douthwaite, N. Petch, The plastic deformation of polycrystalline aggregates, The Philosophical Magazine: A Journal of Theoretical Experimental and Applied Physics 7(73) (1962) 45-58.

[291] D. Wu, J. Zhang, J. Huang, H. Bei, T.-G. Nieh, Grain-boundary strengthening in nanocrystalline chromium and the Hall–Petch coefficient of body-centered cubic metals, Scripta Materialia 68(2) (2013) 118-121.

[292] L. Murr, Dislocation ledge sources: dispelling the myth of Frank–Read source importance, Metallurgical and Materials Transactions A 47 (2016) 5811-5826.

[293] J.C. Li, High‐angle tilt boundary—a dislocation core model, Journal of Applied Physics 32(3) (1961) 525-541.

[294] Y. Hao, S. Li, B. Sun, M. Sui, R. Yang, Ductile titanium alloy with low Poisson's ratio, Physical review letters 98(21) (2007) 216405.

[295] B.-T. Wang, P. Zhang, H.-Y. Liu, W.-D. Li, P. Zhang, First-principles calculations of phase transition, low elastic modulus, and superconductivity for zirconium, arXiv preprint arXiv:1007.4913 (2010).

[296] M.E. Gurtin, E. Fried, L. Anand, The mechanics and thermodynamics of continua, Cambridge university press2010.

[297] T.Y. Thomas, Plastic flow and fracture in solids by tracy Y Thomas, Elsevier1961.

[298] S.D. Antolovich, R.W. Armstrong, Plastic strain localization in metals: origins and consequences, Progress in Materials Science 59 (2014) 1-160.

[299] C.C. Tasan, J.P. Hoefnagels, M. Diehl, D. Yan, F. Roters, D. Raabe, Strain localization and damage in dual phase steels investigated by coupled in-situ deformation experiments and crystal plasticity simulations, International Journal of Plasticity 63 (2014) 198-210.

[300] M. Linne, A. Venkataraman, M. Sangid, S. Daly, Grain boundary sliding and slip transmission in high purity aluminum, Experimental Mechanics 59 (2019) 643-658.

[301] M.A. Linne, T.R. Bieler, S. Daly, The effect of microstructure on the relationship between grain boundary sliding and slip transmission in high purity aluminum, International Journal of Plasticity 135 (2020) 102818.

[302] R. Gates, The role of grain boundary dislocations in grain boundary sliding, Acta Metallurgica 21(7) (1973) 855-864.

[303] S. Wei, C.C. Tasan, On the plastic deformation of a CoCrFeNiW-C alloy at elevated temperatures: Part II. Grain boundary sliding and damage mechanisms, Acta Materialia 252 (2023) 118898.

[304] T. Watanabe, T. Murakami, S. Karashima, Misorientation dependence of grain boundary segregation, Scripta Metallurgica 12(4) (1978) 361-365.

[305] T. Duh, J. Kai, F. Chen, L. Wang, Effects of grain boundary misorientation on the solute segregation in austenitic stainless steels, Journal of nuclear materials 258 (1998) 2064-2068.

[306] T.G. Langdon, Grain boundary sliding as a deformation mechanism during creep, Philosophical Magazine 22(178) (1970) 689-700.

[307] M. Ashby, R. Verrall, Diffusion-accommodated flow and superplasticity, Acta metallurgica 21(2) (1973) 149-163.

[308] A. Ball, Superplasticity in the aluminium-zinc eutectoid—an early model revisited, Materials Science and Engineering: A 234 (1997) 365-369.

[309] H. Kokawa, T. Watanabe, S. Karashima, Sliding behaviour and dislocation structures in aluminium grain boundaries, Philosophical Magazine A 44(6) (1981) 1239-1254.

[310] J. Luster, M. Morris, Compatibility of deformation in two-phase Ti-Al alloys: Dependence on microstructure and orientation relationships, Metallurgical and Materials Transactions A 26 (1995) 1745-1756.

[311] Y. Li, P. Gao, J. Yu, S. Jin, S. Chen, M. Zhan, Mesoscale deformation mechanisms in relation with slip and grain boundary sliding in TA15 titanium alloy during tensile deformation, Journal of Materials Science & Technology 98 (2022) 72-86.

[312] Y. Wei, L. Anand, Grain-boundary sliding and separation in polycrystalline metals: application to nanocrystalline fcc metals, Journal of the Mechanics and Physics of Solids 52(11) (2004) 2587-2616.

[313] R. Feng, B. Feng, M.C. Gao, C. Zhang, J.C. Neuefeind, J.D. Poplawsky, Y. Ren, K. An, M. Widom, P.K. Liaw, Superior high‐temperature strength in a supersaturated refractory high‐entropy alloy, Advanced materials 33(48) (2021) 2102401.

[314] O.N. Senkov, G.B. Wilks, D.B. Miracle, C.P. Chuang, P.K. Liaw, Refractory high-entropy alloys, Intermetallics 18(9) (2010) 1758-1765.

[315] T. Li, S. Wang, W. Fan, Y. Lu, T. Wang, T. Li, P.K. Liaw, CALPHAD-aided design for superior thermal stability and mechanical behavior in a TiZrHfNb refractory high-entropy alloy, Acta Materialia 246 (2023) 118728.

[316] Y. Wan, J. Mo, X. Wang, Z. Zhang, B. Shen, X. Liang, Mechanical Properties and Phase Stability of WTaMoNbTi Refractory High-Entropy Alloy at Elevated Temperatures, Acta Metallurgica Sinica (English Letters) 34(11) (2021) 1585-1590.

[317] Y. Guo, J. Peng, S. Peng, F. An, W. Lu, Z. Li, Improving oxidation resistance of TaMoZrTiAl refractory high entropy alloys via Nb and Si alloying, Corrosion Science 223 (2023) 111455.

[318] Y.F. Ye, Q. Wang, J. Lu, C.T. Liu, Y. Yang, High-entropy alloy: challenges and prospects, Materials Today 19(6) (2016) 349-362.

[319] N. Xu, C. Pang, W. Tong, J. Liu, L. Li, P. Xu, Evaluation of microstructure, mechanical properties and osseointegration capacity of laser cladding β-type TiNbZr coatings, Materials Today Communications 41 (2024) 110298.

[320] Q. Meng, S. Guo, Q. Liu, L. Hu, X. Zhao, A β-type TiNbZr alloy with low modulus and high strength for biomedical applications, Progress in Natural Science: Materials International 24(2) (2014) 157-162.

[321] B. Li, P. Ji, B. Chen, F. Wang, W. Ma, X. Zhang, M. Ma, R. Liu, The effect of Zr addition on the microstructure evolution and mechanical properties of hot-rolled TiAlNbZr alloy, Materials Science and Engineering: A 828 (2021) 142114.

[322] Ş. Karadeniz, E. Arslan, Microstructural Characterization and Wear Behavior of Porous Equimolar TiNbZr Medium-Entropy Alloys Scaffolds Produced by Mechanical Alloying, Materials Research 25 (2022).

[323] X. Wang, Y. Li, J. Xiong, P.D. Hodgson, C.e. Wen, Porous TiNbZr alloy scaffolds for biomedical applications, Acta Biomaterialia 5(9) (2009) 3616-3624.

[324] C.R. Weinberger, B.L. Boyce, C.C. Battaile, Slip planes in bcc transition metals, International Materials Reviews 58(5) (2013) 296-314.

[325] S. Tekumalla, M. Seita, S. Zaefferer, Delineating dislocation structures and residual stresses in additively manufactured alloys, Acta Materialia 262 (2024) 119413.

[326] E. Mak, B. Yin, W.A. Curtin, A ductility criterion for bcc high entropy alloys, Journal of the Mechanics and Physics of Solids 152 (2021) 104389.

[327] G. Dirras, H. Couque, L. Lilensten, A. Heczel, D. Tingaud, J.P. Couzinié, L. Perrière, J. Gubicza, I. Guillot, Mechanical behavior and microstructure of Ti20Hf20Zr20Ta20Nb20 high-entropy alloy loaded under quasi-static and dynamic compression conditions, Materials Characterization 111 (2016) 106-113.

[328] R. Salloom, R. Banerjee, S.G. Srinivasan, Effect of β-stabilizer elements on stacking faults energies and ductility of α-titanium using first-principles calculations, Journal of Applied Physics 120(17) (2016).

[329] S. Chen, K.-K. Tseng, Y. Tong, W. Li, C.-W. Tsai, J.-W. Yeh, P.K. Liaw, Grain growth and Hall-Petch relationship in a refractory HfNbTaZrTi high-entropy alloy, Journal of Alloys and Compounds 795 (2019) 19-26.

[330] B. Kang, J. Lee, H.J. Ryu, S.H. Hong, Microstructure, mechanical property and Hall-Petch relationship of a light-weight refractory Al0.1CrNbVMo high entropy alloy fabricated by powder metallurgical process, Journal of Alloys and Compounds 767 (2018) 1012-1021.

[331] W. Huang, S. Yin, X. Wang, R. Guo, Y. Wu, J. Qiao, Grain growth and Hall–Petch relationship in Ti37V15Nb22Hf23W3 refractory high-entropy alloys, Journal of Materials Research 38(6) (2023) 1719-1729.

[332] K. Lee, Y. Jung, J. Han, S.H. Hong, K.B. Kim, P.K. Liaw, C. Lee, G. Song, Development of Precipitation-Strengthened Al0.8NbTiVM (M = Co, Ni) Light-Weight Refractory High-Entropy Alloys, Materials 14(8) (2021) 2085.

[333] T. Li, T. Liu, S. Zhao, Y. Chen, J. Luan, Z. Jiao, R.O. Ritchie, L. Dai, Ultra-strong tungsten refractory high-entropy alloy via stepwise controllable coherent nanoprecipitations, Nature Communications 14(1) (2023) 3006.

[334] B.H. Toby, R.B. Von Dreele, GSAS-II: the genesis of a modern open-source all purpose crystallography software package, Applied Crystallography 46(2) (2013) 544-549.

[335] S.V. Ushakov, A. Navrotsky, Q.-J. Hong, A. van de Walle, Carbides and nitrides of zirconium and hafnium, Materials 12(17) (2019) 2728.

[336] W. Ma, F.W. Herbert, S.D. Senanayake, B. Yildiz, Non-equilibrium oxidation states of zirconium during early stages of metal oxidation, Applied Physics Letters 106(10) (2015).

[337] P. Marcus, On some fundamental factors in the effect of alloying elements on passivation of alloys, Corrosion science 36(12) (1994) 2155-2158.

[338] J. Badding, D. Nesting, Thermodynamic analysis of the formation of carbon nitrides under pressure, Chemistry of materials 8(2) (1996) 535-540.

[339] G. Neumann, C. Tuijn, Self-diffusion and impurity diffusion in pure metals: handbook of experimental data, Elsevier2011.

[340] N. Peterson, Self-diffusion in pure metals, Journal of Nuclear Materials 69 (1978) 3-37.

[341] I. Gutiérrez-Urrutia, D. Raabe, Multistage strain hardening through dislocation substructure and twinning in a high strength and ductile weight-reduced Fe–Mn–Al–C steel, Acta Materialia 60(16) (2012) 5791-5802.

[342] L. Han, F. Maccari, I.R. Souza Filho, N.J. Peter, Y. Wei, B. Gault, O. Gutfleisch, Z. Li, D. Raabe, A mechanically strong and ductile soft magnet with extremely low coercivity, Nature 608(7922) (2022) 310-316.

[343] L. Feigin, D.I. Svergun, Structure analysis by small-angle X-ray and neutron scattering, Springer1987.

[344] A. Isihara, Determination of molecular shape by osmotic measurement, Journal of Chemical Physics 18(11) (1950) 1446-1449.

[345] D. McKenzie, Y. Yin, W. McFall, N. Hoang, The orientation dependence of elastic strain energy in cubic crystals and its application to the preferred orientation in titanium nitride thin films, Journal of Physics: Condensed Matter 8(32) (1996) 5883.

[346] P. Littlewood, T. Britton, A. Wilkinson, Geometrically necessary dislocation density distributions in Ti–6Al–4V deformed in tension, Acta Materialia 59(16) (2011) 6489-6500.

[347] J.F. Nye, Some geometrical relations in dislocated crystals, Acta metallurgica 1(2) (1953) 153-162.

[348] S. Birosca, G. Liu, R. Ding, J. Jiang, T. Simm, C. Deen, M. Whittaker, The dislocation behaviour and GND development in a nickel based superalloy during creep, International Journal of Plasticity 118 (2019) 252-268.

[349] F. Liang, B. Zhang, Y. Yong, X.-M. Luo, G.-P. Zhang, Enhanced strain delocalization through formation of dispersive micro shear bands in laminated Ni, International Journal of Plasticity 132 (2020) 102745.

[350] S. Liu, F. Yang, H. Yang, G. Huang, A. Tang, X. Chen, B. Jiang, F. Pan, High-resolution mapping of the strain heterogeneity in heterogeneous and homogeneous structured Mg13Gd alloy, Materials Characterization 193 (2022) 112335.

[351] Z. Liu, R. Li, D. Chen, Y. Sun, B. He, Y. Zou, Enhanced tensile ductility of an additively manufactured near-α titanium alloy by microscale shear banding, International Journal of Plasticity 157 (2022) 103387.

[352] P. Frint, M.F.-X. Wagner, Strain partitioning by recurrent shear localization during equal-channel angular pressing of an AA6060 aluminum alloy, Acta Materialia 176 (2019) 306-317.

[353] X. Jiang, X. Fan, M. Zhan, R. Wang, Y. Liang, Microstructure dependent strain localization during primary hot working of TA15 titanium alloy: Behavior and mechanism, Materials & Design 203 (2021) 109589.

[354] P. Castany, A. Ramarolahy, F. Prima, P. Laheurte, C. Curfs, T. Gloriant, In situ synchrotron X-ray diffraction study of the martensitic transformation in superelastic Ti-24Nb-0.5N and Ti-24Nb-0.5O alloys, Acta Materialia 88 (2015) 102-111.

[355] M. Tahara, H.Y. Kim, H. Hosoda, S. Miyazaki, Cyclic deformation behavior of a Ti–26 at.% Nb alloy, Acta Materialia 57(8) (2009) 2461-2469.

[356] L. Liu, L. Li, Z. Liang, M. Huang, Z. Peng, J. Gao, Z. Luo, Towards ultra-high strength dual-phase steel with excellent damage tolerance: The effect of martensite volume fraction, International Journal of Plasticity 170 (2023) 103778.

[357] J.W. Hutchinson, K.W. Neale, Influence of strain-rate sensitivity on necking under uniaxial tension, Acta Metallurgica 25(8) (1977) 839-846.

[358] P. Haasen, Plastic deformation of nickel single crystals at low temperatures, The Philosophical Magazine: A Journal of Theoretical Experimental and Applied Physics 3(28) (1958) 384-418.

[359] H. Mecking, U.F. Kocks, Kinetics of flow and strain-hardening, Acta Metallurgica 29(11) (1981) 1865-1875.

[360] U.F. Kocks, The relation between polycrystal deformation and single-crystal deformation, Metallurgical Transactions 1(5) (1970) 1121-1143.

[361] J.P. Couzinié, L. Lilensten, Y. Champion, G. Dirras, L. Perrière, I. Guillot, On the room temperature deformation mechanisms of a TiZrHfNbTa refractory high-entropy alloy, Materials Science and Engineering: A 645 (2015) 255-263.

[362] L. Lilensten, J.P. Couzinié, L. Perrière, A. Hocini, C. Keller, G. Dirras, I. Guillot, Study of a bcc multi-principal element alloy: Tensile and simple shear properties and underlying deformation mechanisms, Acta Materialia 142 (2018) 131-141.

[363] 李亦庄, 黄明欣, 基于中子衍射和同步辐射 X 射线衍射的 TWIP 钢位错密度计算方法, 金属学报 56(4) (2020) 487-493.

List of figures

Fig. 1.1 Possible mixing reactions for the case of an alloy containing three principle elements [2]. 2

Fig. 1.2 (a) Schematic diagram depicting the typical microstructural features with the corresponding size [8]. (b) Scheme illustrating the connection of fundamental properties of materials to the associated deformation mechanisms, which in turn, result in the observable macroscopic mechanical behaviors [6]. (c) Room-temperature uniaxial tensile strength vs. elongation of complex concentrated alloys (CCAs), categorized according to the presence of constituent phases [6]......... 4

Fig. 1.3 (a) The formation of tangled dislocations, forming dislocation cell structures at a true strain of ~22% at room temperature, leading to forest hardening [9]. (b) In-situ TEM snapshots showing a sequence of gliding dislocations ($\{111\}\langle 110\rangle$) activated under external loading [10]. (c) Representative TEM images showing the formation of deformation twinning in a CrMnFeCoNi CCA when strained to ~9% under cryogenic condition (77 K) [9]. 5

Fig. 1.4 (a) Differential displacement maps for the non-degenerate core structure as a function of shear stress (τ) [15]. (b) Schematic diagram demonstrating the composite slip in RCCA, where slip producing macroscopic strain on one particular $\{110\}$ plane is accompanied by the second system to fulfill the boundary conditions [16]. (c) The yield strength of refractory alloys as a function of temperature and T/T_{liquid}, where T_{liquid} denotes the melting temperature, showing the high strength of this class of RCCA across the entire temperature spectrum [19]. 7

Fig. 1.5 (a) Illustrations of the prototypical body-centered cubic (BCC) lattice structure of a refractory complex concentrated alloy (RCCA) consisting of four principle elements [23]. Two kinds of interstitial sites (tetrahedral and octahedral) are pointed out with red spheres. (b) Scheme showing the various microstructural features in RCCA and the possible accommodation sites for interstitial atoms [23]. 9

Fig. 1.6 Ellingham diagrams for (a) nitrides [36], (b) carbides [37], and (c) oxides [38]. 11

Fig. 1.7 (a) Three-dimensional elemental distribution in the as-cast NbMoTaW RCCA, illustrating the segregation of O impurities at the grain boundaries (GBs) [32]. (b) Three-dimensional elemental distribution for the B-doped NbMoTaW RCCA, showing the B segregation at the GBs [32]. (c) Three-dimensional reconstruction of a TiNbZr RCCA tip including the GB, and the corresponding 1D compositional profile following the arrow across the GB [49]. 14

Fig. 1.8 (a) Scanning transmission electron microscopy (STEM) images and the corresponding elemental distribution maps of the as-received and H-absorbed TiZrNbTa RCCA [50]. (b) Comparison of the microstructures of the TiNbZrHfTa RCCAs (left: contaminated with O, middle: no contamination, right: with the addition of 3 at.% O) aged at 900 °C for 1000 h [34]. (c) Image quality map and the corresponding electron backscattered diffraction (EBSD) phase map of the as-cast NbMoTaWHfN RCCA [53]. 16

Fig. 1.9 (a) STEM-HAADF image revealing the existence of the ordered oxygen complexes in $(TiZrHfNb)_{98}O_2$ alloy, and the associated dislocation pinning occurring at these ordered oxygen complexes [33]. (b) Schematic diagram for the design of ordered oxygen complexes, and the 3D reconstruction of ordered oxygen complexes obtained in $TiZr_{30}Nb_{26}O_3$, along with their pinning effects on dislocations [62]. (c) Representative STEM-BF image and (d) TEM image, along with the marked selected-area electron diffraction (SAED) patterns of the O-incorporated TiVHfNb RCCA [52]. 18

Fig. 2.1 Scheme depicting the processing of as-received (or as-homogenized) equiatomic TiNbZr and TiNbZrHfTa refractory complex concentrated alloys (RCCAs). 20

Fig. 2.2 Overviews of the (a) dilatometer (DIL 805, TA Instruments), (b) tensile rig (Kammrath & Weiss stage) equipped with an optical camera for digital image correction (DIC), and (c) set-up for in-situ tensile test at Powder Diffraction and Total Scattering Beamline P02.1 of PETRA III, at Deutsches Elektronen Synchrotron (DESY, Hamburg, Germany) employed in this study [70]. 21

Fig. 2.3 (a) Schematics illustrating the basic circuit and principle of the equipment using the thermal conductivity detector (TCD) method [https://www.horiba.com/int/process-and-environmental/measuring-principles/thermal-conductivity-detector/#TCD-0]. (b) Overview of the thermal desorption spectroscopy (TDS) for determining the dissolved hydrogen, nitrogen, and oxygen contents. 23

Fig. 2.4 Schematics depicting (a) the comparison between scattered beams stemming from one single crystal (top) and a powder (bottom) and (b) the simplified derivation of Bragg's law. (c) Optical train with the major optical elements and the associated distances to the undulator at Powder Diffraction and Total Scattering Beamline P02.1 of PETRA III, at DESY (Hamburg, Germany) [70]. (d) Snapshot of the beamline P02.1 and the corresponding in-situ setup for heat treatment under H_2 and Ar. 24

Fig. 2.5 Schematic representation of scattering patterns for: (a) diluted, randomly oriented rod-like cylindrical particles, (b) non-interacting but oriented rod-like cylindrical particles, (c) concentrated hexagonal cylindrical clusters that are randomly oriented, and (d) concentrated hexagonal cylindrical clusters that are oriented, respectively. (e) Illustration of the Diffraction & Imaging at the Swedish Beamline P21.2 of PETRA III, at DESY (Hamburg, Germany) for in-situ deformation test coupled with WAXS/SAXS study. Insert is the snapshot of the Beamline P21.2 [78]. 26

Fig. 2.6 (a) Illustration showing the interaction between the primary beam and the specimen in scanning electron microscopy (SEM), generating multiple species for imaging and chemical composition determination [From Wikipedia]. (b) Overview of the used SEM in this study. 27

Fig. 2.7 (a) The basic pinciples of backscttering and forward scattering for SEM [81]. Illustration showing the (b) formation of (backscatter) Kikuchi patterns due to the interaction of the electron beam with specimen, and (c) the corresponding backscattering profile for the two-beam case. 30

Fig. 2.8 Schematic drawing of the principles of micrograph and diffraction modes in a transmission electron microscopy (TEM) [81]. 33

Fig. 2.9 Schematics of (a) working mechanism of an atom probe tomography (APT) with a straight flight-path instrument, and (b) field evaporation and post-ionization processes in the case of a metal [8]. (c) Overview of the local electrode atom probe (LEAP 5000 XR) used for the study. UHV denotes ultra-high vacuum. 34

Fig. 2.10 (a) The developed cryogenic APT infrastructure in Max Planck Institute for Sustainable Materials. (b) Overall mass spectrum and (c) the corresponding sectioned mass spectrum of an acquired dataset of D_2O ice [87]. (d) Three-dimensional reconstruction map of D_2O. Insert shows the SEM image of the prepared tip for APT measurement [87]...............35

Fig. 2.11 Schematic diagrams illustrating (a) the visualization of the Hohenberg-Kohn theorem, and (b) the framework of DFT computational methods [90]..37

Fig. 3.1 Schematic illustration of the experimental setup of the in-situ synchrotron high-energy X-ray diffraction (B_I and B_D indicate the vectors of the incident and diffracted beams, respectively; D is the distance between the sample and the two-dimensional detector; $2\theta_{hkl}$ indicates scattering angle; Q stands for the scattering vector). Insert figure (marked by the black dash box) shows the integrated diffractogram of pristine TiNbZr powders at 30 °C, demonstrating a single body-centered cubic (BCC) structure with a lattice parameter of 3.3836 Å...42

Fig. 3.2 Secondary electron images of (a) TiNbZr powder and (b) a particle at high magnification in the pristine state. (c) The corresponding size distribution measured from (a) using the software ImageJ over 200 particles. (d) Backscattered electron imaging of a particle and the corresponding individual elemental maps of Ti, Nb, and Zr probed by electron dispersive spectroscopy. (e) Elemental distribution across dendrites along the red arrow in (d). (f) Inverse pole figure (IPF), image quality overlaid with grain boundaries (IQ + GB), and kernel average misorientation (KAM) maps of the particle probed by the electron backscatter diffraction. The red arrow in (f) represents the the same line scan in (d)...............................44

Fig. 3.3 Contour maps of the diffraction intensity integrated over the azimuth angle of 180° probed by in-situ high-energy X-ray diffraction (HEXRD) during heat treatment of the TiNbZr alloy in (a) H_2 and (c) Ar. (b) and (d)The corresponding temperature profiles. HEXRD profiles of the sample treated in H_2 for (e1) 1700 s, (e2) 1800 s, (e3) 1900 s (at the beginning of the isothermal process at 500 °C), (f1) 3800 s, (f2) 4000 s, and (f3) 4200 s (upon cooling). (g) Lattice parameter and the relative change (*Δ*) in the lattice parameters of the sample during heating from room temperature to 500 °C in H_2..45

Fig. 3.4 Deconvoluted BCC_{110} peaks of the sample treated in H_2 at 500 °C for (a) 1700 s (starting time for isothermal heat treatment), (b) 1800 s (isothermal holding for 100 s), and (c) 1900 s (isothermal holding for 200 s). (d) Evolution of the lattice parameters (Here the initial time point (0 s) represents 1700 s during the elapsed time for the HEXRD experiment, which is the starting point for isothermal heat treatment). (e) Detailed view of lattice parameters and (f) corresponding fractions of multiple BCC structures in the early stage of the hydrogen uptake. (g) Schematic diagram showing the gradual expansion of the BCC lattices during the isothermal heat treatment process at 500 °C. a and XH represent lattice parameter and hydrogen concentration, respectively. 48

Fig. 3.5 Deconvoluted {110} peak of the sample treated in H_2 during cooling at (a) 3800 s, (b) 4000 s, and (c) 4200 s (elapsed time). The evolution of (d) lattice parameters and (e) phase fractions of the deconvoluted BCC, BCT-1 and BCT-2 crystal structures.............................49

Fig. 3.6 (a) A representative high-resolution TEM (HRTEM) image of TiNbZr powder after heat treatment in H_2 with the zone direction of [001], along with (b) its corresponding Fast Fourier transform (FFT) pattern and (c) inverse FFT (IFFT) image of the body-centered tetragonal (BCT) crystal structure. (d) Simulated selected area electron diffraction (SAED) pattern of the coexistence of body-centered cubic (BCC) and BCT crystal structures along the [001] zone axis...50

Fig. 3.7 Relative volume change of the crystal lattices in TiNbZr samples treated in H_2 and Ar. 52

Fig. 3.8 Secondary electron images of (a) TiNbZr particles and (b) an individual TiNbZr particle after the treatment in H_2. (c) Size distribution of the TiNbZr particles. (d) Backscattered electron imaging of a particle and the corresponding elemental maps of Ti, Nb, and Zr probed by electron dispersive spectroscopy. (e) Elemental distribution across dendrites, as marked by the red arrow in (d). (f) Inverse pole figure (IPF), image quality overlaid with grain boundaries (IQ + GB), and kernel average misorientation (KAM) maps of the particle probed by the electron backscatter diffraction. The red arrow in (f) represents the same scan in (d)...........53

Fig. 3.9 Statistical distribution of solution enthalpy per hydrogen atom in a TiNbZr special quasirandom supercell after a full stress relaxation with one hydrogen atom initially positioned at all possible (a) octahedral interstitial sites and (b) tetrahedral interstitial sites. Corresponding distribution of relaxed hydrogen states in (c) octahedral and (d) tetrahedral sites. DFT calculations were conducted with a 3 × 3 × 3 supercell (54 metallic atoms) at T=0 K. (e) Calculated frequency for the tetrahedral and octahedral occupancy assuming a Fermi-Dirac distribution of energy states in the case of dilute and concentrated hydrogen solution corresponding to 1 and 45 hydrogen atoms in the supercell, respectively (hydrogen mole fraction: 2 at.% and 45.4 at.%, respectively). 56

Fig. 3.10 (a) Statistical distribution of calculated solution enthalpy per hydrogen atom before and after atomic relaxation when 45 hydrogen atoms are positioned at octahedral or tetrahedral sites in a supercell with 54 metal atoms. The data has been obtained from DFT calculations. (b) Statistical distribution of calculated c/a ratio with all hydrogen initially settling at the tetrahedral and octahedral sites after relaxation based on DFT calculations. DFT calculations were conducted with a 3 × 3 × 3 supercell (54 metallic atoms) at T=0 K. 58

Fig. 3.11 (a) The proposed lattice configurations, which are possible to result in lattice tetragonality, namely, the asymmetric expansion along the c-axis. Scenario I with all hydrogen atoms positioned at the tetrahedral (0, 12, 14) and (0, 12, 34) sites (In this case, only half of the marked sites are occupied by hydrogen atoms), while about all hydrogen atoms are located at the octahedral sites (hydrogen occupancy: (0, 0, 12) and (12, 12, 0)) in Scenario II. Statistical distribution of (b) calculated solution enthalpy per hydrogen atom and (c) calculated c/a ratio of Scenario I and Scenario II after stress relaxation. DFT calculations were conducted with a 3 × 3 × 3 supercell (54 metallic atoms) at T=0 K. 60

Fig. 3.12 Calculated statistical distribution of the hydrogen solution enthalpy per hydrogen atom of TiNbZr with one hydrogen solute relaxed to either tetrahedral interstitial sites or octahedral interstitial sites surrounded by different amounts of nearest neighbor (a, d) Ti atoms, (b, e) Nb atoms and (c, f) Zr atoms. DFT calculations were conducted with a 3×3×3 supercell (54 metallic atoms) at T=0 K. 63

Fig. S3.1 Morphological statistic of TiNbZr powders determined from **Fig. 3.2**a, showing up to 94.4% of the prepared TiNbZr powders are spherical. Therefore, in this study, we can exclude the effects of size morphology on the microstructural evolution. 65

Fig. S3.2 Elemental distribution of all constituent elements (Ti, Nb, and Zr) across different particles. More specifically, in total 20 line scans are performed on 10 particles (2 line scans per particle). The mean and standard deviation values of each line scan are presented in the figure. 65

Fig. S3.3 Overall contour map of the intensity integrated over azimuth angle from 5° to 355° for the calibrant (LaB6). All the lines shown are relatively straightforward, indicating the good quality of the synchrotron experiment. 66

Fig. S3.4 (a) Overall and (b) local pair distribution function (PDF) profiles of the TiNbZr powders during H_2 charging. (c) Peak widths (σ) and (d) interatomic distance for the first three coordination shells. 66

Fig. S3.5 (a) Overall and (b) local pair distribution function (PDF) profiles for the TiNbZr powders under Ar flow at different times. 67

Fig. S3.6 Evolution of the lattice parameters of TiNbZr powders with pure Ar flow (a) during heating, (b) the isothermal heat treatment (500 °C), and (c) cooling. 67

Fig. S3.7 Diffractograms of TiNbZr powders upon isothermal heat treatment (500 °C) with H_2 charging at 2000 s, 2500 s, and 3000 s. No obvious changes in shapes and positions are detected from 2000 s (isothermal holding for 400 s) on. 68

Fig. S3.8 Overall Rietveld refinement profiles of the X-ray diffractograms of the H_2-charged TiNbZr powders at (a) 1700 s, (b) 1800 s, (c) 1900 s, (d) 3800 s, (e) 4000 s, and (f) 4200 s. The weighted profile R-factor (R_{wp}) values for all the refinements are below 10.0%, indicating the high reliability of the refinement results. 68

Fig. S3.9 Change of local Debye-Scherrer rings on (110) peaks of the H_2-charged TiNbZr powders during the isothermal process (500 °C), implying the gradual transition of the lattice structure and the co-existence of the BCC structures with different lattice parameters (indicated by white circles). The yellow arrow indicates the evolution direction from left to right of the Debye-Scherrer rings, indicating the gradual increase of the lattice parameters. One intense yellow spot indicates one series of specific crystal planes. 69

Fig. S3.10 Change of local Debye-Scherrer rings on (110) peaks of the H_2-charged TiNbZr powders during the isothermal process (500 °C). Data was collected every 5 s. Following the trajectory of ①, the intense spots on the left sides gradually disappear, indicating that the proportion of original (110) crystal planes with smaller lattice parameters decreases, whereas the gradual enhancement of the intensity of the spots on the right sides is detected following the trajectory of ②, showing the increase of the (110) crystal planes with larger lattice parameters. Meanwhile, although some intense spots have reached the rightmost region of the ring, they disappear during the isothermal process. This may be ascribed to the fact that not all H is trapped in stable sites during hydrogenation. Following the trajectory of ③, the gradual transition of the intense spot from the left side to the right is observed, demonstrating the sequential expansion of the lattice structure during the isothermal process. 69

Fig. S3.11 Local Debye-Scherrer rings on different peaks of the TiNbZr powders after high-temperature H_2 charging for 40 s and 1825 s. All rings display similar phenomena with the broadening of rings and co-existence of a series of intense spots along the rings. 70

Fig. S3.12 The change of c/a ratio upon cooling for BCT-1 and BCT-2 crystal structures inside TiNbZr alloy while charging with pure H_2 flow. 70

Fig. S3.13 Diffractograms of TiNbZr powders while charging with Ar for 100 s, 1800 s, and 3600 s, the related temperatures are also indicated. No obvious changes in shapes and positions are detected during the whole process of the Ar-charged TiNbZr powders. 71

Fig. S3.14 (a) Representative TEM images of TiNbZr powder after heat treatment in H_2 along the [113] zone axis, and (b) its corresponding Fast Fourier transform (FFT) pattern. (c) Simulated SAED pattern of the coexistence of BCC and BCT crystal structures along the [113] zone axis. The split of diffraction spots can be observed from the experimental SAED pattern, indicating the coexistence of BCC (a = 3.385 Å) and BCT (a = 3.335 Å and c = 3.462 Å) crystal structures. The c/a ratio is calculated to be around 1.04. The simulated SAED pattern also confirms the coexistence of BCC and BCT crystal structures. 71

Fig. S3.15 Calculated liquidus temperature of the TiNbZr ternary alloy systems based on TCTI2 database by using Thermo-Calc 2024b. Iso-temperature lines indicating the onset of solidification (from the melt) are presented in the figure, with temperatures given in Kelvin (K). 72

Fig. S3.16 Inverse pole figure (IPF, left), image quality overlaid with grain boundaries (IQ + GB, middle), and kernel average misorientation (KAM, right) maps of the particle after the heat treatment under Ar. 72

Fig. S3.17 (a) Calculated zero-point energies (ZPE) of H for selected tetrahedral interstitial H atoms. The dashed black line shows the ZPE calculated for H_2 molecular (per H atom) using the same harmonic approximation. (b) Calculated zero-point energies (ZPE) contribution to the H solution energy. 72

Fig. S3.18 (a) Calculated H-H force as a function of H-H distance before relaxation (positive means attractive, while negative means repulsive). (b) H-H interaction energy as a function of H-H distance before relaxation. (c) calculated solution energy per H atom (averaged over two H atoms) as a function of H-H distance before/after relaxation. 73

Fig. S3.19 Frequency of the calculated volume expansion ($VH/Veq.-1$, where $Veq.$ and VH represent the volume before and after the incorporation of hydrogen solutes respectively) after each Murnaghan equation of state (EOS) fitting. 73

Fig. 4.1 (a) Overall high-energy X-ray diffraction (HEXRD) profiles and (b) enlarged view of BCC_{211} peaks of the as-received, HT-Ar, and HT-H_2 specimens. (c) The plot of $(\sin\theta)^2$ as a function of $(h^2+k^2+l^2)$ of individual HEXRD peaks to determine the lattice parameters of the As-received and HT-Ar samples. (d) Enlarged image showing the deconvolution of BCC_{211} peaks of the HT-H_2 specimen. 84

Fig. 4.2 Backscattered electron (BSE) and representative enlarged images of (a, d) As-received, (b, e) HT-Ar, and (c, f) HT-H_2 samples, respectively. Insert in (f) shows the width distribution of the region with dark (black) and bright (red) contrast. 85

Fig. 4.3 (a) Typical bright-field transmission electron microscopy (TEM) image, and corresponding (b) selected area electron diffraction pattern exhibiting a single BCC phase. The electron beam is along the [001] zone axis. Three-dimensional reconstruction map of (c) Ti distribution, Zr distribution, and superimposed Ti and Zr distribution probed by atom probe tomography (APT). (d, e) APT maps showing the Ta-rich nanofeatures in the matrix. The Ta-rich nanofeatures are highlighted using iso-concentration surfaces containing 22 at.% Ta. (f) 1D concentration profiles computed along the cyan cylinder marked in (e) with a binning size of 0.5 nm. The error bar represents the standard deviation of the counting statistics in each bin. 86

Fig. 4.4 Three-dimensional APT maps of the distribution of Ti and Zr in (a) as-received specimen and (b) HT-Ar specimen. Concentration profiles of principal elements along the yellow cylinders in (c) as-received specimen and (d) HT-Ar specimen, respectively. The fifth nearest neighboring distribution (NND) of Ti atoms of (e) as-received, (f) HT-Ar, and (g) HT-H_2 specimens, respectively. 87

Fig. 4.5 APT reconstruction of Zr iso-concentration surfaces of the specimens treated in H_2 for (a) 0.5 h, (b) 1 h, and (c) 2 h and the corresponding 2D contour plots. (d) 1D concentration profiles of Zr along the yellow cylinders marked in (a-c), the error bar represents the standard deviation of the counting statistics in each bin of the cylinder. (e) Evolution of spinodal wavelength with annealing time under H_2. 89

Fig. 4.6 (a) Image-corrected high-resolution transmission electron microscopy (HR-TEM) image of the HT-H_2 specimen along [001] zone axis. (b) Map of strain distribution (εxx) of the HT-H_2 specimen determined by geometric phase analysis (GPA) of HR-TEM image from the same area in (a). (c) Hardness (HV0.2) of as-received, HT-Ar, and HT-H_2 specimens after the heat treatment (hardness measurements were conducted one week after the heat treatment). (d) Hardness (HV0.2) evolution of specimens treated in H_2 at 500 °C for 0.5 h (HT-H_2), 1 h (HT-H_2-1h), and 2 h (HT-H_2-2h). 91

Fig. 4.7 Three-dimensional profiles of the wear surface of (a) the as-received and (b) HT-H_2-2h samples. (c) The corresponding two-dimensional cross-sectional depth profiles and (d) friction coefficients as a function of the scratch distance. (e) Averaged friction coefficients of the as-received and HT-H_2-2h samples, primarily from the (110), (100), and (111) crystallographic planes 92

Fig. 4.8 Zr composition dependence of Gibbs free energy in the TiZrHf-NbTa pseudo-binary system (a) without and (b) with the presence of hydrogen. Insert in (b) showing the existence of miscibility gap, indicated by the points where the second derivative of Gibbs free energy with respect to Zr composition is 0. (c) Eigenvalues ($\lambda 1$) as a function of temperature for TiNbZrHfTa with and without the incorporation of hydrogen. (d) Calculated vacancy concentration as a function of temperature. 95

Fig. S4.1 Normalized voltage amplitude when measuring hydrogen (a) and oxygen (b) as a function of time of as-received, HT-Ar, and HT-H_2 samples. Normalization was calculated over the individual weight of samples, Normalized amplitude. = $V_{samples}/m_{samples}$, where $V_{samples}$ is the voltage during measurement, and $m_{samples}$ is the weight of the individual measured sample. 97

Fig. S4.2 (a-c) Inverse pole figure (IPF + IQ) and (d-f) grain boundaries (GB + IQ) overlaid with the image quality of as-received, HT-Ar and HT-H_2 samples probed by the electron backscatter diffraction (EBSD), respectively. (g) Distribution of grain sizes of different samples. The pristine microstructure of TiNbZrHfTa exhibits randomly oriented grains. All the results indicate that heat treatments (500 °C) in pure Ar and H_2 have negligible effects on grain orientation, low / high-angle grain boundary fractions, and grain size. 97

Fig. S4.3 Individual elemental maps of Ti, Nb, Zr, Hf, and Ta of the (a) as-received, (b) HT-Ar, and (HT-H_2) samples probed by electron dispersive spectroscopy (EDS). All of the principal elements are evenly distributed without obvious partitioning or segregation phenomena. 98

Fig. S4.4 μ values determined from the frequency distribution analysis (FDA)[205] of each principal element in as-received, HT-Ar, and HT-H_2 specimens. 98

Fig. S4.5 High-energy X-ray diffraction (HEXRD) profiles of specimens after heat treatment in H_2 for 1 h (HT-H_2-1h) and 2 h (HT-H_2-2h). Both two specimens exhibit a single body-centered cubic crystal structure without the formation of secondary phases, such as hydride. 99

Fig. S4.6 Representative autocorrelation coefficient profiles of Zr for comparison. 99

Fig. S4.7 Residual cross-sectional profiles for the as-received TiNbZrHfTa and HT-H_2, 2 h alloys. hpH, and hrH represent the pile-up height and residual height for the HT-H_2, 2h sample respectively, while h_p and h_r represent the pile-up height and residual height for the as-received TiNbZrHfTa alloy respectively. These values will be used in the calculation for the strain hardening exponent (n) and yield strength (σ_y). 100

Fig. 5.1 Representative scanning electron microscopy (SEM) images of the (a) B-free and (b) B-doped TiNbZrHfTa CCAs, and their corresponding energy-dispersive X-ray spectroscopy (EDS) mapping of individual principal elements. The regions for EDS mapping are indicated by white dashed lines. The inserts represent the grain size distribution obtained over 50 grains from (a) and (b), respectively. 113

Fig. 5.2 (a) Synchrotron high-energy X-ray diffraction (HEXRD) profiles of the TiNbZrHfTa CCAs without and with 30 ppm B. (b) Plots of βcosθ versus 4sinθ and their corresponding linear-fitted curves. β represents the full width of half maximum (FWHM) while θ is the diffraction angle. (c) Calculated dislocation density of the TiNbZrHfTa CCAs without and with 30 ppm B. 114

Fig. 5.3 Atom probe tomography (APT) analysis for the grain boundary of TiNbZrHfTa CCAs with (a-d) 0 ppm B and (e-h) 30 ppm B. Grain boundaries are indicated by black arrows. B atomic distribution (in blue) with a 0.08 at.% and 0.80 at.% B isosurface for TiNbZrHfTa CCAs containing (b) 0 ppm B and (f) 30 ppm B, respectively. Insert in (f) shows the enrichment of B atoms (depicted in spheres) within the grain boundary. 1D concentration profiles of B, Ti, Zr, Hf, Nb, and Ta across the grain boundary of the TiNbZrHfTa CCAs containing (d) 0 ppm B and (h) 30 ppm B as highlighted with a 25-nm cylinder of purple cylinders. Red arrows indicate the direction of the cylinders........ 115

Fig. 5.4 (a) Engineering stress-strain curves of the TiNbZrHfTa CCAs with 0 and 30 ppm B. The mean values (shown as open circles) and corresponding scale bars are obtained over three repeated tests. Insert is the enlarged view of the strain range from 0.5 % to 3.0 %, revealing the yield strength softening after the addition of 30 ppm B. (b) Strain-hardening rates as a function of true strain. 116

Fig. 5.5 Representative B-doped grains at a global strain of 2% with (a) multiple-slip activity and (b) cross-slip activity and the corresponding inverse pole figure (IPF) maps as well as the slip trace analysis for identifying the operating slip systems, respectively. (c) Observation of grain boundary shear localization acquired at an incident plastic deformation (2% strain). The top insert in (c) is the SEM image of the cross-sectional view of the grain couple with a tilt angle of 52°, showing the height misfit between the adjacent two grains (marked with G1 and G2). The bottom insert in (c) is the post-processed SEM image with a color transform using blue lookup table, revealing the sharp increase in contrast at the grain boundary region. (d) The gray values across the grain boundary as highlighted by a red arrow in (c)........ 117

Fig. 5.6 (a) Calculated activation energy for grain growth as a function of B concentration. *: data used in the calculation is shown in **Fig. S11**. (b) Calculated shear modulus across the GB with the composition obtained from APT analysis. (c) Hall-Petch constant of non-B sample over Hall-Petch constant of B-containing sample ($KyB/KynoB$) plotted against Zr concentration. 120

Fig. 5.7 Scheme diagrams showing the competition effect between B and Zr on yield strength: (a) The strengthening effect of B is the dominant part, contributing to the continuous increment of yield strength; (b) The strengthening effect from B and the weakening effect from Zr is comparable, so there exists a crossover point from the combination effect. (c) The weakening effect from Zr is dominant, thus leading to a drop of yield strength as compared to the non-B sample. 121

Fig. 5.8 Statistical analysis of plastic accommodation modes of TiNbZrHfTa CCAs with (a) 0 ppm B, and (b) 30 ppm B at a strain of 2%. Quantitative assessments of the (c) activated slip systems and (d) plastic accommodation modes of both the TiNbZrHfTa CCAs with 0 ppm B and 30 ppm B. (e) Further assessment of the GB shear localization frequency versus the types of GBs. LAGB and HAGB represent the low-angle GB and high-angle GB, respectively. .. 123

Fig. 5.9 Kernel average misorientation (KAM) maps of the TiNbZrHfTa CCAs with (a) 0 ppm B and (d) 30 ppm B, and the corresponding exemplary KAM maps of the (b, e) grain interior regions and (c, f) GB regions subjected to the regression analysis, respectively. Lognormal regression analysis for the corresponding KAM maps of the (g) grain interior regions and (h) GB regions. 125

Fig. 5.10 Statistical analysis of slip transfer activities of TiNbZrHfTa CCAs with (a) 0 ppm B, and (b) 30 ppm B at a strain of 2%. (c) Scheme diagram demonstrating the competition between slip transfer and GB shear localization. (d) Luster-Morris factor (m') versus misorientation angle for all surveyed grain couples. (e) Geometric correlation chart concerning the angles between slip directions and slip planes for all the surveyed grain couples with slip transfer. 128

Fig. S5.1 EBSD image quality (IQ) overleid with inverse pole figure (IPF) maps and grain boundary (GB) maps of the TiNbZrHfTa CCAs with 0 ppm B and 30 ppm B, respectively. The EBSD scans were acquired at the undeformed regions. 131

Fig. S5.2 Calculated $(\sin\theta)^2$ as a function of $h^2+k^2+l^2$ for the determination of lattice parameters. The typical Bragg's equation is used: $sin\theta 2 = \lambda 24a2h2 + k2 + l2$, where θ, λ, and a represent the diffraction angle, wavelength and lattice parameter respectively, while h, k, l is the Miller indices of the crystallographic plane. Through the slope (S_k) from the linear fitting curve, we can solve the lattice parameter, $a = \lambda 24Sk$. 131

Fig. S5.3 Left: SEM images showing the lift-out position of the lamellar for APT tips with targeted grain boundaries and the corresponding Kikuchi patterns for the adjacent grains. Right: EBSD scans of the same regions shown on the left revealing the misorientation angle of the grain boundaries. The white regions shown in the EBSD maps are due to the contamination of the Ga^+ source during the lift-out of the lamellar. Both the grain boundaries are high-angle grain boundaries with an identical misorientation angle of 44.57° and 47.10° for the 0 ppm B and 30 ppm B samples, respectively. 132

Fig. S5.4 3D dimensional atomic distribution including all the principle elements (Ti, Nb, Zr, Hf, Ta) as well as boron (B) of the TiNbZrHfTa CCAs with 0 ppm B and 30 ppm B. Grain boundaries in both cases are marked with black arrows. 132

Fig. S5.5 The standards used for the determination of different slip activities. For the single slip activity, the fast-Fourier transform (FFT) shows a single-line pattern, while a two-line FFT pattern (intersected with a certain degree) is revealed for the multi slip activity. As for the cross slip, the FFT pattern is diffuse without sharp lines. 133

Fig. S5.6 Typical grain with grain boundary shear localization activity (with a high-angle grain boundary), and the corresponding crystallographic assessment of the slip traces on both grains. 133

Fig. S5.7 Typical grain with grain boundary shear localization activity (with a low-angle grain boundary), and the corresponding crystallographic assessment of the slip trace. 134

Fig. S5.8 Typical grain with grain boundary shear localization activity (with a high-angle grain boundary), and the corresponding crystallographic assessment of the slip trace. 134

Fig. S5.9 Typical grain with grain boundary shear localization activity (with a high-angle grain boundary), and the corresponding crystallographic assessment of the slip traces on both grains. 135

Fig. S5.10 1st derivative of the gray value obtained in **Fig. 5.7**d. In our study, we utilize the first derivative of the gray value as a standard to detect the presence of grain boundary shear localization within the grain boundary region. When the absolute value of the first derivative exceeds 20, we identify it as grain boundary shear localization. 135

Fig. S5.11 Grain size as a function of boron concentration. For the 500 ppm and 1500 ppm cases, the potential formation of borides could also exert the Zener pining effects on the growth of grain boundaries. 136

Fig. S5.12 Representative SEM images of the B-doped TiNbZrHfTa sample showing the dislocation behavior with a global strain of approximately 1.2% (after yielding). (a) The whole grain that we are interested in, where the grain boundary region and grain interior region are enlarged in (b) and (c) respectively to investigate the origin for dislocation emission. (d) Enlarged view of the rectangle region in (b). Dislocation channeling behavior can be observed, while the 121111 slip system is activated with a Schimid factor (m) of 0.4891. 136

Fig. S5.13 (a) Synchrotron high-energy X-ray diffraction (SHEXRD) profiles of the TiNbZrHfTa CCAs with 0 ppm B and 30 ppm B at deformed region (0.5 mm away from fracture). No formation of secondary phases is found after the tensile test. (b) $\beta\cos\theta$ versus $4\sin\theta$ and the corresponding linear fitting curves for the determination of dislocation density. (c) Calculated dislocation density of the TiNbZrHfTa CCAs with 0 ppm B and 30 ppm B at the deformed region. 137

Fig. S5.14 EBSD IQ + IPF maps and IQ + GB maps of the TiNbZrHfTa CCAs with 0 ppm B and 30 ppm B at the deformed region (0.5 mm away from the fracture), respectively. 137

Fig. S5.15 (a) Quantitative assessment of the slip trace direction with the grain boundary for the grain boundary shear localization cases in the TiNbZrHfTa CCA with 30 ppm B. Single: slip is activated on only one grain; Multiple: slips are activated on both two grains and they are all parallel or non-parallel with the grain boundary. Mixed: slips are activated on both two grains. In this case, slip is parallel to grain boundary in one grain while slip is non-parallel to grain boundary in the other grain. (b) Frequency of the GB shear localization versus the misorientation between two grains in the TiNbZrHfTa CCA with 30 ppm B. (c1-c3) Some representative grain couples with grain boundary shear localization activity, where the slip traces on either side of the grains are parallel with the grain boundary. 138

Fig. S5.16 Fractography analysis of the TiNbZrHfTa CCAs with (a) 0 ppm B and (b) 30 ppm B. (c) Dimple size distribution of the TiNbZrHfTa CCAs with 0 ppm B and 30 ppm B. Over 100 dimples were used for statistical analysis, and we noted both cases exhibited a ductile fracture behavior with micro-size dimples, and no significant change on dimple sizes was found between two cases. 138

Fig. 6.1 (a) Scheme depicting the processing of equiatomic TiNbZr complex concentrated alloys (CCAs) after homogenization and induction treatment. (b) The induction heated tube furnace used for induction treatment in this study. 148

Fig. 6.2 (a) High-energy X-ray diffraction (HEXRD) profiles of the samples after homogenization and induction treatment. The inserted table in (a) shows the measured lattice parameters (a). (b) Normalized voltage amplitude when measuring oxygen (a) and nitrogen (c) as a function of the time of the samples after homogenization and induction treatment. 151

Fig. 6.3 Backscattered electron (BSE) images and the corresponding energy dispersive X-ray spectroscopy (EDS) mapping of the principle elements of the samples after homogenization (a) and induction treatment (b). (c) The distribution of grain sizes of the homogenization and induction treatment samples. The distribution is fitted with a Lognormal function to obtain the mean and standard deviation values. 152

Fig. 6.4 (a) Engineering stress-strain curves and the corresponding (b) Kocks-Mecking plots (strain-hardening rate as a function of $\sigma f - \sigma y$) of the samples after homogenization and induction treatment. Inserts in (a) show the corresponding deformation behaviors acquired one frame prior to fracture. σf, and σy denote the flow stress and the yield stress, respectively. 153

Fig. 6.5 Electron channeling contrast imaging (ECCI) of the dislocation behaviors and the corresponding magnified ECC images of the samples after (a) homogenization and (b) induction treatment. Note that the obvious pinning points are marked by red arrows. (c) Scheme diagram illustrating the change of dislocation behaviors after induction treatment. 154

Fig. 6.6 Three-dimensional elemental distributions of the principle elements, and the corresponding 1D concentration profiles for the samples after (a, b) homogenization, and (d, e) induction treatment, respectively. The 1D concentration profiles are obtained following the blue columns (10 nm in diameter) in (a) and (d) with a binning size of 0.5 nm. Ti distribution and the Ti-enriched regions delineated by iso-concentration surfaces containing 38.5 at.% of Ti for the samples after (c) homogenization, and (f) induction treatment. Insert is a table showing the volume density of the Ti-enrich features. 155

Fig. 6.7 (a) A highly magnified view of a single particle from the APT results in **Fig. 6.6**f, along with its approximate geometric shape. (b) Small-angle X-ray diffraction (SAXS) profiles of the samples after homogenization and induction treatment, and the corresponding fitting curves using an ellipsoid model. Inserts are the two-dimensional SAXS patterns. 156

Fig. 6.8 BSE images and the corresponding inverse pole figures overlaid with image quality (IPF + IQ) maps of the samples after (a, b) homogenization and (e, f) induction treatment. The images are captured both at the regions close to fracture with a similar local strain of ~70%. Inserts in (b) and (f) are the kernel average misorientation (KAM) maps. (c, d, g, h) Quantitative misorientation line profiles excerpted from (b) and (f). 158

Fig. 6.9 (a) BSE image, and the corresponding (b) IPF + IQ and (c) KAM maps of the induction-treated sample at the necking region. (d, e) Quantitative misorientation line profiles following the direction of arrows in (b). 159

Fig. 6.10 (a) Schematic detailing a dislocation advancing in a field of pointlike slip obstacles (equilibrium state: $\sigma = \tau$, where σ and τ indicate the applied stress and shear strength, respectively). (b) The interspacing (l) of the obstacles and (c) the bowing angle (θ_c) of the dislocations statistically analyzed over 50 dislocations for the samples after homogenization and induction treatment. 160

Fig. 6.11 (a) Measured strain rate sensitivities (m) and (b) apparent activation volumes ($V_{app.}$) of the samples after homogenization and induction treatment with respect to increasing true plastic strain. (c) Haasen plots of the samples after homogenization and induction treatment 163

Fig. S6.1 EBSD scans of the samples after (left) homogenization and (right) induction treatment. 165

Fig. S6.2 Cross-sectional views of the tensile samples after (a) homogenization and (b) induction treatment. (c) Statistical analysis of the amount and width of deformation bands from the regions with identical local strains. 165

Fig. S6.3 Fractography of the samples after homogenization and induction treatment. The ductile regions with dimple structures are indicated by red dash lines. Insert table shows the fraction of the ductile and brittle regions. The sample after induction treatment displays larger ductile region as compared with that of homogenized one, suggesting a good ductility. 166

Fig. S6.4 The distributions of dimple size of the samples after homogenization and induction treatment. The dimple sizes are 5.41±1.78 μm and 4.50±1.60 μm for the homogenized and induction-treated samples, respectively. 166

Fig. S6.5 (a) High-energy X-ray diffraction (HEXRD) profiles of the homogenized and induction-treated samples captured at the undeformed and derformed (close to fracture) regions. (b) Plots of $\beta cos\theta$ as a function of $4sin\theta$ and their corresponding linear-fitted curves. β represents the full width of half maximum (FWHM) while θ is the diffraction angle. (c) Calculated dislocation density (ρ) at the undeformed and derformed (close to fracture) regions for samples after homogenization and induction treatment. 167

Fig. S6.6 Debye-Scherrer rings of the induction-treated sample during in-situ tensile tests. The snapshots of the two-dimensional diffractograms with a global strain (ε) of 0, ~2, ~5, and ~10% are shown here. Only single BCC crystal structure is observed during the deformation, without the occurrence of martensite transformation (α''). 168

Fig. S6.7 Cross-sectional SEM images of the tensile samples after fracture to evaluate the damage tolerance of the samples after homogenization and induction treatment. No obvious voids can be observed for both samples after homogenization and induction treatment, suggesting that damage tolerance is not the predominant reason for the increase in toal elongation. 168

Fig. S6.8 Strain rate jump test of the as-homogenized and induction-treated samples. Insert is the enlarged image of the first jump during the tensile test. A strain rate of $2.5 \times 10 - 5$ s^{-1} was used for the down jump, while the strain rate of the up jump is $2.5 \times 10 - 3$ s^{-1}. More details regarding the strain rate jump test can be found in the main text. 169

Fig. 7.1 Preliminary results: In-situ SAXS data of the TiNbZrHfTa RCCA during the heat treatment (at 500 °C) with and without H...175

Fig. 7.2 Preliminary results on TiNbZrHfTa RCCAs: (a) Engineering stress-strain curves of the as-received, HT-Ar, and HT-H_2 samples, and the corresponding images illustrating the fracture surfaces. (b) Three-dimensional reconstruction of the elemental distribution of the sample after heat treatment in H_2 for 2 h, showing a Zr segregation behavior at GB. 176

Fig. 7.3 Preliminary results: (Top) After exposure TiNbZr RCCA to the atmospheric environment (at ~740 °C), the formation of GB secondary phases can be observed. The in-situ HEXRD data reveals a complex reaction, where two BCC phases enriched in different constituent elements are found, while the formation of HCP and oxide phases is also detected during the heating process. (Bottom) The consequent microstructure after the interaction with N (NH_3, at 700 °C) is shown, where the formation of nanoscale features can be found.......178

List of tables

Table 1.1 The values of mixing enthalpy ($\Delta HABmix$, kJ/mol) between refractory elements and interstitial elements (H, B, C, and N) [35]. 10

Table S3.1 Summary of reported characteristics and hydrogen-storage performances of the TiNbZr-based CCAs. 74

Table S3.2 Chemical compositions of TiNbZr powders. The values shown in the brackets indicate the nominated values. 75

Table S3.3 The H/M ratios at 1 bar H_2 of TiNbZr MEA in our study as well as different refractory CCAs from the literature. 75

Table S3.4 Lattice parameters and volumes of the unit cell under Ar flow at different temperatures. 76

Table S3.5 Lattice parameters and volumes of unit cells under H_2 flow at different temperatures. a_1, c_1 and a_2, c_2 indicate the lattice parameters of BCT-1 and BCT-2, respectively. 77

Table S3.6 The corresponding tetrahedral and octahedral interstitial sites of TiNbZr lattice with a lattice parameter of 3.3836 Å. 78

Table S3.7 Number of hydrogen atomic configurations used to calculate statistical distributions of solution enthalpy and c/a ratio, with the distribution 45 hydrogen atoms randomly. 78

Table S4.1 The hydrogen content and oxygen content measured by thermo desorption spectrometer (TDS) of the as-received, HT-Ar, and HT-H_2 specimens, respectively. Three individual specimens were used for the TDS measurements 101

Table S4.2 The concentrations and μ values of each principal element of the as-received, HT-Ar, and HT-H_2 specimens, respectively. The concentrations and μ values shown here are calculated from the whole APT tip. The concentrations were analyzed on the basis of three individual tips 101

Table S4.3 Elastic compliance tensors of the pure β-Ti or Ti alloys with a BCC crystal structure adopted for the calculation of Gibbs free energy. 103

Table S4.4 Thermodynamic parameters adopted for binary and ternary excess free-energy calculation. The quantities shown here are all the available parameters to the best of our literature search. Part of the ternary interaction parameters, all of the quaternary, quinary and senary interaction parameters are not available. 105

Table S4.5 Vacancy formation enthalpy (Hfv) adopted for the calculation of vacancy concentration change. 107

Table S5.1 Principle element composition obtained from energy-dispersive X-ray spectroscopy (EDS) analysis 139

Table S5.2 Shear modulus (G) of each principle elements [292, 293]. 139

Table S5.3 Summary of all the grain couples with grain boundary shear localization activity observed in the TiNbZrHfTa CCA with 0 ppm B as well as the corresponding crystallographic assessment of the observed slip traces. 139

Table S5.4 Summary of all the grain couples with grain boundary shear localization activity observed in the TiNbZrHfTa CCA with 30 ppm B as well as the corresponding crystallographic assessment of the observed slip traces. 139

Table S5.5 Summary of all the grain couples where slip traces intersect with the grain boundaries in the TiNbZrHfTa CCA with 0 ppm B as well as the corresponding misorientation angle between two grains and the Luster-Morris m' factor. Cases with or without slip transfer are surveyed over 20 sets of grain couples. 140

Table S5.6 Summary of all the grain couples where slip traces intersect with the grain boundaries in the TiNbZrHfTa CCA with 30 ppm B as well as the corresponding misorientation angle between two grains and the Luster-Morris m' factor. Cases with or without slip transfer are surveyed over 20 sets of grain couples. 141

Table S5.7 Summary of the slip direction misalignments and slip plane misalignments of all the cases with slip transfer in both the non-boron and boron-doped TiNbZrHfTa CCAs alloys. 143

Table S6.1 The dissolved oxygen and nitrogen contents of the samples after homogenization and induction treatment........170

Table S6.2 The element composition of the samples after homogenization and induction treatment. 170

Table S6.3 The morphological information of the formed Ti-rich regions in the samples after homogenization and induction treatment........170

Curriculum Vitae

Chengguang Wu

Date of birth: 14th April 1996

Place of birth: Guangdong, PR China

Education

PhD candidate:

Max-Planck-Institute for Sustainable Materials (Used to be Max-Planck-Institute for Iron Research)

RWTH Aachen University

Major in Materials Science *Nov. 2021- Present*

Master degree:

Jinan university

Major in biomedical engineering *Sep. 2018 - Jun. 2021*

Bachelor degree:

Jinan university

Major in biomedical engineering *Sep. 2014 - Jun. 2018*

Research Experiences

Max-Planck-Institute for Sustainable Materials / RWTH Aachen University

PhD candidate (Supervisor: Prof. Dierk Raabe) *Nov. 2021- Present*

Research on the effects of interstitial atoms on the phase stability / mechanical properties

Jinan University

Master (Supervisor: Prof. Wei Xue) *Sep. 2018 - Jun. 2021*

Master thesis: The design of theranostic nanoplatforms for nitric oxide delivery and enhanced antitumor gas therapy

Ph.D. defense:

Chair:

Univ-Prof. Jochen M. Schneider, Ph.D.

Examiner:

1. Prof. Dr.-ing Dierk Raabe
2. Prof. Dr.-ing Yan Ma

List of publications

1. During my PhD studies

Chengguang Wu, *et al.*, Hydrogen-assisted spinodal decomposition in a TiNbZrHfTa complex concentrated alloy, *Acta Mater.* 15(285) (2025): 120707.

Chengguang Wu, *et al.*, Hydrogen accommodation and its role in lattice symmetry in a TiNbZr medium-entropy alloy, *Acta Mater.* 15(288) (2025): 120852.

Chengguang Wu, *et al.*, Role of boron in yield strength softening and plastic deformation mechanisms in a refractory high-entropy alloy, Ready for submission.

Chengguang Wu, *et al.*, Enhanced ductility in a TiNbZr alloy via nanoscale elemental heterogeneity induced by a short-term induction treatment, In preparation.

2. During my Master studies

Chengguang Wu[1], Jinglan Liang[1], *et al.*, Light-activated nitric-oxide overproduction theranostic nanoplatform based on long-circulating biomimetic nanoerythrocyte for enhanced cancer gas therapy, *Sci. China Chem.* 64(2021): 1796-1810.

Chengguang Wu[1], Xiang Wang[1], *et al.*, Transforming sustained release into on-demand release: Self-healing guanosine–borate supramolecular hydrogels with multiple responsiveness for Acyclovir delivery, *Biomater. Sci.* 8(2020): 6190-6203.

Jinglan Liang[1], **Chengguang Wu**[1], *et al.*, Host-Guest Interaction-Based Dual response core/shell nanoparticles as efficient siRNA carrier for killing breast cancer cells, *Colloids Surf. B Biointerfaces*, 205(2021): 111918.

Yinci Zhang[1], **Chengguang Wu**[1], *et al.*, Oxaliplatin and gedatolisib (PKI-587) co-loaded hollow polydopamine nano-shells with simultaneous upstream and downstream action to re-sensitize drugs-resistant hepatocellular carcinoma to chemotherapy, *J. Biomed. Nanotechnol.*, 17(1) (2021): 18-36.

Shihao Zhou, **Chengguang Wu**, *et al.*, Tumor microenvironment-responsive multifunctional nanoplatform with selective toxicity for MRI-guided photothermal/photodynamic/nitric oxide combined cancer therapy, *Chem. Eng. J.*, 481(2024): 148618.

Lingli Zhang, **Chengguang Wu**, *et al.*, A chemotherapeutic self-sensibilized drug carrier delivering paclitaxel for the enhanced chemotherapy to human breast MDA-MB-231 cells, *Colloids and Surf. B: Biointerfaces*, 181(2019): 902-909.

Haijie Zhao, Junkun Duan, Yongcheng Xiao, Guoheng Tang, **Chengguang Wu**, *et al.*, Microenvironment-driven cascaded responsive hybrid carbon dots as a multifunctional theranostic nanoplatform for imaging-traceable gene precise delivery, *Chem. Mater.*, 30(10) (2018): 3438-3453.

---

[1] These authors are contributed equally to the work as co-first authors